NOTICE

The quality of this microform is heavily dependent upon the quality of the original thesis submitted for microfilming. Every effort has been made to ensure the highest quality of reproduction possible.

If pages are missing, contact the university which granted the degree.

Some pages may have indistinct print especially if the original pages were typed with a poor typewriter ribbon or if the university sent us an inferior photocopy.

Reproduction in full or in part of this microform is governed by the Canadian Copyright Act, R.S.C. 1970, c. C-30, and subsequent amendments.

AVIS

La qualité de cette microforme dépend grandement de la qualité de la thèse soumise au microfilmage. Nous avons tout fait pour assurer une qualité supérieure de reproduction.

S'il manque des pages, veuillez communiquer avec l'université qui a conféré le grade.

La qualité d'impression de certaines pages peut laisser à désirer, surtout si les pages originales ont été dactylographiées à l'aide d'un ruban usé ou si l'université nous a fait parvenir une photocopie de qualité inférieure.

La reproduction, même partielle, de cette microforme est soumise à la Loi canadienne sur le droit d'auteur, SRC 1970, c. C-30, et ses amendements subséquents.

UNIVERSITY OF ALBERTA

Visualizations and Measurements of Laminar Flow in Complex Curved Ducts and in Heated Horizontal Rectangular Channels

by

Lei Shi

A THESIS

SUBMITTED TO THE FACULTY OF GRADUATE STUDIES AND RESEARCH

IN PARTIAL FULFILMENT OF THE REQUIREMENTS FOR THE DEGREE

OF Master of Science

Department of Mechanical Engineering

EDMONTON, ALBERTA

Spring, 1991

ISBN 0-315-66573-4

Canada

UNIVERSITY OF ALBERTA

RELEASE FORM

NAME OF AUTHOR Lei Shi

TITLE OF THESIS Visualizations and Measurements of Laminar Flow in Complex Curved Ducts and in Heated Horizontal Rectangular Channels

DEGREE FOR WHICH THESIS WAS PRESENTED Master of Science

YEAR THIS DEGREE GRANTED Spring, 1991

Permission is hereby granted to THE UNIVERSITY OF ALBERTA LIBRARY to reproduce single copies of this thesis and to lend or sell such copies for private, scholarly or scientific research purposes only.

The author reserves other publication rights, and neither the thesis nor extensive extracts from it may be printed or otherwise reproduced without the author's written permission.

(SIGNED) Lei Shi .....

PERMANENT ADDRESS:

.....

.....

.....

DATED February 8 19 91

THE UNIVERSITY OF ALBERTA

FACULTY OF GRADUATE STUDIES AND RESEARCH

The undersigned certify that they have read, and recommend to the Faculty of Graduate Studies and Research, for acceptance, a thesis entitled Visualizations and Measurements of Laminar Flow in Complex Curved Ducts and in Heated Horizontal Rectangular Channels submitted by Lei Shi in partial fulfilment of the requirements for the degree of Master of Science.

.....K.C.Cheng.....

K.C. Cheng

Supervisor

.....

M.D. Checkel

.....

P. Steffler

Date. February 8, 1991.....

Abstract

Flow visualizations and axial velocity measurements were conducted to study the laminar flow in curved ducts with and/or without offset bend. Secondary flow patterns were made visible by the smoke injection method, and photographs were taken to study the secondary flow patterns at the exit of each bend. Axial velocity profiles were measured by a hot-film anemometer along vertical and horizontal axes at the exit of each bend.

The experiments were carried out for both circular and square bends. The curvature ratio a/R_c of circular bends with 2" inside diameter was 0.2, and a/R_c=0.2, 0.4 for square bends with 2"×2" cross-section. For the experiments of flow visualization, Dean number K is varied from 25 to 350 for circular and square bends with a/R_c=0.2, and from 100 to 450 for square bends with a/R_c=0.4. The ranges of the first bend angle ψ and the second bend angle ϕ are 45, 90, 135, 180, 225°, while the offset angle θ is set at 90, 180°. For the experiments of axial velocity measurement, Dean number is 300 and 350 for circular bends, and is 350 for square bends. The offset angle is 180°.

Attention is given to the effects of Dean number K, curvature ratio a/R_c and second(offset) bends on the secondary flow patterns and on the axial velocity profiles. The developing secondary flow patterns in curved ducts with offset bends at different Dean number K are presented. The Dean's instability phenomena are observed. The developing

axial velocity profiles in s-bend are provided, and the typical velocity profiles are discussed.

The developing buoyancy force induced secondary flow patterns in the simultaneous hydrodynamic and thermal entrance region of horizontal rectangular channels heated isothermally from below and/or cooled isothermally from above were also investigated. Photographs of the secondary flow patterns with cross-sectional view are presented. The difference in flow phenomena between heating from below and cooling from above is discussed. Experiments were conducted for the following conditions: aspect ratio a/b=2 and 7, mean velocity of main stream U_m=0.1, 0.2, 0.3, 0.4m/sec., Grashof number $Gr=1.5\times10^5 \sim 5.0\times10^5$ for channel with a/b=2, and $Gr=3.6\times10^5 \sim 1.2\times10^6$ for channel with a/b=7.

Acknowledgement

The author wishes to express his sincere gratitude to Dr. K.C. Cheng, the author's research supervisor, for his devoted guidance and consultation during the course of this thesis project.

Special thanks are given to the technical staff of the Department of Mechanical Engineering for their excellent assistance.

The author also wishes to thank Dr. K. Sasaki, Akita University, Japan, for his coorperation and immeasurable help.

Finanical aid in the form of research assistantship from the Natural Sciences and Engineering Research Council of Canada throughout this research work is greatly appreciated.

The author is grateful to his mom and dad as well as his wife, Hong-Quan Liu, for their considerate understanding and support.

Table of Contents

List of Tables

List of Figures

Figure Page

Nomenclature

a	inside radius of curved pipe, or half of the side length of square curved duct, or width of a rectangular channel, m
b	height of rectangular channel, m
De	hydraulic diameter, m
E	output reading of hot-film anemometer, volt
Er	reference output reading of hot-film anemometer, volt
Gr	Grashof number, $g\beta(T_h-T_c)De^3/\nu^2$
K	Dean number, $Re(a/R_c)^{1/2}$
l	distance from the inlet of rectangular channel,m
Pr	Prandtl number, ν/κ
r	distance from the center of circular pipe cross section, m
R_c	radius of curvature of a curved duct, m
Re	Reynolds number, $U_m(2a)/\nu$, or U_mDe/ν
T_{air}	temperature of inlet air, °C
T_c	temperature of top plate, °C
T_h	temperature of bottom plate, °C
ΔT	temperature difference between heating plate and cooling plate, T_h-T_c, °C
U	local velocity of main air flow, m/sec.
U_m	mean velocity of main air flow, m/sec.
U_o	center velocity of main air flow in straight duct, m/sec.

x	coordinate of x-axis, mm
y	coordinate of y-axis, mm
z	inverse Graetz number, (1/De)/(RePr)
ϕ	angle of second(offset) bend
ψ	angle of first bend
θ	offset angle
β	coefficient of thermal expansion, 1/°K
ν	kinematic viscosity, m^2/sec.
κ	thermal diffusivity, m^2/sec.
ρ	density of air, kg/m^3

1. Introduction

1.1 Background Information

1.1.1 Laminar Flow in Curved Pipes

Laminar flow in curved pipes has been one of the most widely studied topics in fluid mechanics in recent years. Owing to the presence of secondary flow caused by centrifugal forces, the heat and momentum transfer between the fluid and its surroundings are expected to be enhanced. This is very important for various engineering applications, such as piping systems, intakes in aircraft, nuclear reactors, compact heat exchangers, etc. In recent years, blood flow in the human arterial system has been of particular interest.

In a curved duct, centrifugal forces are induced by the moving fluid in the duct. As the flow enters a curved duct, a centrifugal force of order $\rho U^2/R_c$, where U is the local fluid velocity and R_c is the radius of curvature of curved pipes, acts outward from the center of curvature on the fluid particles. Because of the no-slip condition at the wall, the axial velocity in the core region is much larger than that near the wall. To maintain the momentum balance between the centrifugal force and the pressure gradient, slower-moving fluid particles must move along paths whose radii of curvature are smaller than those of faster-moving fluid particles. This results in the onset of secondary flow

such that the fluid near the outer wall moves toward the inner wall along upper and lower walls while the fluid in the core region flows toward the outer wall. The motion of the secondary flow is then superimposed on the main axial flow and generates a helical path in the fluid motion.

Since the qualitative observation of secondary motion by Thompson [1](1876) in his explanation of the winding course of rivers, and by Eustice [2,3](1910, 1911) who demonstrated the existence of a secondary motion in a coiled pipe from dye-injection experiments, numerous studies on laminar flow in curved pipes have been made theoretically and experimentally.

Dean [4,5] made the pioneering studies and obtained the first analytical solution for the axial velocity and stream function of the secondary flow in low Dean number flow regime. He showed that the flow in curved pipes depends primarily on a single new non-dimensional parameter called Dean number,

$$K=Re(a/R_c)^{1/2} \qquad (1.1)$$

where $Re=U_m(2a)/\nu$ is the Reynolds number, a=inside radius of circular pipes, and R_c=radius of curvature of a pipe. The physical meaning of the Dean number is the ratio of square root of product of the inertial and centrifugal forces to the viscous forces.

Improved theoretical solutions were obtained by Barua [6], McConalogue and Srivastava [7], and Greenspan [8]. For

developing flow in a curved duct, Patankar, Pratap & Spalding [9], and Soh & Berger [10] reported numerical calculations of flow in a circular curved pipe.

Humphrey, Taylor and Whitelaw [11] also reported flow calculations for a square curved duct. Soh and Berger showed the appearance of an additional weak vortex pair near the inner wall of a curved circular pipe in a developing region. Dennis & Ng [12] and Nandakumar & Masliyah [13] reported non-unique solutions in their calculations of fully developed flow through a curved circular pipe. They showed that the solutions bifurcate into two branches if the Dean number exceeds some critical value. Either a one vortex pair pattern or a two pairs pattern will appear in the secondary flow at a certain Dean number, depending on which branch is followed. They also pointed out that the two-vortex-pair solution is relatively easier to obtain for a curved pipe of semicircular cross-section with flat outer wall than for a full circular curved pipe. Later, Hille, Vehrenkamp and Schulz-DuBois [14] found experimentally an additional weak vortex pair near the outer wall in the developing region of a 180° turning square bend. The flow visualization experiments by Cheng & Yuen [15] showed the two-vortex-pair secondary flow pattern at the exit plane of a 180° circular curved pipe, by inserting a needle at the outer wall at a 90° bend angle in order to provoke the observed flow pattern. Austin and Seader [16] measured the development of the axial-velocity profiles at various angular planes by

means of a hot-film anemometry system. Agrawal, Talbot and Gong [17] carried out an experimental investigation on the development of steady, laminar, incompressible flow in the entry region of a curved pipe with uniform motion entry flow.

A detailed review on curved pipe flows was conducted by Berger, Talbot & Yao [18] and by Ito [19].

Although the literature on theoretical and experimental studies on flow in curved pipes is extensive, little work has been done on flow in curved ducts with offset bends. It is noted that the literature on flow visualization studies and axial-velocity profile measurement is rather limited for such configuration. It is believed that the results of these studies will provide further physical understanding of the secondary flow structures and complement some of the theoretical studies.

1.1.2 Flow in Horizontal Rectangular Channels Heated from Below and/or Cooled from Above

Laminar flow heat transfer in rectangular channels is encountered in a wide variety of engineering applications, such as flat plate solar collectors and concentrators, compact heat exchangers, and the cooling of electronic components and circuitry. Because of its importance in various engineering applications, the problem of mixed convection flows in rectangular channels under different thermal boundary conditions has been studied both

theoretically and experimentally by many investigators in the past.

In the case of flow in a horizontal parallel-plate channel heated from below, as fluid passes through this channel, the density of the fluid near the bottom plate becomes smaller than that of the fluid at the top plate. This top-heavy situation is potentially unstable due to the bouyancy forces. If the temperature difference between the two horizontal plates is increased over a critical value, in other words, if the destabilization caused by buoyancy is large enough to overcome the stabilizing effects of viscous and thermal diffusion, convective instability occurs and longitudinal vortices are formed in the passage, resulting in the increase of convective heat transfer. If the temperature difference is increased further, the vortex rolls split and the size of each roll decreases. Eventually, the regularity of the fluid motion disappears and turbulent convection occurs.

The buoyancy effects in laminar forced convective flow over a heated horizontal semi-infinite flat were first studied by Mori [20] and by Sparrow et al. [21] independently. They considered perturbations of the two-dimensional boundary layer equations and predicted that buoyancy forces would increase heat transfer by inducing a pressure gradient. These early studies motivated further investigations. The occurrence of longitudinal vortices in natural convection boundary-layer flows along inclined

isothermal surfaces was confirmed by Sparrow and Husar [22]. Mori and Uchida [23] applied linear stability analysis to determine the onset of an infinitesimally small disturbance for fully developed laminar flow between two parallel plates. The convective instability problem concerning the onset of longitudinal vortices due to buoyancy forces for fully developed laminar forced convection between two horizontal parallel plates was studied theoretically by Nakayama et al. [24] and experimentally by Akiyama et al. [25]. Hwang and Cheng [26] theoretically determined the conditions for the onset of convective instability in a hydrodynamically fully developed but thermally developing region.

To confirm the predictions of Hwang and Cheng, some experimental studies were reported in [27, 28, 29, 30]. More recently, Cheng and Kim [31] published their results of flow visualization studies on vortex instability of natural convection flow over horizontal and slightly inclined plates. Maughan and Incropera [32] performed experiments on mixed convection heat transfer in the thermal entry region of a parallel-plate channel heated uniformly from below.

Wu and Cheng [33] determined numerically the onset of instability for fully developed Hartmann laminar flow in the thermal entrance region of horizontal parallel-plate channels. Ou et al. [34] obtained a numerical solution for laminar flow in a rectangular duct with uniform wall temperature for larger Prandtl number fluids. Chou and Lin

[36] reported their recent numerical study on convective instability in the thermal entrance region of horizontal rectangular channels.

While the past investigations have contributed much to the understanding of thermal instability for flow in rectangular channels, the experimental studies on the problem with boundary conditions of cooling from above and heating from below simultaneously are rather limited. The differences in phenomena between cooling from above and heating from below have not been reported yet. All of these are the motivations of the present studies.

1.1.3 Scope of the Study

Visualization studies on laminar flow in bends of curvature ratio a/R_c=0.2 and 0.4 with and without offset bends are presented in Chapter 2. Many photographs are provided to reveal the effects of Dean number K, second(offset) bend angle ϕ and curvature ratio a/R_c on secondary flow patterns. Attention was also given to the influence of bend geometry.

Experiments were conducted for three cases. First, circular cross-sectionl bends with curvature ratio a/R_c=0.2, Dean number K=25~350, offset angle θ=90° and 180°. Second, square cross-sectional bends with a/R_c=0.2, K=25~350, θ=90° and 180°. Third, square cross-sectional bends with a/R_c=0.4, K=100~450, θ=90° and 180°.

In Chapter 3, results of axial velocity profile measurements are presented. Axial velocity profiles were measured at the exit of each bend by a hot-film anemometer with a single hot-film sensor along vertical and horizontal axes for circular s-bends with a/R_c=0.2, K=200, 350, and for square bend with a/R_c=0.2, 0.4, K=350.

Attention was focused on the development of velocity profiles in s-bends and on effects of Dean number K, curvature ratio a/R_c and secondary flow on the axial velocity profiles.

Chapter 4 deals with the buoyancy force induced secondary flow patterns for developing laminar flow in horizontal rectangular channels with aspect ratio a/b=2 and 7. The height of the channel is 28.6 mm. Flow visualization studies were conducted for three cases, (1) heating from below with $T_c=T_{air}$=23°C, T_h=51°C, (2) cooling from above with T_c=-6, -16°C, $T_h=T_{air}$=23°C, and (3) simultaneous heating from below and cooling from above with T_c=-6, -16°C, T_h=51°C. The mean velocity U_m of the main flow in the channels was varied from 0.1 to 0.4 m/sec. for each case.

Photographs of cross-sectional view of the secondary flows are presented. The effects of aspect ratio, temperature difference and velocity of main flow were studied. The difference between heating and cooling was also discussed.

1.2 References

1. Thomson, J., "On the Origin of Windings of Rivers in Alluvial Plains, with Remarks on the Flow of Water Round Bends in Pipes", Proc. R. Soc. Lond., 1876, Vol. A25, pp. 5-8.

2. Eustice, J., "Flow of Water in Curved Pipes", Proc. R. Soc. Lond., 1910, Vol. A84, pp. 107-118.

3. Eustice, J., "Experiments of Streamline Motion in Curved Pipes", Proc. R. Soc. Lond., 1911, Vol. A85, pp. 119-131.

4. Dean, W.R., "Note on the Motion of Fluid in a Curved Pipe", Phil. Mag., 1927, Vol. 4, pp. 208-223.

5. Dean, W.R., "The Streamline Motion of Fluid in a Curved Pipe", Phil. Mag., 1928, Vol. 5, pp. 673-693.

6. Barua, S.N., "On Secondary Flow in Stationary Curved Pipes", Q. J. Mech. Appl. Math., 1963, Vol. 16, pp. 61-77.

7. McConalogue, D.J. and Srivastava, R.S., "Motion of Fluid in a Curved Tube", Proc. R. Soc. London Ser., Vol. A307, 1968, pp. 37-53.

8. Greenspan, A.D., "Secondary Flow in a Curved Tube", J. Fluid Mech., 1973, Vol. 57, pp. 167-176.

9. Patankar, S.V., Pratap, V.S. and Spalding, D. B., "Prediction of Laminar Flow and Heat Transfer in Helically Coiled Pipes", J. Fluid Mech., 1974, Vol. 62, pp. 539-551.

10. Soh, W.Y. and Berger, S.A., "Laminar Entrance Flow in a Curved Pipe", J. Fluid Mech., 1984, Vol. 148, pp. 109-135.

11. Humphrey, J.A.C., Taylor, A.M.K. & Whitelaw, J.H., "Laminar Flow in a Square Duct of Strong Curvature", J. Fluid Mech. Vol. 83, pp. 509-527.

12. Dennis, S.C.R. and Ng, M., "Dual Solution for Steady Lamimar Flow Through a Curved Tube", Q. J. Mech. Appl. Maths., 1982, Vol. 35, pp. 305-324.

13. Nandakumar, K. and Masliyah, J.H., "Bifurcation in Steady Laminar Flow Through Curved Tubes", J. Fluid Mech., 1982, Vol. 119, pp. 475-490.

14. Hille, P., Vehrenkamp, R. and Schulz-Dubois, E.O., "The Development and Structure of Primary and Secondary Flow in a Curved Square Duct", J. Fluid Mech., 1985, Vol. 151, pp. 219-241.

15. Cheng, K.C. and Yuen, F.P., "Flow Visualization Studies on Secondary Flow Patterns in Straight Tubes Downstream of a 180° Bend and Isothermally Heated Horizontal Tubes", ASME J. Heat Transfer, 1987, Vol. 109, No. 3, pp. 49-54.

16. Austin, L.R. and Seader, J.D., "Entry Region for Steady Viscous Flow in Coiled Circular Pipes", AICHE J., 1974, Vol. 20, No. 4, pp. 820-822.

17. Agrawal, Y., Talbot, L. and Gong, K., "Laser Anemometer Study of Flow Development in Curved Circular Pipes", J. Fluid Mech., 1978, Vol. 85, pp. 497-518.

18. Berger, S.A., Talbot, L. and Yao, L.S., "Flow in Curved Pipes", Ann. Rev. Fluid Mech., 1983, Vol. 15, pp. 337-512.

19. Hidesato Ito, "Flow in Curved Pipes", JSME International Journal, 1987, Vol. 30, No. 263, pp. 543-552.

20. Y. Mori, "Buoyancy Effects in Forced Laminar Convection Flow Over a Horizontal Flat Plate", ASME J. Heat Transfer, 1961, Vol. 83, pp. 479-482.

21. Sparrow, E.M., and Minkowycz, W.J., "Buoyancy Effects on Horizontal Boundary Layer Flow and Heat Transfer", Int. J. Heat Transfer, 1962, Vol. 5, pp. 501-511.

22. Sparrow, E.W., and Husar, R.B., "Longitudinal Vortices in Natural Convection Flow on Inclined Plates", J. Fluid Mech., 1969, Vol. 37, pp. 251-255.

23. Mori, Y., and Uchida, Y., "Forced Convective Heat Transfer Between Horizontal Flat Plates", Int. J. Heat Mass Transfer, 1966, Vol. 9, pp. 803-817.

24. Nakayama, W., Hwang, G.J., and Cheng, K.C., "Thermal Instability in Plane Poiseuille Flow", ASME J. Heat Transfer, 1970, Vol. 92, pp. 61-68.

25. Akiyama, M., Hwang, G.J., and Cheng, K.C., "Experiments on the Onset of Longitudinal Vortices in Laminar Forced Convection Between Horizontal Plates", ASME J. Heat Transfer, 1971, Vol. 93, pp. 335-341.

26. Hwang, G.J., and Cheng, K.C., " Convective Instability in the Thermal Entrance Region of a Horizontal Parallel Plate Channel Heated From Below", ASME J. Heat Transfer, 1973, Vol. 95, pp. 72-77.

27. Hwang, G.J., and Liu, C.L., "An Experiment Study of Convective Instability in the Thermal Entrance Region of a Horizontal Parallel-Plate Channel Heated From Below", Candian J. Chem. Eng., 1976, Vol. 54, pp. 521-525.

28. Kamotani, Y., and Ostroch, S., "Effect of Thermal Instability on Thermally Developing Laminar Channel Flow", ASME J. Heat Transfer, 1976, Vol. 98, pp. 62-66.

29. Kamotani, Y., Ostrach, S., and Miao, H., "Convective Heat Transfer Augmentation By Means of Thermal Instability", ASME J. Heat Transfer, 1979, Vol. 101, pp. 222-226.

30. Incropera, F.P., Knox, A.L., and Schutt, J.A., "Onset of Thermally Driven Secondary Flow in Horizontal Rectangular Ducts", Procs. 8th Int. Heat Transfer Conf., 1986, pp. 1395-1400.

31. Cheng, K.C., and Kim, W., "Flow Visualization Studies on Vortex Instability of Natural Convection Flow Over Horizontal and Slightly Inclined Contant Temperature Plates", ASME Winter Annual Meeting, Dec. 1986, 86-WA/HT-85.

32. Maughan, J.R., and Incropera, F.P., "Experiments on

Mixed Convection Heat Transfer for Airflow in a Horizontal and Inclined Channel", Int. J. Heat Mass Transfer, 1987, Vol. 30, pp. 1307-1318.

33. Wu, R.S., and Cheng, K.C., "Thermal Instability of Hartmann Flow in the Thermal Entrance Region of Horizontal Parallel-Plate Channels Heated From Below", Int. J. Heat Mass Transfer 1976, Vol. 19, pp. 1343-1349.

34. Ou, J.W., Cheng, K.C., and Lin, R.C., "Natural Convection Effect on Graetz Problem in Horizontal Rectangular Channels with Uniform Wall Temperature for Large Pr", Int. J. Heat Mass Transfer, 1974, Vol. 17, pp. 835-843.

35. Chou, F.C., and Lin, J.N., "Convective Instability in the Thermal Entrance Region of Horizontal Rectangular Channels", National Heat Transfer Conference, 1989, HTD-Vol. 107.

2. Flow Visualization Studies of Developing Secondary Flow in Curved Ducts with and without Offset Bends

2.1 Introduction

Curved ducts have many applications in industry, because they can improve the efficiency of heat and mass transfer due to the secondary flow motion caused by centrifugal forces. Curved ducts are widely used in fluid flow, heat transfer, mass transfer and chemical reaction applications, such as compact heat exchangers, nuclear reactors, heat engines and intakes in aircrafts, for examples. Laminar or turbulent flow in curved ducts is one of the fundamental problems in fluid mechanics and has been studied extensively since Dean published his classical work in 1927 and 1928 on the fully developed laminar flow in curved pipes [1,2,3].

According to Dean's work, it is known that the dynamical similarity for laminar flow in a curved pipe depends primarily on the Dean number $K=Re(a/R_c)^{1/2}$, where $Re=U_m(2a)/\nu$ is the Reynolds number, a/R_c=curvature ratio. The Dean number can also be considered as a measure of the importance of inertial and centrifugal forces relative to viscous forces, and since secondary flows result from the interaction of centrifugal and viscous forces, the Dean number provides an estimate of their intensity.

It is understood that laminar flow through a curved pipe is accompanied by the development of secondary flows in

the form of a pair of counter-rotating vortices. In a curved duct, the centrifugal force acting on the flowing fluid elements does not balance with the pressure gradient across the cross section. Under the action of centrifugal forces, the faster-moving fluid in the core region moves toward the outer wall. Flow near this wall is slowed down by viscous forces, and then moves inward along the upper and the lower walls driven by the pressure gradient. From the inner wall the fluid repeats its cyclic motion. Therefore, a secondary flow is set up in the cross section of the curved duct.

In recent years, much attention was focused on the laminar flow in the entrance region of a curved pipe. Many studies have been carried out both numerically and experimentally. Patankar et al. [4] obtained the development of axial velocity profiles by numerical solutions of parabolic Navier-Stokes equations using the finite-difference method. This problem has also been studied numerically by Yao and Berger [5], Liu [6,7], and Yeung [8]. Liu solved the full elliptic Navier-Stokes equations for developing flow in a 90° elbow with K=179. Yao and Berg, and Yeung solved the entry-flow problem for larger Dean numbers. Further numerical studies can be found in [9, 10, 11]. For experimental studies, Austin and Seader [12] measured the development of axial velocity profiles at various angular planes by a hot-wire anemometer system. Experiments of secondary flow visualization were carried out by Cheng et al. [13,14]. Agrawal et al. [15], Bovendeerd [16] and

Sugiyama et al. [17] measured the axial and radial velocities in curved pipes by means of a Laser Doppler velocimeter system. The literature on the flows in curved pipes is well surveyed by Berger et al. [18], Masliyah et al. [19] and Ito [20].

Literature review shows that studies on developing flow in bends with larger curvature ratio a/R_c, and especially with offset bends, are rather limited.

The purpose of the present flow visualization studies is to provide further physical understanding of laminar flow in bends with larger curvature ratio, and with and without offset bends. Attention was given to the effects of Dean number, offset bends and the curvature ratio. Visualizations were made for circular bends with 2" inside diameter, a/R_c=0.2, and for square bends with 2"×2" cross-section, a/R_c=0.2, 0.4. The visualization results are also believed to be useful for future comparison with numerical solutions for this kind of problem.

2.2 Experimental Apparatus and Procedure

2.2.1 General Description of Test Setup

The experimental apparatus for flow visualization is shown schematically in Fig. 2.1. The fluid medium used was the building compressed air. The flow was first filtered by a Fulflo air filter (model B5A3/4D) to remove undesirable dust and moisture. A pressure regulator and an air tank were

used to reduce the pressure fluctuations of the compressed air. As a result, the variation of flow rate was less than 0.2%. The air flow rate was adjusted by a needle valve and was measured by a Merian laminar flow meter (model 50MW 20-1). Details of the flow rate measurement will be given in the next section.

The main air flow, after passing the filter, the pressure regulator, and the flow meter, was split into two separate circuits. One of them went into the smoke generating device to keep the Chinese incense burning. Then the two circuits joined together and entered the settling chamber.

The settling chamber was composed of a steel drum with ten layers of screen to steady the incoming flow. The bell-shaped outlet region with a large contraction ratio (1:0.12) at the exit created a quite uniform flow. A 6.8 m long straight entrance pipe was installed between the settling chamber and the test section to ensure that the flow at the inlet of the test section was fully developed. This straight entrance pipe and the test bends were made from acrylic tubes with inside diameter of 2 inch. Photographs were taken at the exit of each test section. Fig. 2.2 shows a schematic diagram of the test section. For circular bends, the inside diameter is 2a=2" and the curvature ratio is $a/R_c=0.2$. For square bend, the cross-section is 2"×2" and the curvature ratios are $a/R_c=0.2$, 0.4. Fig. 2.3 shows the co-ordinate system at the

exit of the test section. Symbols A, B, C, D denote the tube walls in counter-clockwise direction with A and C indicating outer walls and inner walls. Hence, C-A always reprents the direction of centrifugal forces.

2.2.2 Air Flow Rate Measurement

The air flow rate was measured by a Merian laminar flow meter (Model 50MW 20-1) with a Validyne differential pressure transducer. The laminar flow meter consists of many longitudinal triangular passages small enough to ensure the flow through these passages is laminar so that the correlation between the pressure drop and the flow rate is linear. This correlation was calibrated by the manufacturer of the flow meter, and the overall calibration error was less then 1.0%. A straight tube approximately 20 diameters long was connected to both ends of the flow meter to meet the requirements for measurement.

The pressure transducer with its Validyne carrier demodulator (model CD 15) was calibrated against a U-tube manometer and the calibration error was less than 1.0%. The output of the Validyne carrier demodulator at one inch water pressure difference was one volt, and the outputs were acquired by a data acquisition/control unit (model HP 3497A) and converted to flow rates by a HP-85 micro-computer.

2.2.3 Visualization Method and Photographic Observation

The flow visualization was made possible by injecting smoke. The main air supply was split into two lines. One line went into the smoke generator to provide oxygen for the burning of Chinese incenses and carried the smoke into the settling chamber. The air split ratio is about 1:1 and 4 to 8 sticks of Chinese incense were used. These could be varied to obtain good contrast for flow patterns, depending on the air flow rate and the experience of researcher. The smoke particles were very fine and dispersed into streamlines. So the effect of the smoke on the flow was negligible.

At the exit of each test section, a thin light sheet was provided by a 300 W slide projector, paralleling the exit plane of the test sections. The light sheet was created by making a slit on a slide with round shape. The round slide can be rotated to make sure that the light sheet is parallel to the plane of test section exits. Then pictures were taken in the direction facing the exit with dark surroundings while only the smoke-filled test section exit plate was highlighted by the projector. Therefor, the obtained flow patterns are the cross-sectional views of the helical motion in bends. These flow patterns are caused by secondary flows and can be used to understand the phenomena of secondary flows. A Nikon FM2 single lens reflex camera with 55mm micro lens and Kodak Tri-X black and white film (ASA 400) were used. The aperture was set at f3.5 while the shutter speed ranged from 1/2 to 1 sec..

2.3 Experimental Parameters

Tables 2.1 and 2.2 show the ranges of the experimental parameters for the secondary flow visualization experiments.

Table 2.1 Ranges of Experimental Parameters for Circular Bends

Curvature ratio, a/R_c	0.2
Reynolds number, Re	783
Dean number, K	25 ~ 350
First bend angle, ψ	45°, 90°, 135°, 180°, 225°
Second bend angle, ϕ	45°, 90°, 135°, 180°, 225°
Offset angle, θ	90°, 180°

Table 2.2 Ranges of Experimental Parameters for Square Bends

Curvature ratio, a/R_c	0.2, 0.4
Reynolds number, Re	57 ~ 783(a/R_c=0.2)
	157 ~ 712(a/R_c=0.4)
Dean number, K	25 ~ 350 (a/R_c=0.2)
	100 ~ 450(a/R_c=0.4)
First bend angle, ψ	45°, 90°, 135°, 180°,
	225°(a/R_c=0.2)
Second bend angle, ϕ	45°, 90°, 135°, 180°,
	225°(a/R_c=0.2)

2.4 Results and Discussion

2.4.1 Results for the Circular Cross-sectional Bend

The flow patterns at the end of the straight entrance pipe are shown in Fig. 2.4. At lower flow rate, smoke appears at the lower part of the cross-section due to its larger density. These patterns show that the effect of buoyancy force is not obvious, especially for larger flow rate.

Figs. 2.5 to 2.9 show the effect of Dean number on the secondary flow patterns at the exit of each first bend. Figs. 2.10 to 2.17 show the development of secondary flow patterns in the first bend at each Dean number. One can see that the flow patterns are in good contrast. The region without smoke appears dark while the region filled with smoke looks white. It is noted that the dark region originates from the upper portion or the portion along the upper edge at the inlet position because of the helical motion caused by secondary flows. Therefor, the mass trasfer within the fluid is enhanced.

At the exit of each first bend, the secondary flow becomes more intense with the increase of Dean number. Similarly, at a fixed Dean number, the secondary flow develops in the first bend and becomes more intense at downstream locations. These kinds of secondary flow have been studied quite extensively for bends with smaller curvature ratio. It is noted that, for flows in the bend

with curvature ratio $a/R_c=0.2$, the secondary flow patterns are not much different as compared with the works of other researchers [11, 15]. However, for bends with larger curvature ratio, the pair of secondary flow vortices moves farther away from the outer wall region as the Dean number increases.

The effect of Dean number on the secondary flow patterns at the exit of each offset bend with offset angle $\theta=90°$ is illustrated in Figs. 2.18 to 2.22, and the development of secondary flow patterns in the offset bend is shown in Figs. 2.23 to 2.30. The direction of the centrifugal force caused by the second bend is from C to A, and the direction of the one caused by the first bend is from D to B. At small Dean Number, it seems that the secondary flow patterns in the offset bend are caused by the offset bend. That is, the effect of the offset bend is dominant when Dean number is small. However, at high Dean number, the first bend has strong effect on the secondary flow patterns in the offset bend. Because, at higher Dean number, the secondary flow in the first bend becomes more intense. In other words, the momentum of the secondary flow in the first bend becomes larger and allows the flow patterns of the first bend to continue and last longer through the second bend. In Fig. 2.20, it is seen that a two-vortex secondary flow pattern appears due to the effect of the second bend at K=26. Then this pattern is distorted gradually as the Dean number increases. At K=303, another

pair of large vortices is formed horizontally. One can see clearly that the fluid flows generally from point D toward point B along the line D-B, and then moves back toward point D along the wall BAD and wall BCD. Obviously, this motion is a residual of that caused by the first bend.

From Figs. 2.23 to 2.30, it is noted that the effect of the offset bend becomes larger while the influence of the first bend becomes smaller as the position of the cross-section is moved downstream in the second bend. The symbol A on the first photograph in the Figs. 2.23 to 2.30 indicates the outer wall of the first bend.

When the offset angle is θ=180°, the first bend and the second bend are in the same horizontal plane. The test section becomes an s-bend, and the inner wall of the first bend becomes the outer wall of the second bend. Figs. 2.31 to 2.35 show the effects of Dean number K on the secondary flow patterns at the exit of the second bend with different bend angles. Symbol A indicates the outer wall of the second bend. Thus the centrifugal force caused by the second bend is in the direction C to A, and the one caused by the first bend is in the opposite direction, A to C.

It is noted that the secondary flow is mainly controlled by the first bend if the second bend angle is less than 45°, because the second bend is not long enough for the secondary flow caused by the second bend to show up. From Fig. 2.34, one can see that, for longer second bends, the second bend controls the secondary flow pattern at

smaller Dean number. The effect of the first bend becomes larger and an additional pair of vortices appears as the Dean number increases. The additional pair of vortices is called Dean's instability vortices. At the exit of the 180° second bend, the Dean's instability vortices appear at K=151. It is seen that Dean's instability vortices are distorted and become asymmetric as the Dean number increases gradually. When it's formed, this pair of vortices is almost horizontal but it becomes vertical at downstream locations. At Dean number K=349, the secondary flow pattern induced by the second bend becomes asymmetric too, and the whole flow pattern becomes very complex.

Figs. 2.36 to 2.43 show the development of the secondary flow patterns in the second bend at each Dean number K. The symbol A on the first photograph indicates the outer wall of the first bend. Similarly, it is also noted that, at small Dean number, $K \leq 100$, the second bend controls the whole flow pattern at downstream location and the Dean instability vortices do not exist. At smaller second bend angle ϕ, the secondary flow is mainly controlled by the first bend. As the position moves downstream in the second bend, the effect of the first bend becomes smaller and the effect of the second bend dominates.

2.4.2 Results for the Square Cross-sectional Bend with $a/R_C=0.2$

Photographs in Fig. 2.44 were taken at the end of the straight entrance pipe. The buoyancy force effect is very small and is observed only at smaller Dean number. Figs. 2.45 to 2.49 show the effect of Dean number on the flow patterns at the exit of the first bend with different bend angle. The development of secondary flow patterns in the first bend is shown in Figs. 2.50 to 2.57. Many studies on this kind of flow have been reported for the case of smaller curvature ratio a/R_C. The present visualization for the flow in the first bend shows similar results. Dean instability vortices are observed at the exit of the 225° bend when the Dean number is K=151. But at larger Dean number, the symmetry of the flow pattern is destroyed, and flow patterns become complex.

For the case of offset angle $\theta=90°$, Figs. 2.58 to 2.62 show the effect of Dean number K on the secondary flow pattern at the exit of each second bend, and Figs. 2.63 to 2.70 show the development of secondary flow pattern in the second bend at each Dean number K. The phenomena are similar to the results for circular cross-sectional bends. At smaller Dean numbers, the secondary flow patterns are mainly affected by the second bend. While at larger Dean numbers, the effect of the first bend dominates. At the same Dean number, the consequence of the first bend effect seems different for each second bend, as shown in Fig. 2.69. At

ϕ=45°, the pair of vortices caused by the first bend appears in the upper region. At ϕ=90°, a big clockwise vortex is formed in the center region. At ϕ=135°, the pair of vortices caused by the first bend appears diagonally from right bottom corner to the left top corner. These vortices appear horizontally from D to B for the positions at ϕ=180° and 225°.

Figs. 2.71 to 2.75 show the effect of Dean number on secondary flow patterns in each second bend with offset angle ϕ=180°. Figs. 2.76 to 2.83 show the development of secondary flow patterns in the second bend of the s-bend at each Dean number K. As shown in Fig. 2.73, the Dean's instability vortices appear in the center region of the outer wall of the second bend. Then they become larger and asymmetric as the Dean number increases. At K=302, another two vortices are formed in the top and bottom corners near the outer wall. The vortices induced by the second bend are pressed back to the outer top and bottom corners.

It is noted that Dean's instability phenomena are observed at position ϕ=180° when K=100. As mentioned before, the Dean's instability phenomena appear at K=151 at the exit of the 180° circular bend. Therefor, the Dean's instability vortices appear more readily for the case of square cross-sectional s-bend. In Fig. 2.80, one can see that the Dean's instability vortices are pressed severely by the centrifugal force induced by the second bend as the flow moves downstream.

2.4.3 Results for the Square Cross-sectional Bend with $a/R_C=0.4$

In order to understand the effect of the curvature ratio a/R_C on the secondary flow pattern, visualization was also made for square cross-sectional bends with curvature ratio $a/R_C=0.4$. Figs. 2.84 to 2.88 show the Dean number effect on secondary flow patterns at the exit of each first bend. Figs. 2.89 to 2.96 show the development of secondary flow patterns in the first bend at each Dean number K.

It is noted that the secondary flow pattern at the exit of a 45° bend is weaker at the same Dean number K than that of the case $a/R_C=0.2$, because the bend with $a/R_C=0.4$ is shorter. The Dean's instability vortices are not observed throughout the experiment. However, a pair of vortices seems to appear in the center of the inner wall, as shown in Fig. 2.87.

Figs. 2.97 to 2.101 and Figs. 2.110 to 2.114 show the effect of Dean number K on secondary flow patterns at the exit of each second bend for offset angle $\theta=90°$ and 180°, respectively. Figs. 2.102 to 2.109 and Figs. 2.115 to 2.122 show the development of secondary flow pattern in the second bend at each Dean number K for offset angle $\theta=90°$ and 180°, respectively.

It seems that the effect of Dean number K on the secondary flow pattern and the tendency of the secondary flow development in the second bend with curvature ratio $a/R_C=0.4$ are similar to the results for the case with

curvature ratio a/R_C=0.2. Only small differences are observed.

In the s-bend, as shown in Figs. 2.74 and 2.113, it is noted that the Dean's instability vortices appear at higher Dean number, and a pair of vortices seems to appear near the center of inner wall of the second bend for the case of larger curvature ratio.

2.4.4 Concluding Remarks

Visualization results are presented for three cases. First, a circular cross-sectional bend with curvature ratio a/R_C=0.2, Dean number K=25~350, and offset angle θ=90°, 180°. Second, a square cross-sectional bend with a/R_C=0.2, K=25~350, and θ=90°, 180°. Third, a square cross-sectional bend with a/R_C=0.4, K=100~450, and θ=90°, 180°. Photographs were taken for each case by a smoke injection method. Attention was given to the effects of Dean number K, second bend angle ϕ, curvature ratio a/R_C, and the influence of bend geometry on secondary flow patterns.

It is noted that the secondary flow patterns at the exit of the offset bend are mainly affected by the second bend at smaller Dean number K≤100, and are greatly affected by the first bend at higher Dean number. On the other hand, the secondary flow patterns in the second bend are mainly controlled by the first bend if the second bend angle is less than 45°.

In the s-bend, Dean's instability phenomena are observed, and these phenomena appear at lower Dean number K in the square cross-sectional bend. In addition to the Dean's instability vortices, another two vortices begin to appear in the left top and left bottom corners near the inner wall at K=300 for 135° and 180° second bend.

For the square bend with $a/R_c=0.4$, it is found that Dean's instability vortices appear in s-bend at higher Dean number. It is also noted that a pair of small vortices seems to appear near the center of the inner wall of the second bend. However, the effect of Dean number K on secondary flow patterns and the tendency of the secondary flow development in the square bend with $a/R_c=0.4$ are not very different from the case of square bends with $a/R_c=0.2$.

The present visualization study of flow in bends with and without offset bends is a complement to the existing studies on flows in curved pipes, and provides a further insight on flow physics of secondary flow. It is believed that the present photographic results will be useful to confirm the results of numerical studies in the future.

2.5 References

1. Dean, W.R., "Note on the Motion of Fluid in a Curved Pipe", Phil. Mag. 4, 1927, pp. 208-223.

2. Dean, W.R., "The Stream-line Motion of Fluid in a Curved Pipe", Phil. Mag. 5, 1928, pp. 673-695.

3. Dean, W.R., "Fluid Motion in a Curved Channel", Proc. Roy. Soc. London, Vol. 121A, 1928, pp. 402-420.

4. Patankar, S.V., Pratap, V.S. and Spalding, D.B., "Prediction of Laminar Flow and Heat Transfer in Helically Coiled Pipes", J. Fluid Mech., 1974, 62, pp. 539-551.

5. Yao, L.-S. and Berger, S.A., "Entry Flow in a Curved Pipe", J. Fluid Mech., 1975, Vol. 67, pp. 177-196.

6. Liu, N.-S., "Finite-difference Solution of the Navier-Stokes Equations for Incompressible Three-dimensional Internal Flows", Proc. 5th Int. Conf. Numer. Methods Fluids Dyn., 1976, Vol. 35, pp. 330-335.

7. Lui, N.-S., "Developing Flow in Curved Pipe", INSERM-Euromech 92, Vol. 71, pp. 53-64.

8. Yeung, W.-S., "Laminar Boundary-layer Flow Near the Entry of a Curved Circular Pipe", J. Appl. Mech., Vol. 47, pp. 697-702.

9. Soh, W.Y., "Laminar Entrance Flow in Curved Pipe". J. Fluid Mech., 1984, Vol. 148, pp. 109-135.

10. Soh, W.Y., "Developing Fluid Flow in a Duct of Square Cross-section and Its Fully Developed Dual Solution", J. Fluid Mech., 1988, Vol. 188, pp. 337-361.

11. Humphrey, J.A.C., Taylor, A.M.K. and Whitelaw, J.H., "Laminar Flow in a Square Duct of Strong Curvature", J. Fluid Mech., 1977, Vol. 83, pp. 509-527.

12. Austin, L.R. and Seader, J.D., "Entry Region for Steady

Viscous Flow in Coiled Circular Pipes", AICHE J., 1974, Vol. 20, No. 4, pp. 820-822.

13. Cheng, K.C., Nakayama, J and Akiyama, M., " Effect of Finite and Infinite Aspect Ratios on Flow Patterns in Curved Rectangular Channels", Flow Visualization(Tokyo, Japan, 1977), Hemisphere Pub. Corp., 1979, pp. 181-186.

14. Cheng, K.C. and Yuen, F.P., "Flow Visualization Studies on Secondary Flow Patterns in Straight Tubes Downstream of a 180° Bend and in Isothermally Heated Horizontal Tubes", ASME J. Heat Transfer, 1987, vol. 109, No. 3, pp. 49-54.

15. Agrawal, Y., Talbot, L. and Gong, K.," Laser Anemometer Study of Flow Development in Curved Circular Pipes", J. Fluid Mech., 1978, Vol. 85, pp. 497-518.

16. Bovendeerd, P.H.M., Steenhoven, A.A.Ven, Vosse, F.N.Ven De and Vossers, G., "Steady Entry Flow in a Curved Pipe", J. Fluid Mech., 1987, Vol. 177, pp. 233-246.

17. Sugiyama, S., Aoi, T., Yamamoto, M., Narisawa, N., and Miyaki, Y., "Measurements on Developing Laminar Flow in a Curved Rectangular Duct by Means of LDV", Proc. Exp. Heat Transf. Fluid Mech., Thermody., Dubrovnik, 1988, pp. 1185-1191.

18. Berger, S.A., Talbot, L. and Yao, L.S., "Flow in Curved Pipes", Ann. Rev. Fluid Mech., 1983, Vol. 15, pp. 337-512.

19. Masliyah, J.H., "On Laminar Flow in Semi-circular Ducts", J. Fluid Mech., 1980, Vol. 99, pp. 469-479.

20. Hidesato Ito, "Flow in Curved Pipes", JSME, International Journal, 1987, Vol. 30, No. 262, pp. 543-552.

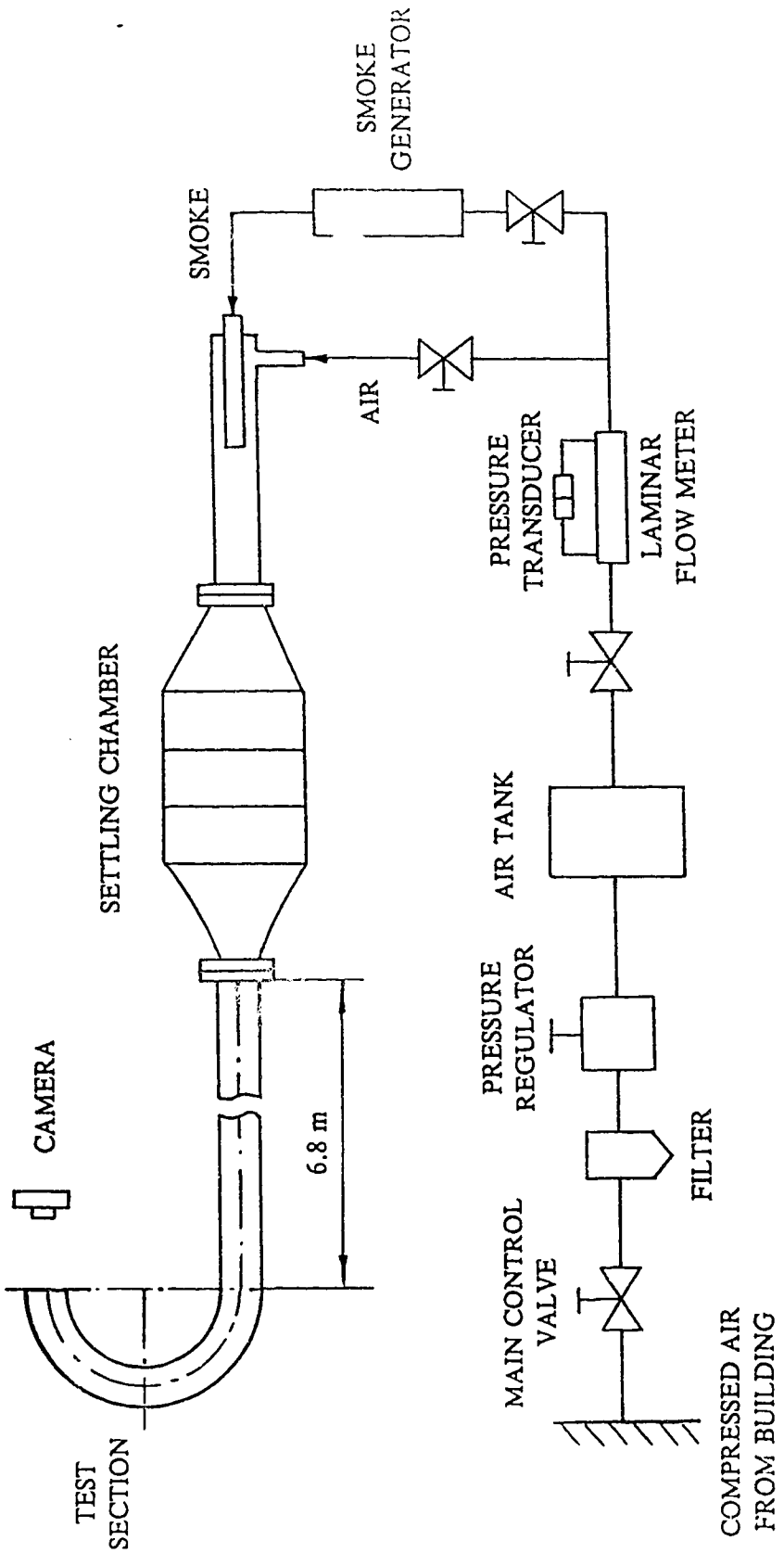

Fig. 2.1 Schematic diagram of test setup

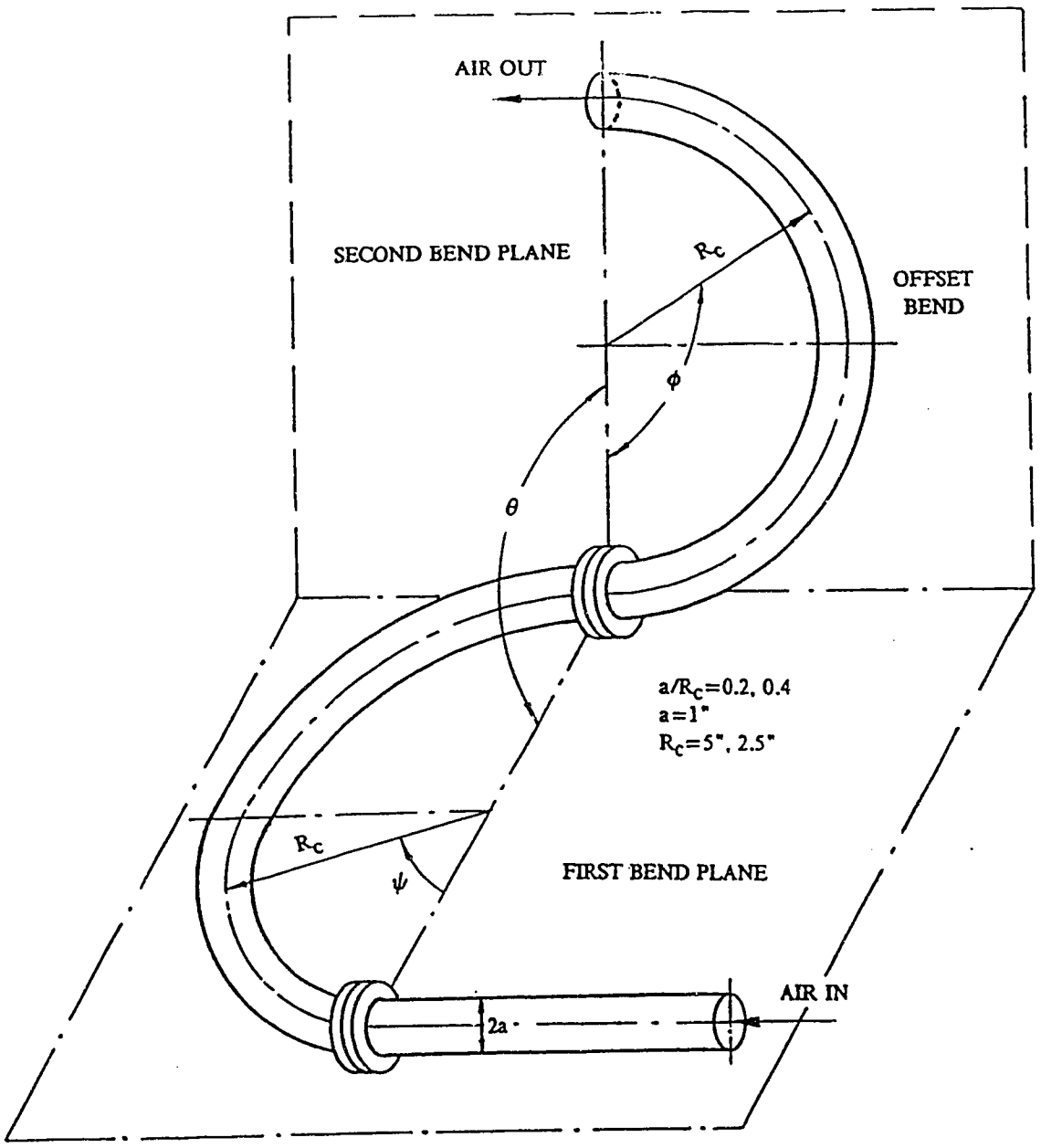

Fig. 2.2 Schematic diagram of the test section

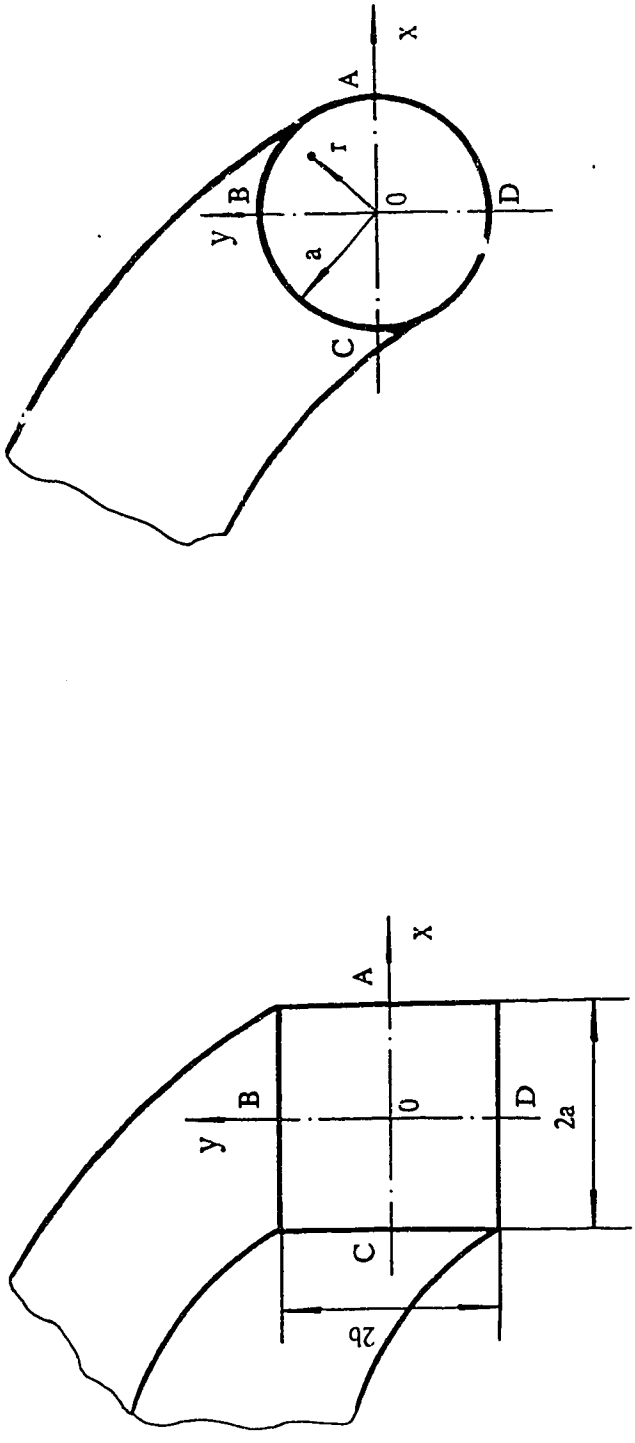

Fig. 2.3 Exit of the test section and coordinate system

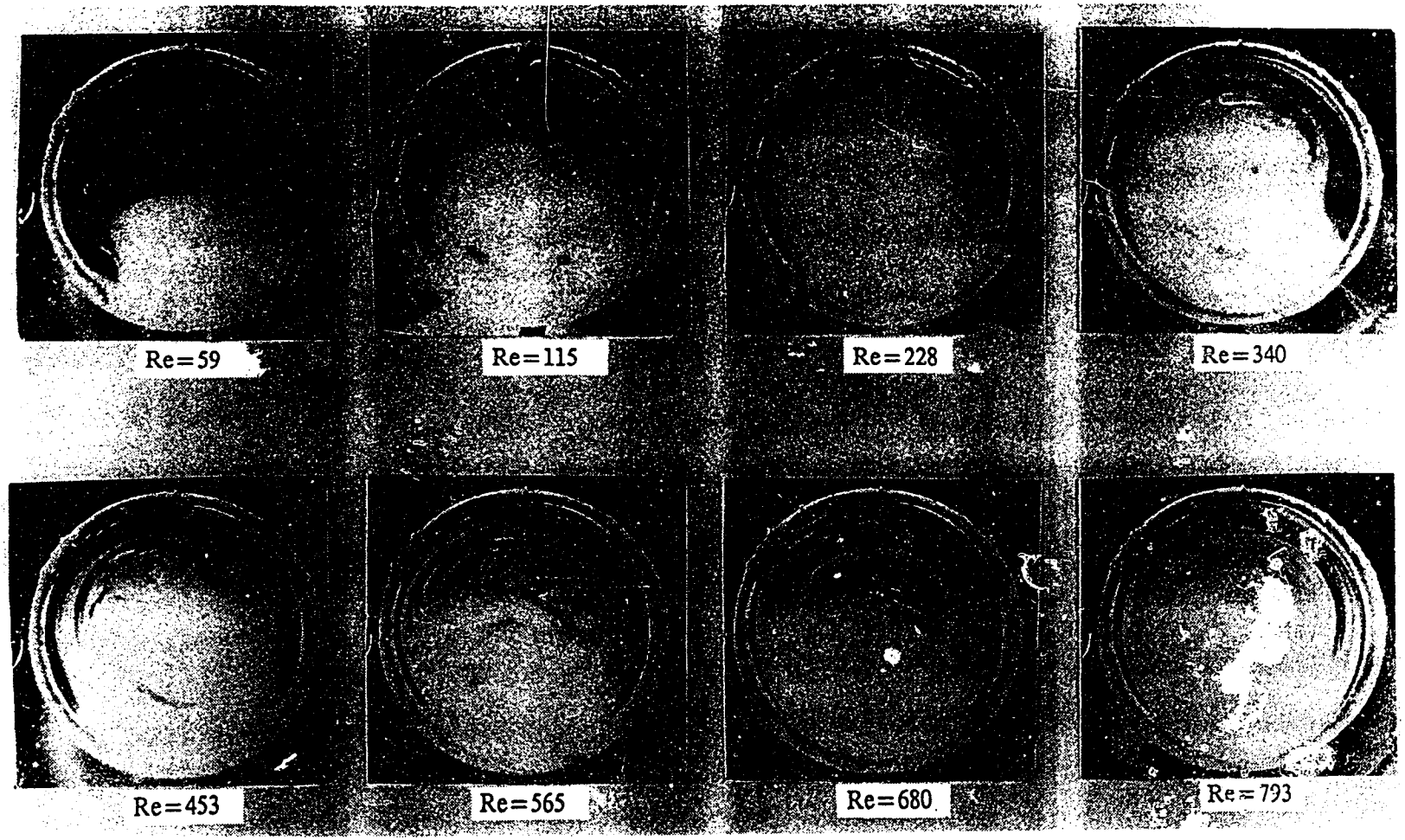

Fig. 2.4 Flow patterns at the end of the straight circular entrance pipe

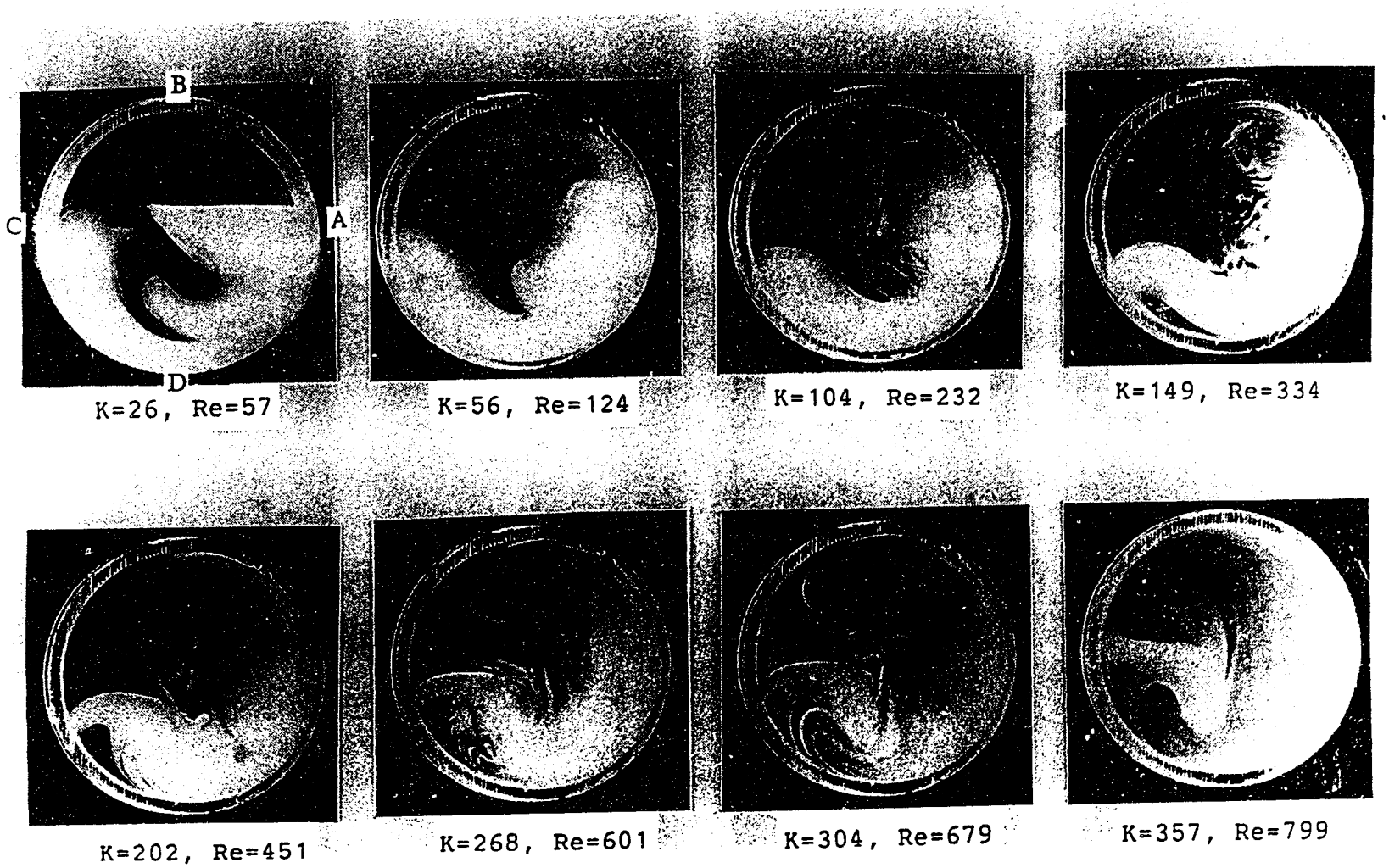

Fig. 2.5 The effect of Dean number on secondary flow patterns at the exit of a 45° circular bend with $a/R_c=0.2$

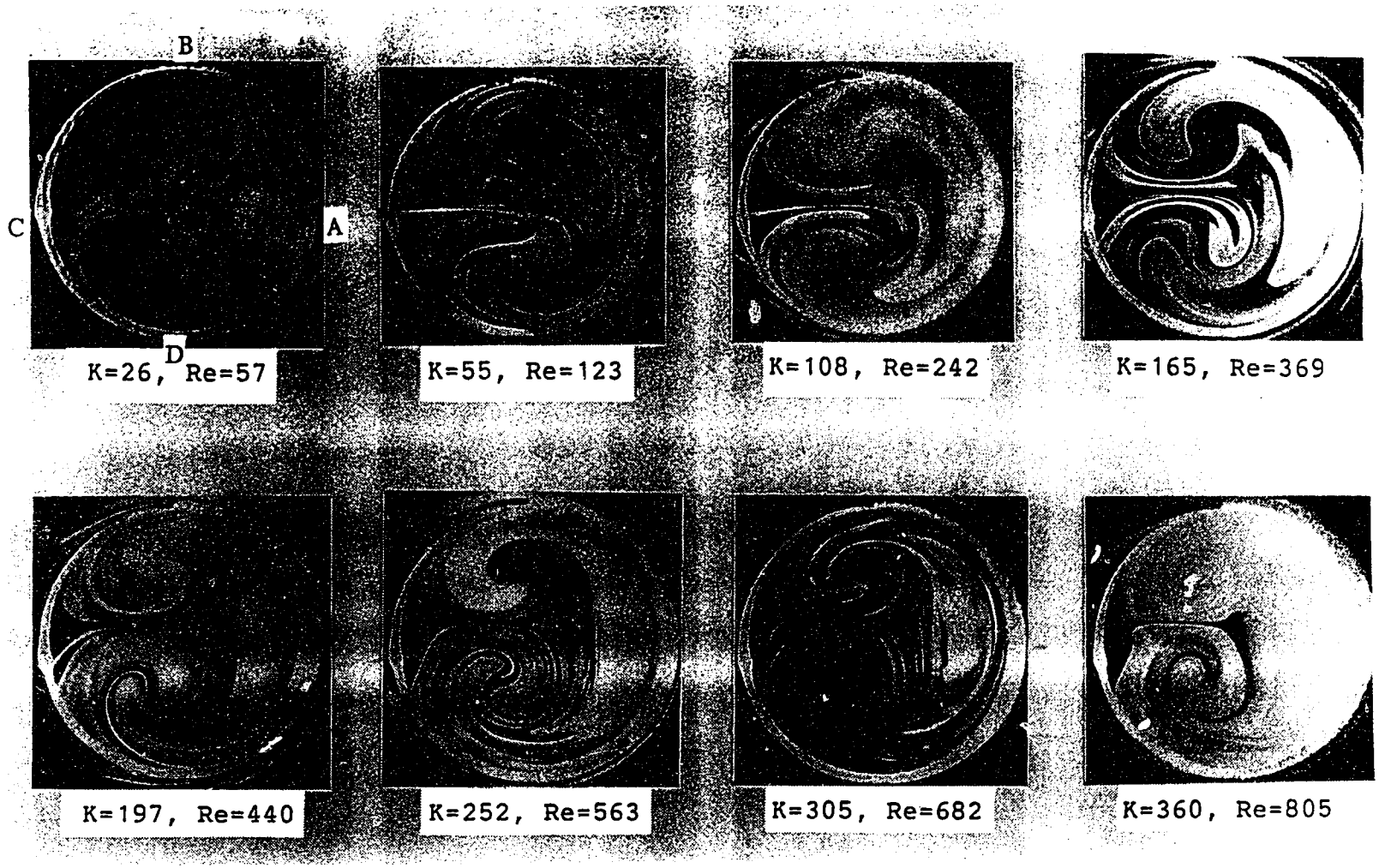

Fig. 2.6 The effect of Dean number on secondary flow patterns at the exit of a 90° circular bend with $a/R_c=0.2$

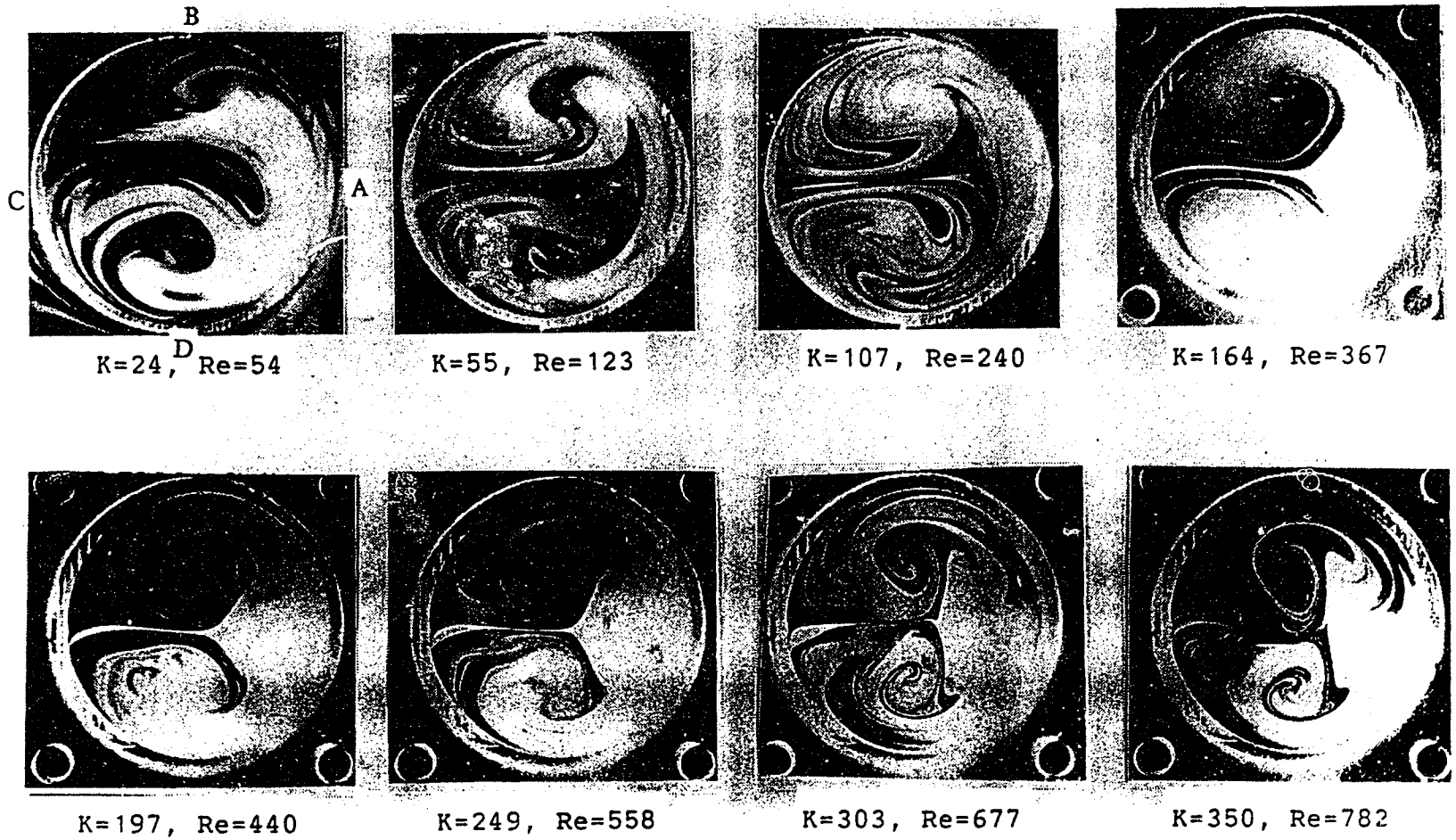

Fig. 2.7 The effect of Dean number on secondary flow patterns at the exit of a 135° circular bend with $a/R_c=0.2$

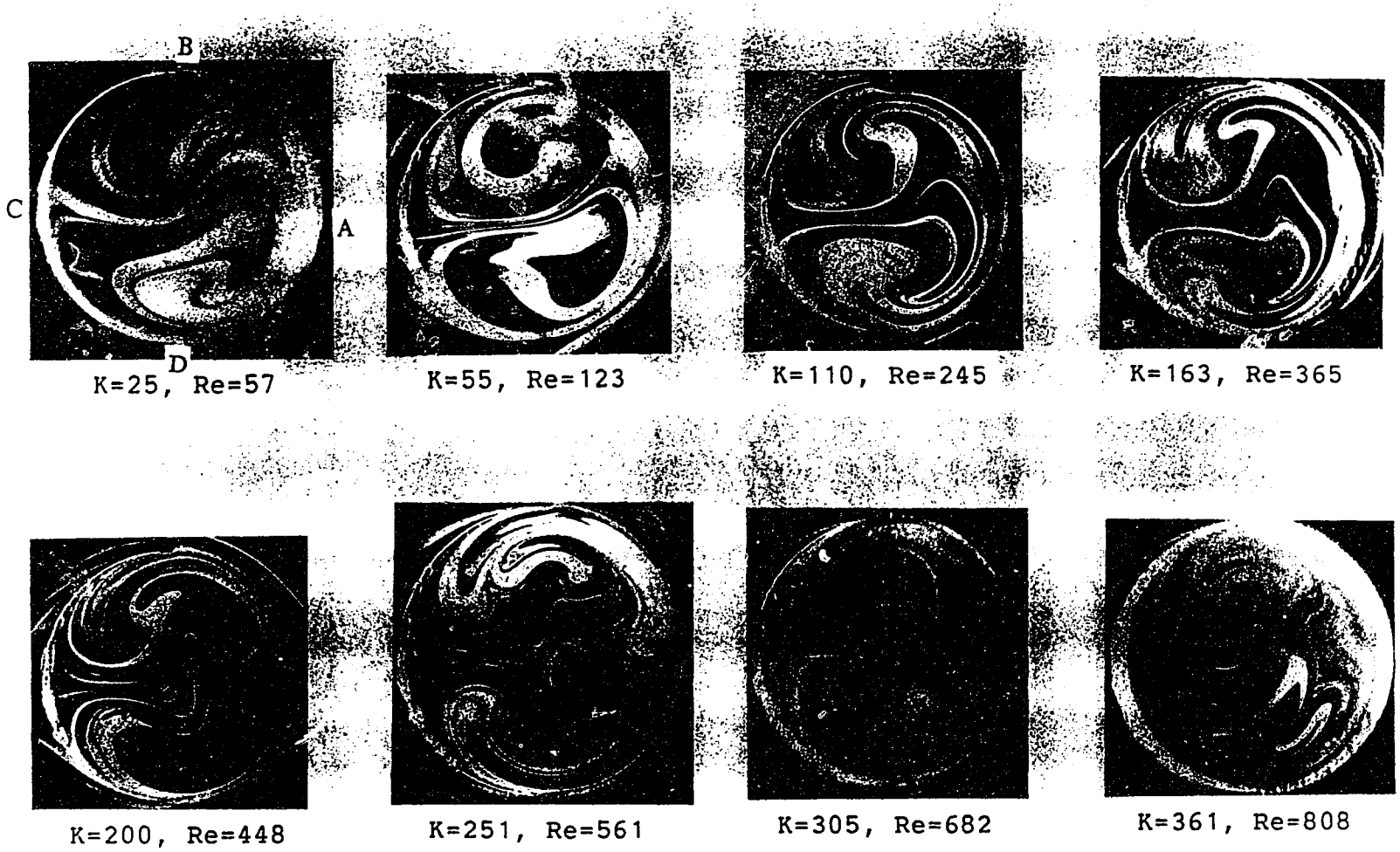

Fig. 2.8 The effect of Dean number on secondary flow patterns at the exit of a 180° circular bend with $a/R_c=0.2$

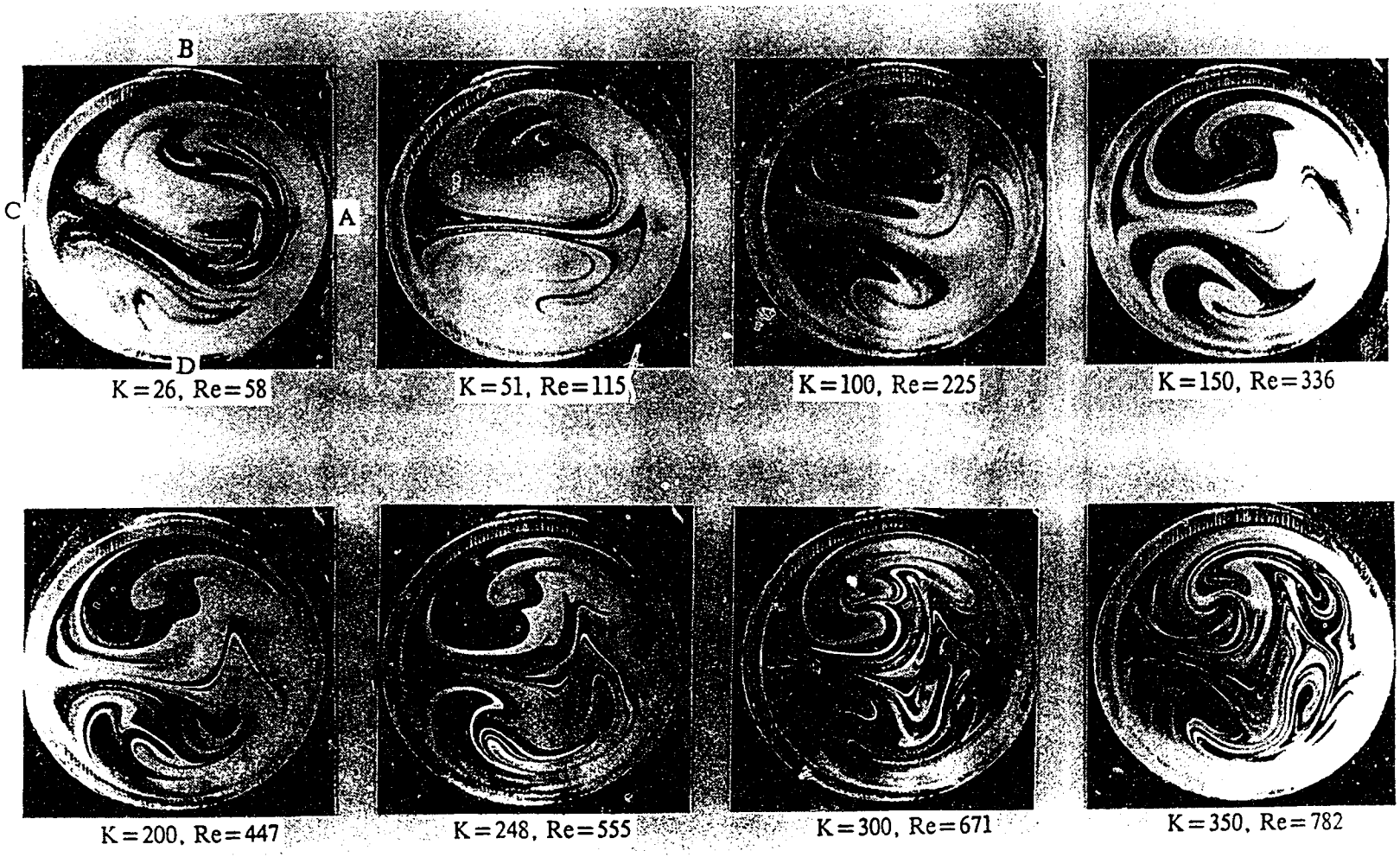

Fig. 2.9 The effect of Dean number on secondary flow patterns at the exit of a 225° circular bend with $a/R_c=0.2$

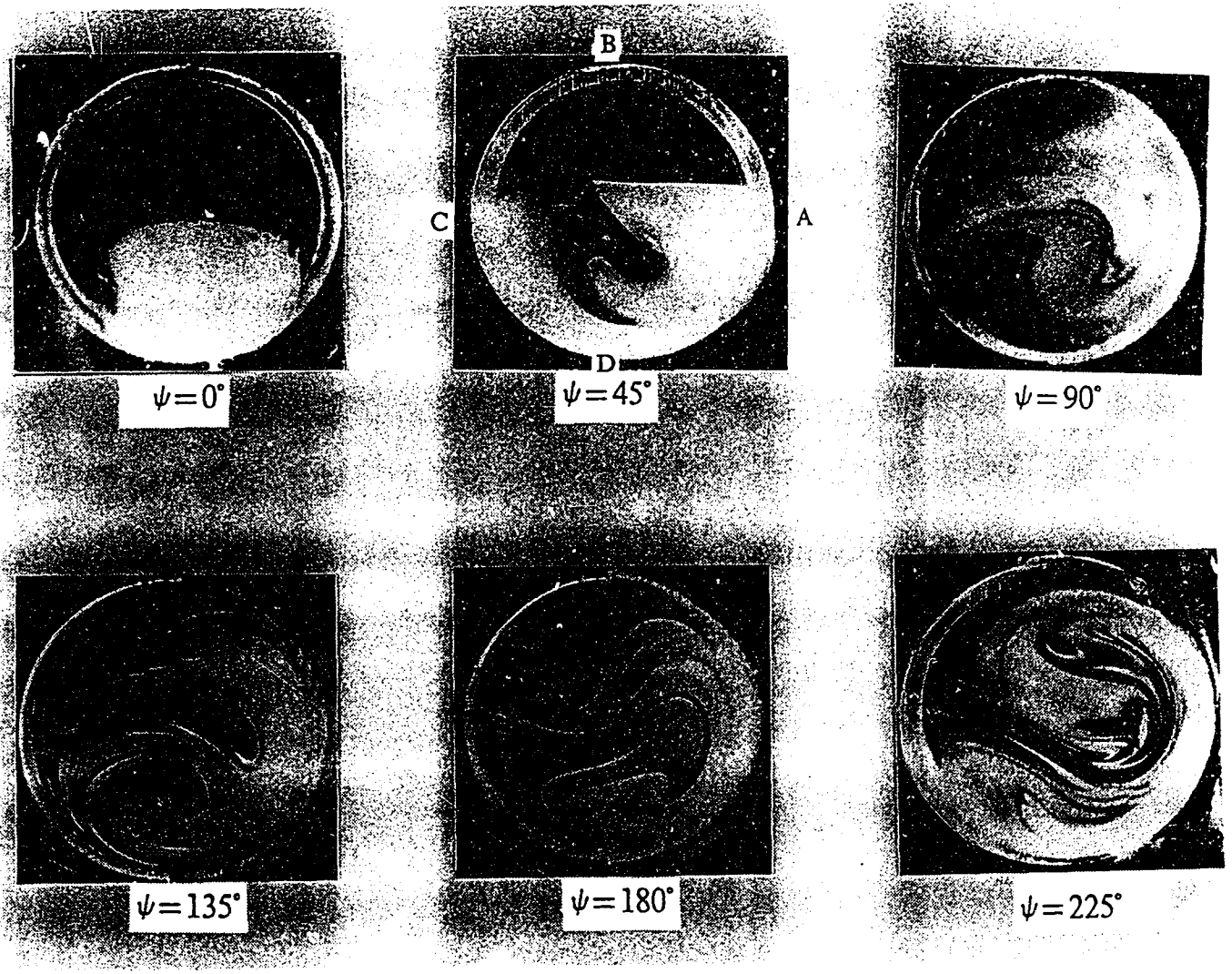

Fig. 2.10 Developing secondary flow patterns in the first circular bend with a/R_c=0.2 at K=25

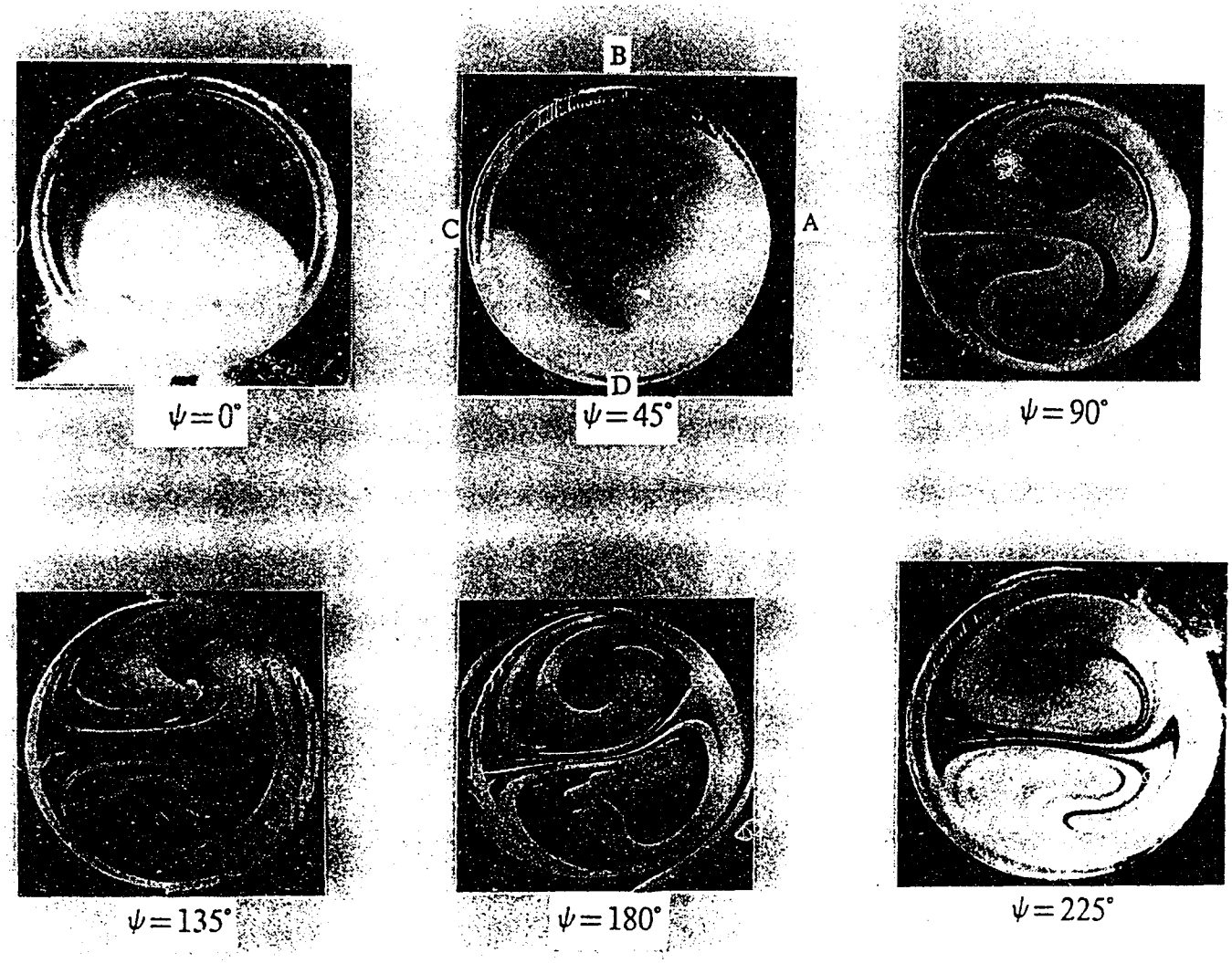

Fig. 2.11 Developing secondary flow patterns in the first circular bend with a/R_c=0.2 at K=50

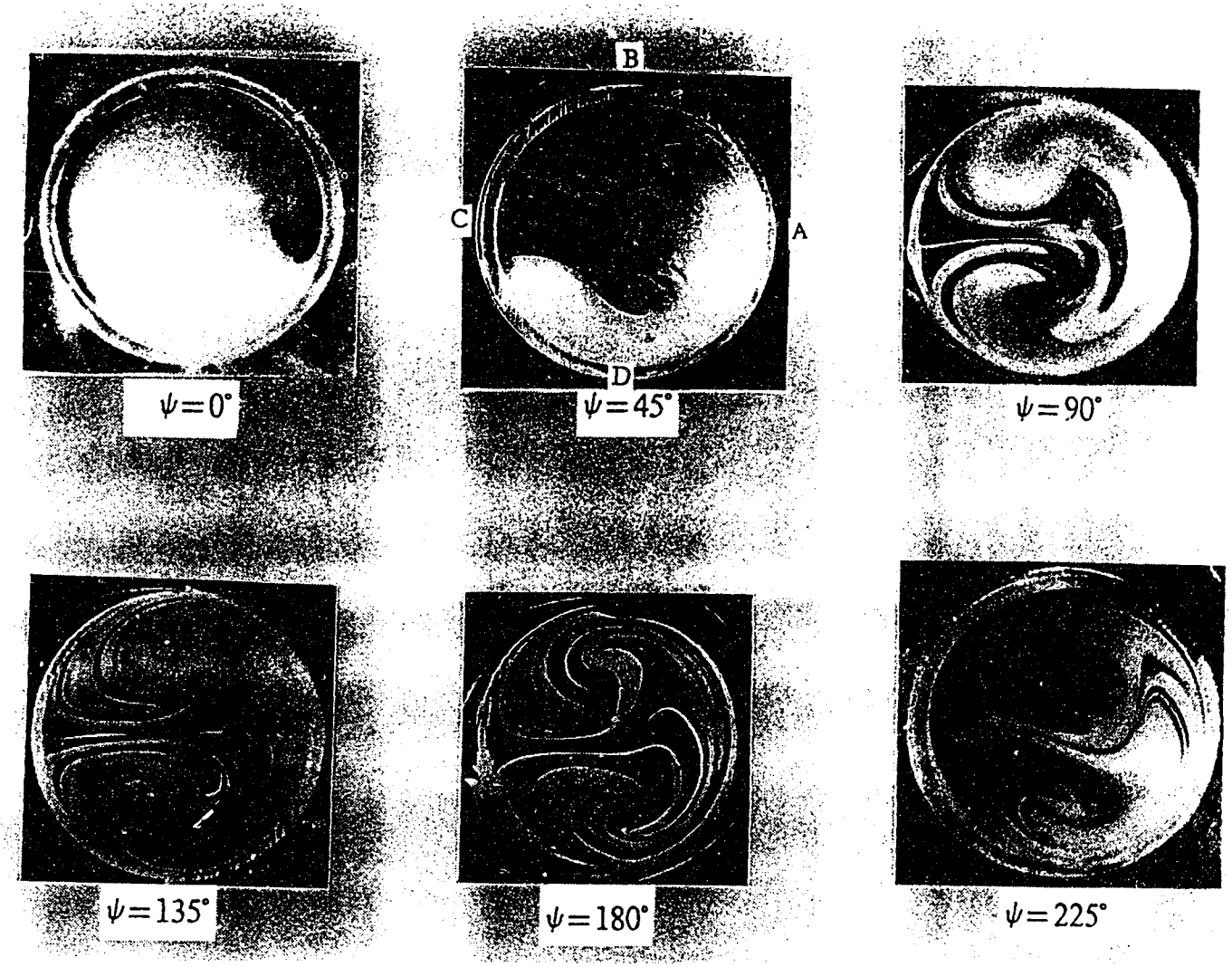

Fig. 2.12 Developing secondary flow patterns in the first circular bend with $a/R_c=0.2$ at K=100

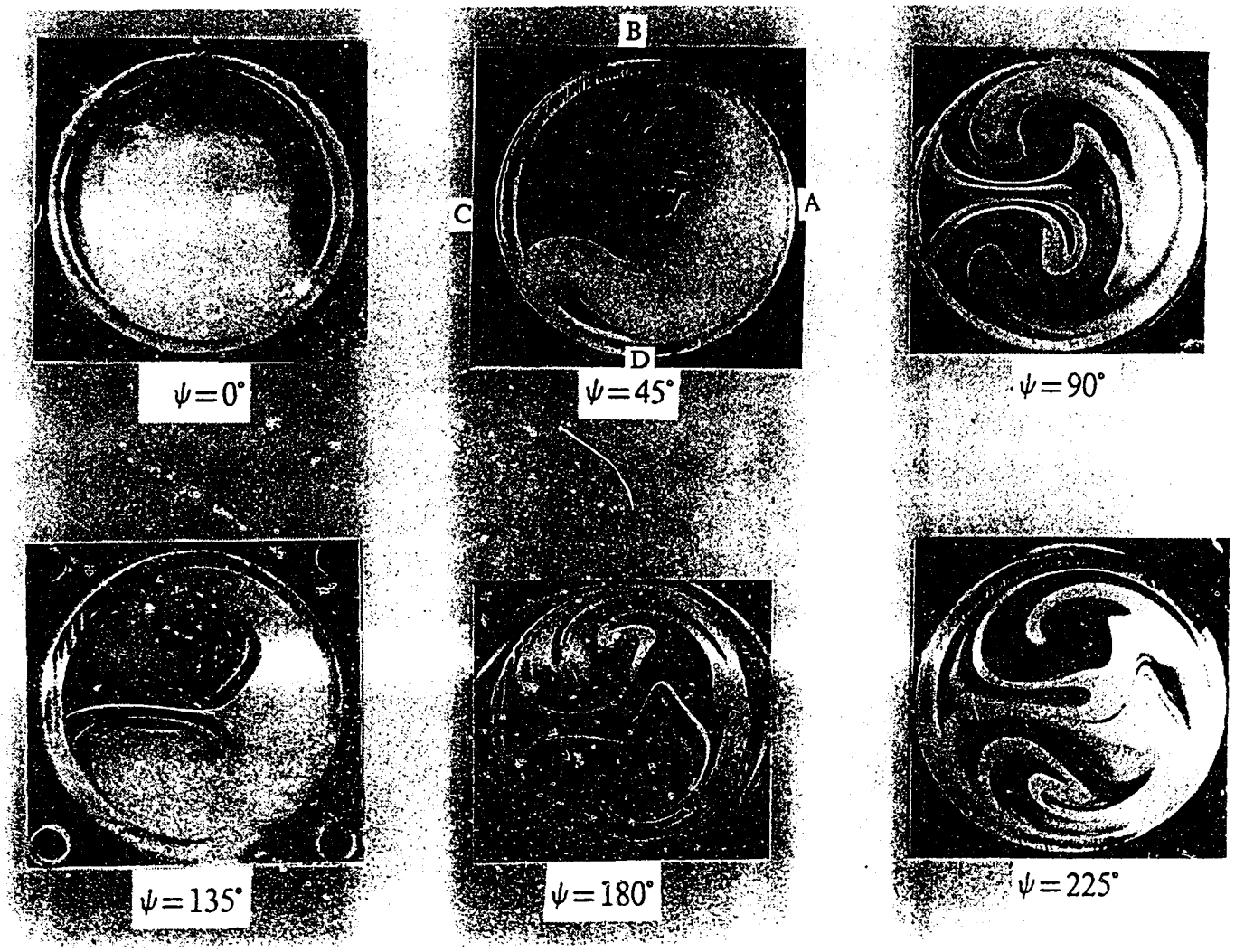

Fig. 2.13 Developing secondary flow patterns in the first circular bend with $a/R_c=0.2$ at K=150

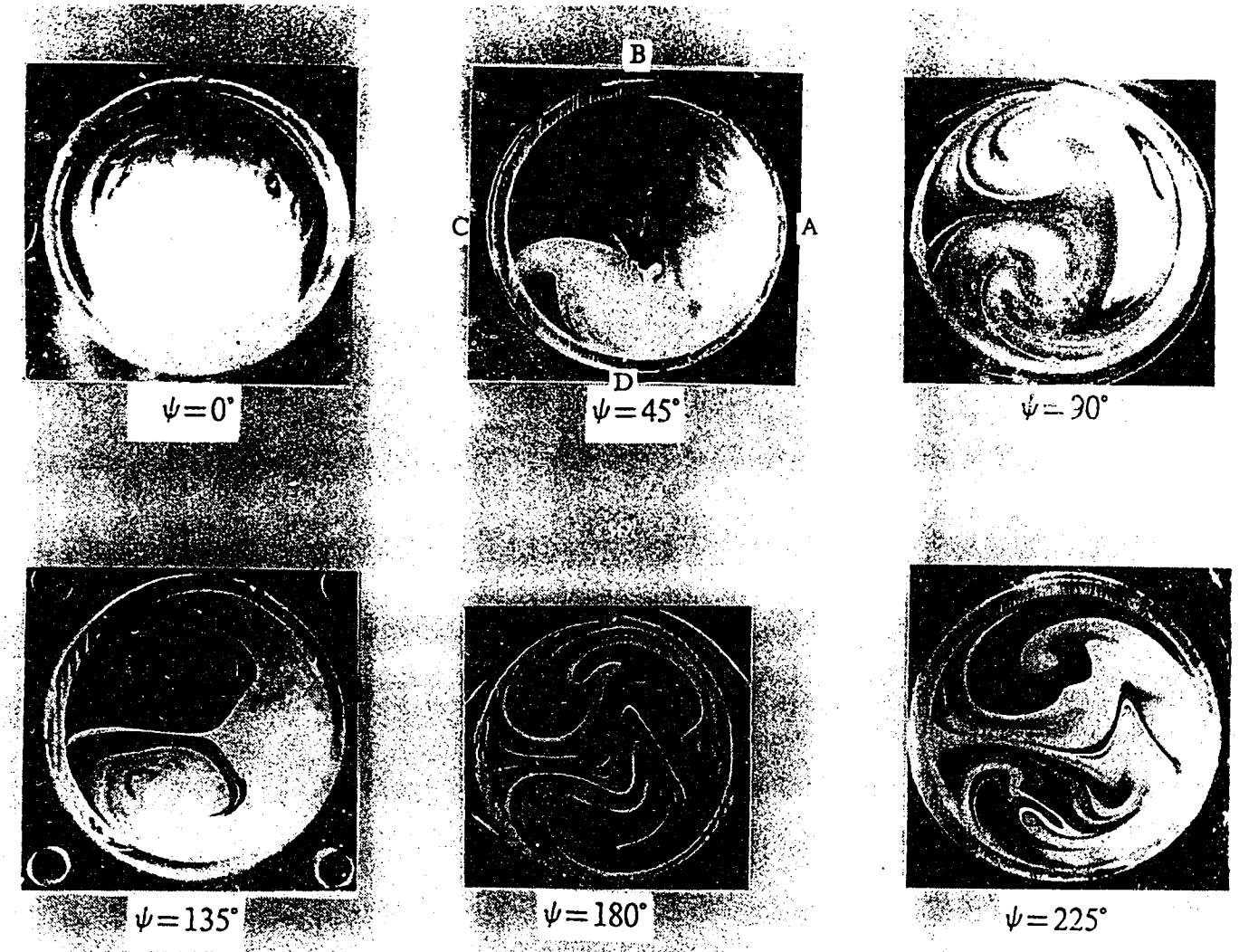

Fig. 2.14 Developing secondary flow patterns in the first circular bend with a/R_c=0.2 at K=200

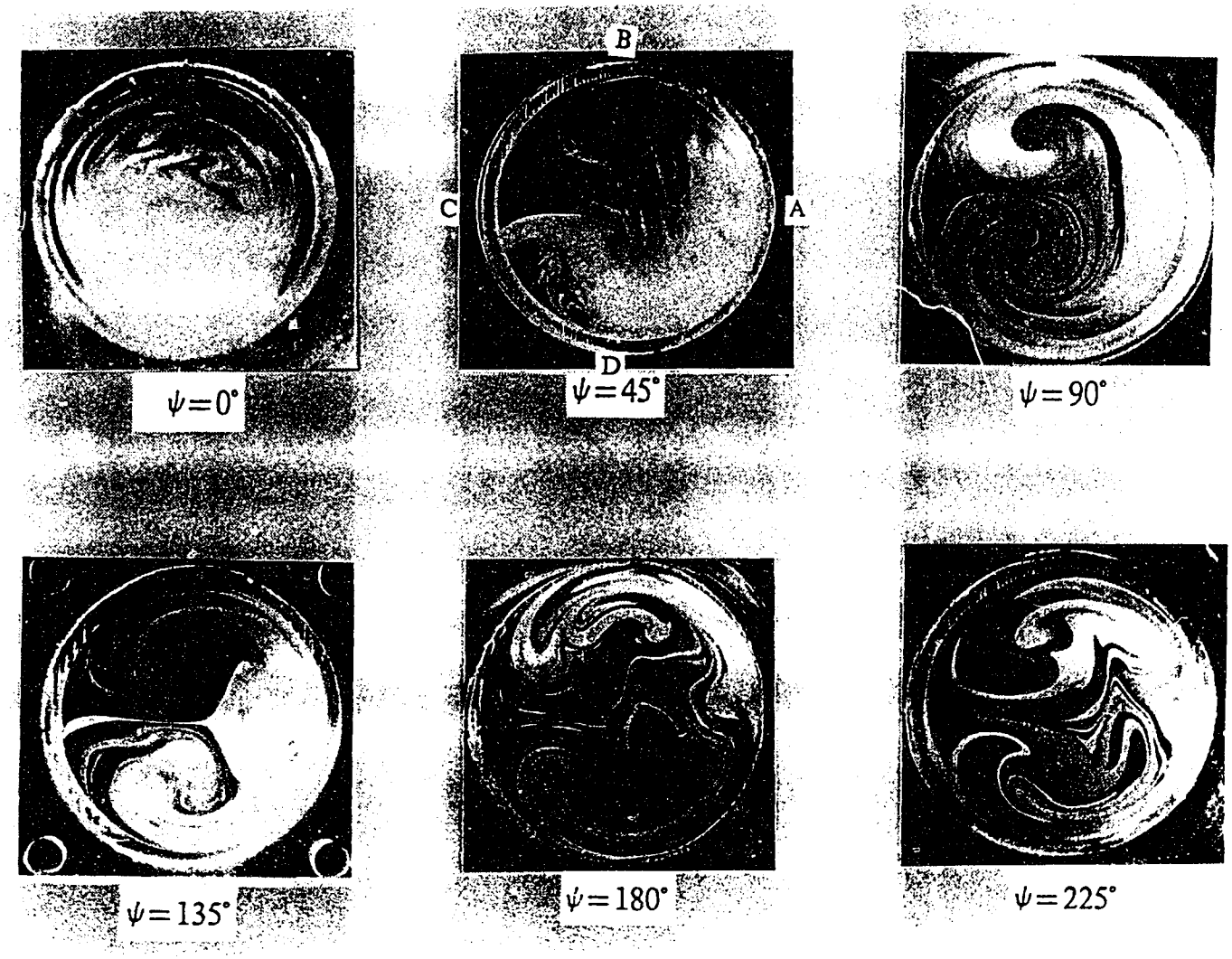

Fig. 2.15 Developing secondary flow patterns in the first circular bend with a/R_c=0.2 at K=250

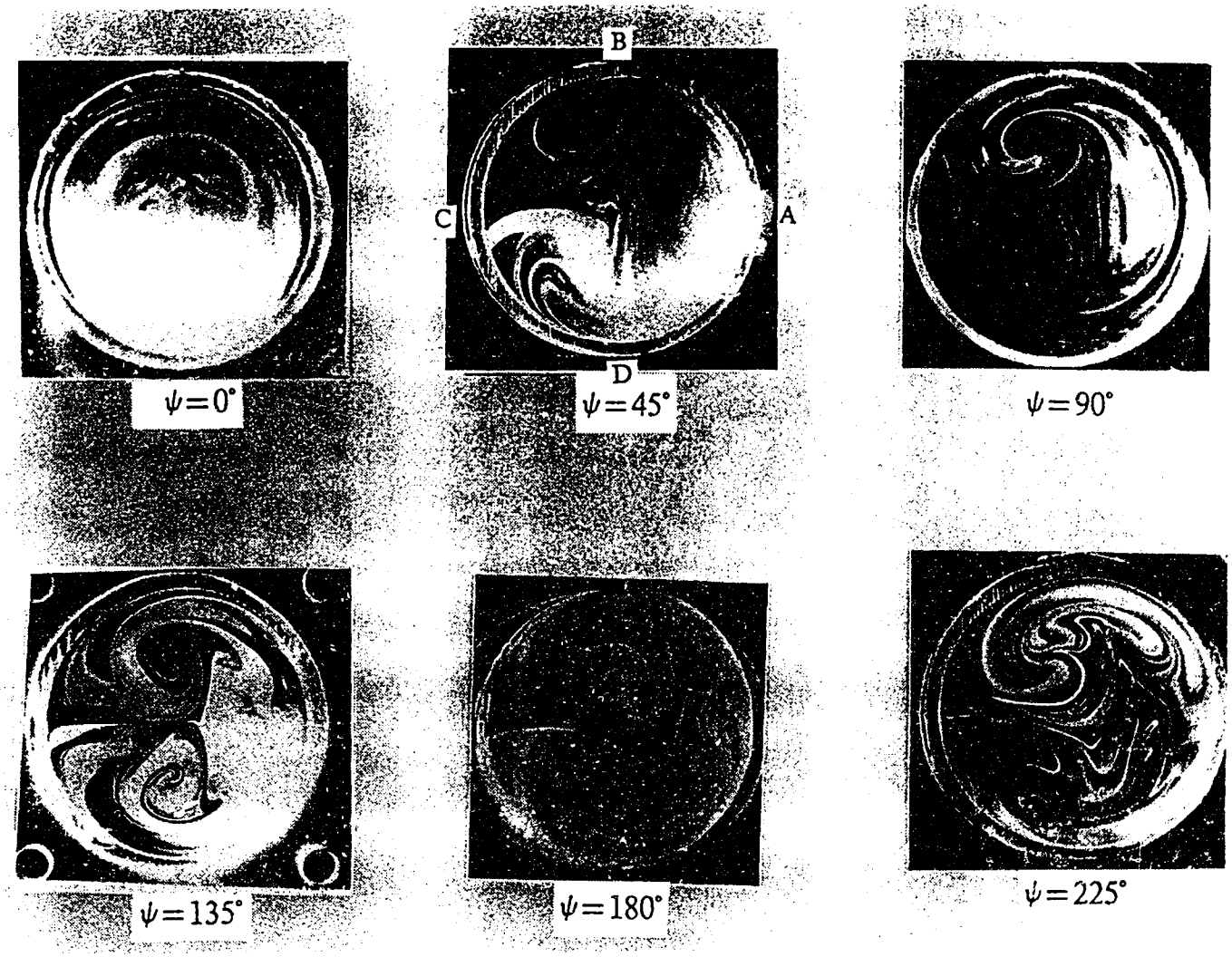

Fig. 2.16 Developing secondary flow patterns in the first circular bend with a/R_c=0.2 at K=300

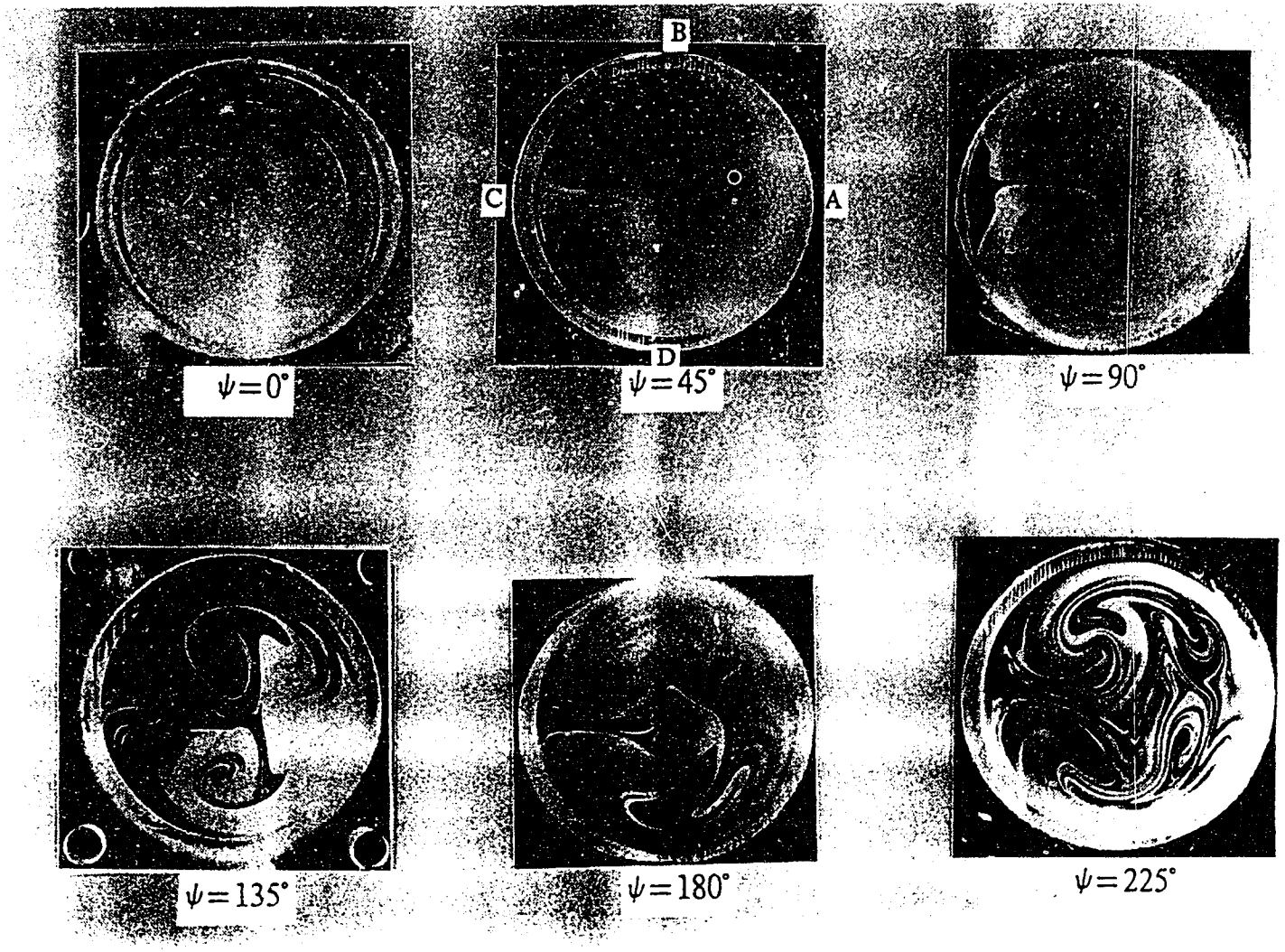

Fig. 2.17 Developing secondary flow patterns in the first circular bend with $a/R_c=0.2$ at K=350

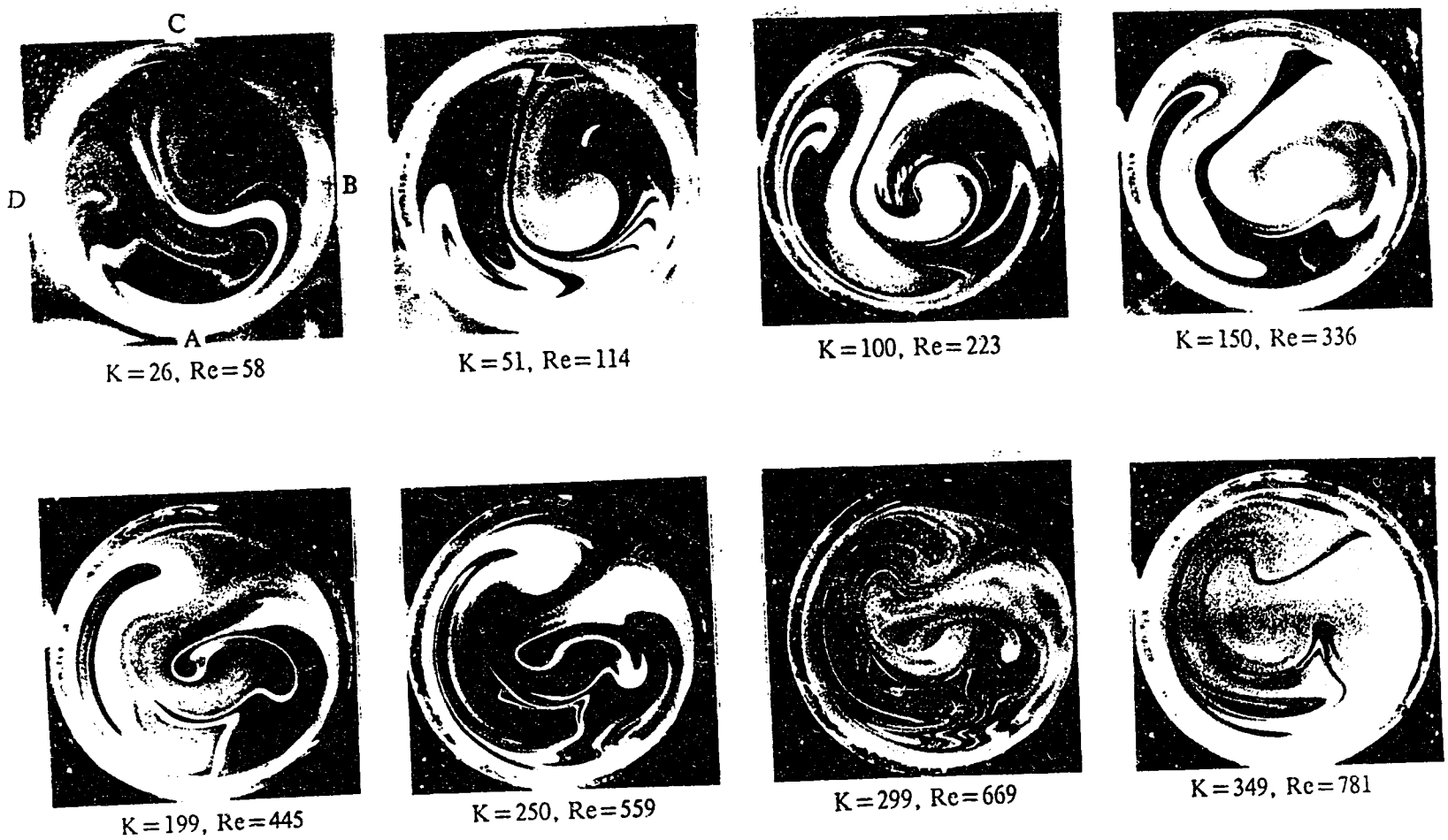

Fig. 2.18 The effect of Dean number on secondary flow patterns at the exit of a 45° second circular bend with $a/R_c=0.2$, $\psi=180°$ and $\theta=90°$

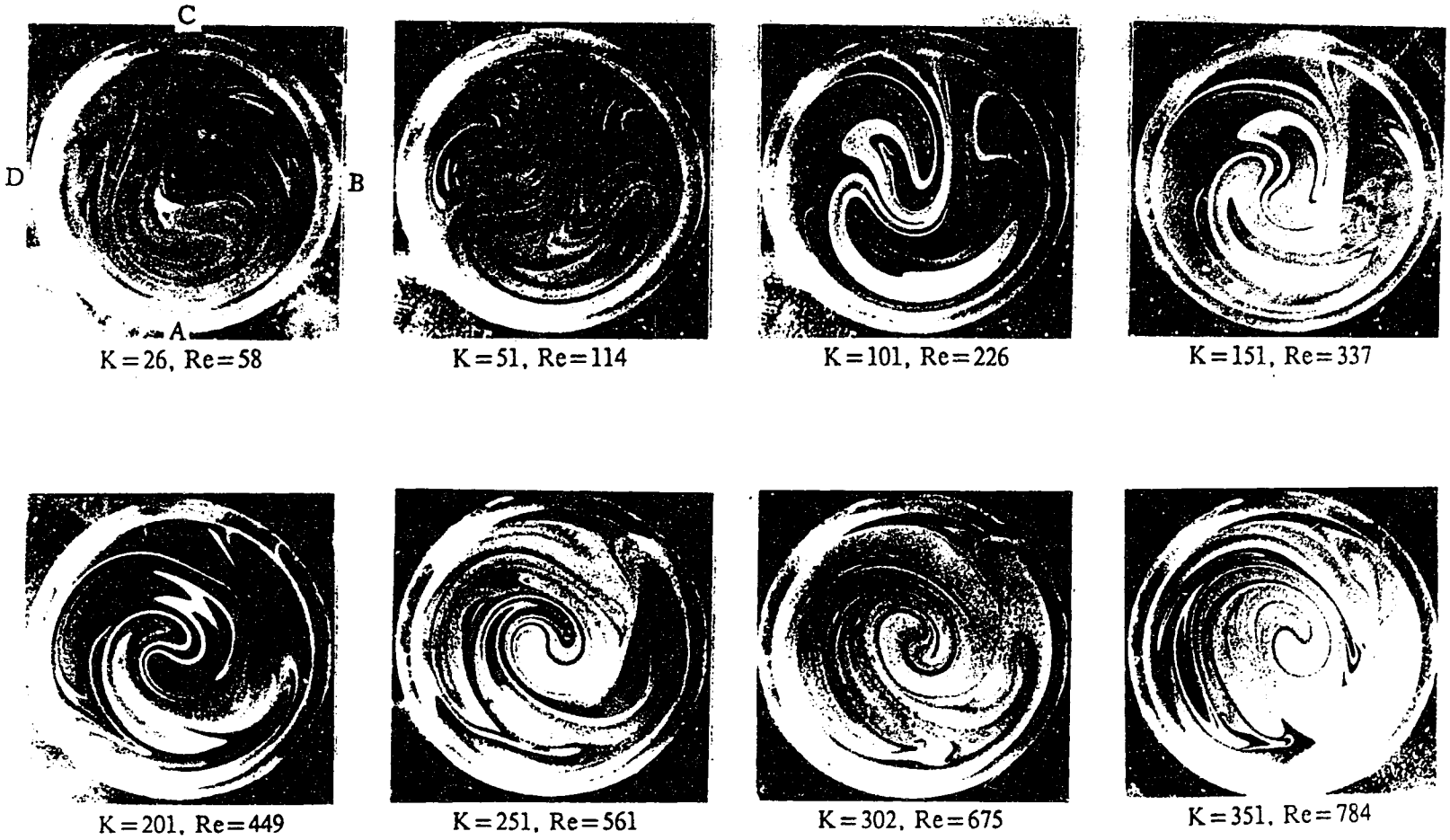

Fig. 2.19 The effect of Dean number on secondary flow patterns at the exit of a 90° second circular bend with $a/R_c=0.2$, $\psi=180°$ and $\theta=90°$

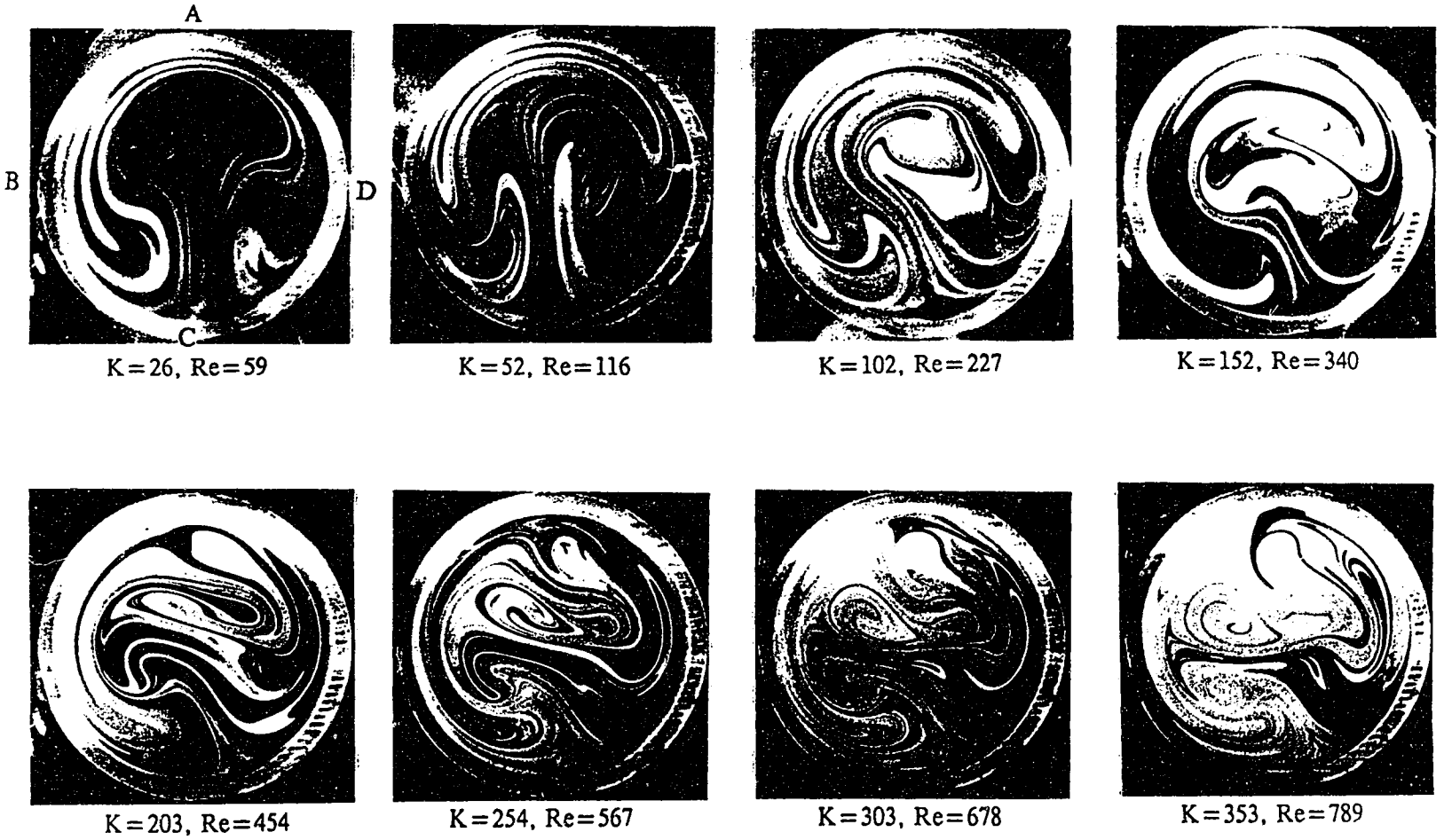

Fig. 2.20 The effect of Dean number on secondary flow patterns at the exit of a 135° second circular bend with $a/R_c=0.2$, $\psi=180°$ and $\theta=90°$

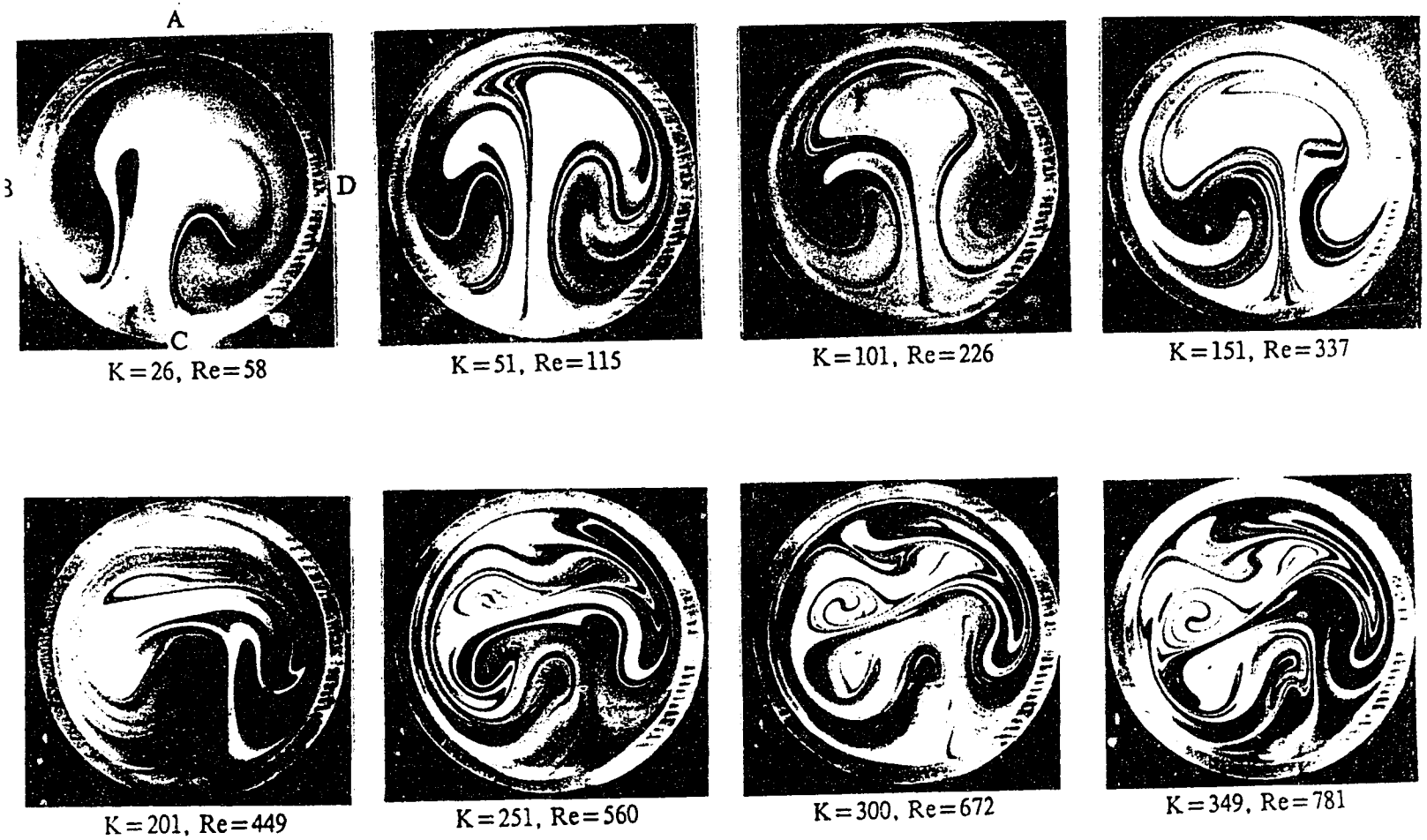

Fig. 2.21 The effect of Dean number on secondary flow patterns at the exit of a 180° second circular bend with $a/R_c=0.2$, $\psi=180°$ and $\theta=90°$

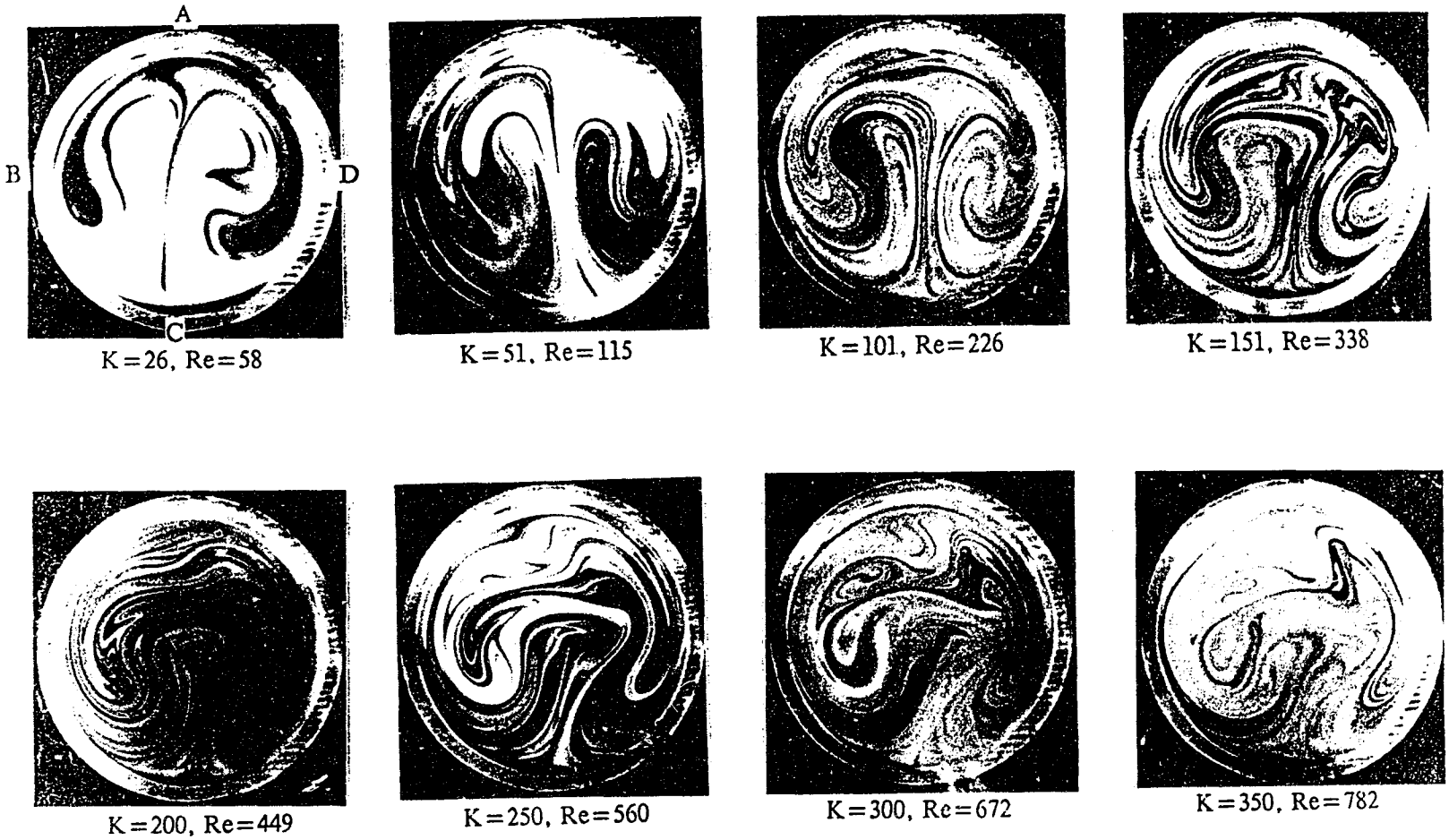

Fig. 2.22 The effect of Dean number on secondary flow patterns at the exit of a 225° second circular bend with $a/R_c=0.2$, $\psi=180°$ and $\theta=90°$

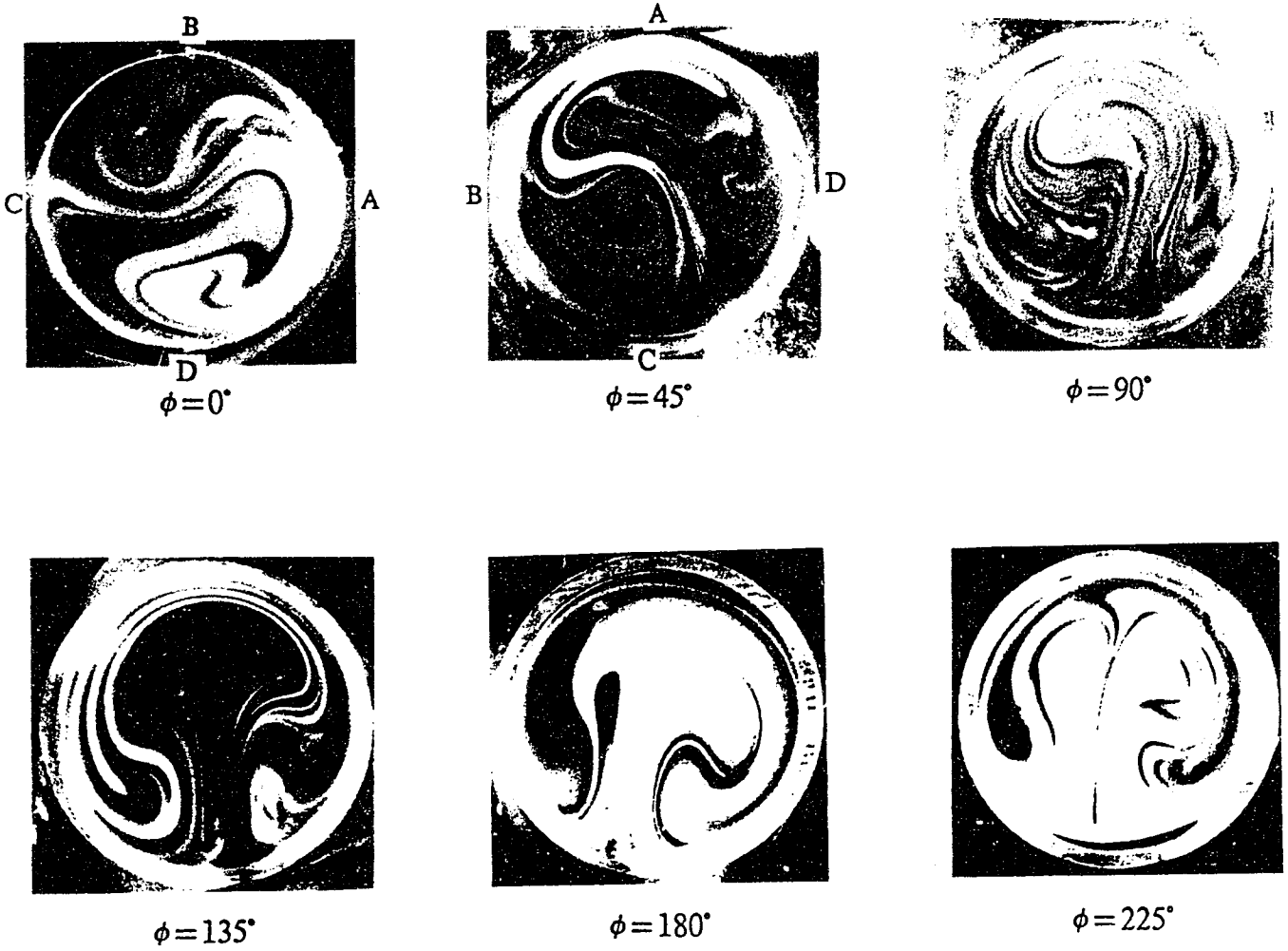

Fig. 2.23 Developing secondary flow patterns in the second circular bend with $a/R_c=0.2$, $\psi=180°$ and $\theta=90°$ at K=25

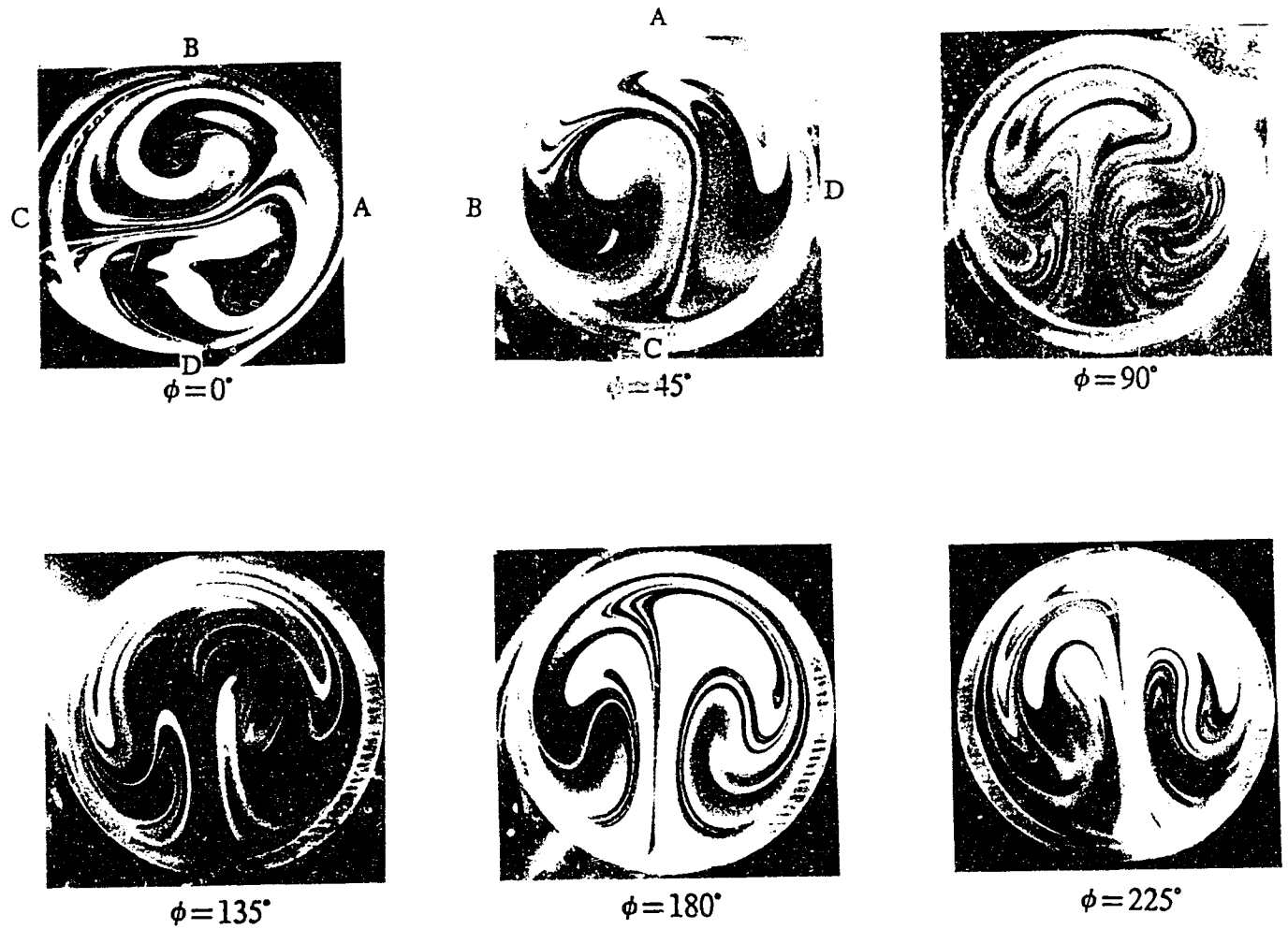

Fig. 2.24 Developing secondary flow patterns in the second circular bend with $a/R_c=0.2$, $\psi=180°$ and $\theta=90°$ at K=50

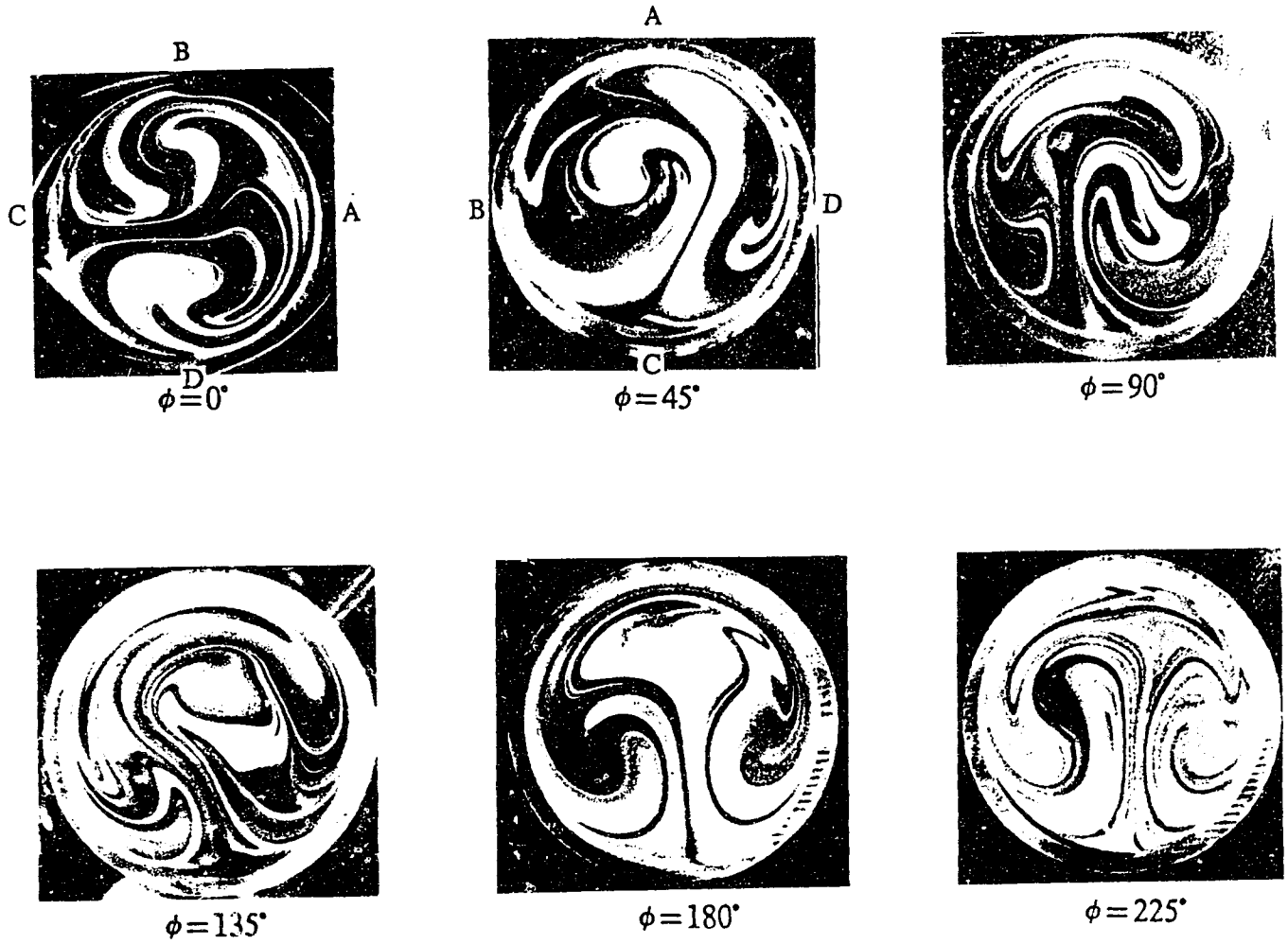

Fig. 2.25 Developing secondary flow patterns in the second circular bend with $a/R_c=0.2$, $\psi=180°$ and $\theta=90°$ at K=100

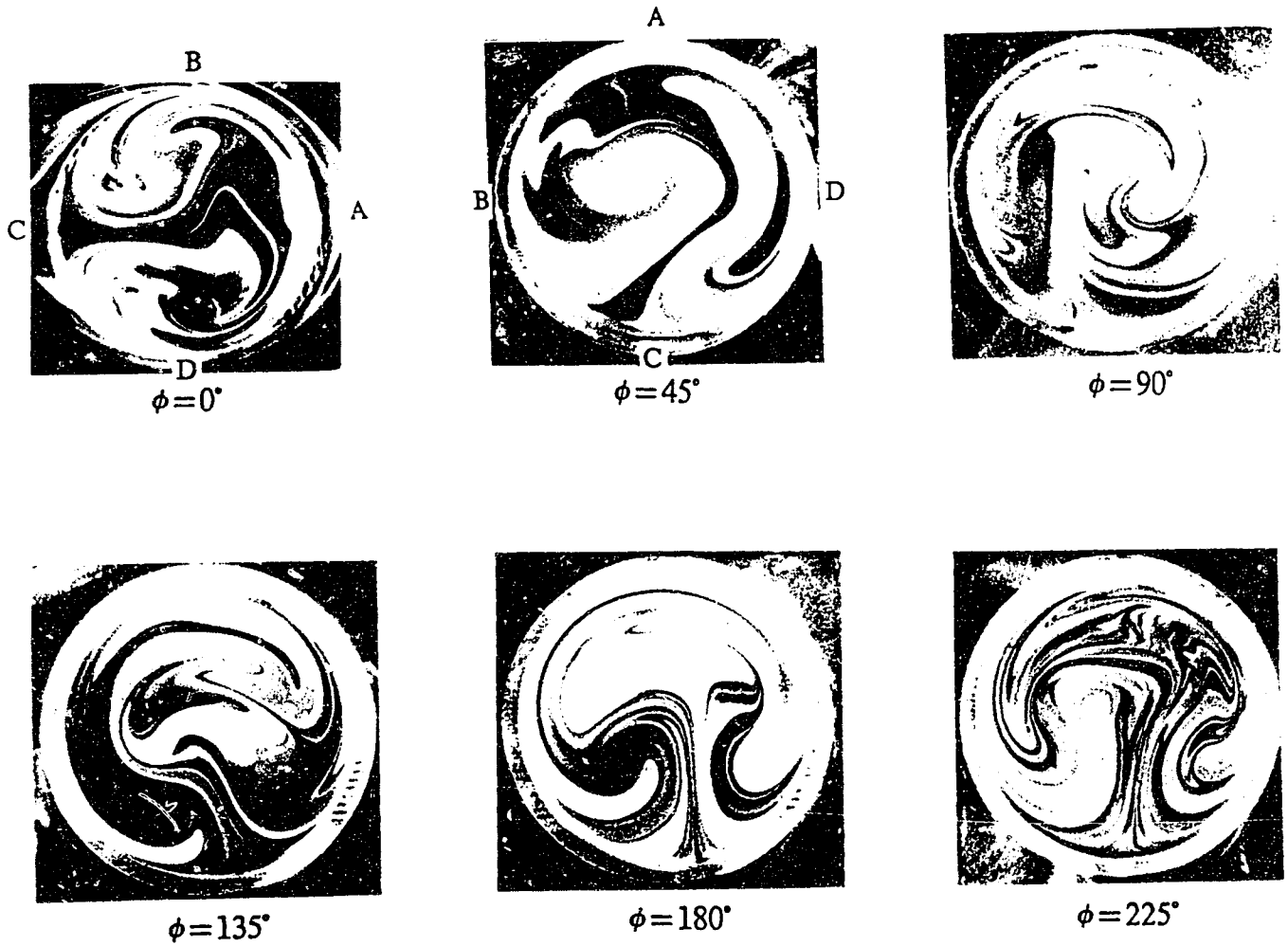

Fig. 2.26 Developing secondary flow patterns in the second circular bend with a/R_c=0.2 , ψ=180° and θ=90° at K=150

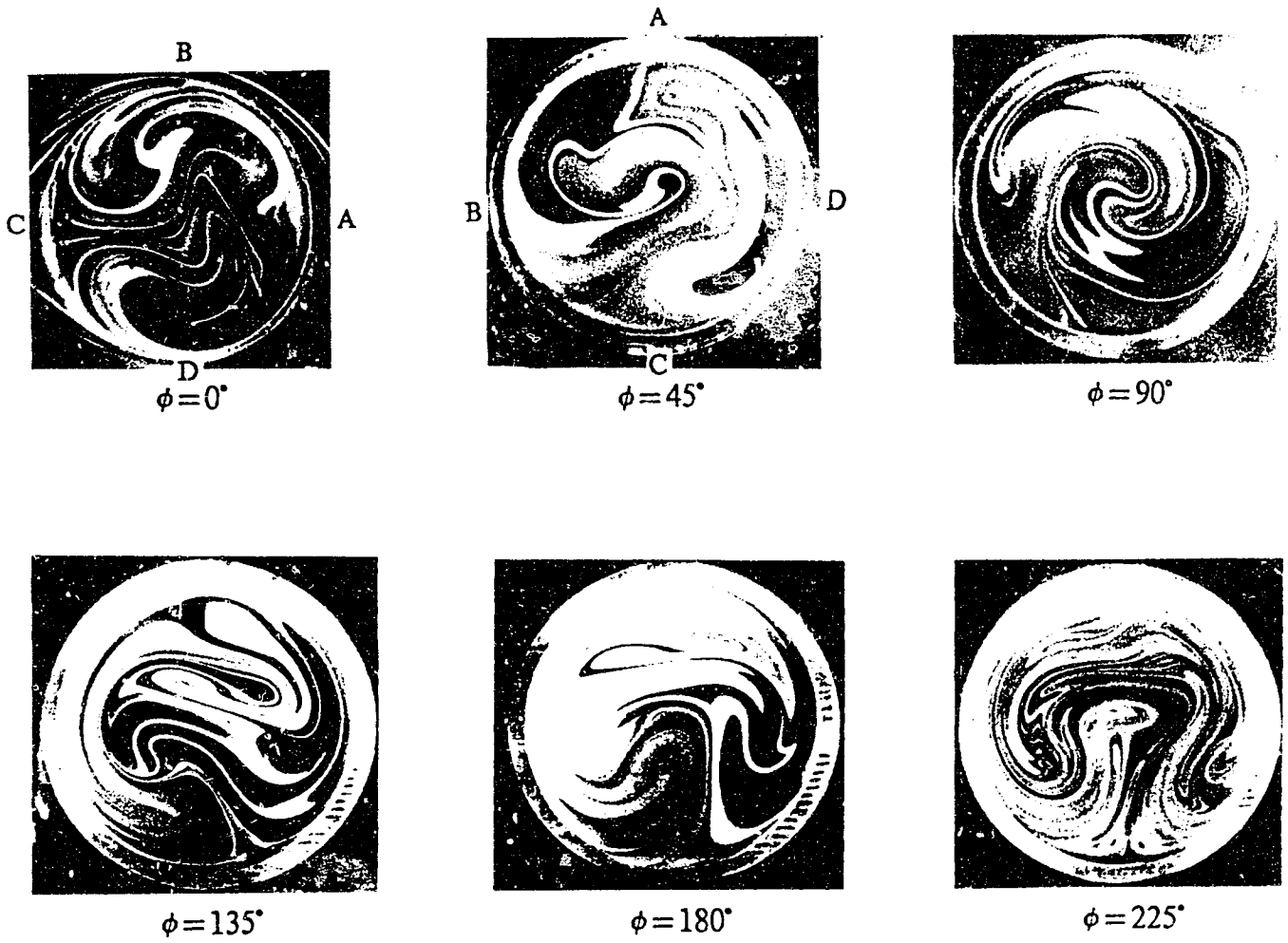

Fig. 2.27 Developing secondary flow patterns in the second circular bend with $a/R_c=0.2$, $\psi=180°$ and $\theta=90°$ at K=200

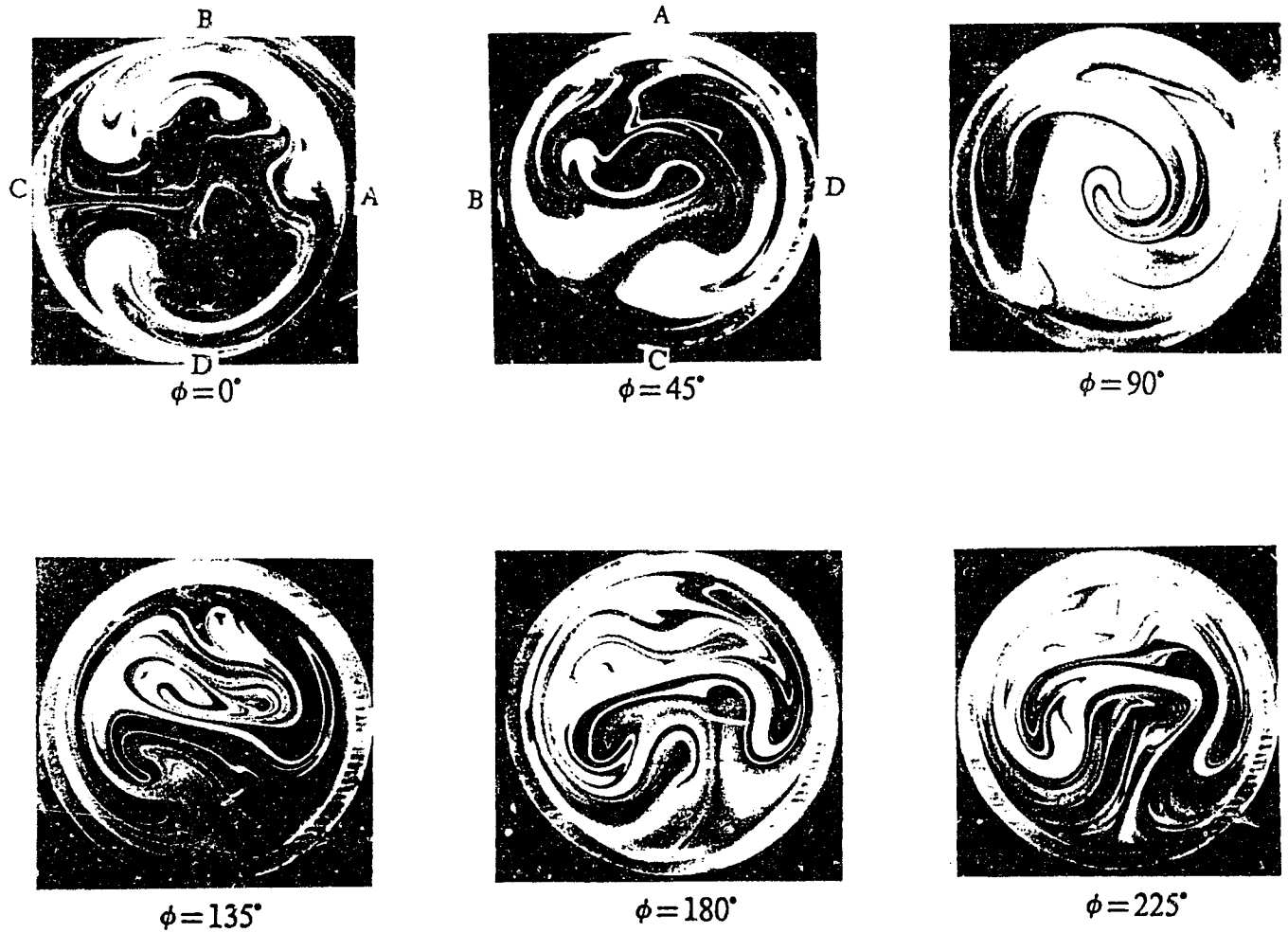

Fig. 2.28 Developing secondary flow patterns in the second circular bend with $a/R_c=0.2$, $\psi=180°$ and $\theta=90°$ at K=250

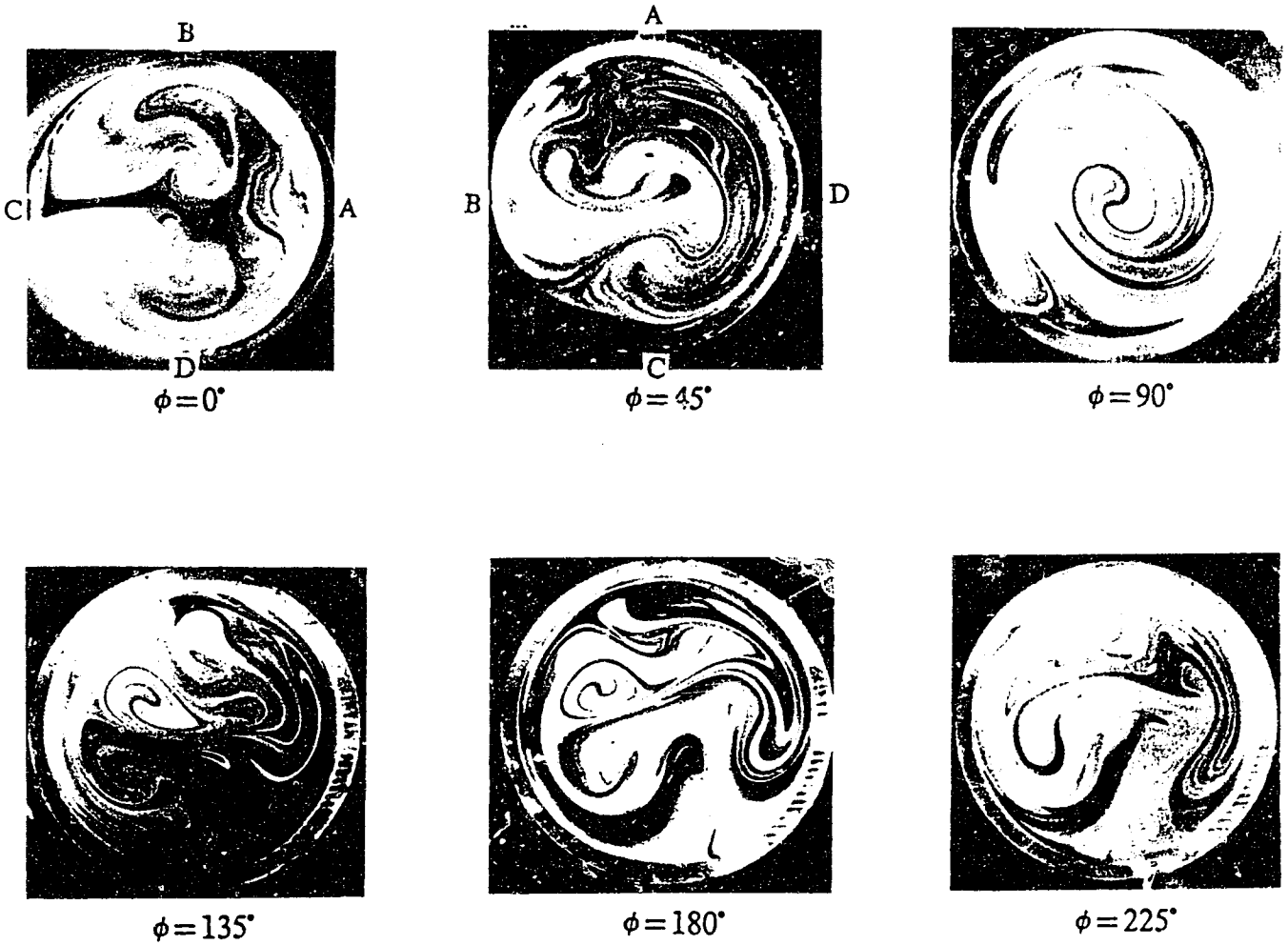

Fig. 2.29 Developing secondary flow patterns in the second circular bend with $a/R_c=0.2$, $\psi=180°$ and $\theta=90°$ at K=300

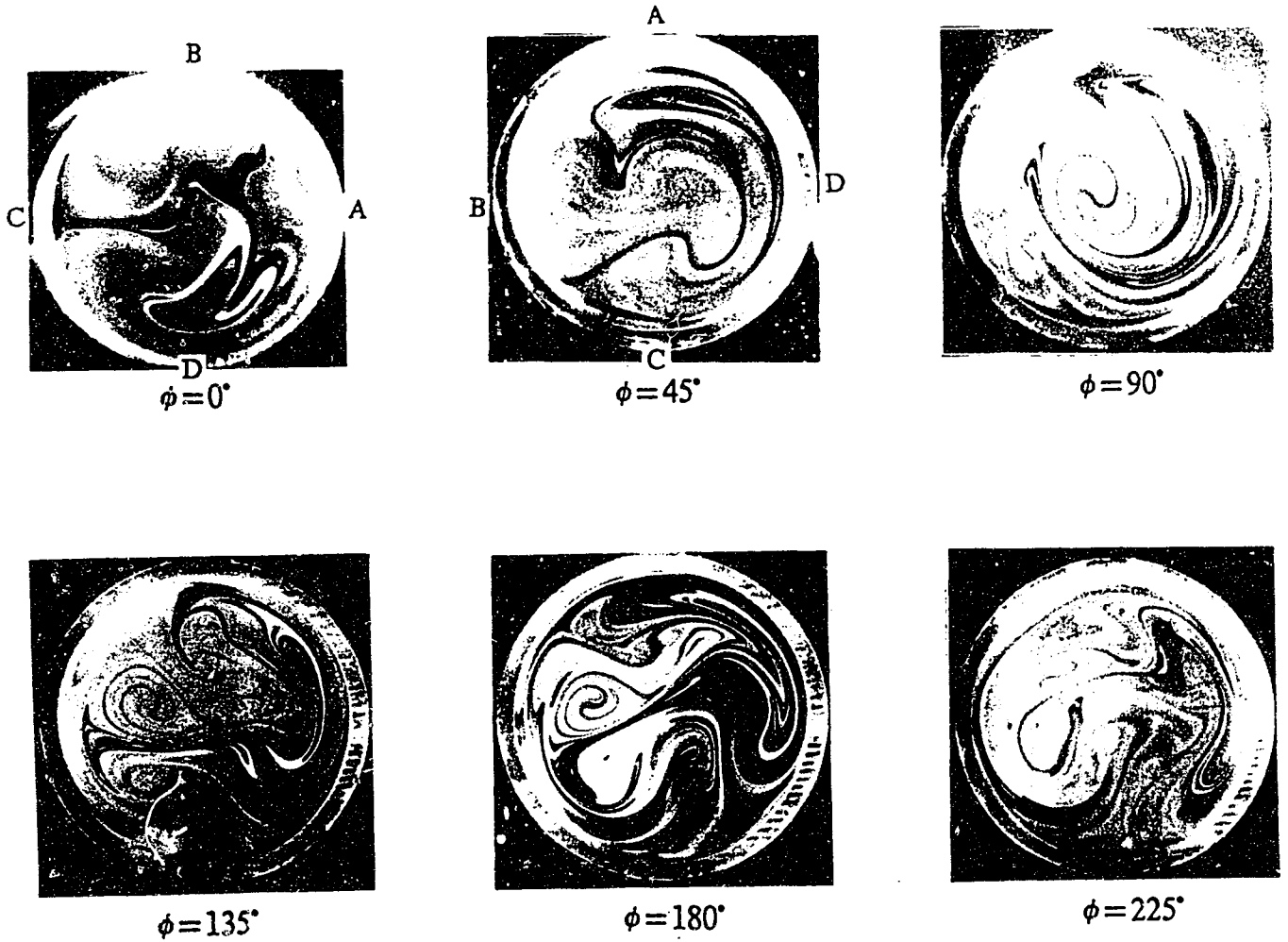

Fig. 2.30 Developing secondary flow patterns in the second circular bend with $a/R_c=0.2$, $\psi=180°$ and $\theta=90°$ at K=350

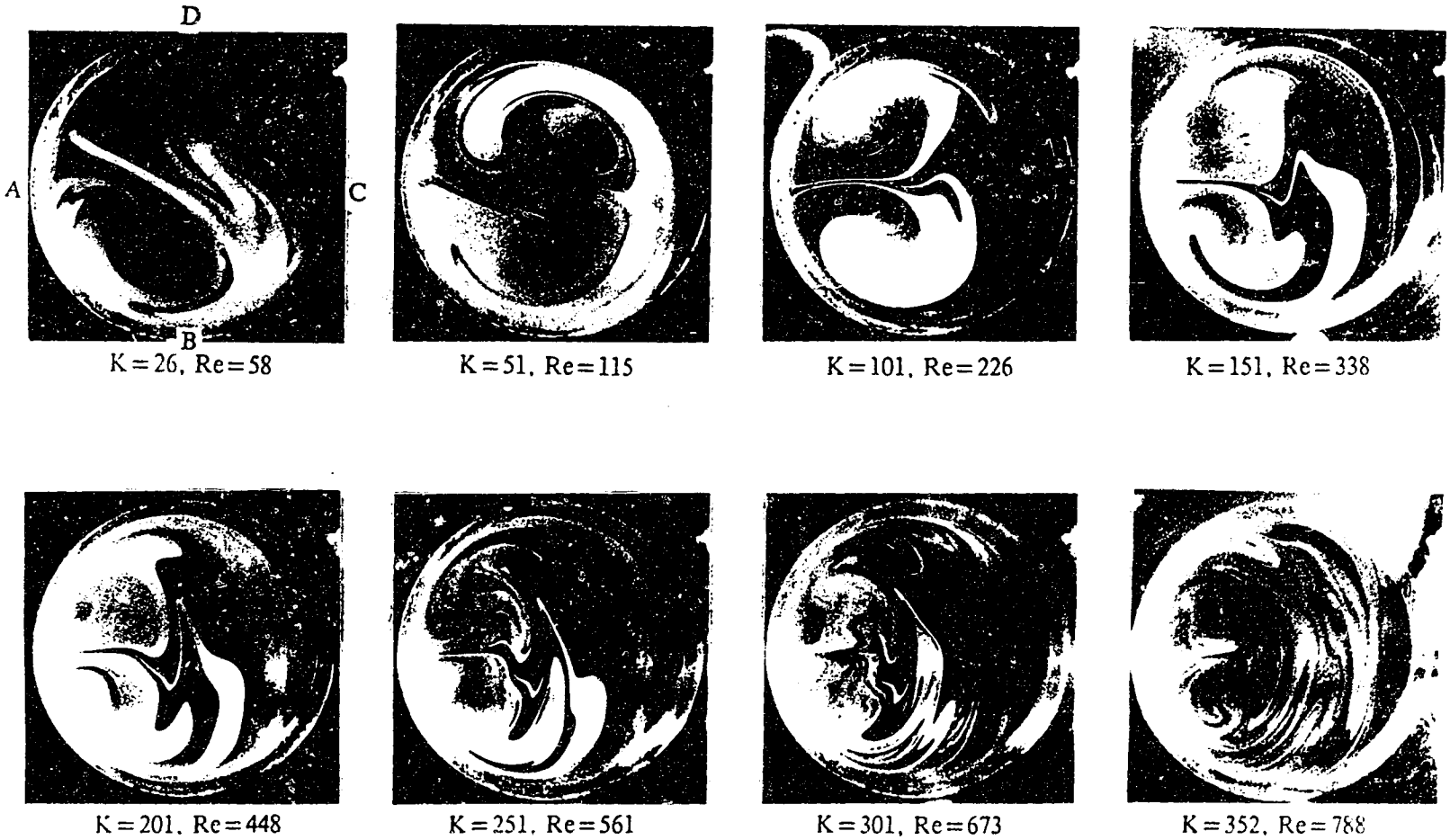

Fig. 2.31 The effect of Dean number on secondary flow patterns at the exit of a 45° second circular bend with $a/R_c=0.2$, $\psi=180°$ and $\theta=180°$

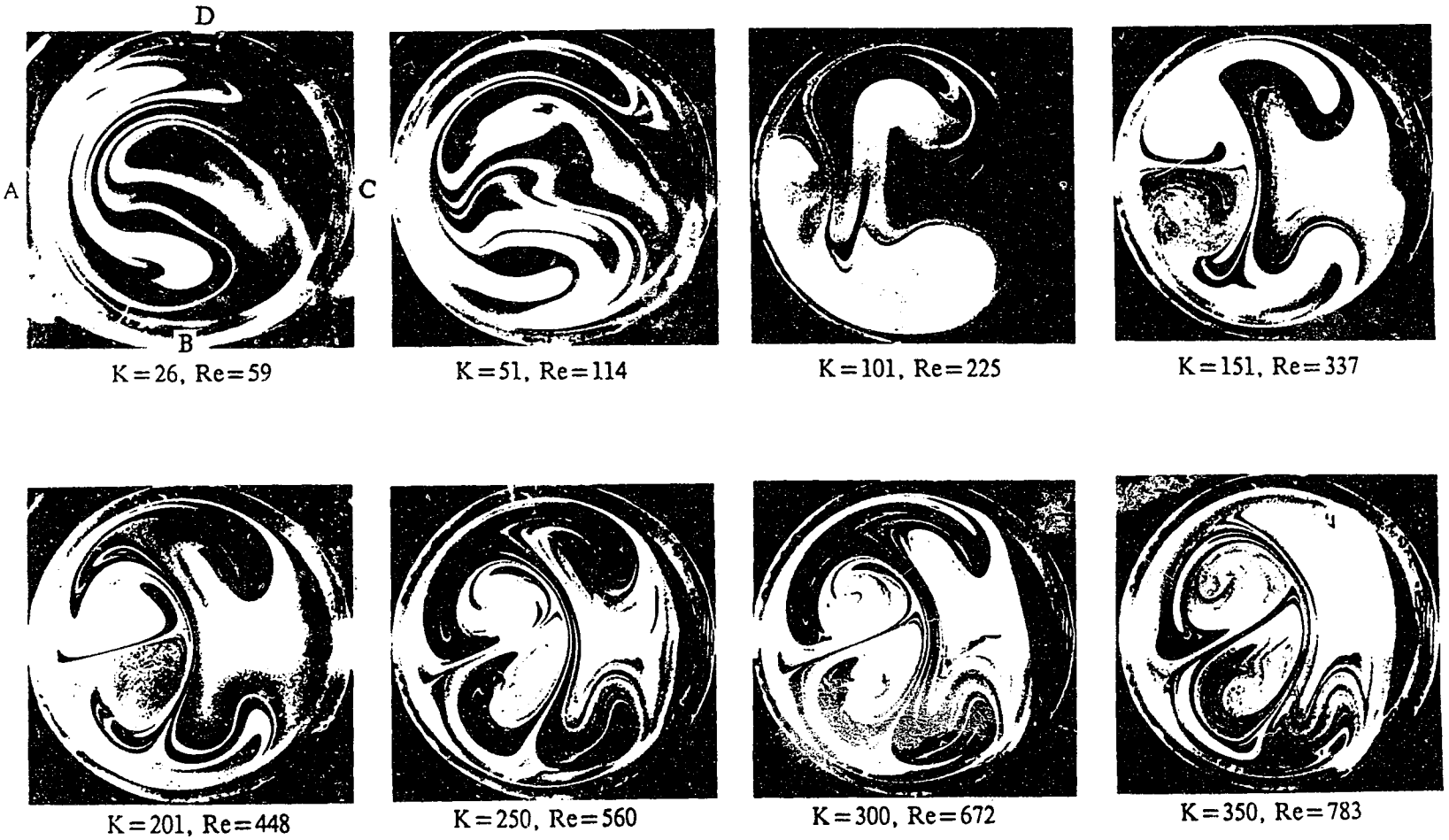

Fig. 2.32 The effect of Dean number on secondary flow patterns at the exit of a 90° second circular bend with $a/R_c=0.2$, $\psi=180°$ and $\theta=180°$

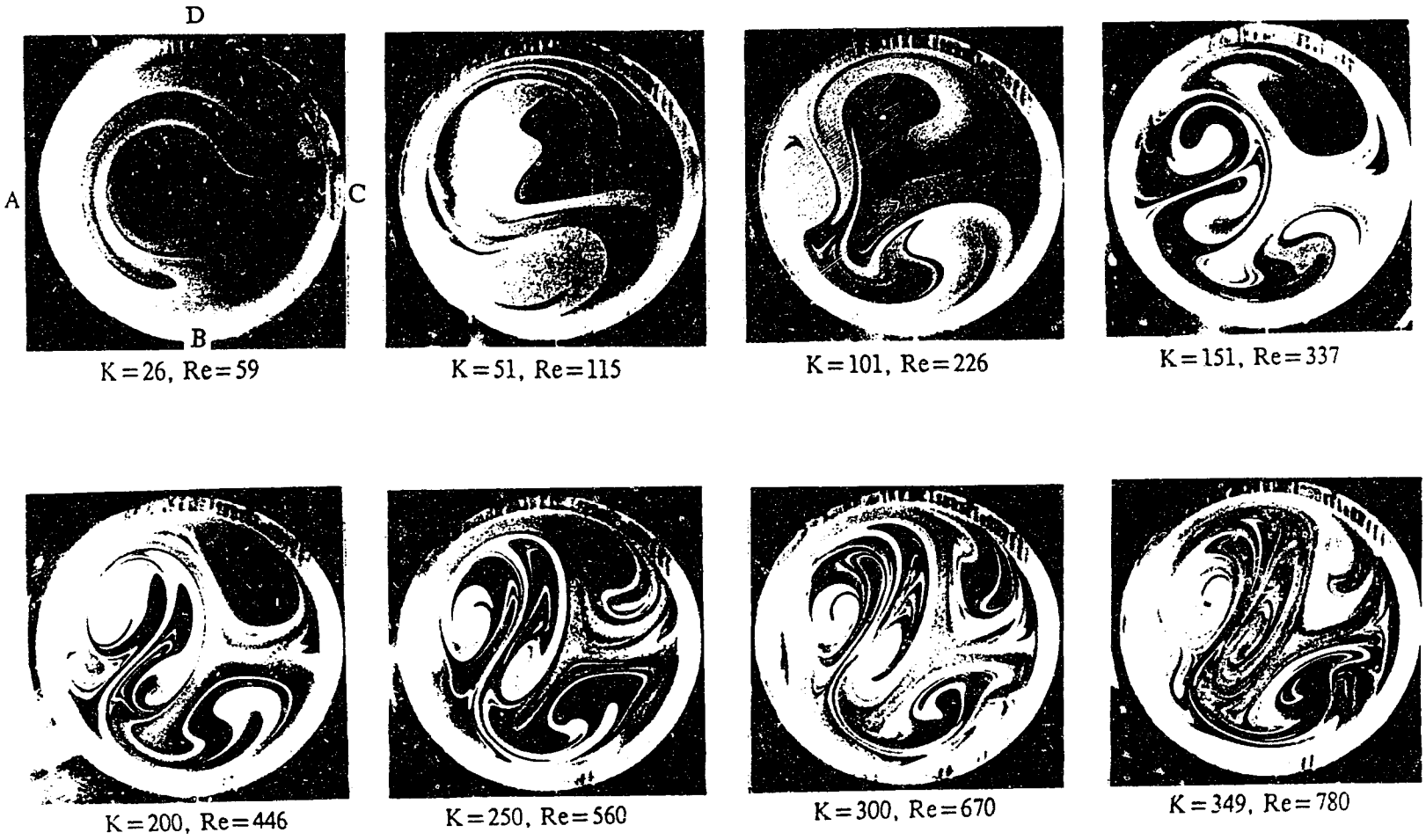

Fig. 2.33 The effect of Dean number on secondary flow patterns at the exit of a 135° second circular bend with $a/R_c=0.2$, $\psi=180°$ and $\theta=180°$

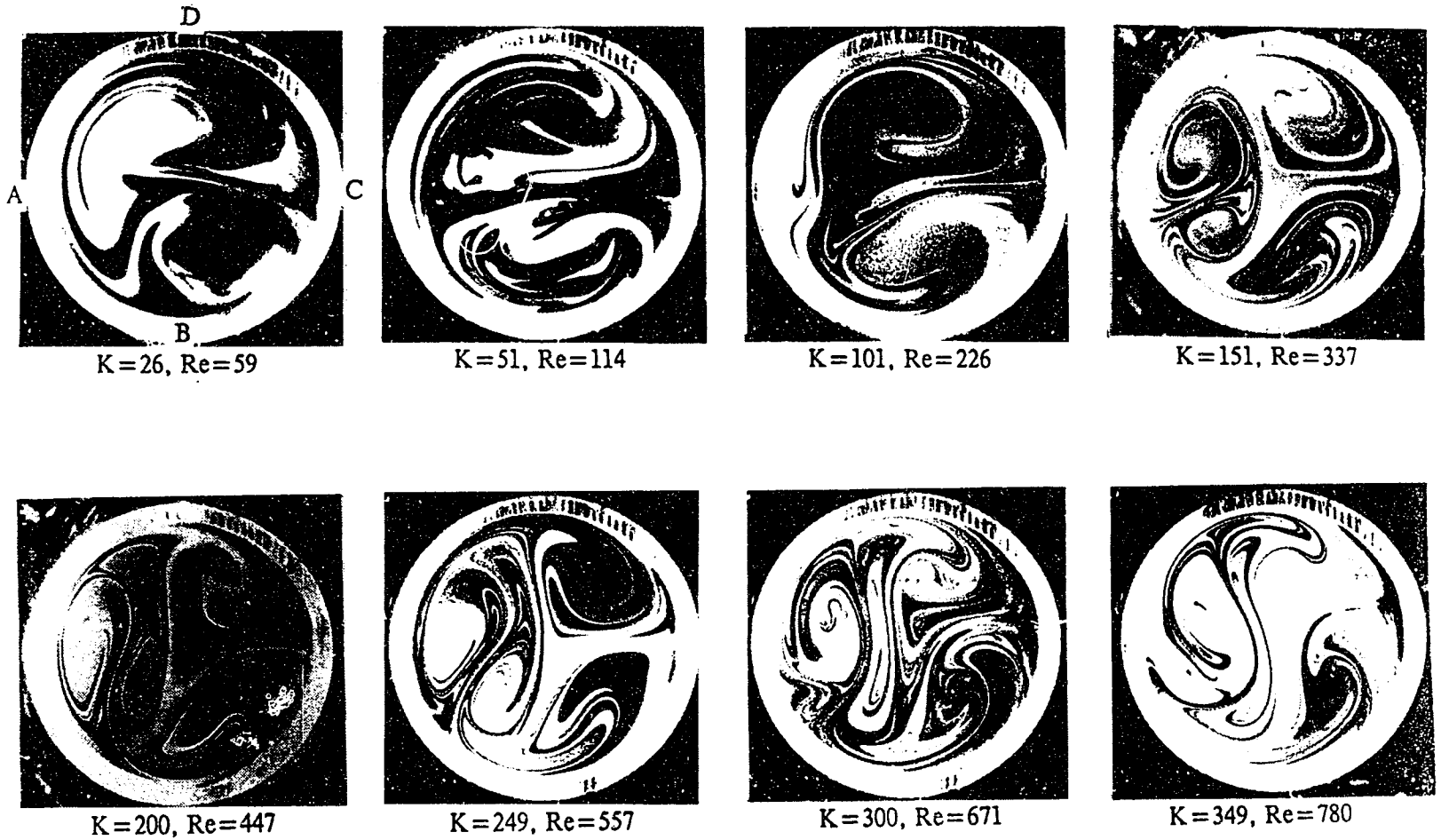

Fig. 2.34 The effect of Dean number on secondary flow patterns at the exit of a 180° second circular bend with $a/R_c=0.2$, $\psi=180°$ and $\theta=180°$

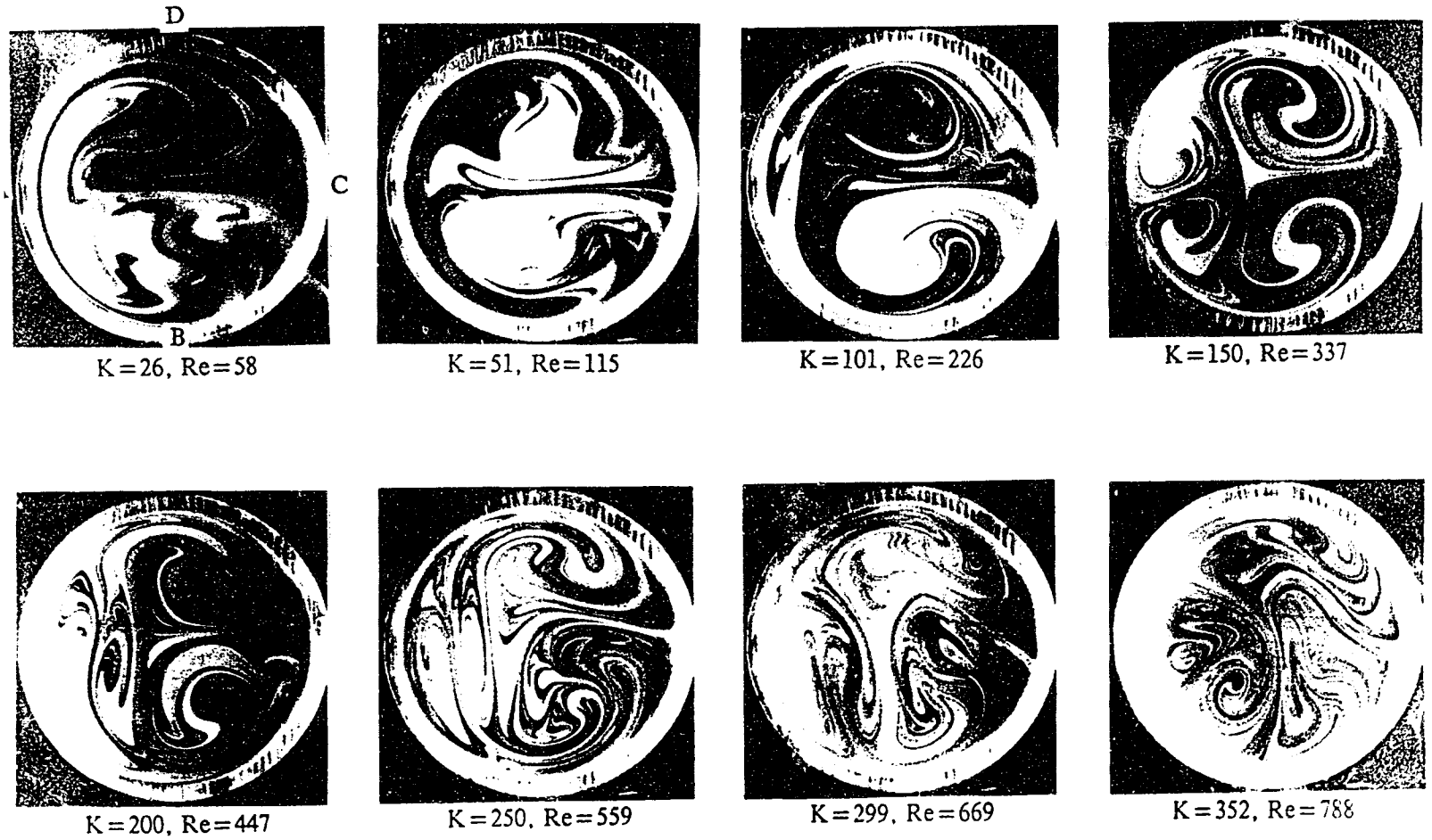

Fig. 2.35 The effect of Dean number on secondary flow patterns at the exit of a 225° second circular bend with $a/R_c=0.2$, $\psi=180°$ and $\theta=180°$

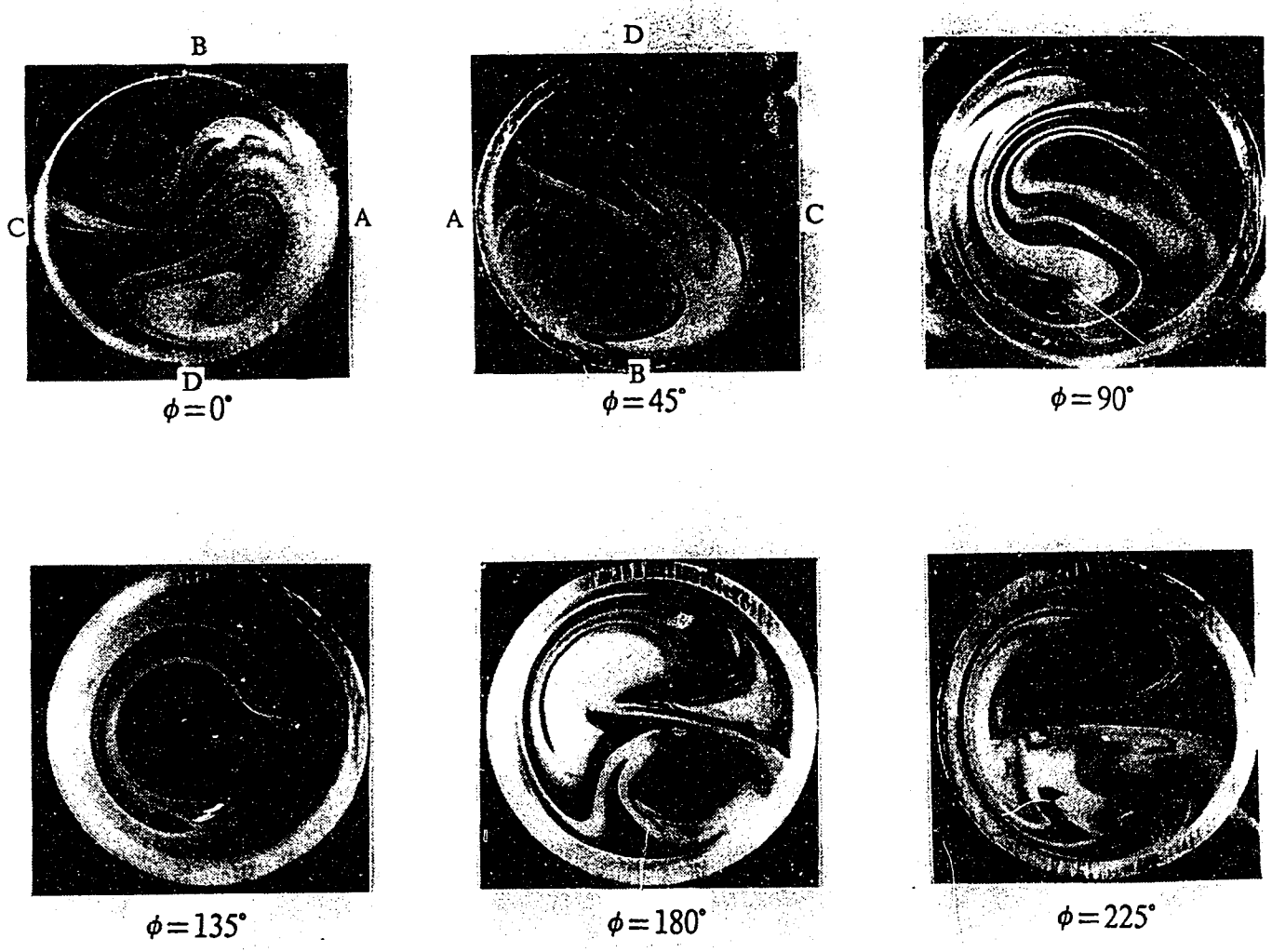

Fig. 2.36 Developing secondary flow patterns in the second circular bend with $a/R_c=0.2$, $\psi=180°$ and $\theta=180°$ at K=25

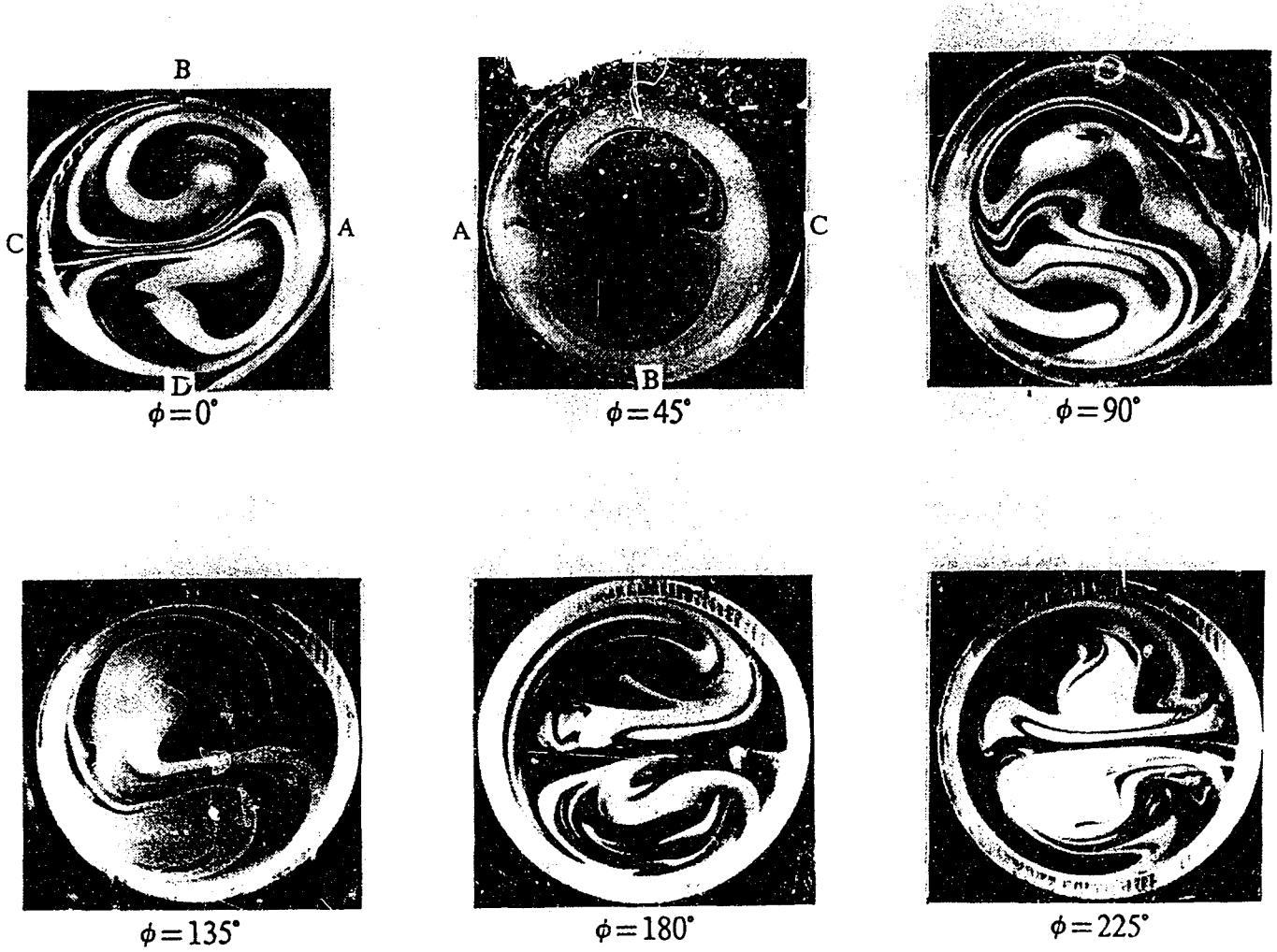

Fig. 2.37 Developing secondary flow patterns in the second circular bend with $a/R_c=0.2$, $\psi=180°$ and $\theta=180°$ at K=50

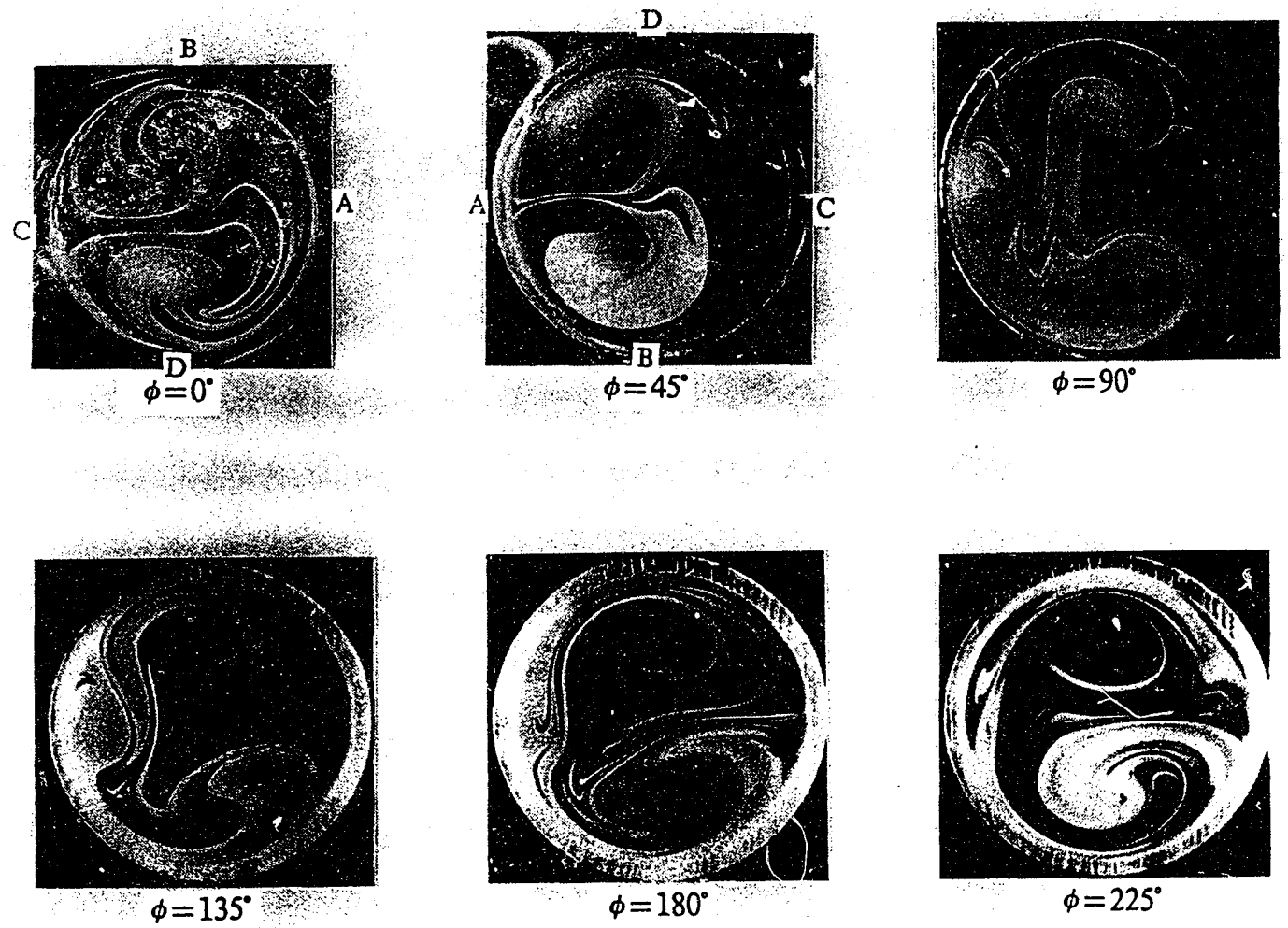

Fig. 2.38 Developing secondary flow patterns in the second circular bend with a/R_c=0.2 , ϕ=180° and θ=180° at K=100

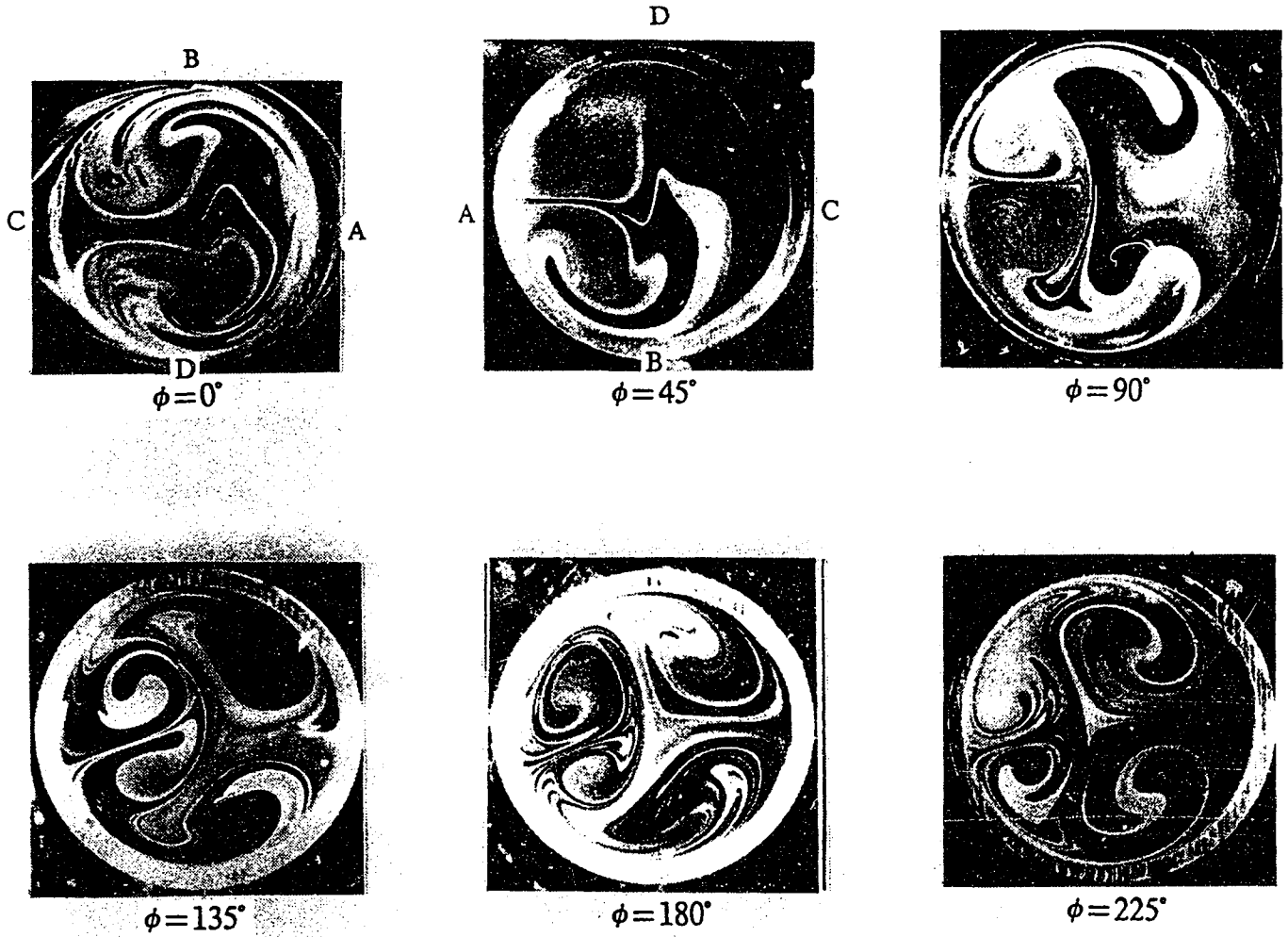

Fig. 2.39 Developing secondary flow patterns in the second circular bend with $a/R_c=0.2$, $\psi=180°$ and $\theta=180°$ at K=150

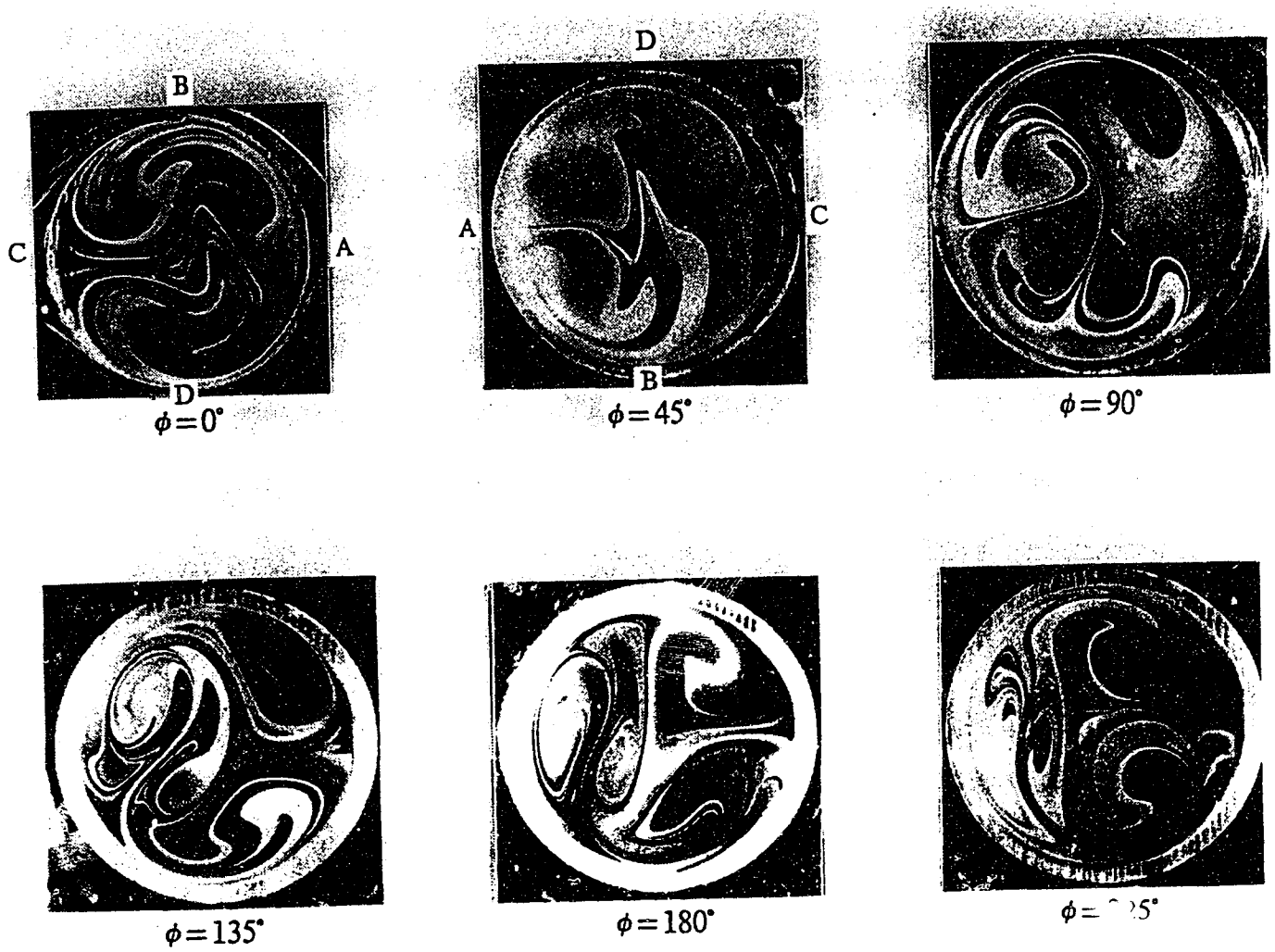

Fig. 2.40 Developing secondary flow patterns in the second circular bend with $a/R_c=0.2$; $\psi=180°$ and $\theta=180°$ at K=200

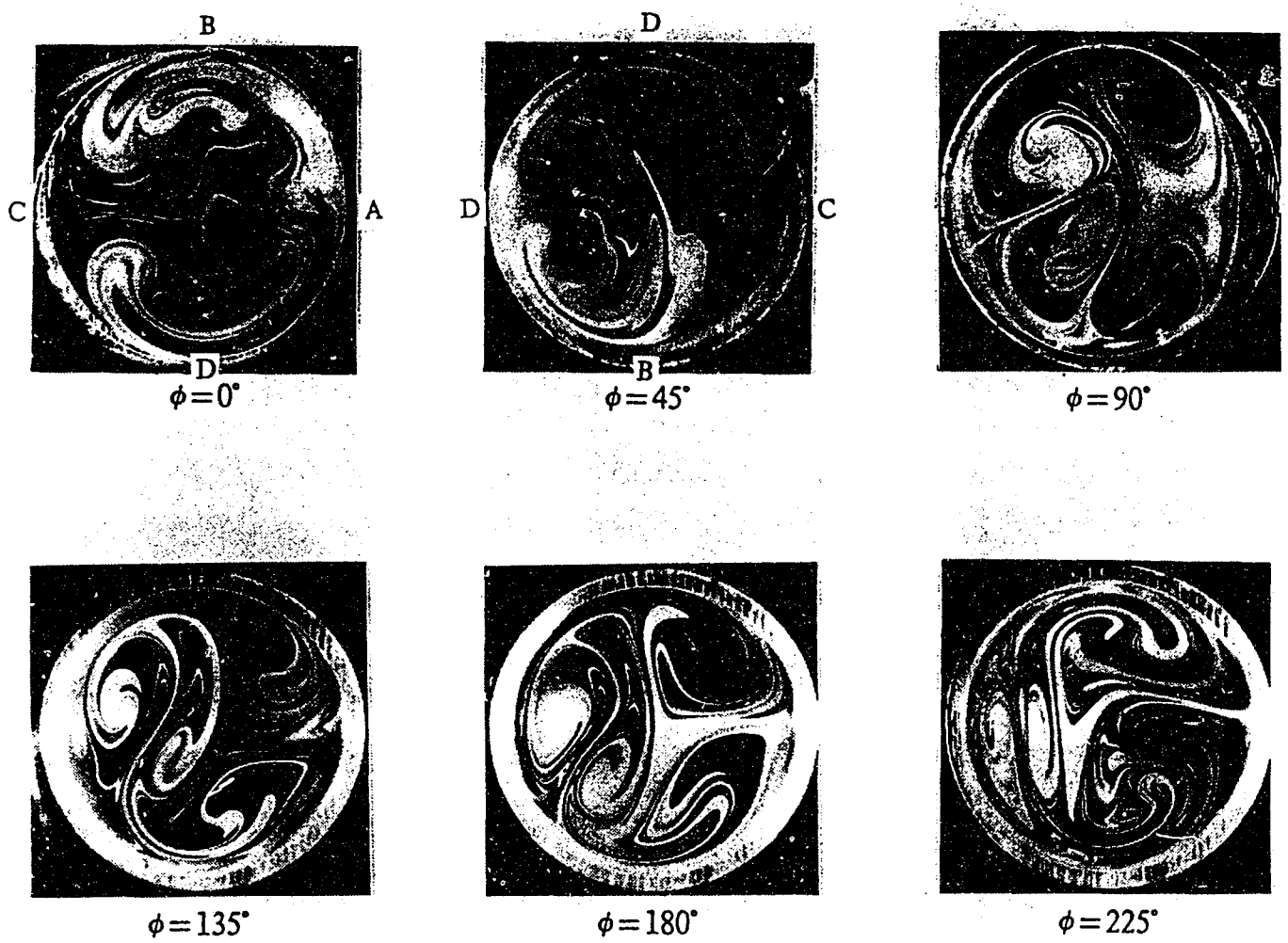

Fig. 2.41 Developing secondary flow patterns in the second circular bend with $a/R_c=0.2$, $\psi=180°$ and $\theta=180°$ at K=250

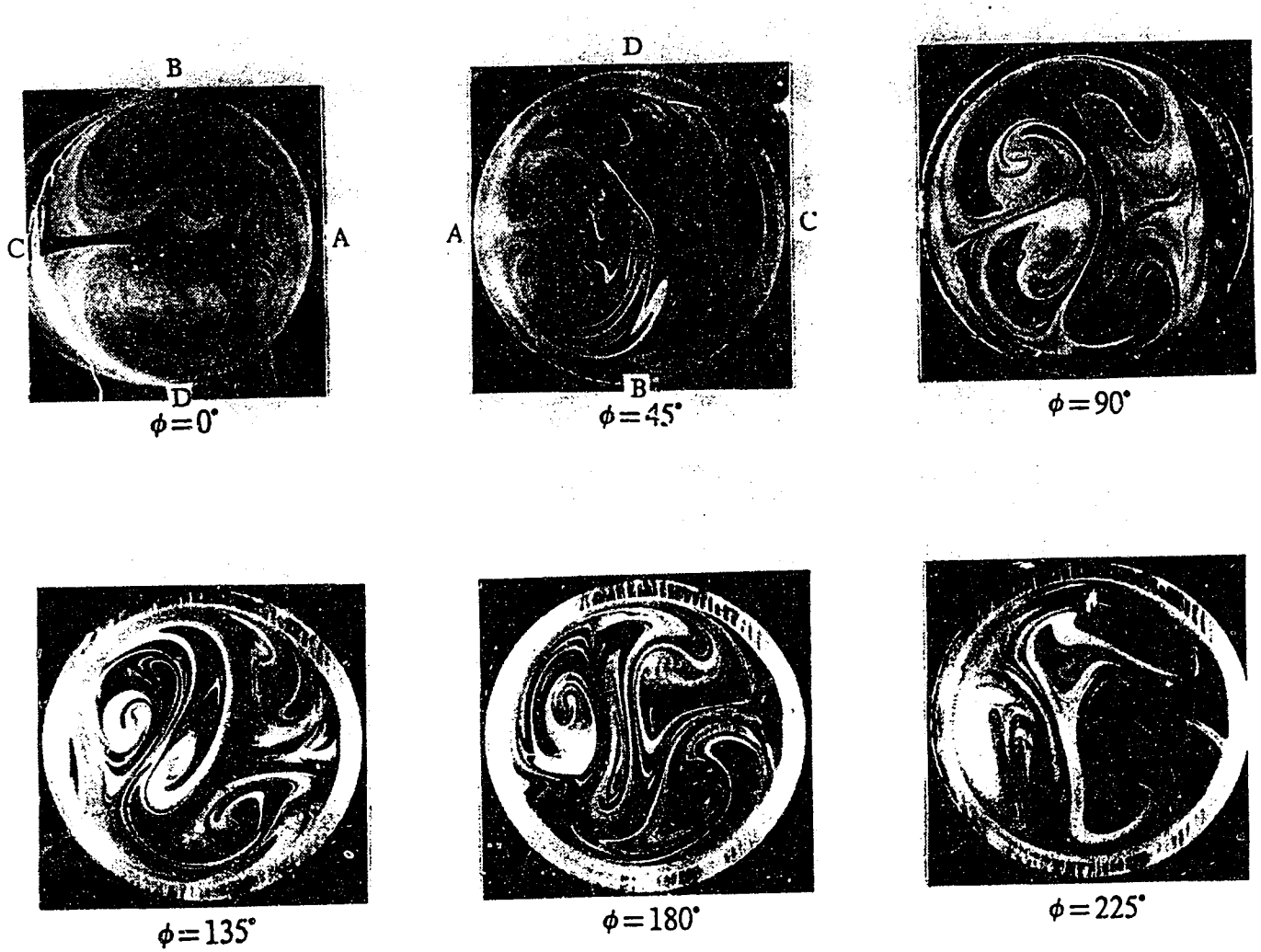

Fig. 2.42 Developing secondary flow patterns in the second circular bend with $a/R_c=0.2$, $\psi=180°$ and $\theta=180°$ at K=300

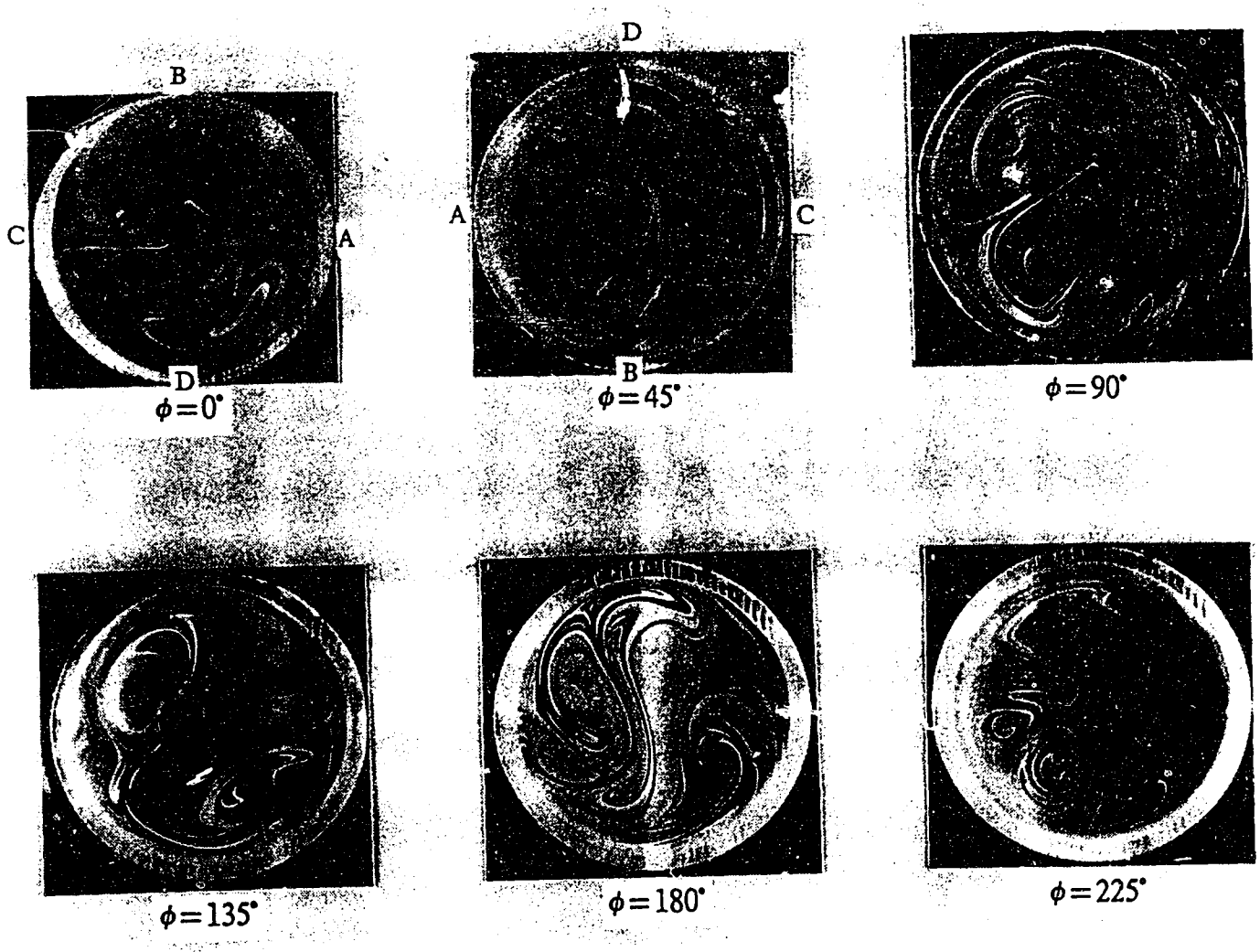

Fig. 2.43 Developing secondary flow patterns in the second circular bend with a/R_c=0.2 , ψ=180° and θ=180° at K=350

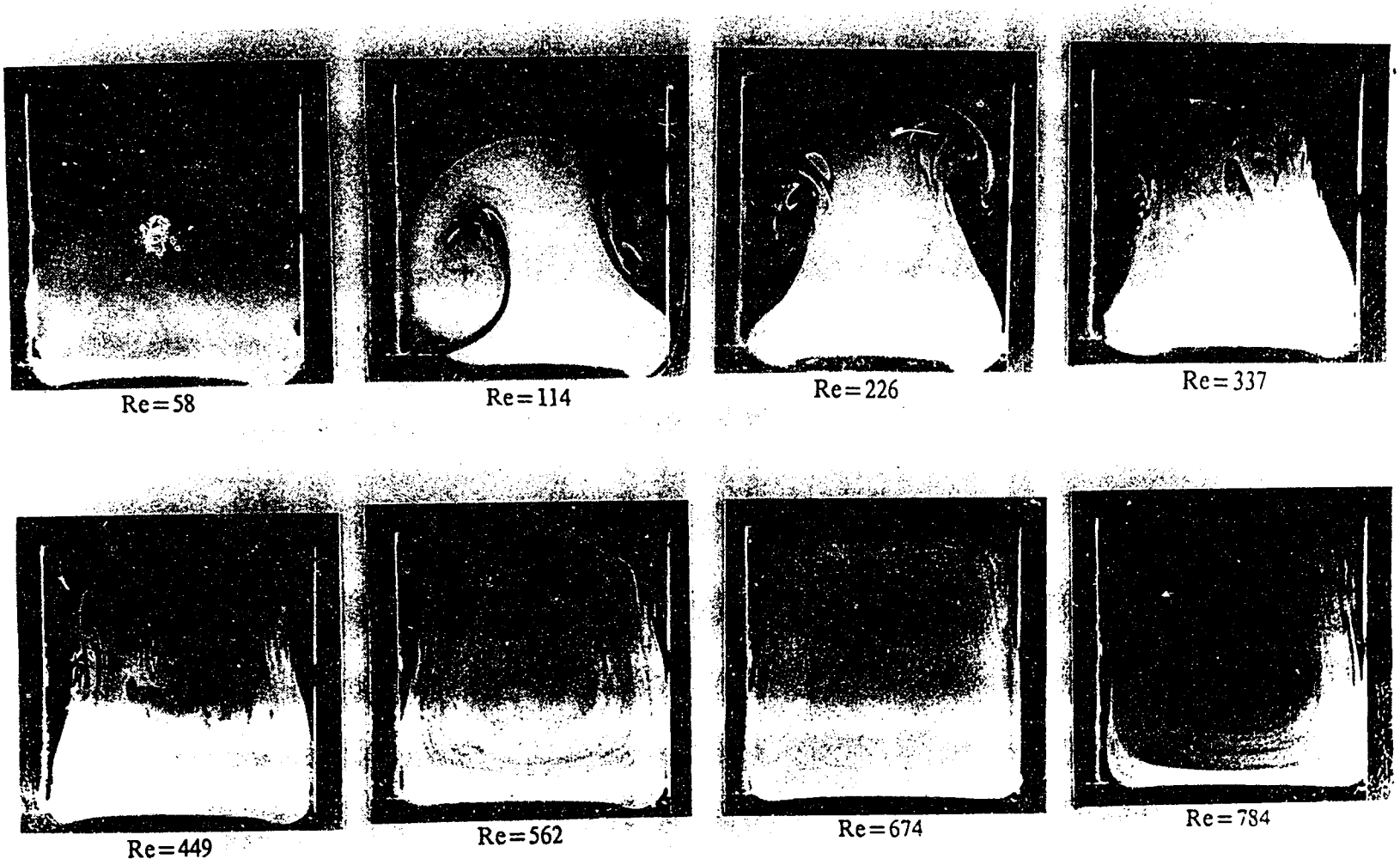

Fig. 2.44 Flow patterns at the end of the straight square entrance pipe

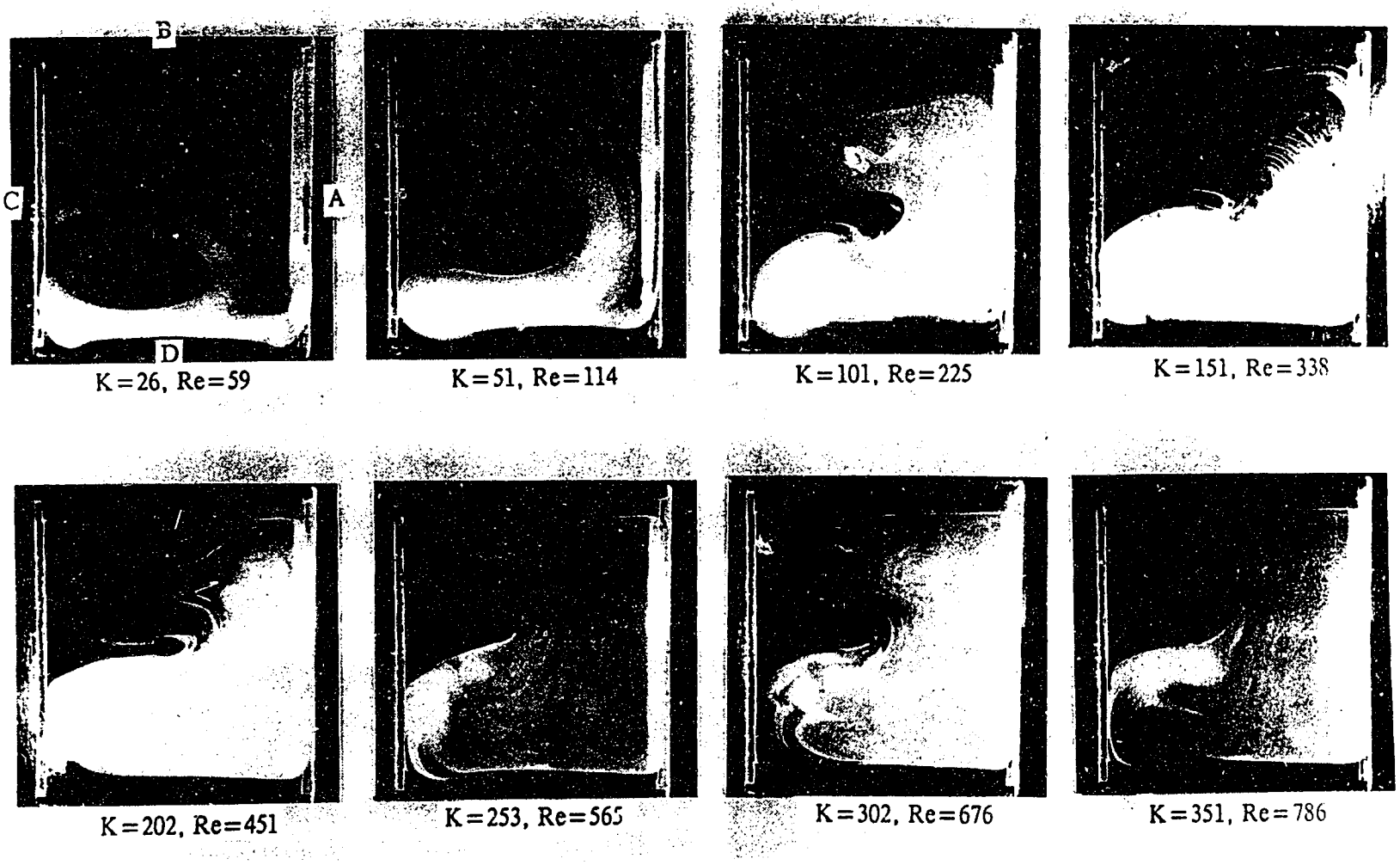

Fig. 2.45 The effect of Dean number on secondary flow patterns at the exit of a 45° square bend with $a/R_c=0.2$

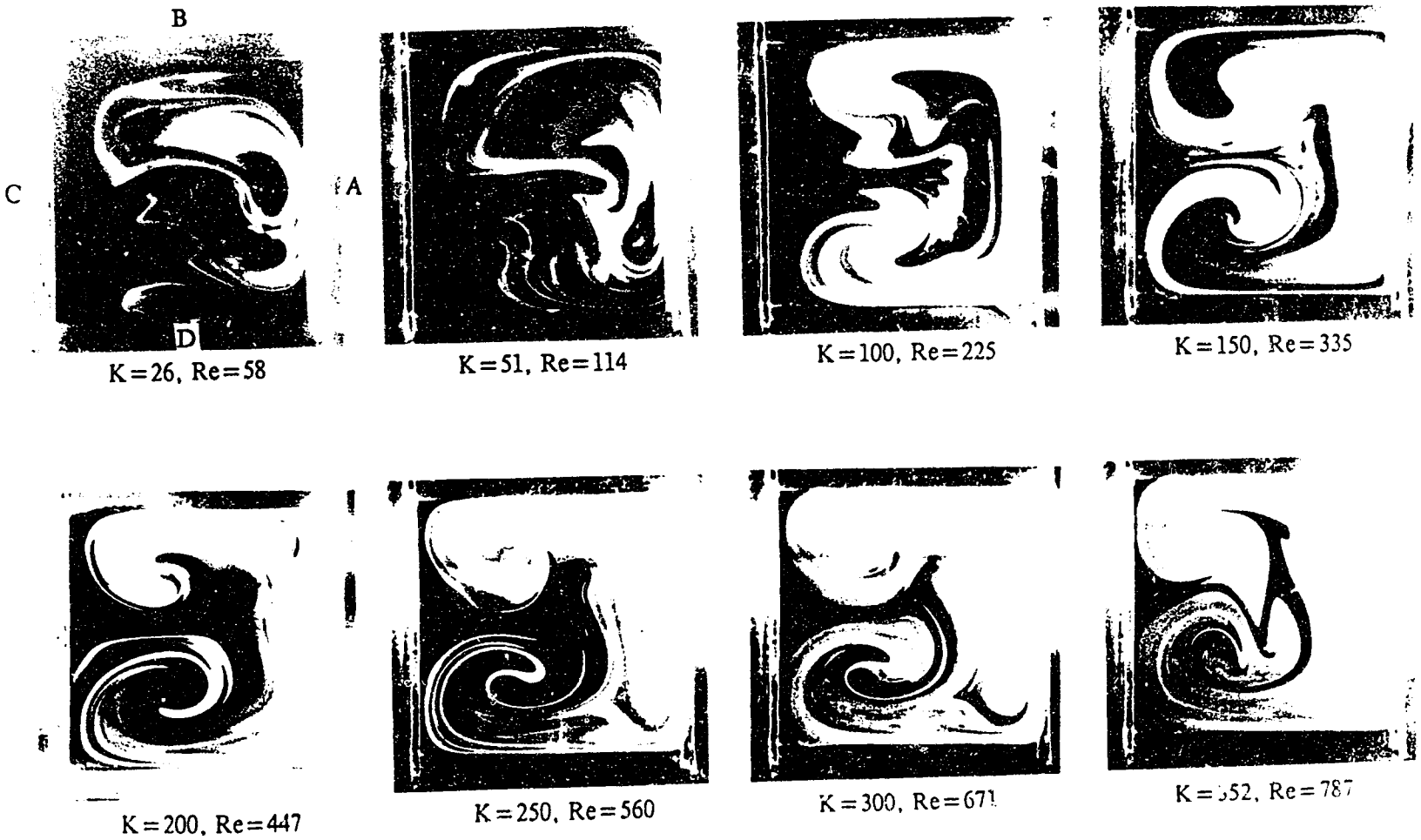

Fig. 2.46 The effect of Dean number on secondary flow patterns at the exit of a 90° square bend with $a/R_c=0.2$

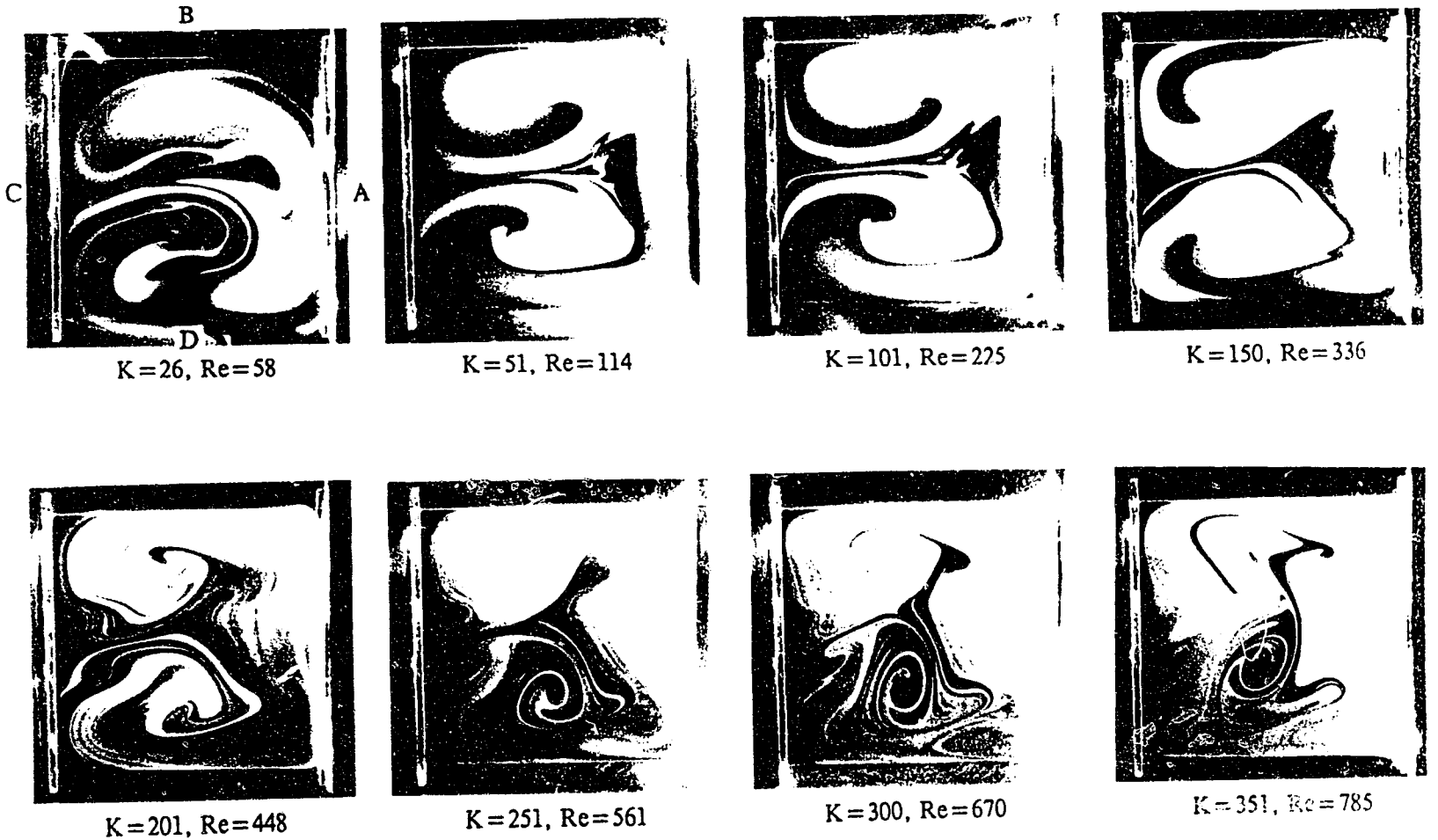

Fig. 2.47 The effect of Dean number on secondary flow patterns at the exit of a 135° square bend with $a/R_c=0.2$

Fig. 2.48 The effect of Dean number on secondary flow patterns at the exit of a 180° square bend with $a/R_c=0.2$

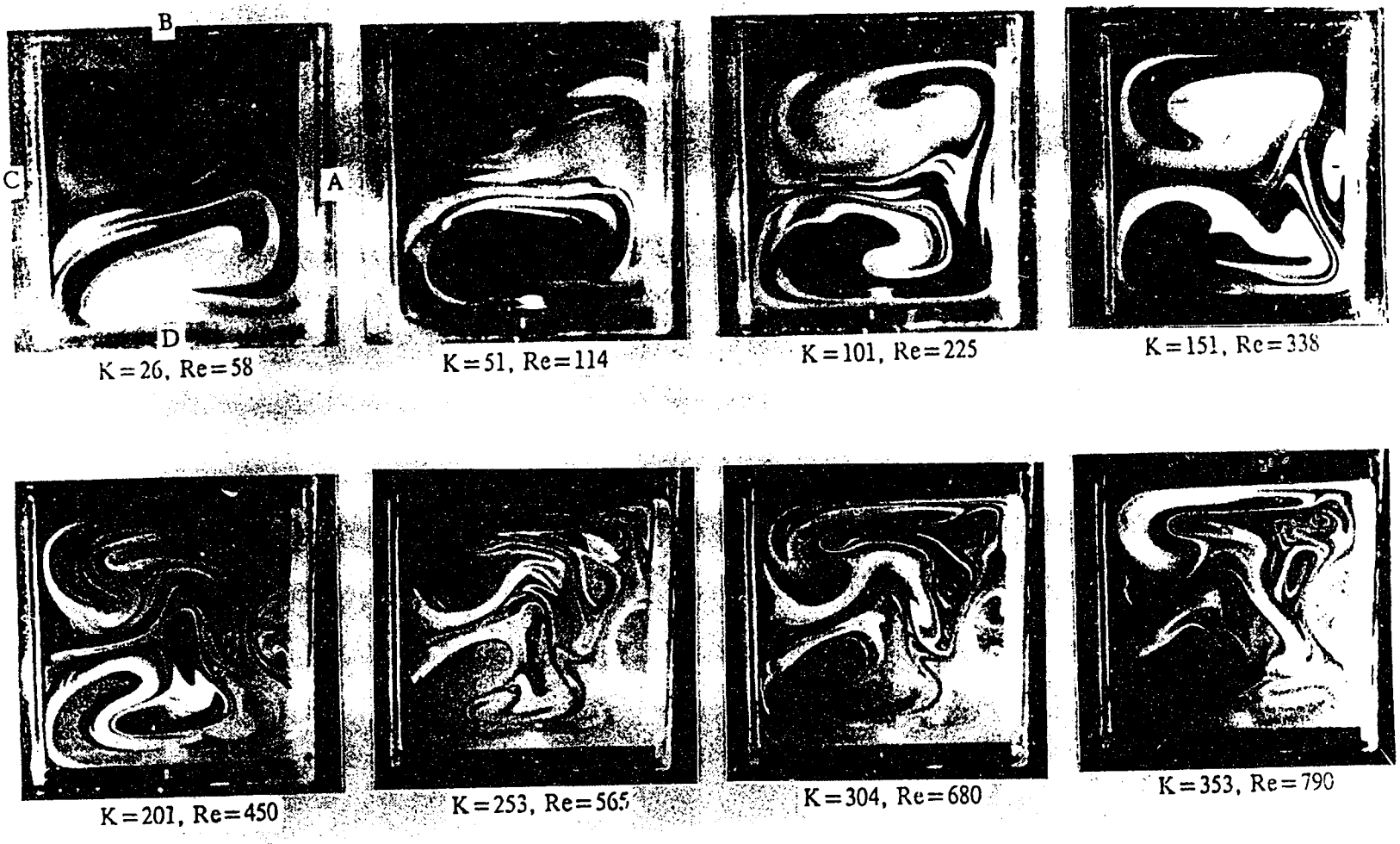

Fig. 2.49 The effect of Dean number on secondary flow patterns at the exit of a 225° square bend with $a/R_c=0.2$

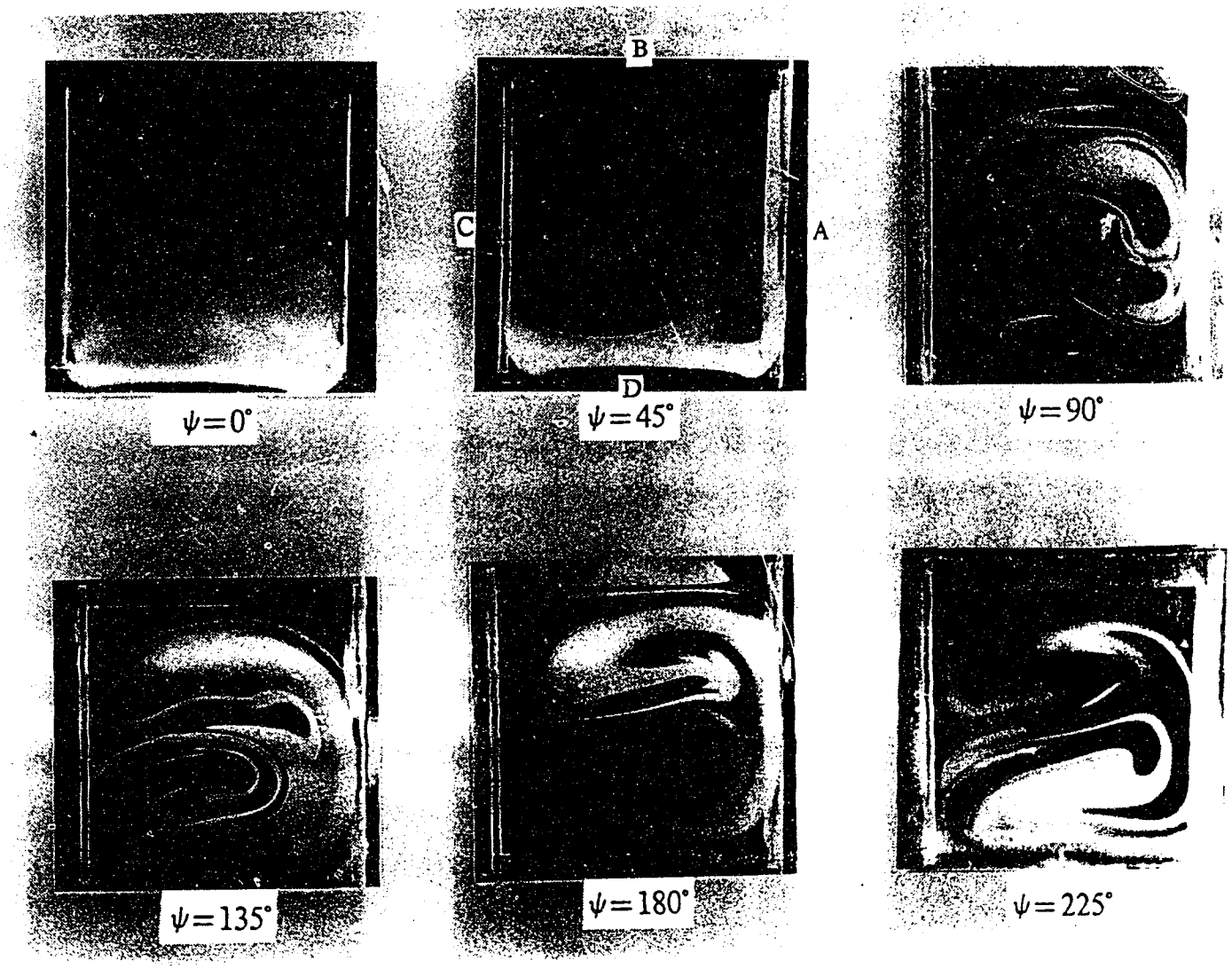

Fig. 2.50 Developing secondary flow patterns in the first square bend with a/R_c=0.2 at K=25

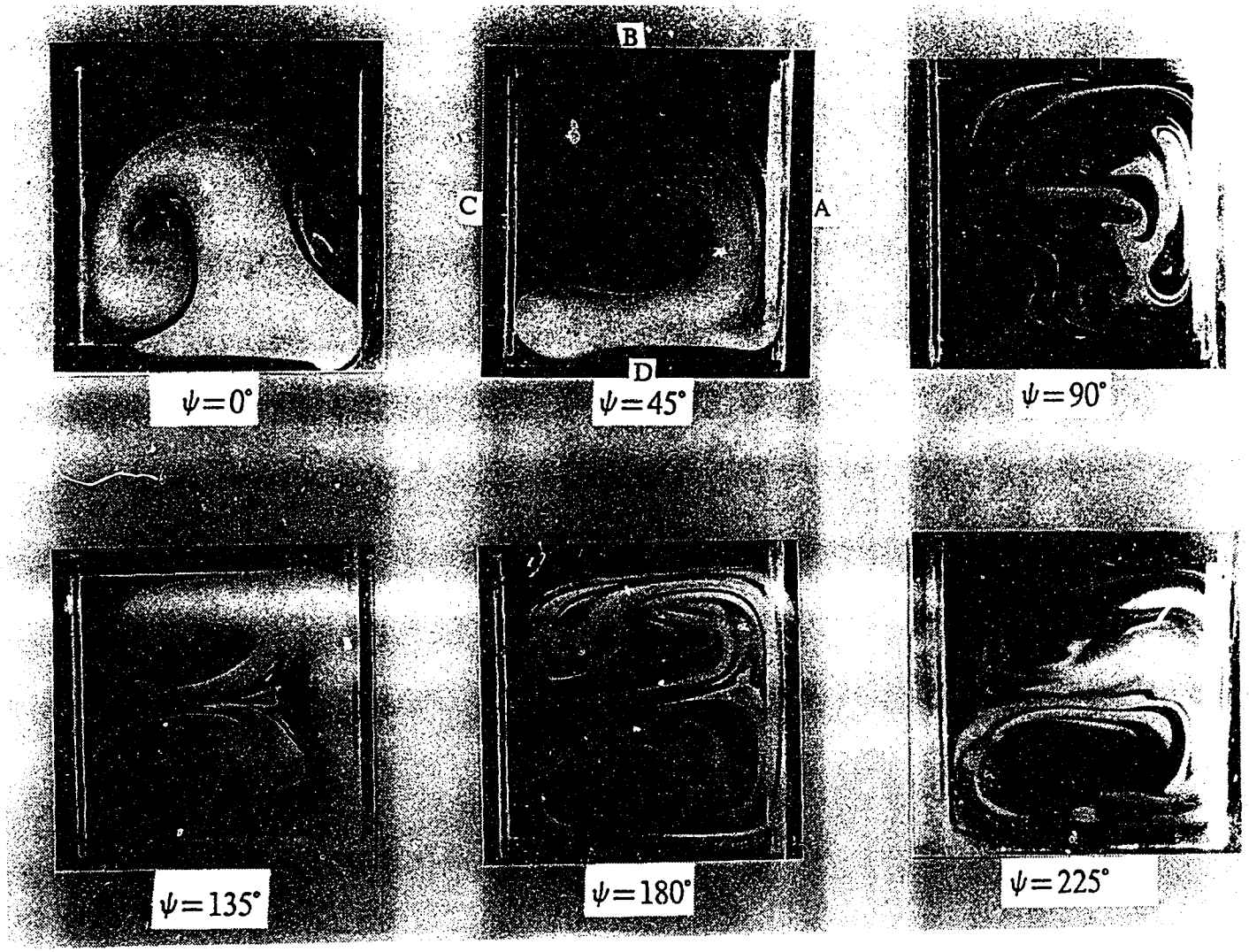

Fig. 2.51 Developing secondary flow patterns in the first square bend with a/R_c=0.2 at K=50

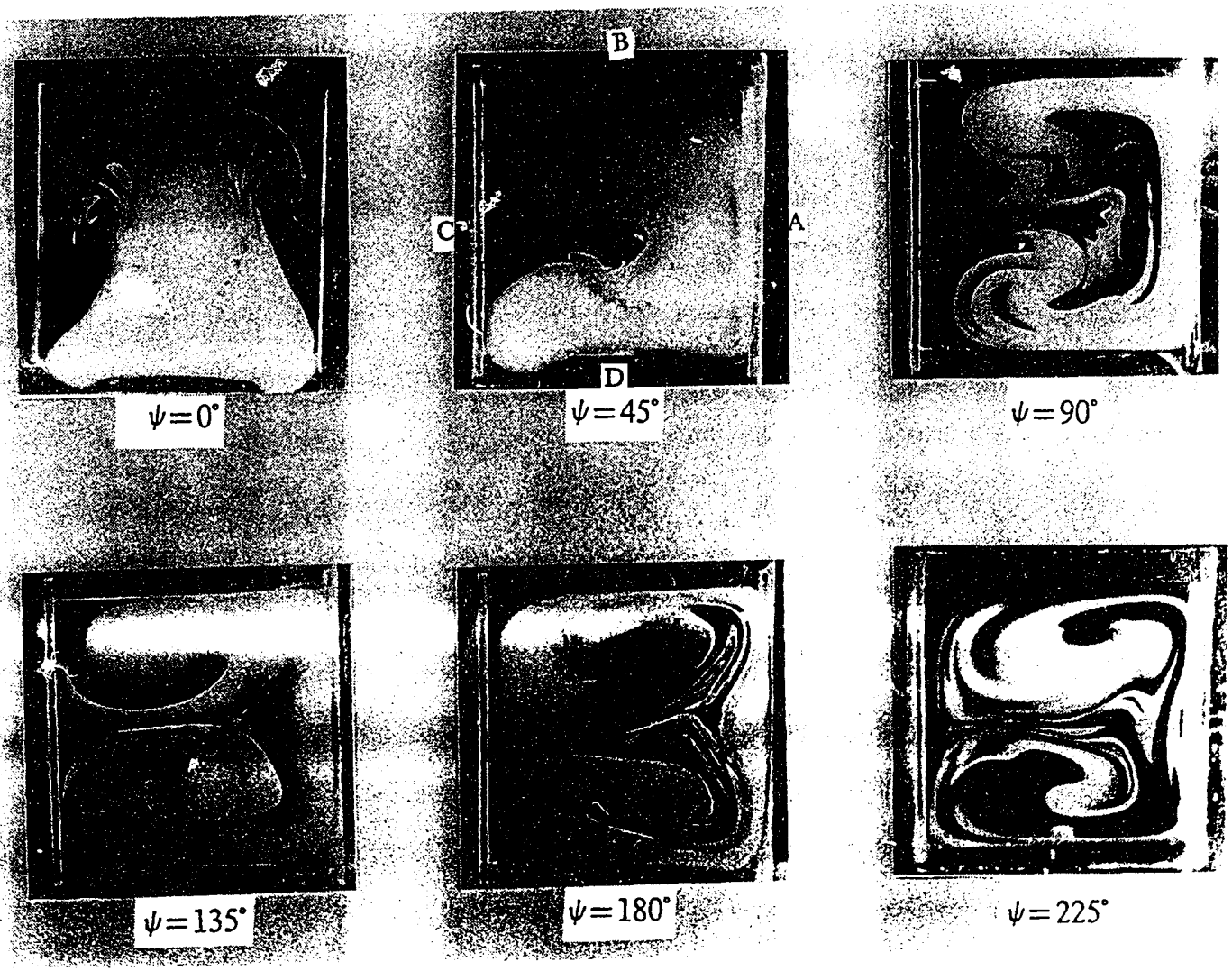

Fig. 2.52 Developing secondary flow patterns in the first square bend with a/R_c=0.2 at K=100

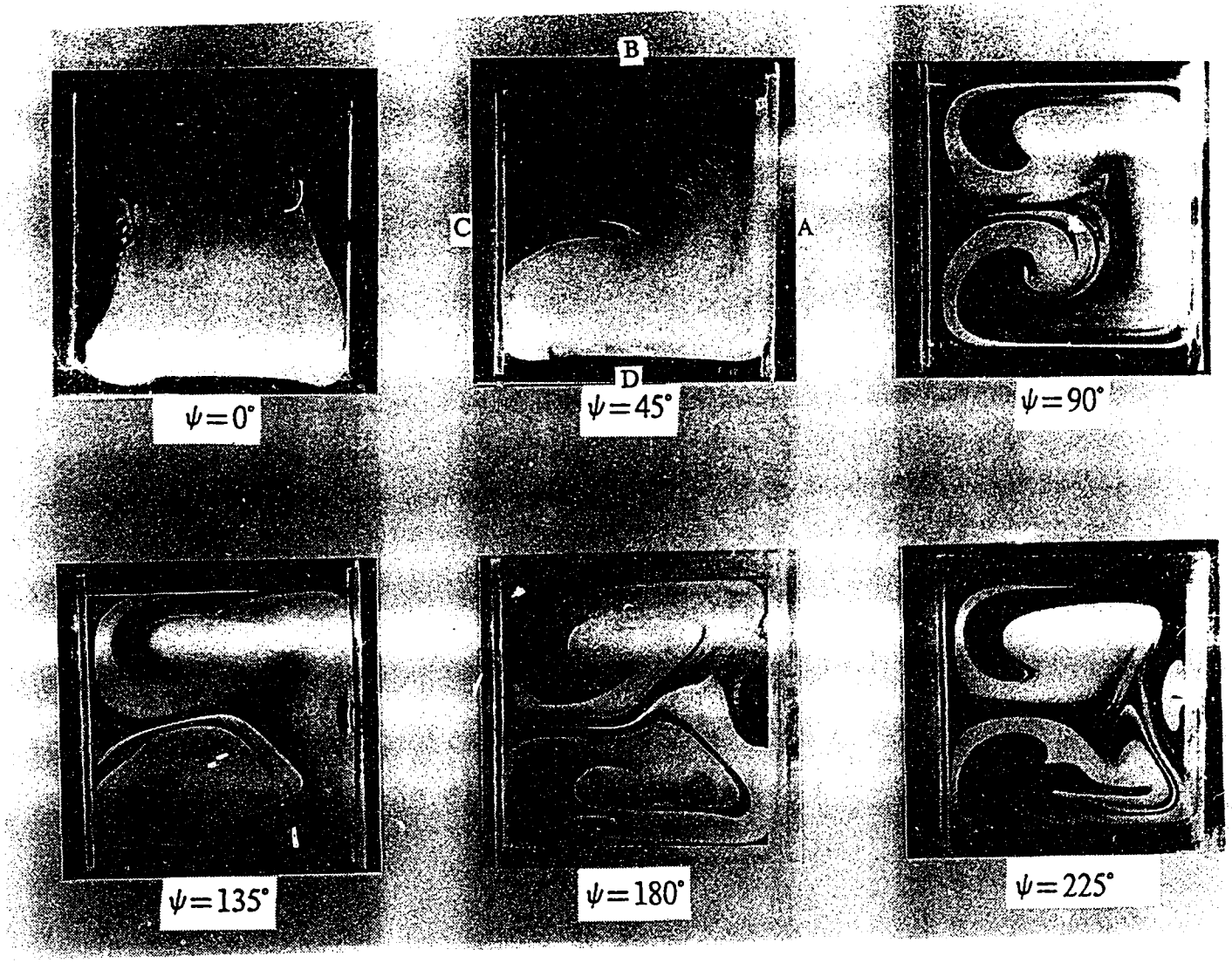

Fig. 2.53 Developing secondary flow patterns in the first square bend with a/R_c=0.2 at K=150

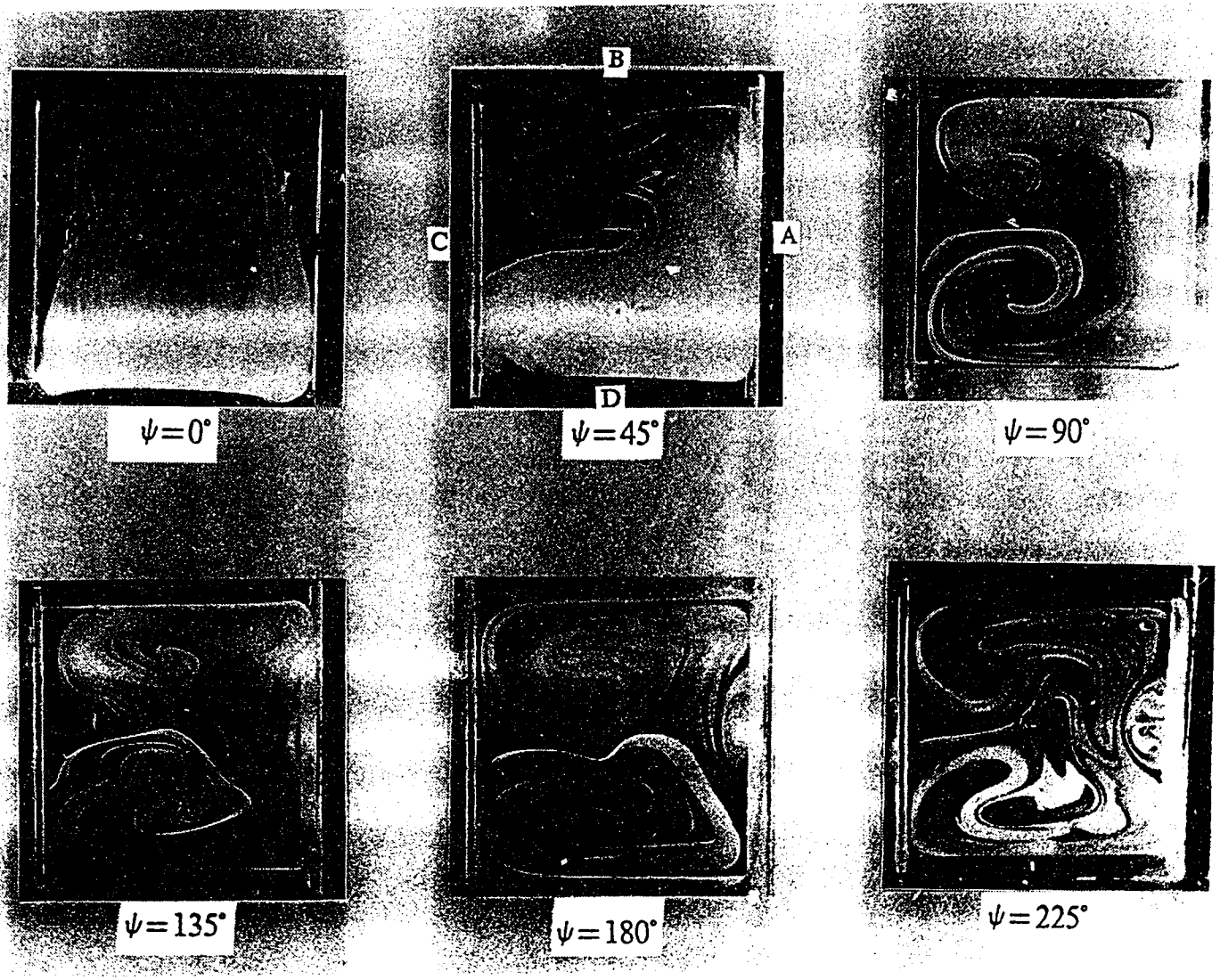

Fig. 2.54 Developing secondary flow patterns in the first square bend with a/R_c=0.2 at K=200

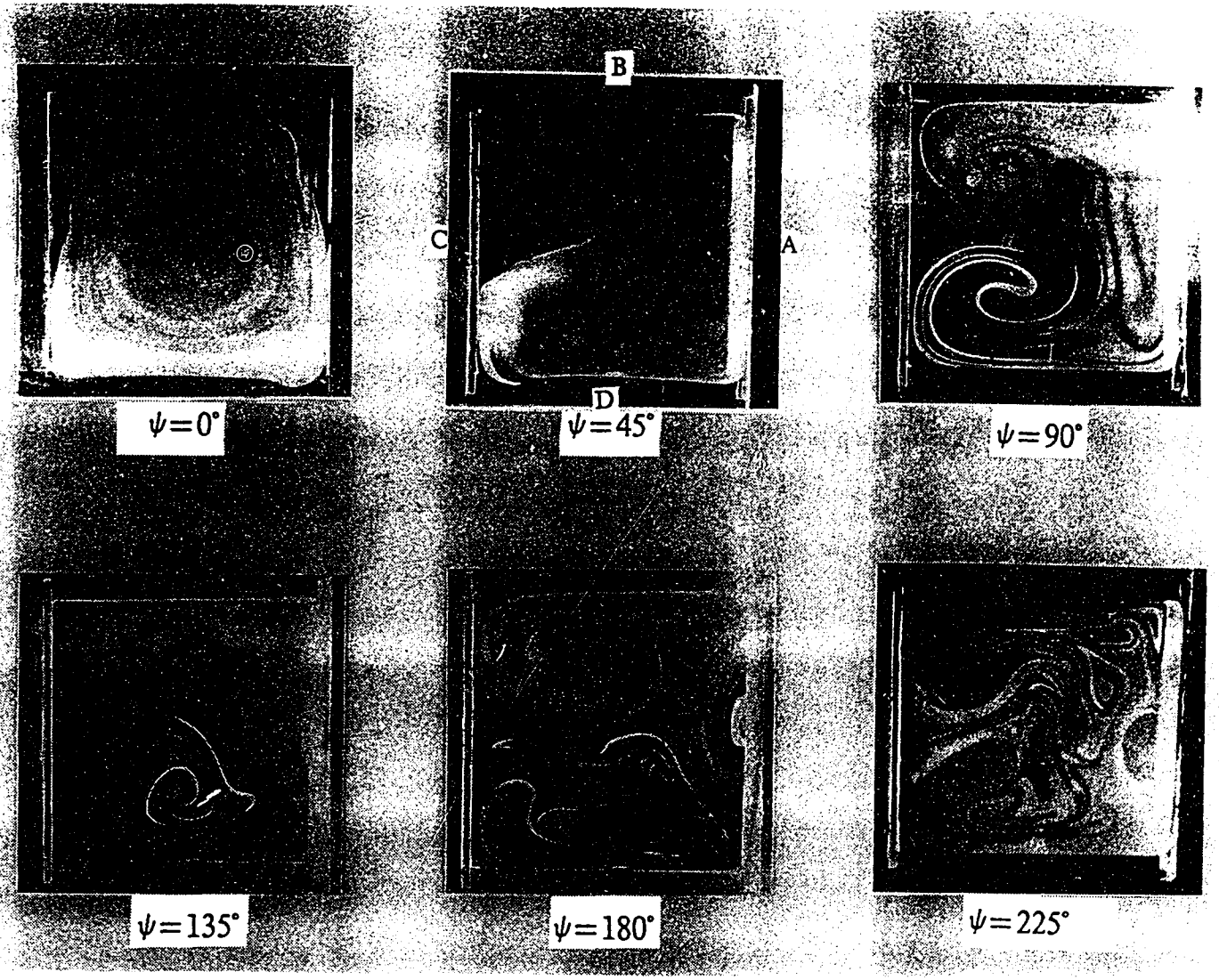

Fig. 2.55 Developing secondary flow patterns in the first square bend with a/R_c=0.2 at K=250

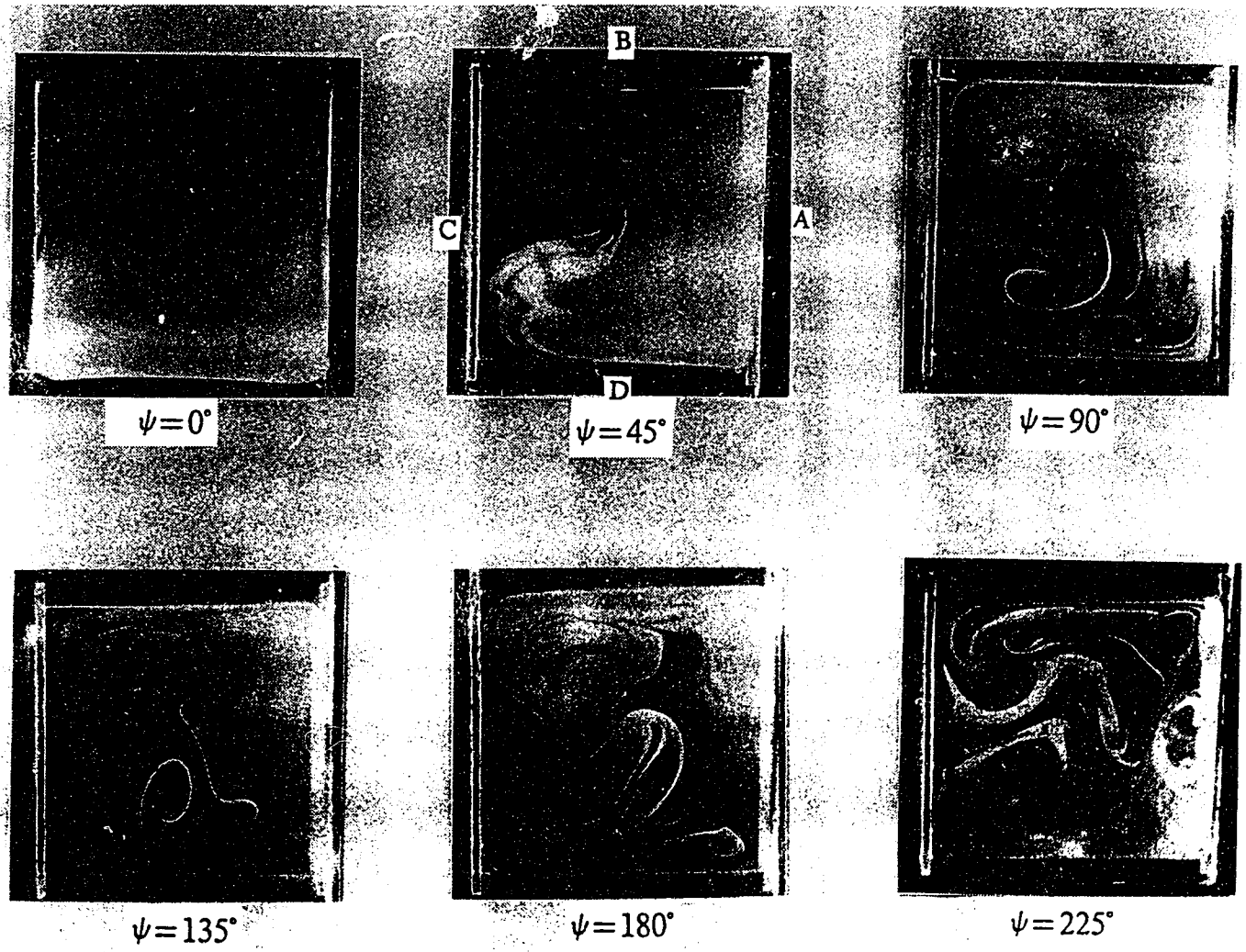

Fig. 2.56 Developing secondary flow patterns in the first square bend with a/R_c=0.2 at K=300

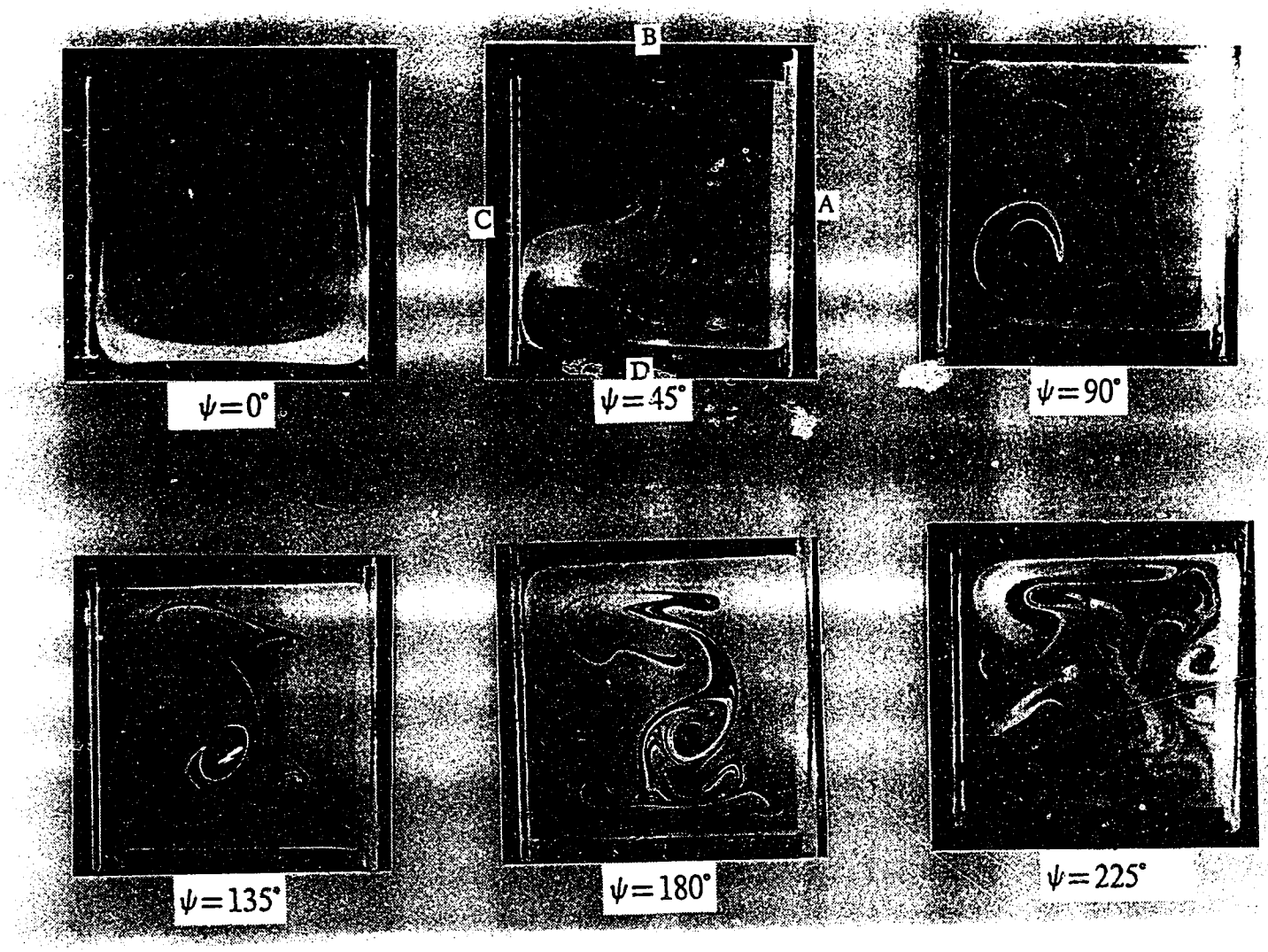

Fig. 2.57 Developing secondary flow patterns in the first square bend with a/R_c=0.2 at K=350

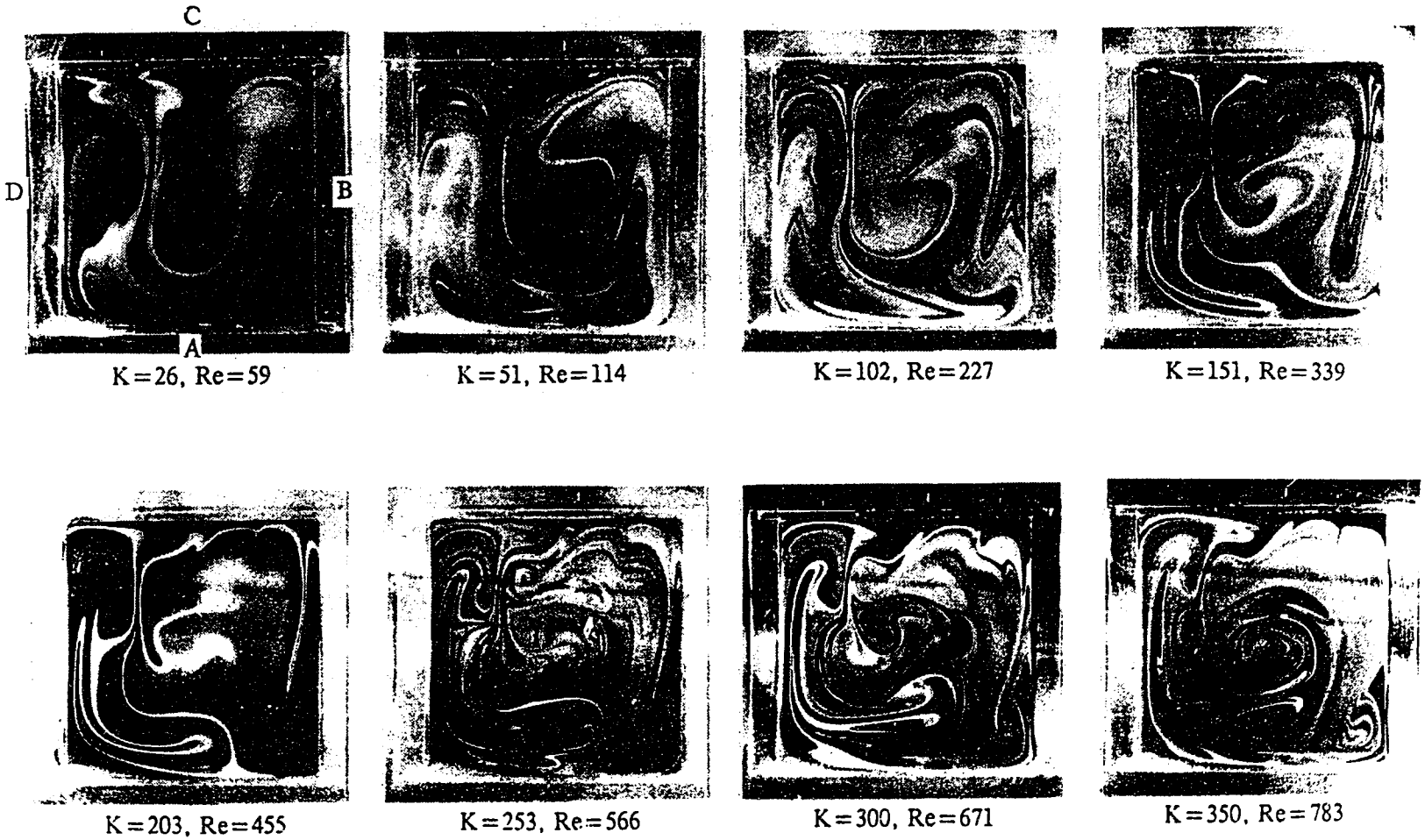

Fig. 2.58 The effect of Dean number on secondary flow patterns at the exit of a 45° second square bend with $a/R_c=0.2$, $\psi=180°$ and $\theta=90°$

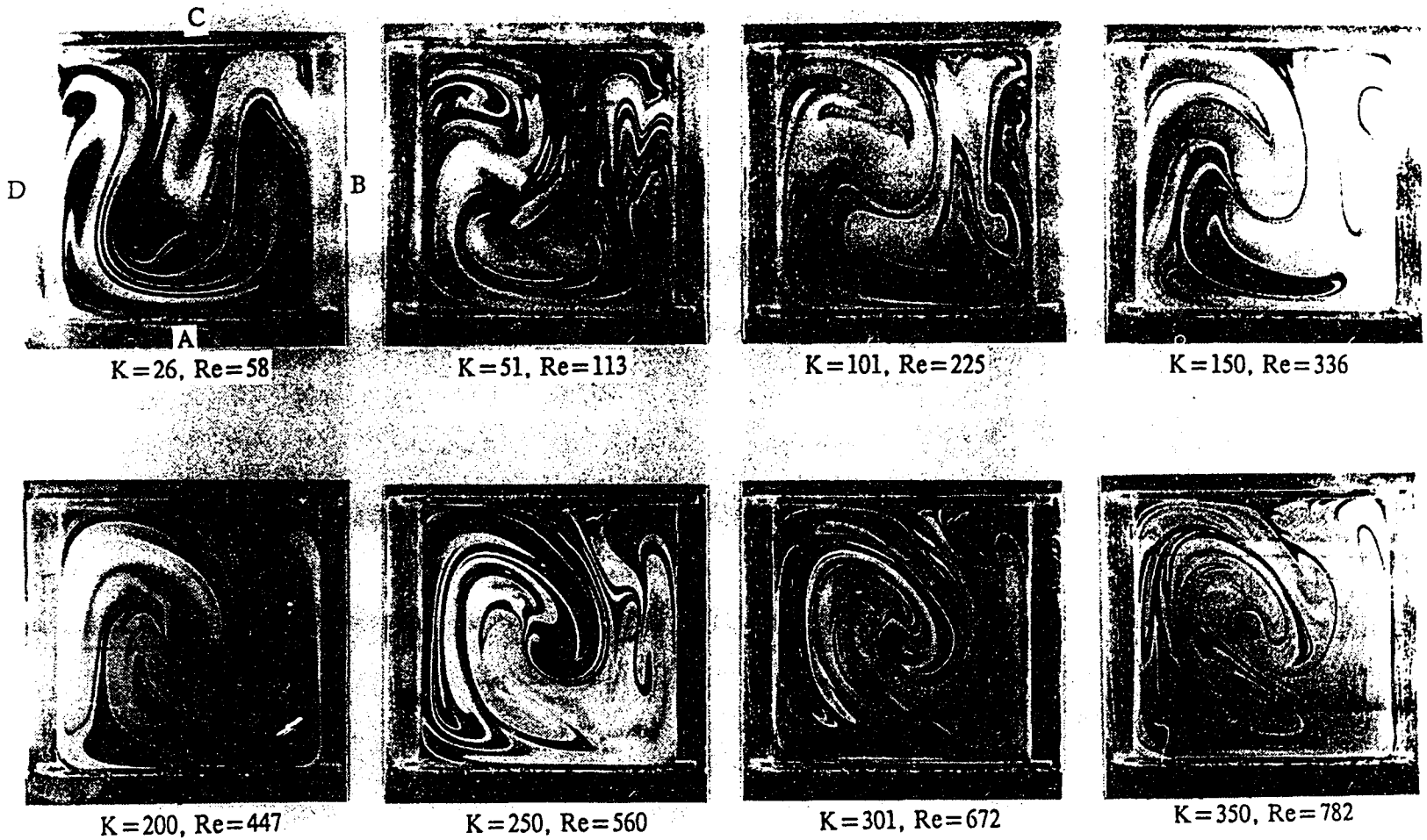

Fig. 2.59 The effect of Dean number on secondary flow patterns at the exit of a 90° second square bend with $a/R_c=0.2$, $\psi=180°$ and $\theta=90°$

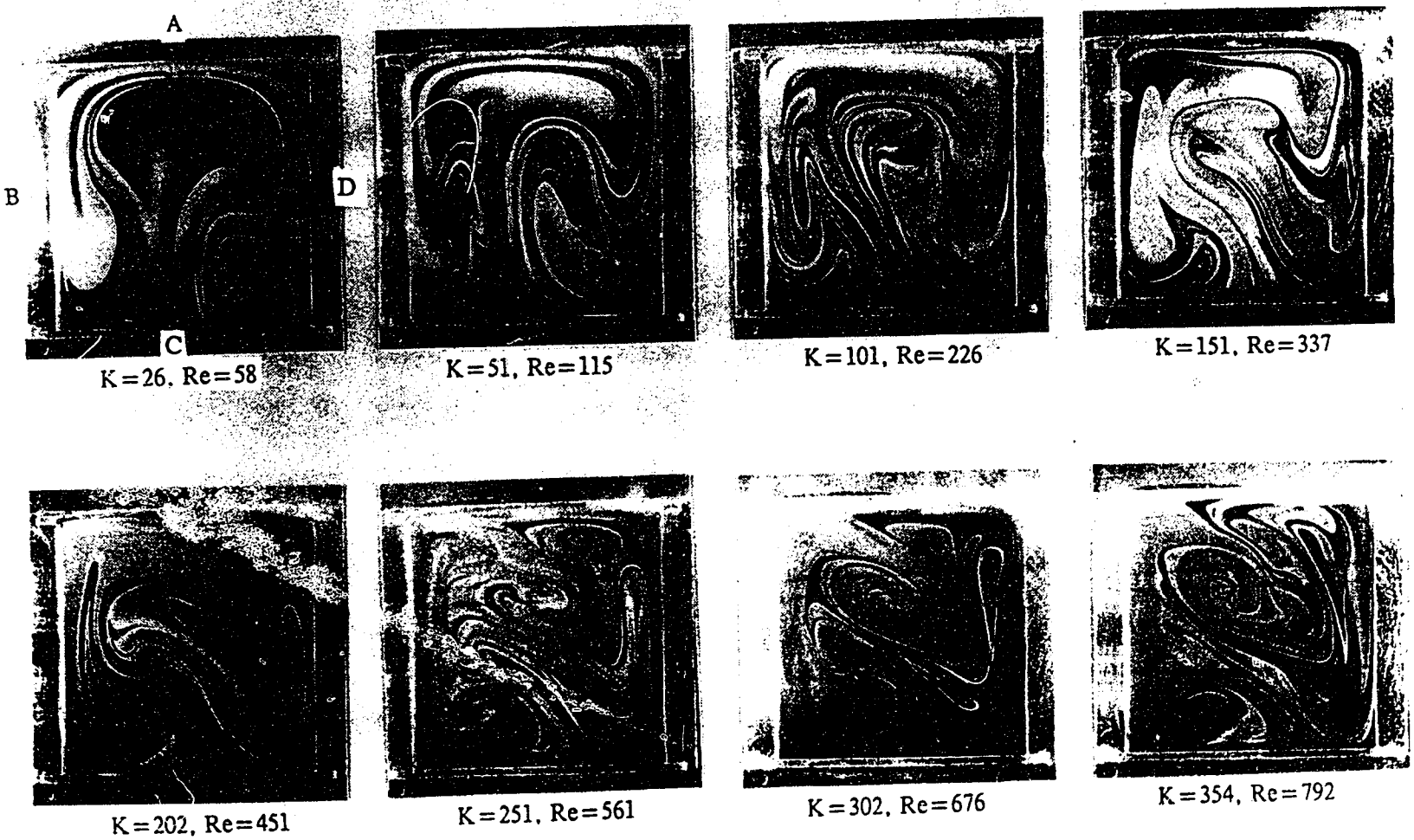

Fig. 2.60 The effect of Dean number on secondary flow patterns at the exit of a 135° second square bend with $a/R_c=0.2$, $\psi=180°$ and $\theta=90°$

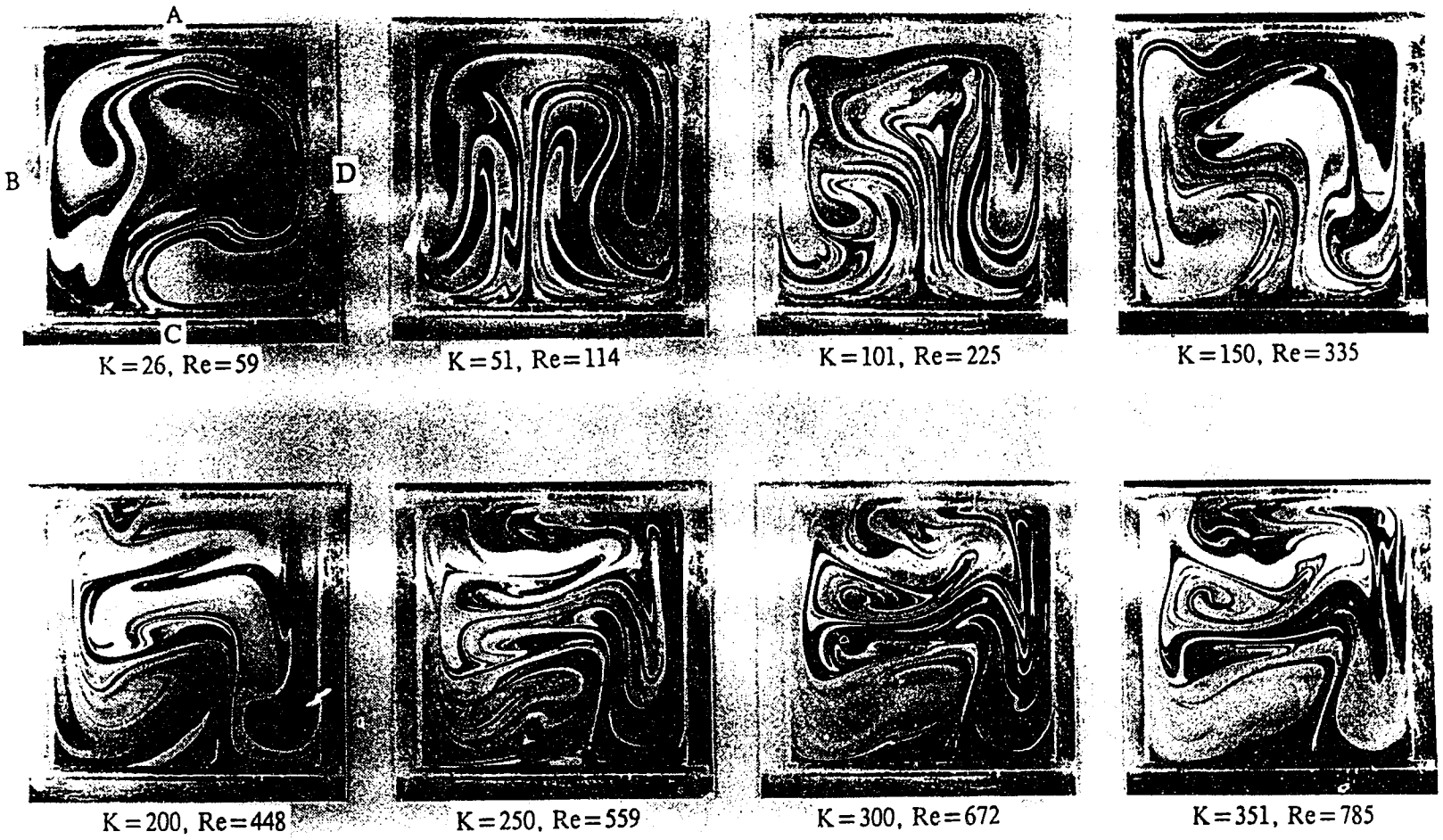

Fig. 2.61 The effect of Dean number on secondary flow patterns at the exit of a 180° second square bend with $a/R_c=0.2$, $\psi=180°$ and $\theta=90°$

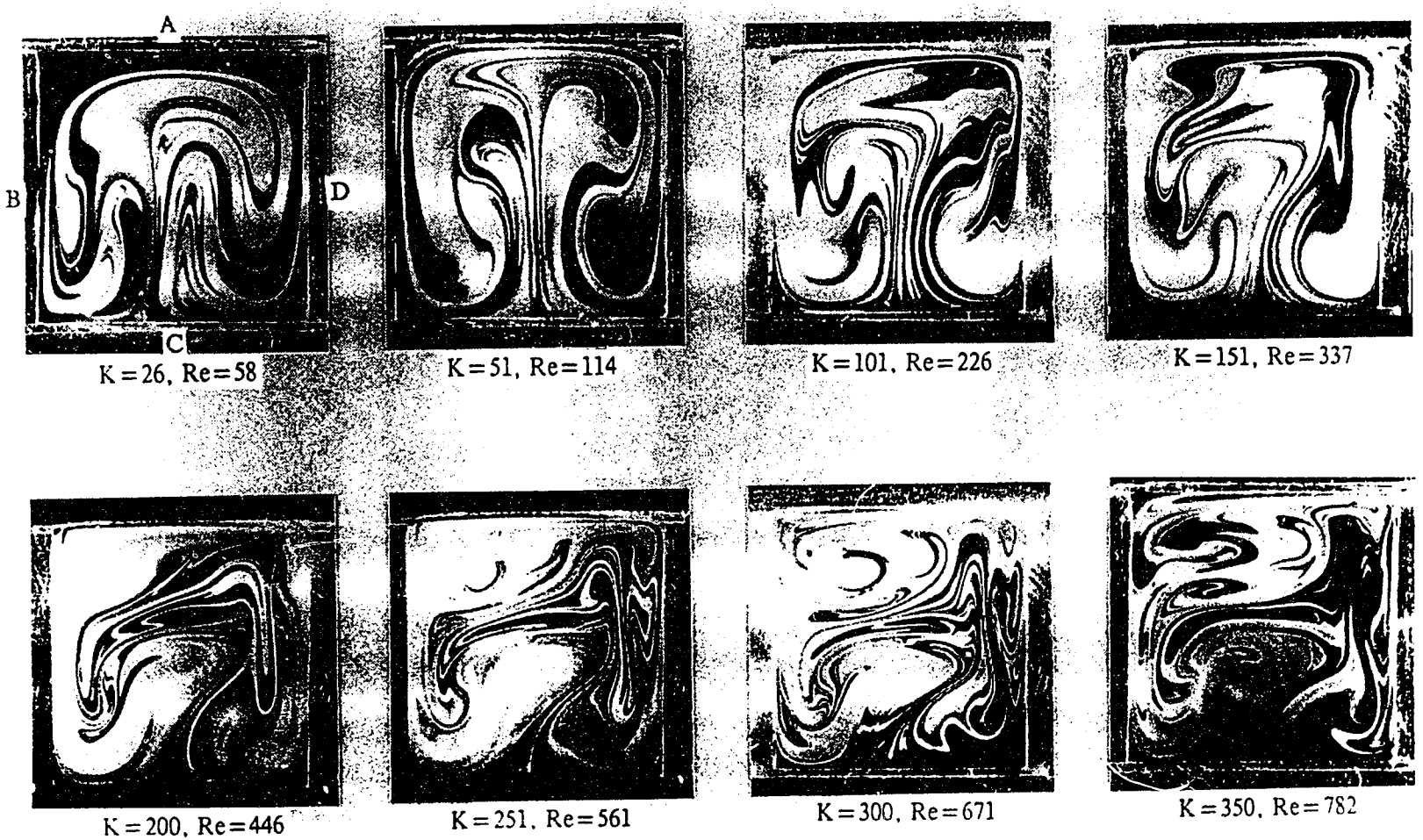

Fig. 2.62 The effect of Dean number on secondary flow patterns at the exit of a 225° second square bend with $a/R_c=0.2$, $\psi=180°$ and $\theta=90°$

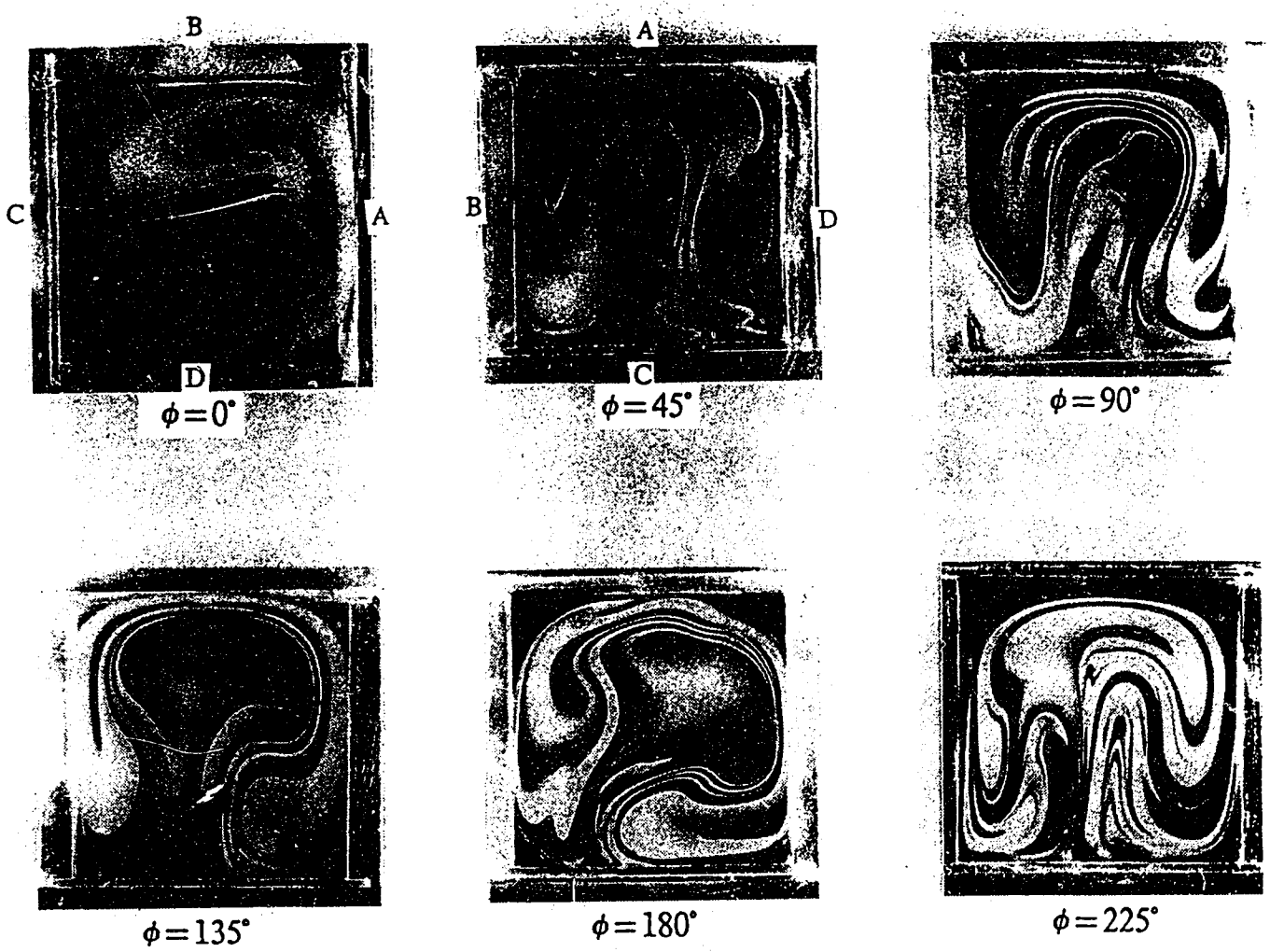

Fig. 2.63 Developing secondary flow patterns in the second square bend with $a/R_c=0.2$, $\psi=180°$ and $\theta=90°$ at K=25

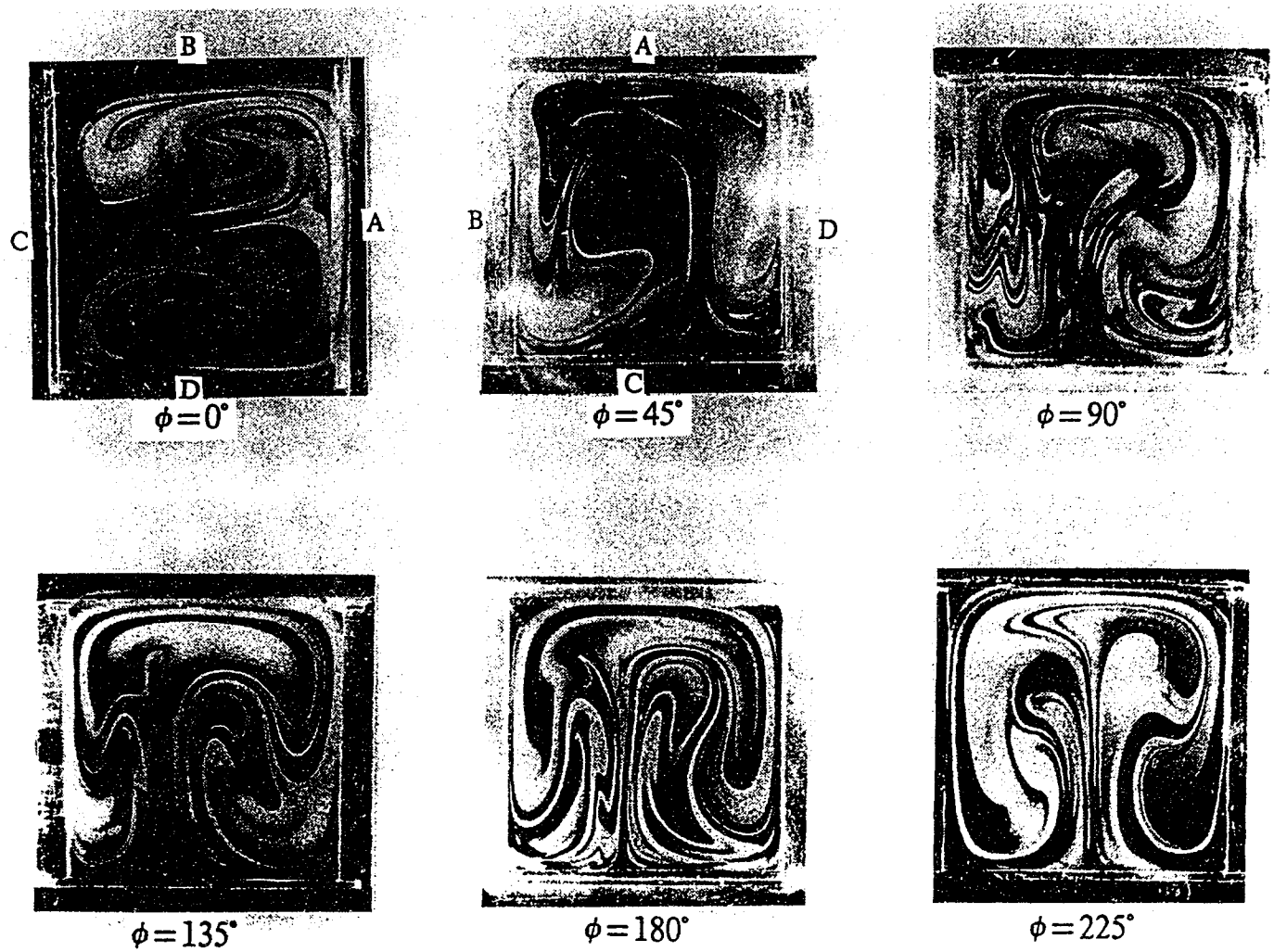

Fig. 2.64 Developing secondary flow patterns in the second square bend with $a/R_c=0.2$, $\psi=180°$ and $\theta=90°$ at K=50

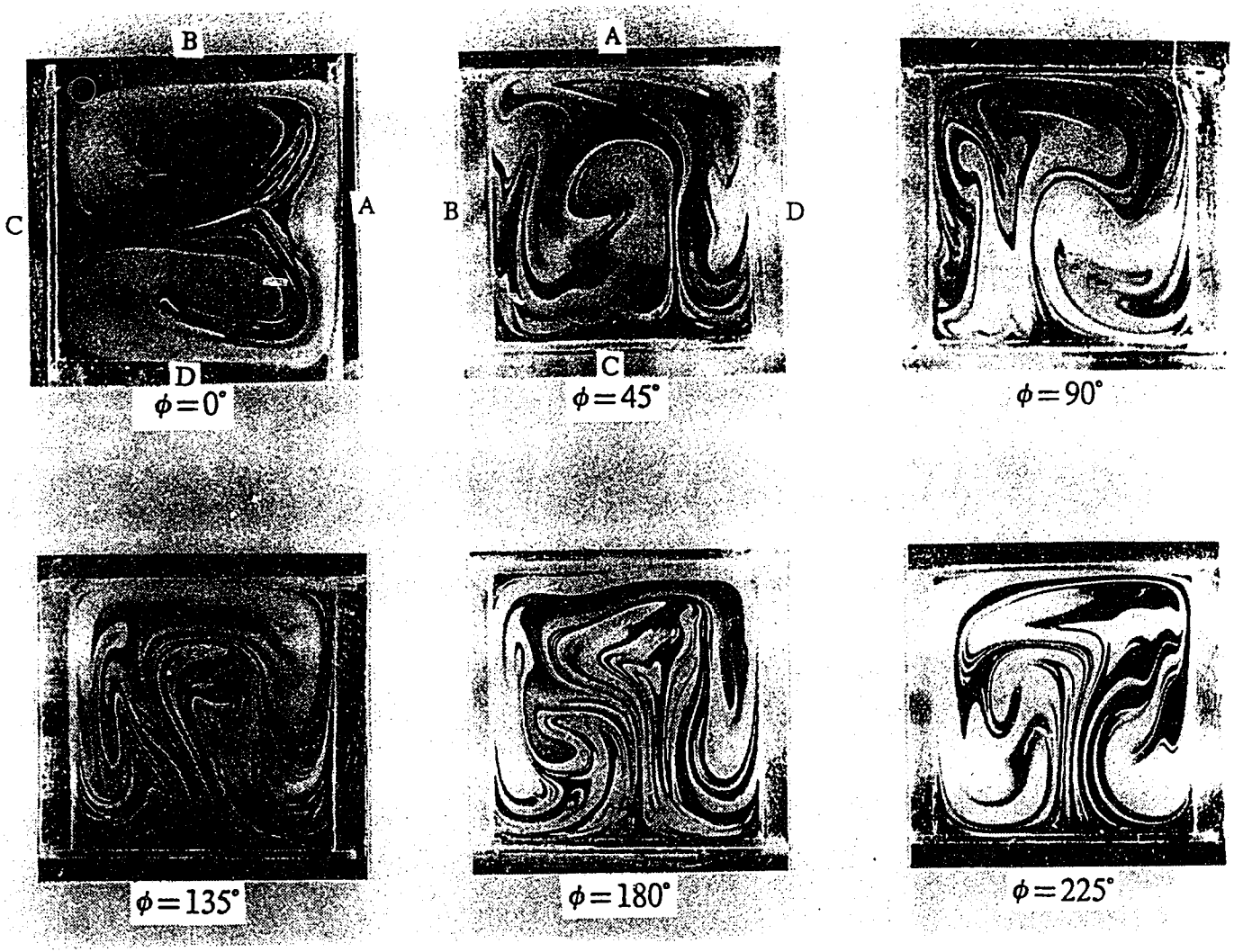

Fig. 2.65 Developing secondary flow patterns in the second square bend with $a/R_c=0.2$, $\psi=180°$ and $\theta=90°$ at $K=100$

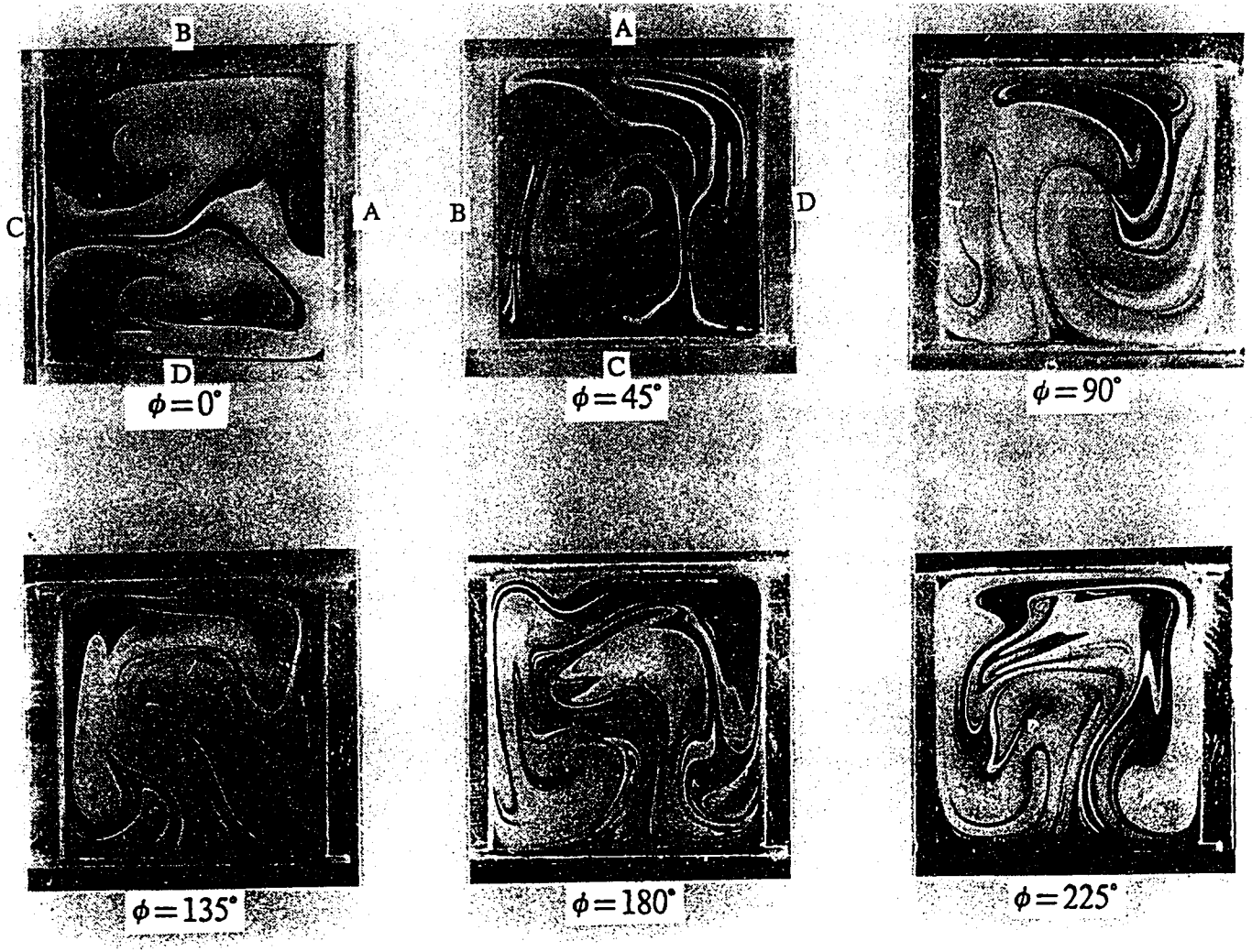

Fig. 2.66 Developing secondary flow patterns in the second square bend with $a/R_c=0.2$, $\psi=180°$ and $\theta=90°$ at $K=150$

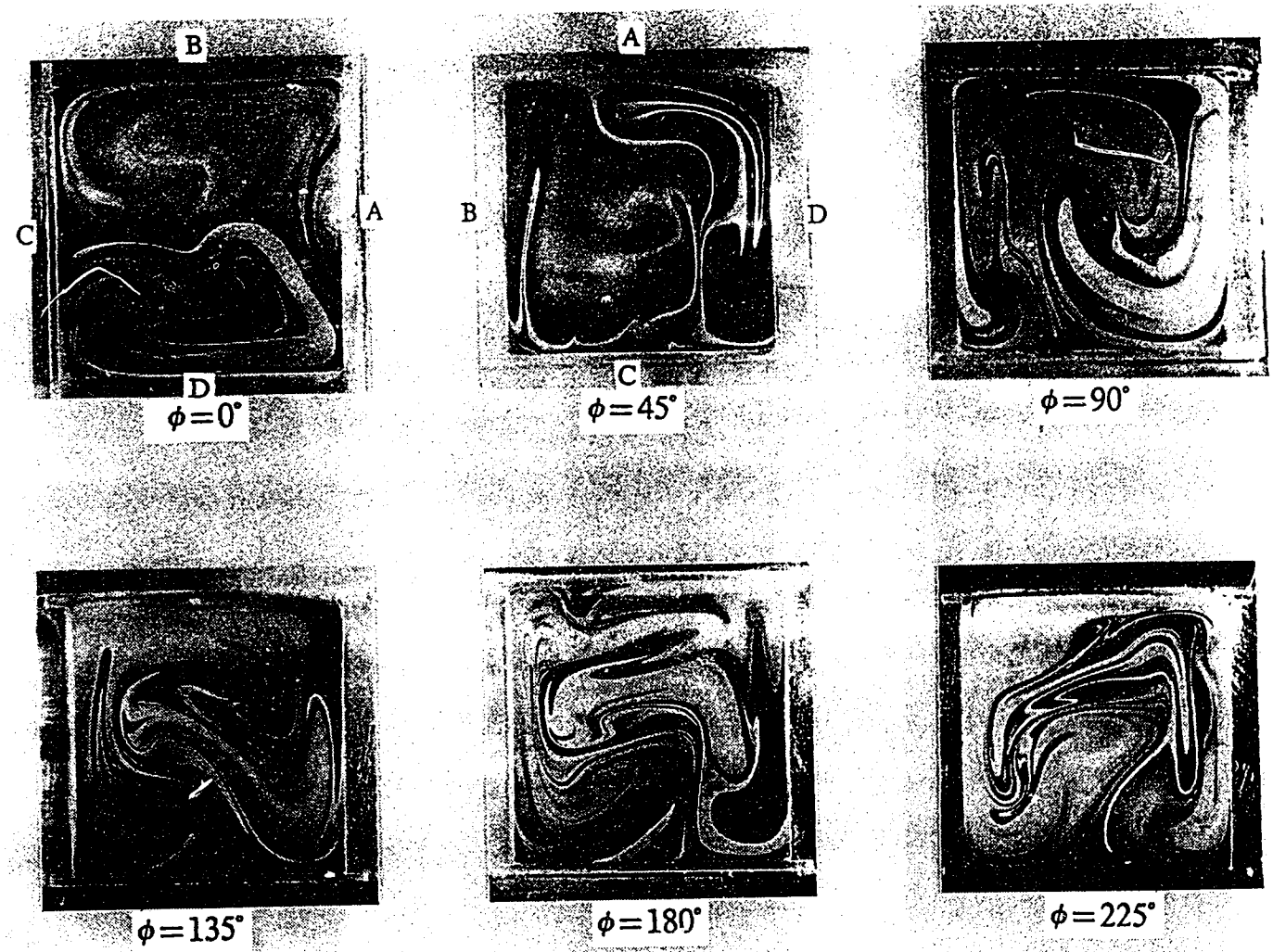

Fig. 2.67 Developing secondary flow patterns in the second square bend with $a/R_c=0.2$, $\psi=180°$ and $\theta=90°$ at $K=200$

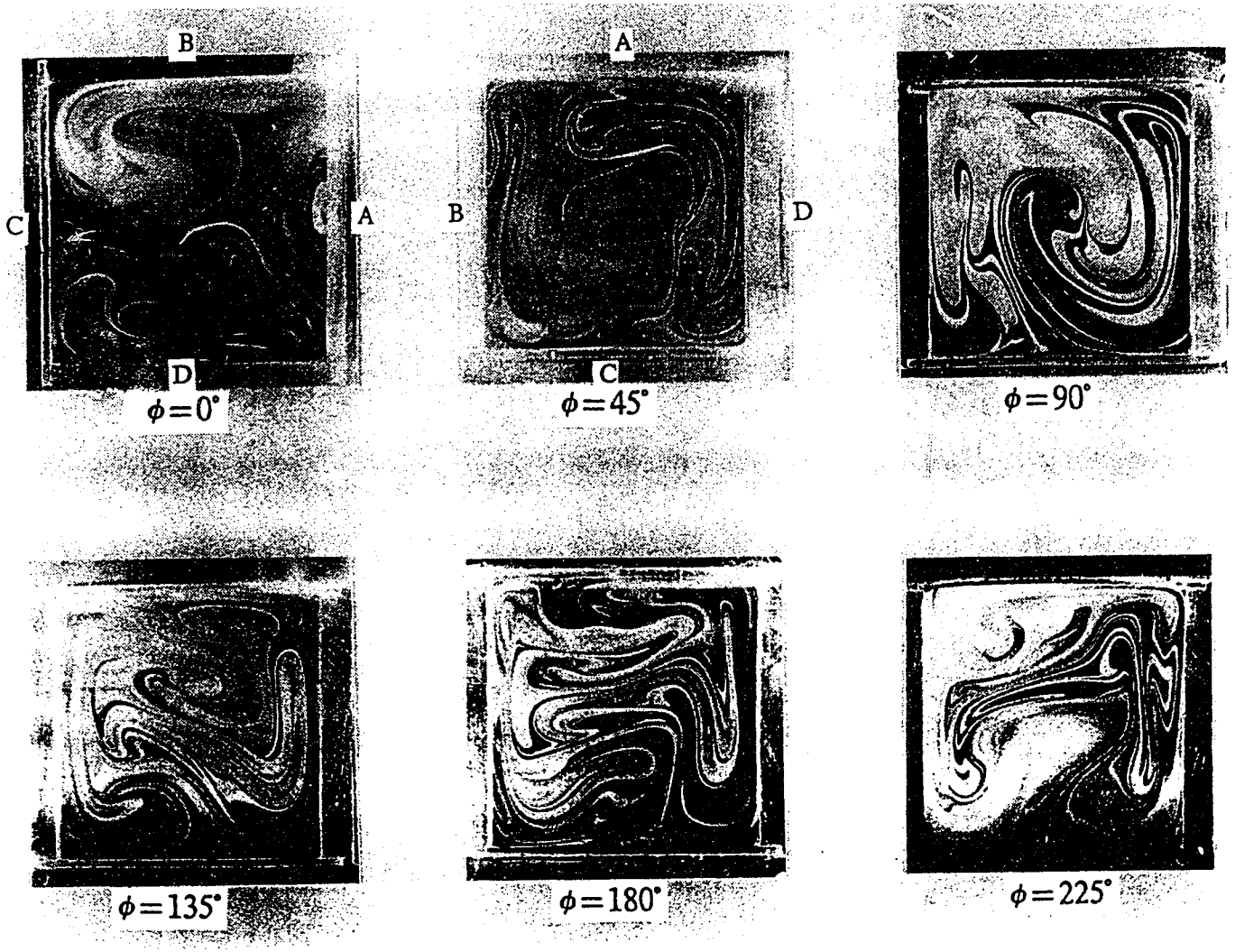

Fig. 2.68 Developing secondary flow patterns in the second square bend with $a/R_c=0.2$, $\psi=180°$ and $\theta=90°$ at K=250

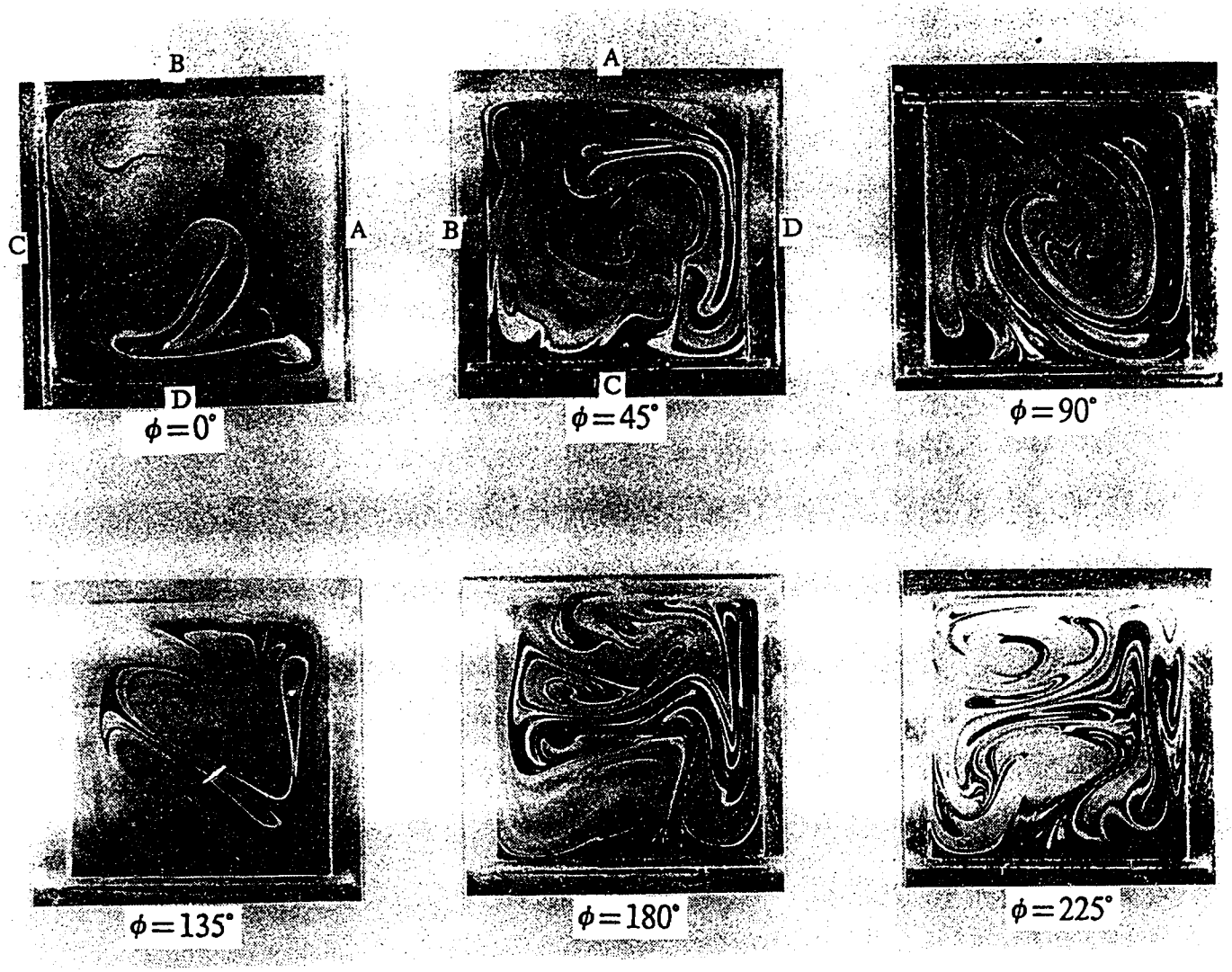

Fig. 2.69 Developing secondary flow patterns in the second square bend with $a/R_c=0.2$, $\psi=180°$ and $\theta=90°$ at K=300

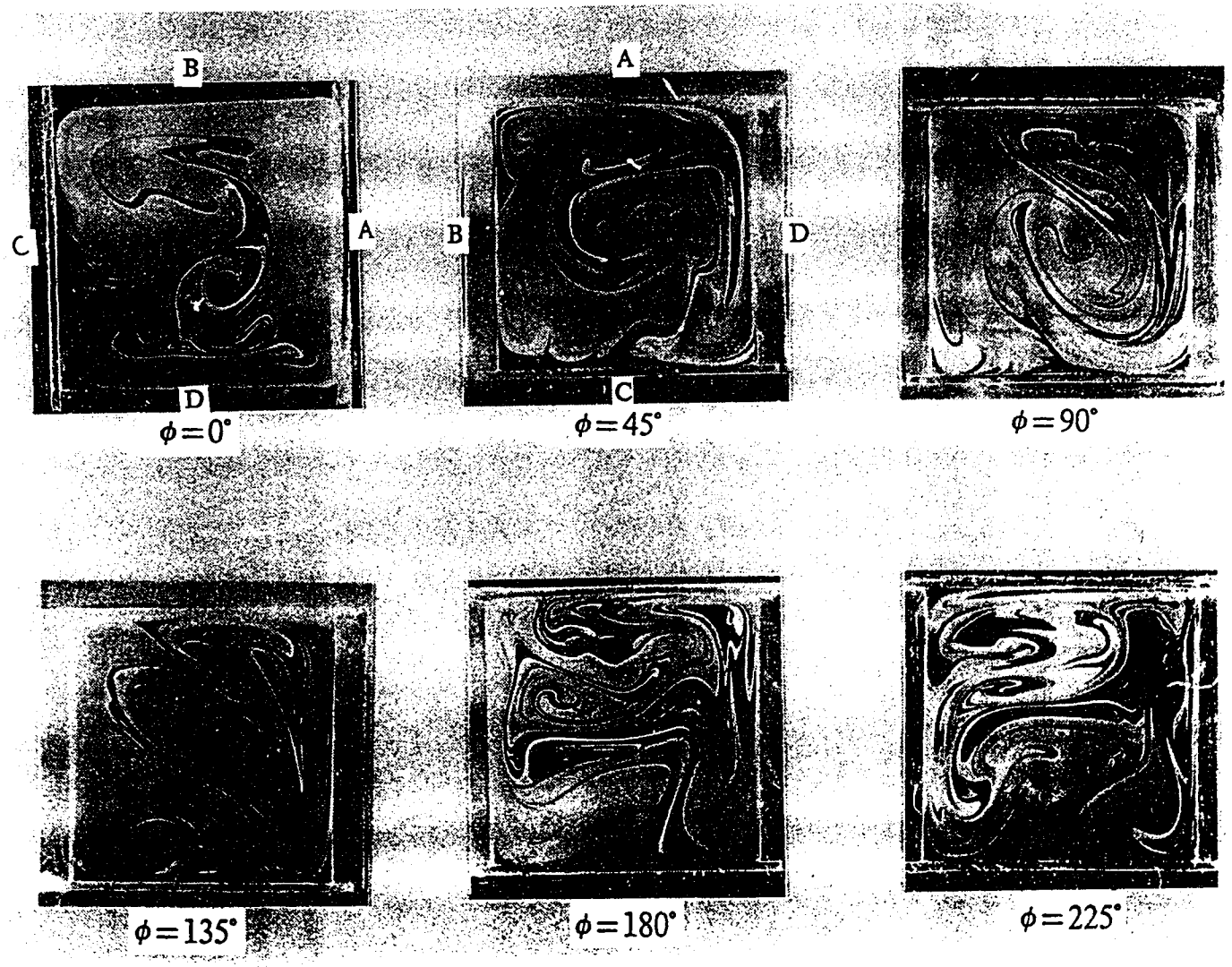

Fig. 2.70 Developing secondary flow patterns in the second square bend with $a/R_c=0.2$, $\psi=180°$ and $\theta=90°$ at K=350

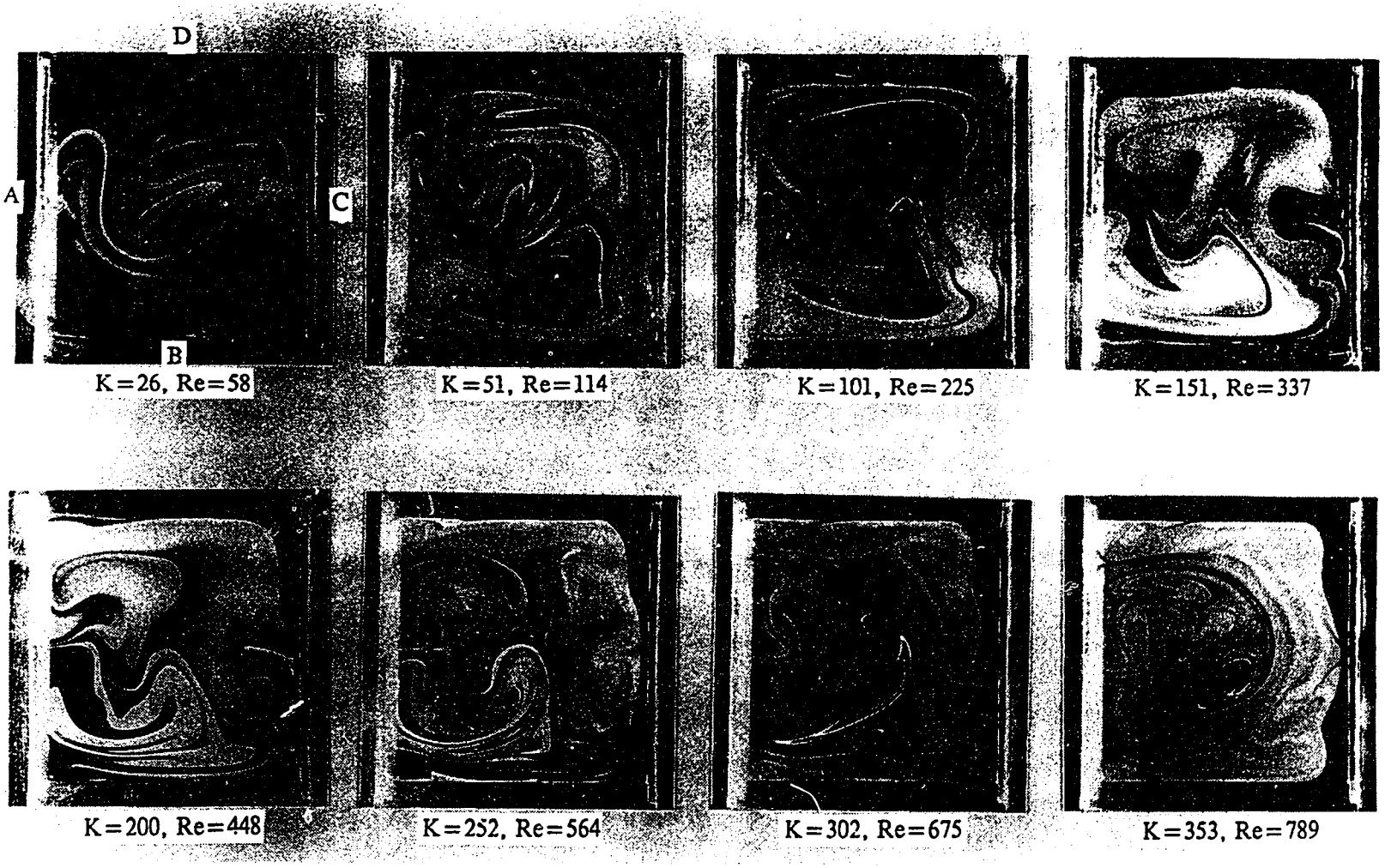

Fig. 2.71 The effect of Dean number on secondary flow patterns at the exit of a 45° second square bend with $a/R_c=0.2$, $\psi=180°$ and $\theta=180°$

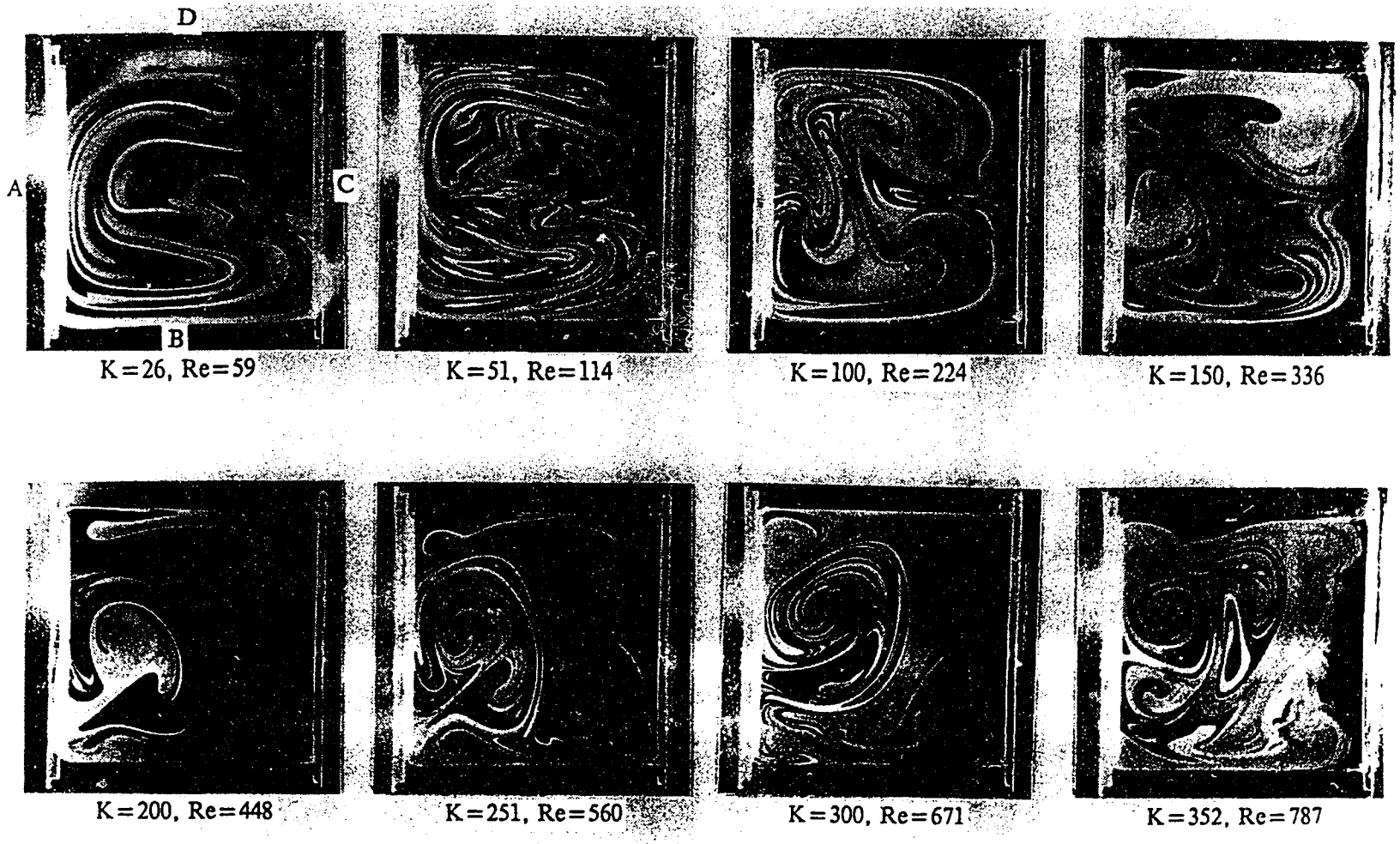

Fig. 2.72 The effect of Dean number on secondary flow patterns at the exit of a 90° second square bend with $a/R_c=0.2$, $\psi=180°$ and $\theta=180°$

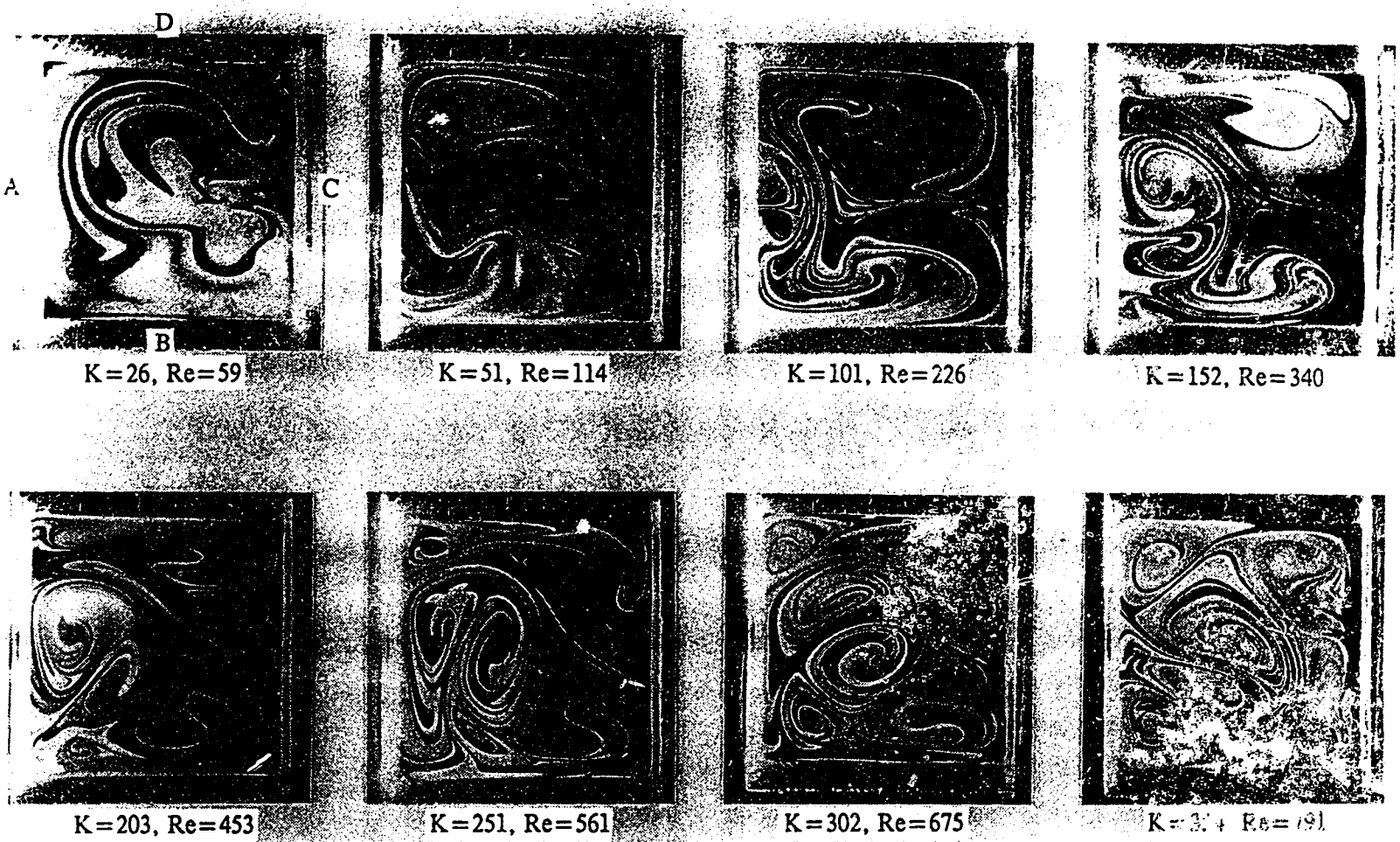

Fig. 2.73 The effect of Dean number on secondary flow patterns at the exit of a 135° second square bend with $a/R_c=0.2$, $\psi=180°$ and $\theta=180°$

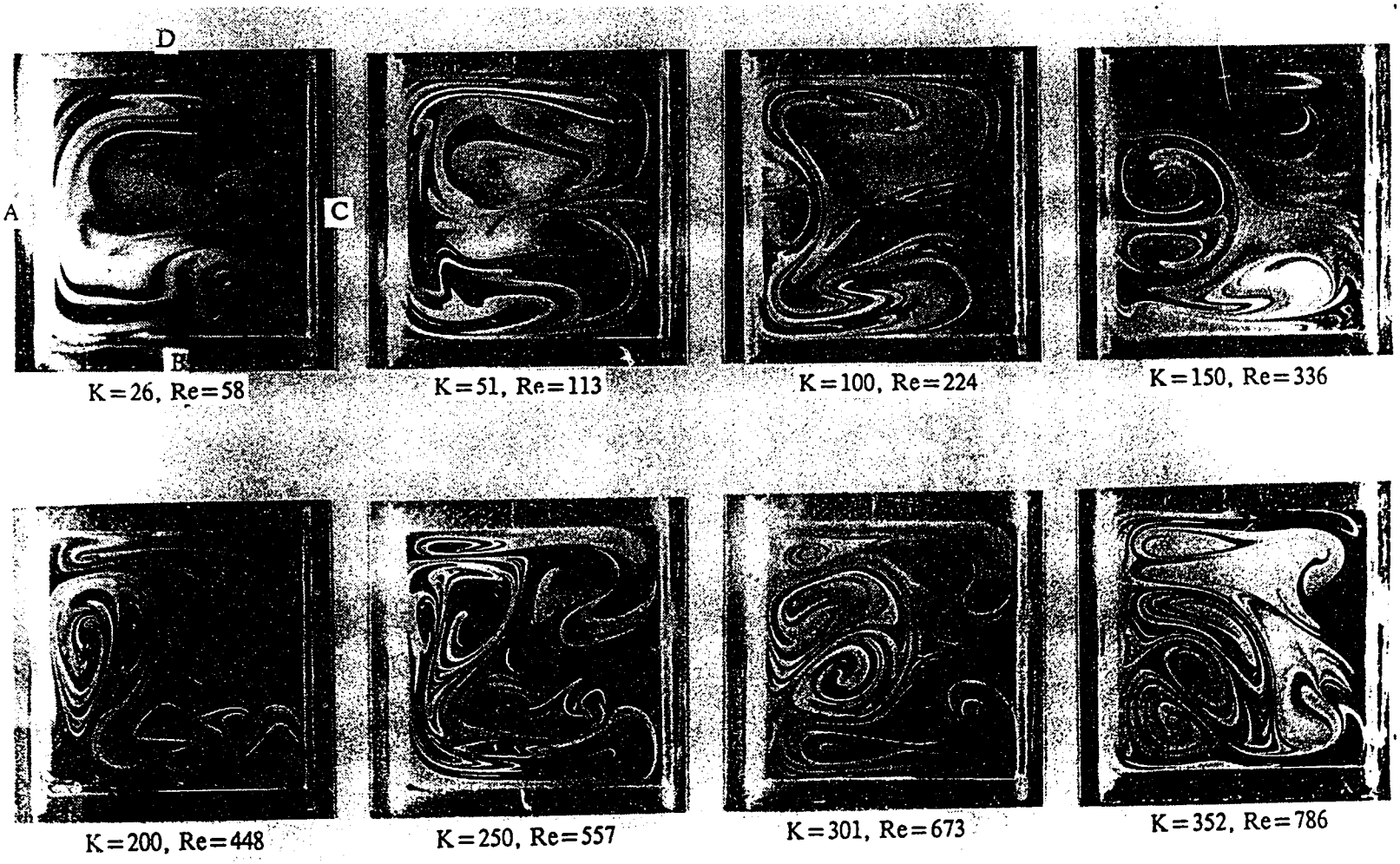

Fig. 2.74 The effect of Dean number on secondary flow patterns at the exit of a 180° second square bend with $a/R_c=0.2$, $\psi=180°$ and $\theta=180°$

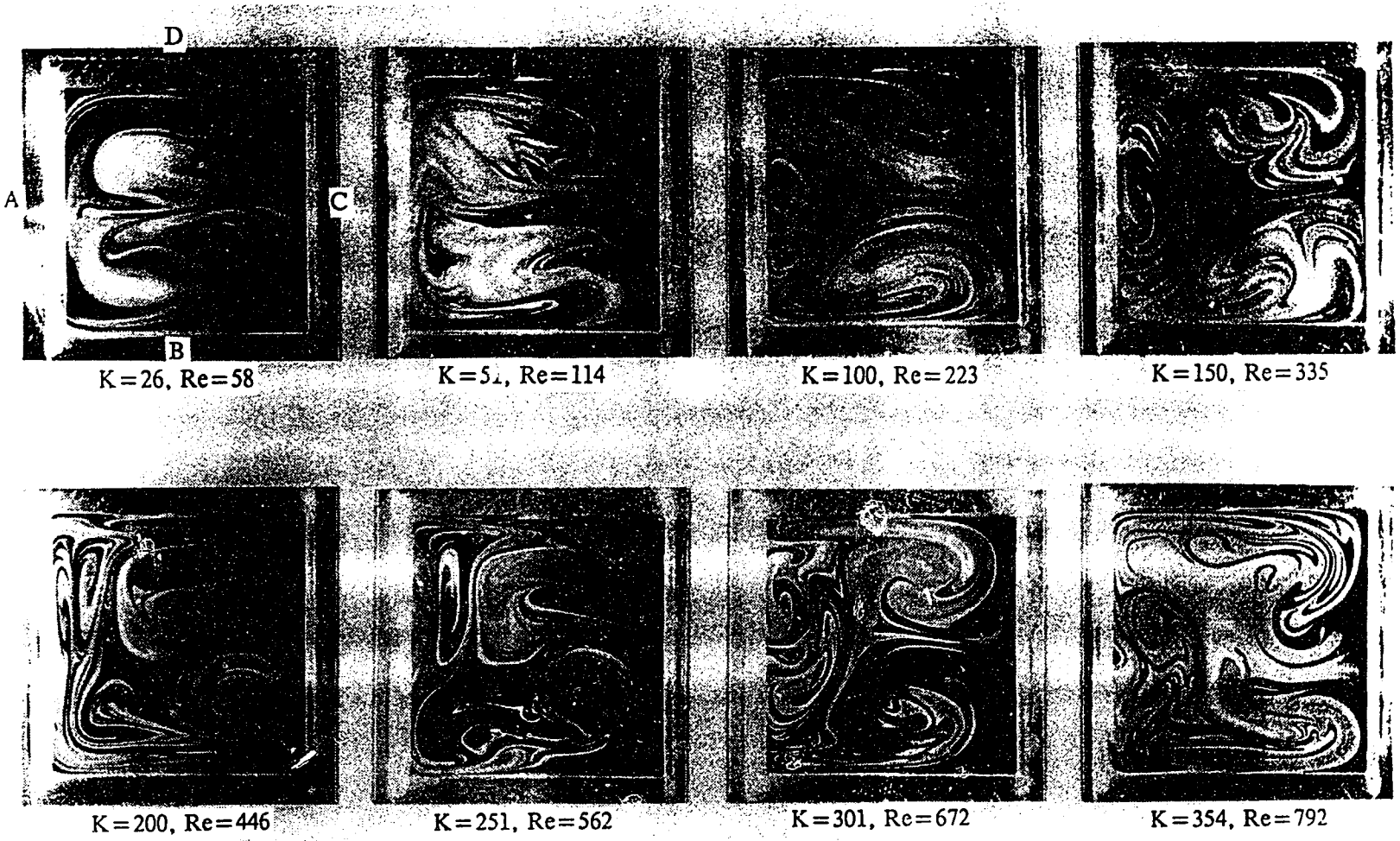

Fig. 2.75 The effect of Dean number on secondary flow patterns at the exit of a 225° second square bend with $a/R_c=0.2$, $\psi=180°$ and $\theta=180°$

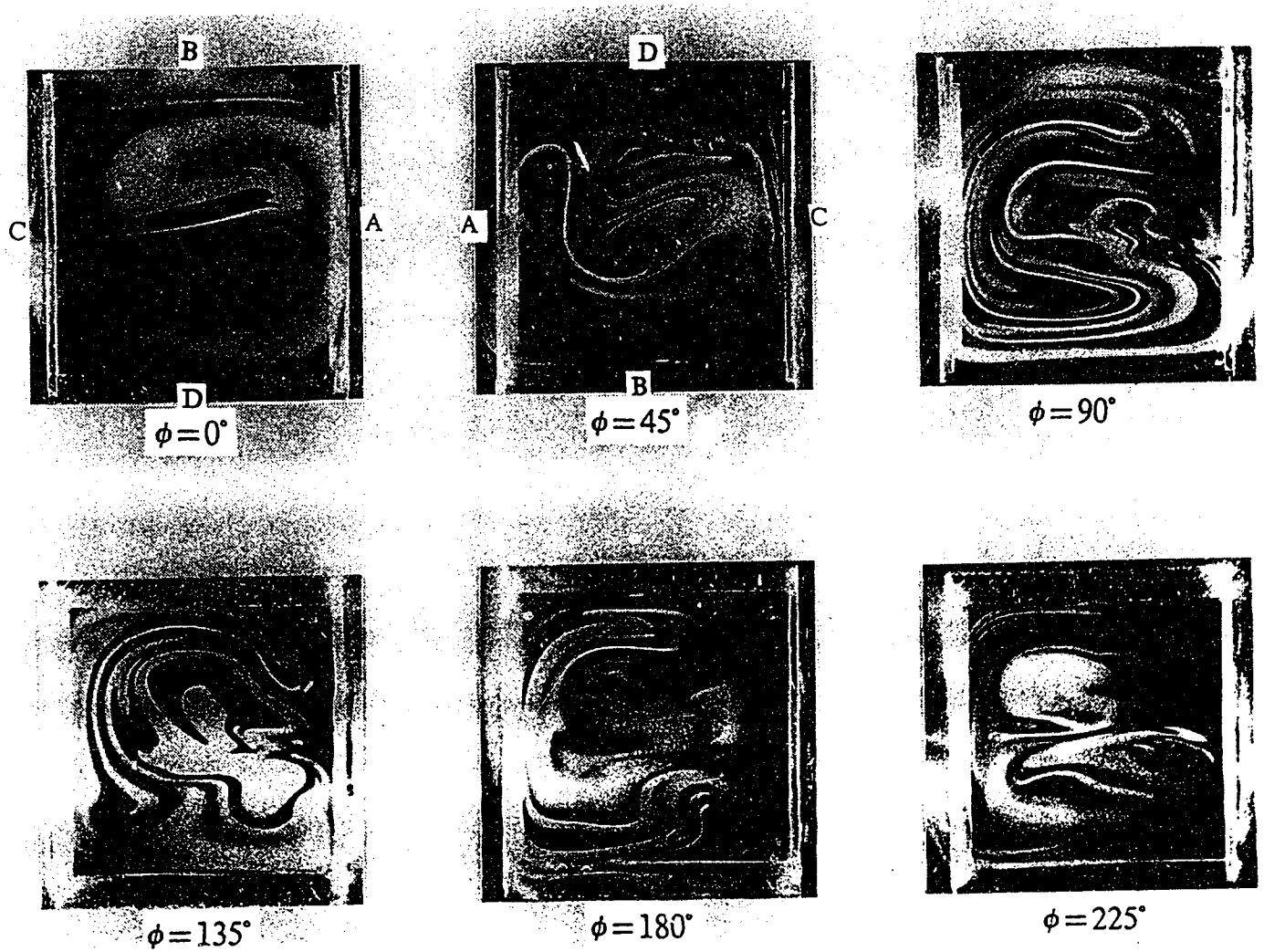

Fig. 76 Developing secondary flow patterns in the second square bend with $a/R_c=0.2$, $\phi=180°$ and $\theta=180°$ at K=25

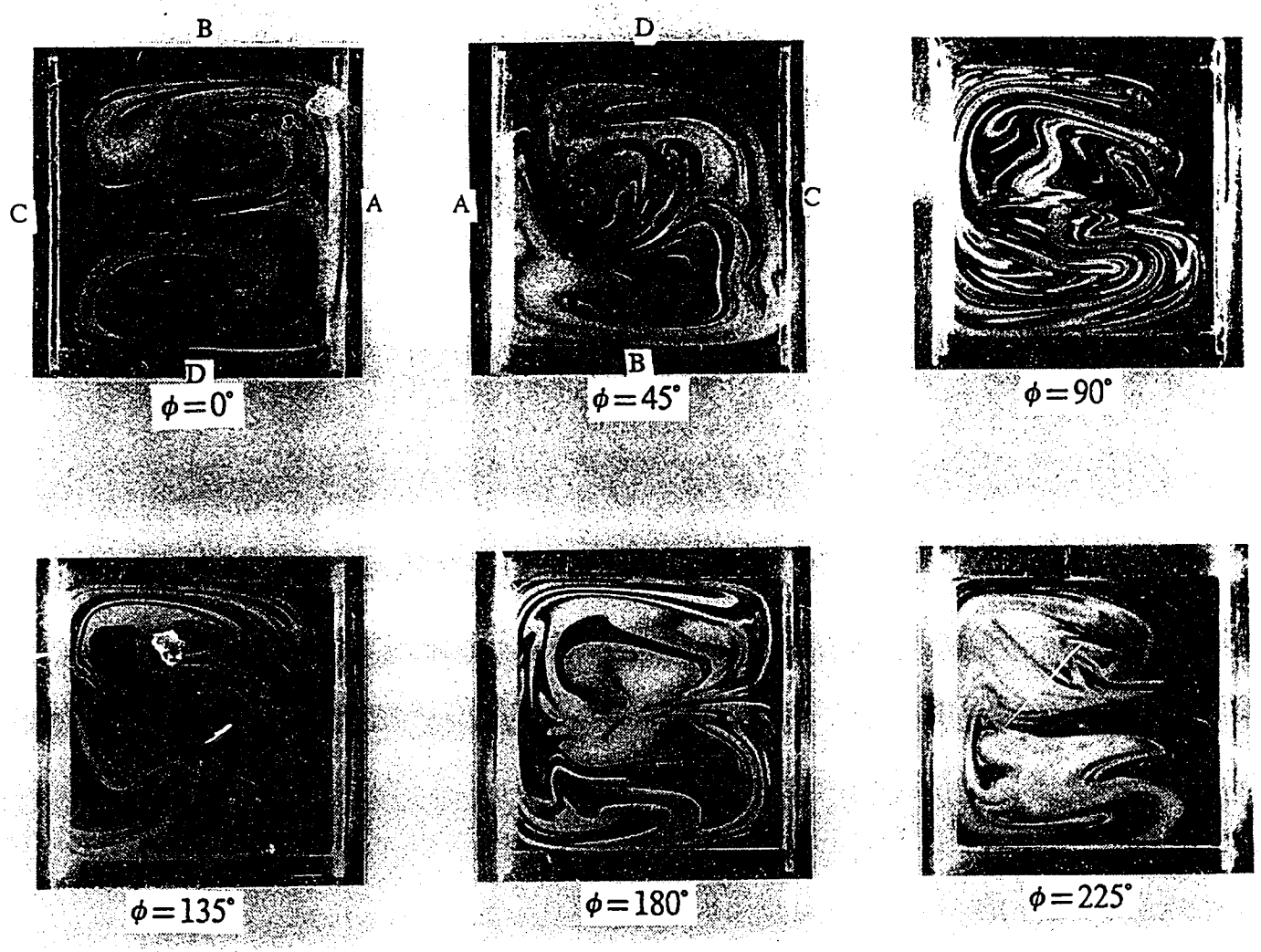

Fig. 2.77 Developing secondary flow patterns in the second square bend with $a/R_c=0.2$, $\psi=180°$ and $\theta=180°$ at K=50

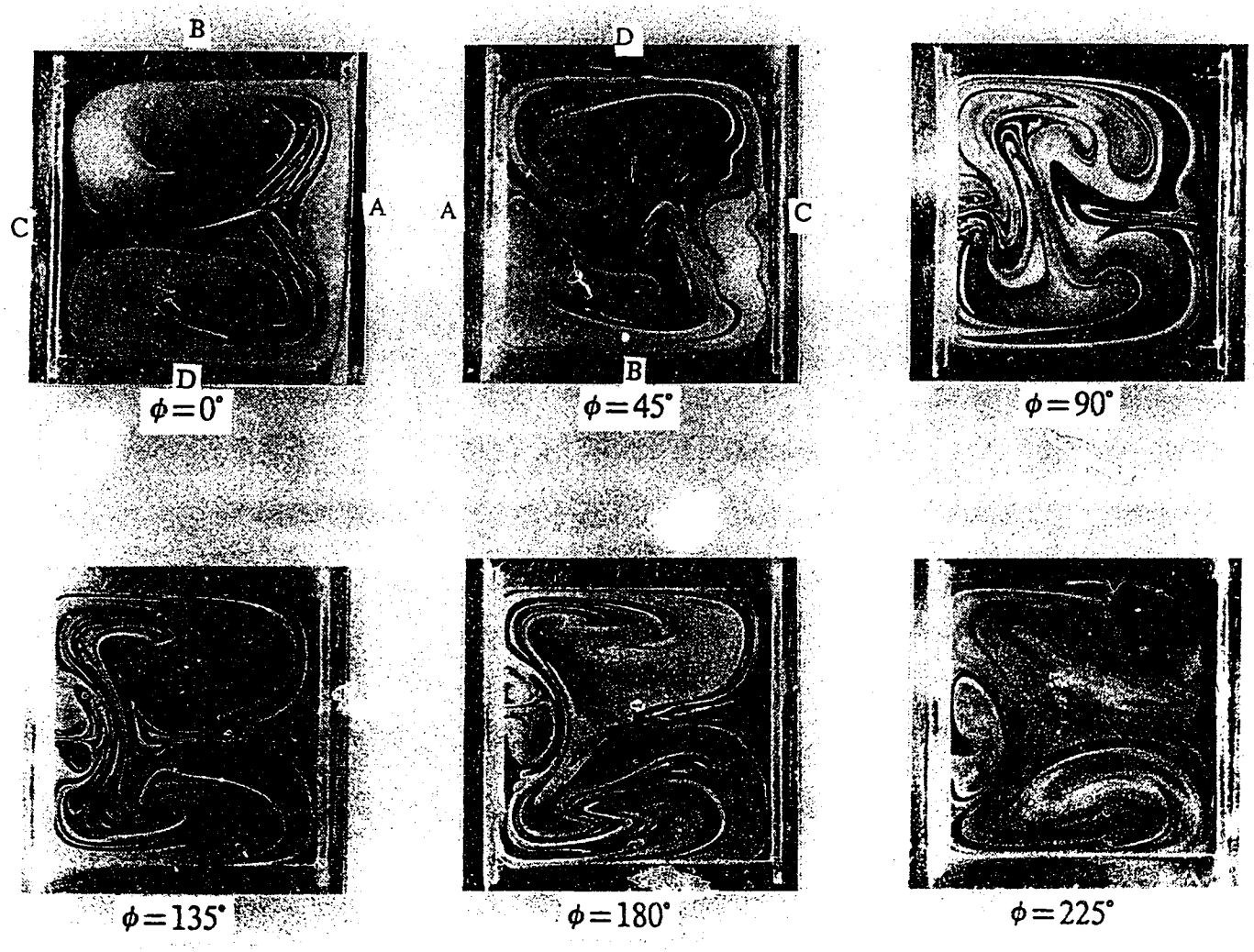

Fig. 2.78 Developing secondary flow patterns in the second square bend with $a/R_C=0.2$, $\psi=180°$ and $\theta=180°$ at $K=100$

Fig. 2.79 Developing secondary flow patterns in the second square bend with $a/R_c=0.2$, $\psi=180°$ and $\theta=180°$ at K=150

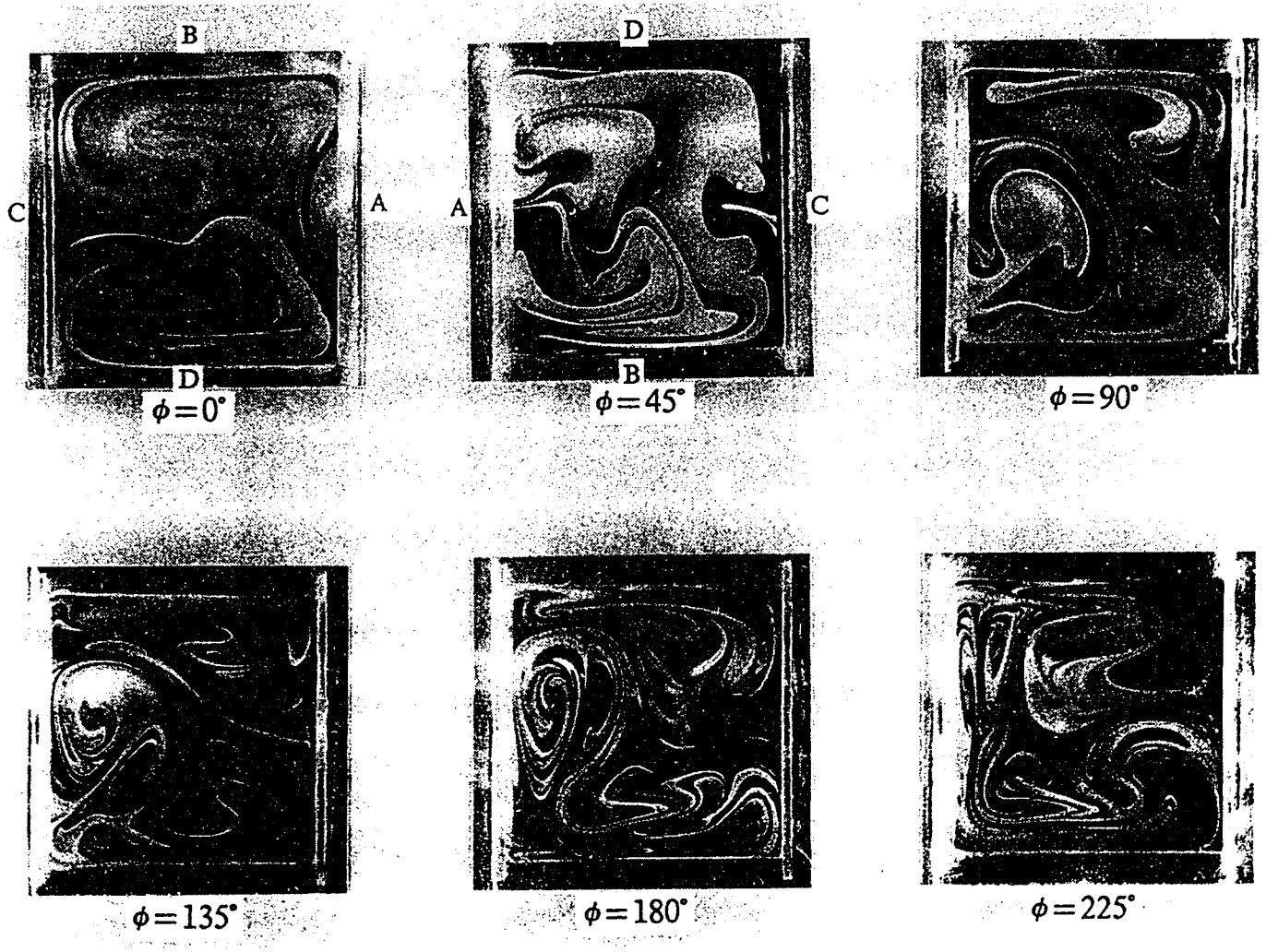

Fig. 2.80 Developing secondary flow patterns in the second square bend with $a/R_c=0.2$, $\psi=180°$ and $\theta=180°$ at K=200

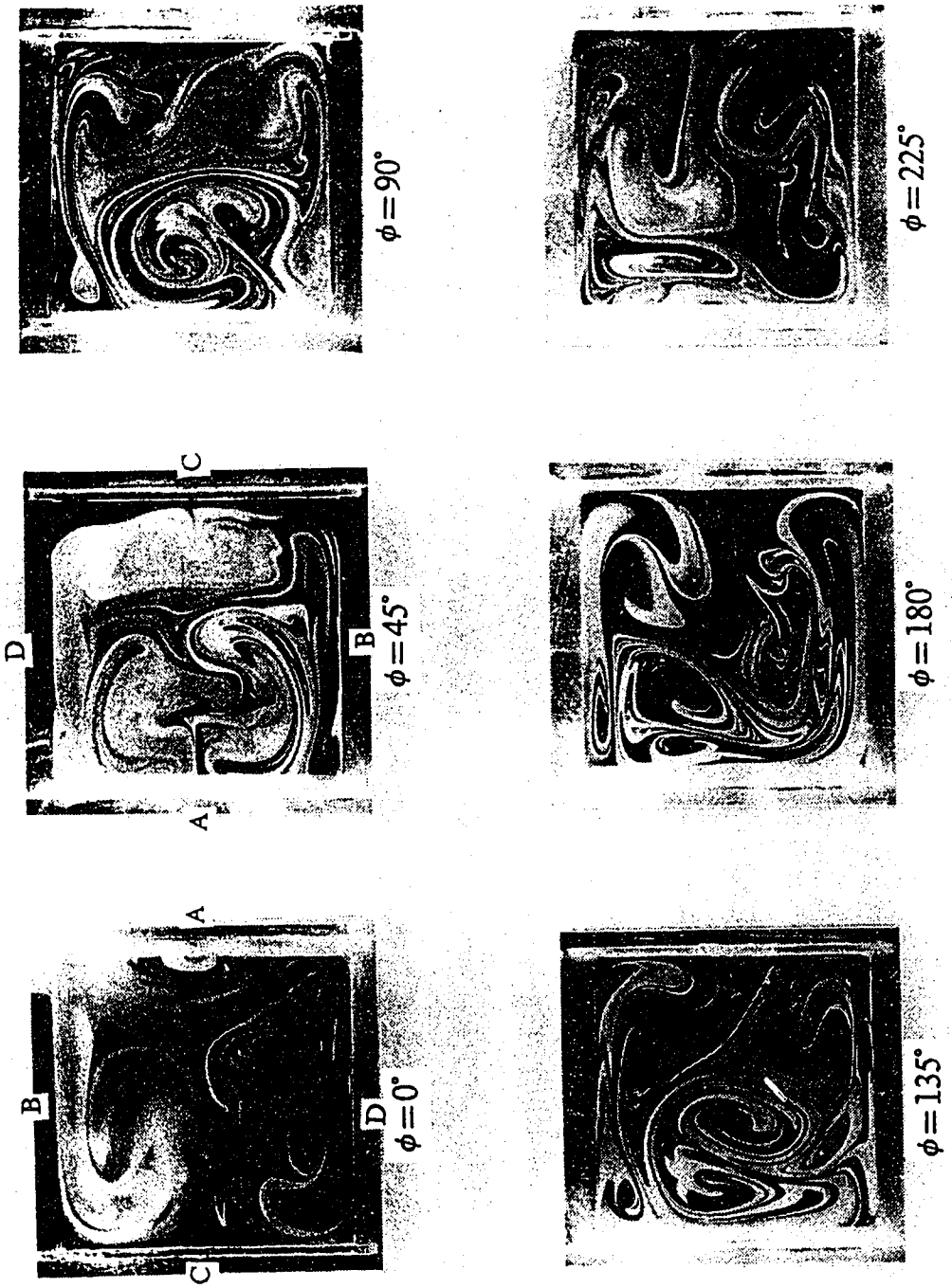

Fig. 2.81 Developing secondary flow patterns in the second square bend with $a/R_c=0.2$, $\psi=180°$ and $\theta=180°$ at K=250

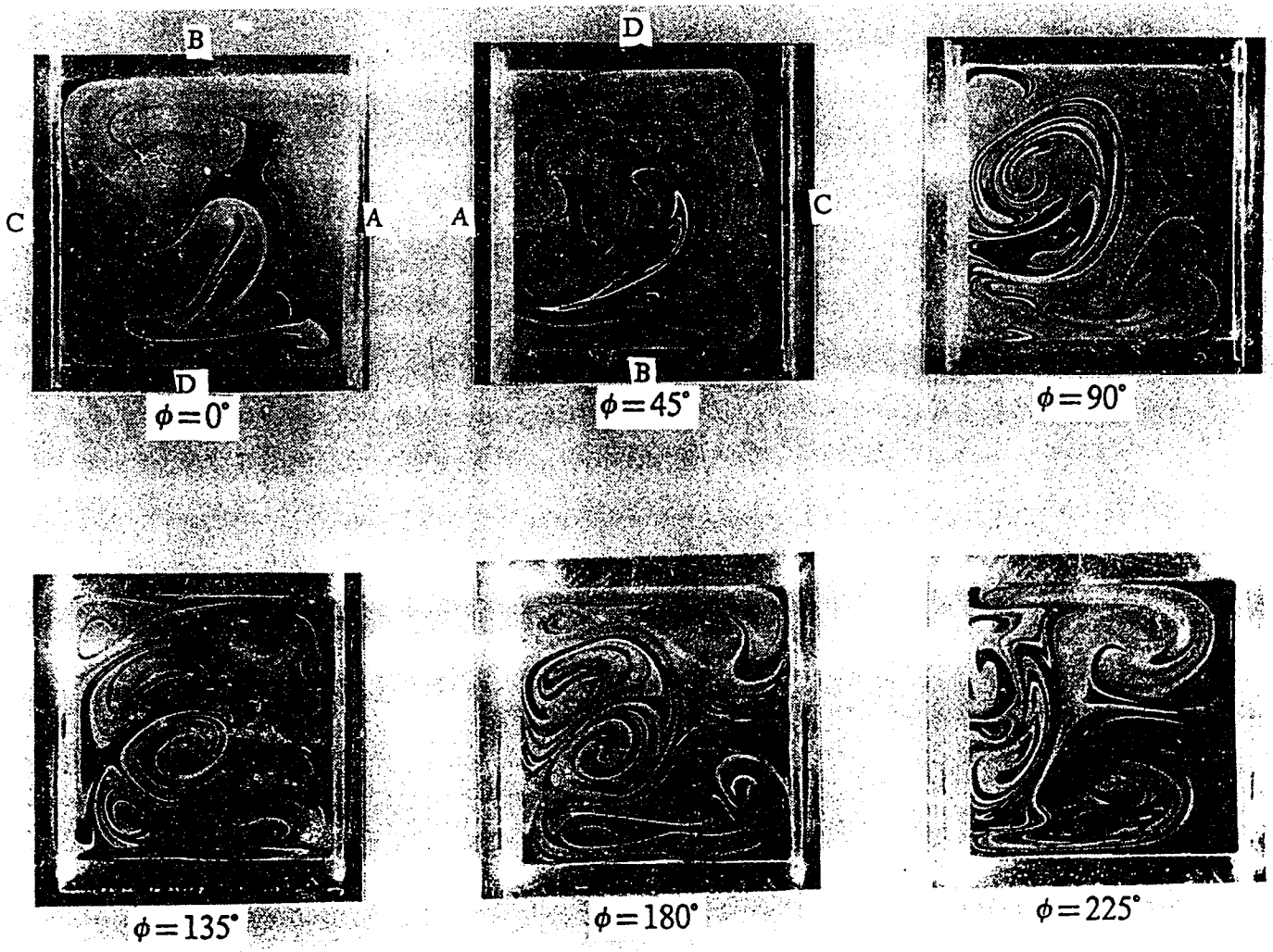

Fig. 2.82 Developing secondary flow patterns in the second square bend with $a/R_c=0.2$, $\psi=180°$ and $\theta=180°$ at K=300

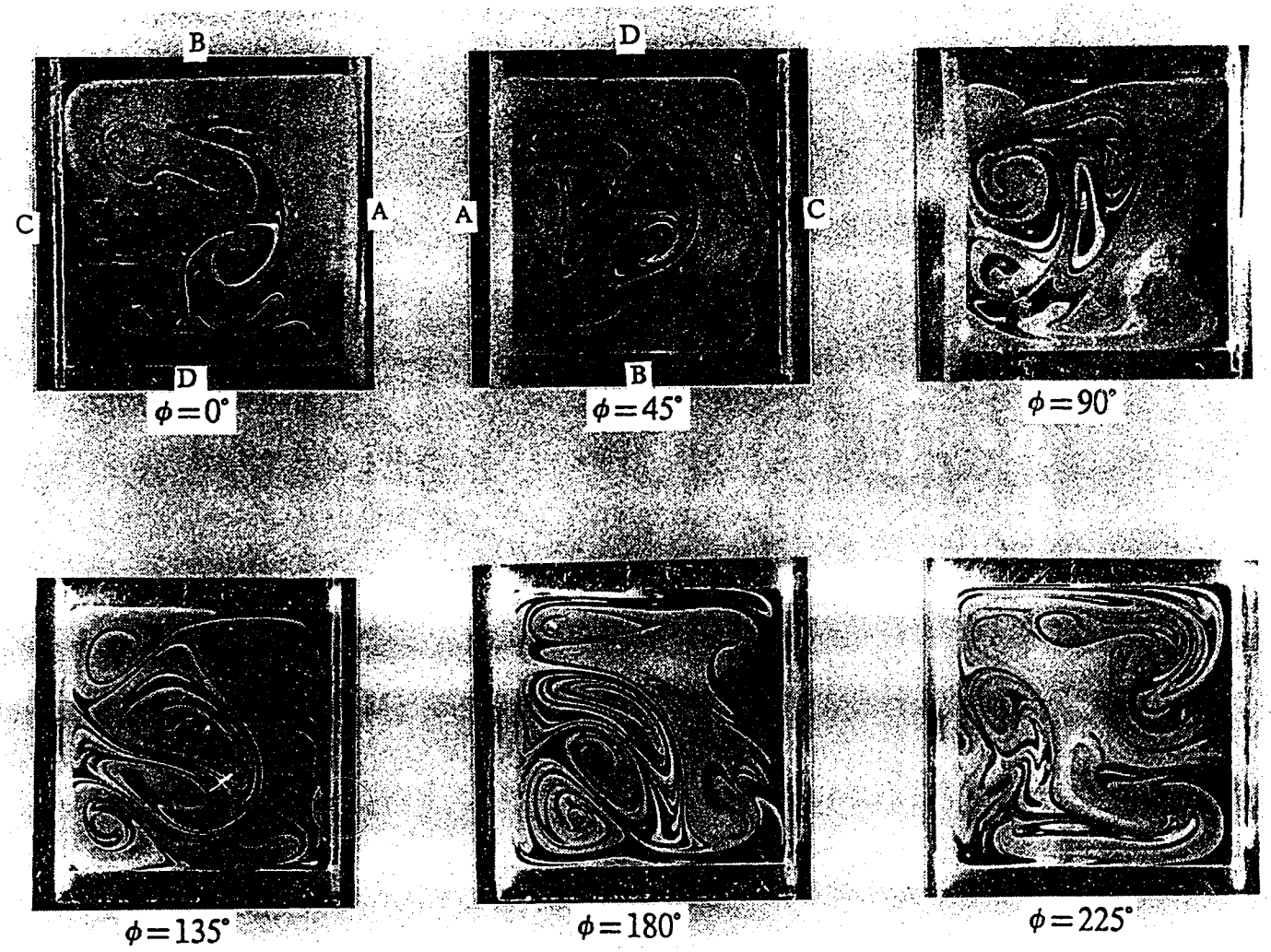

Fig. 2.83 Developing secondary flow patterns in the second square bend with $a/R_c=0.2$, $\psi=180°$ and $\theta=180°$ at K=350

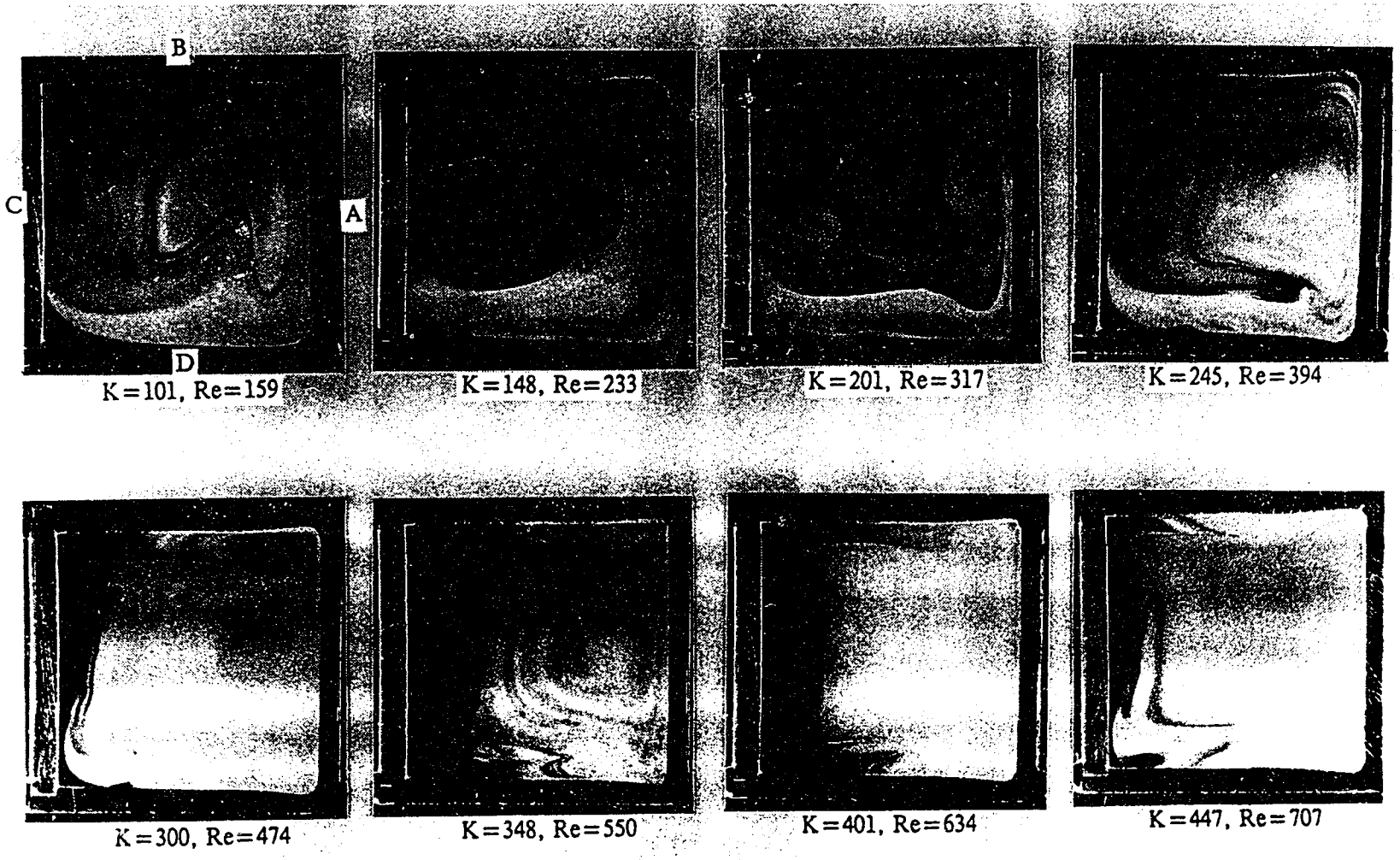

Fig. 2.84 The effect of Dean number on secondary flow patterns at the exit of a 45° square bend with $a/R_c=0.4$

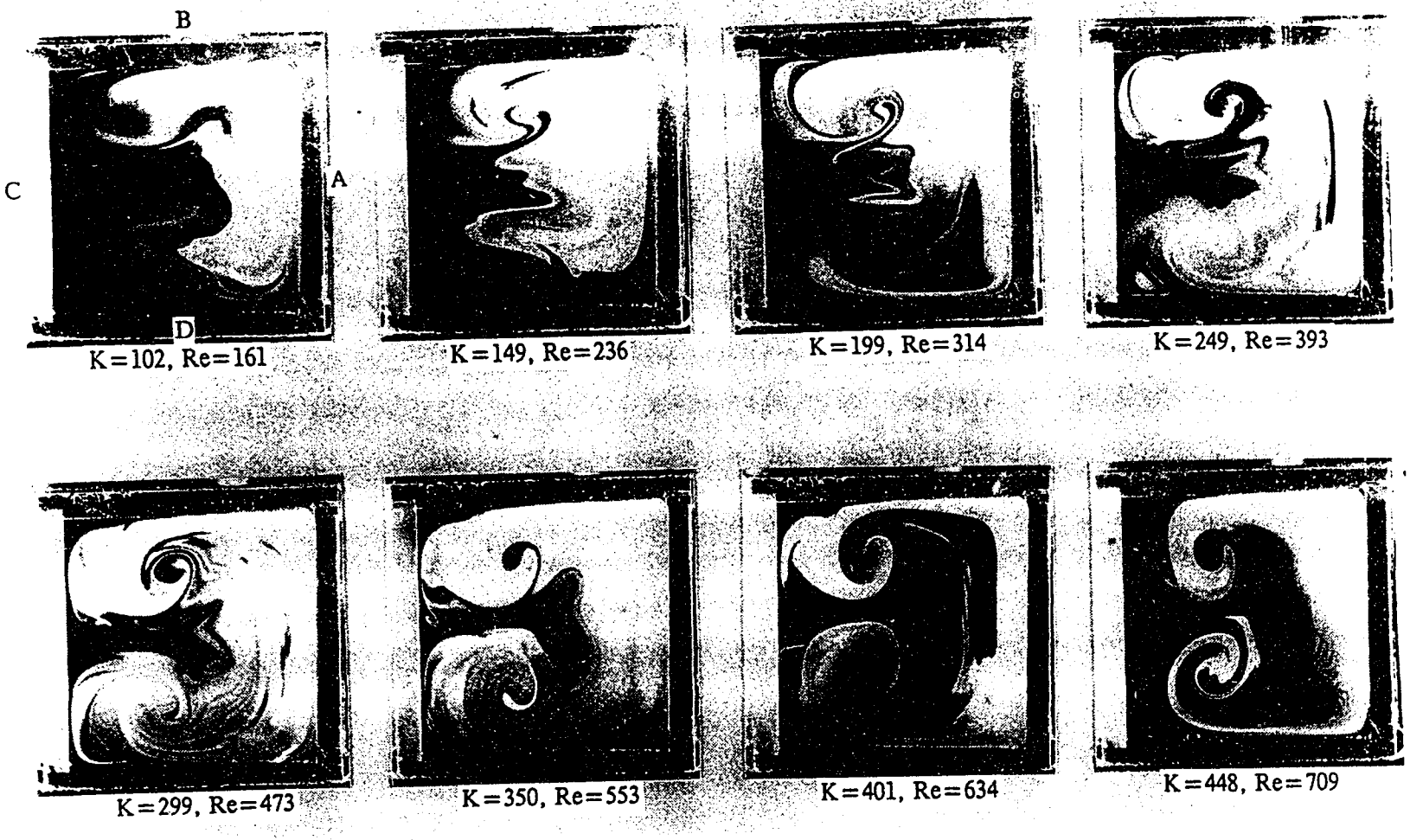

Fig. 2.85 The effect of Dean number on secondary flow patterns at the exit of a 90° square bend with $a/R_c=0.4$

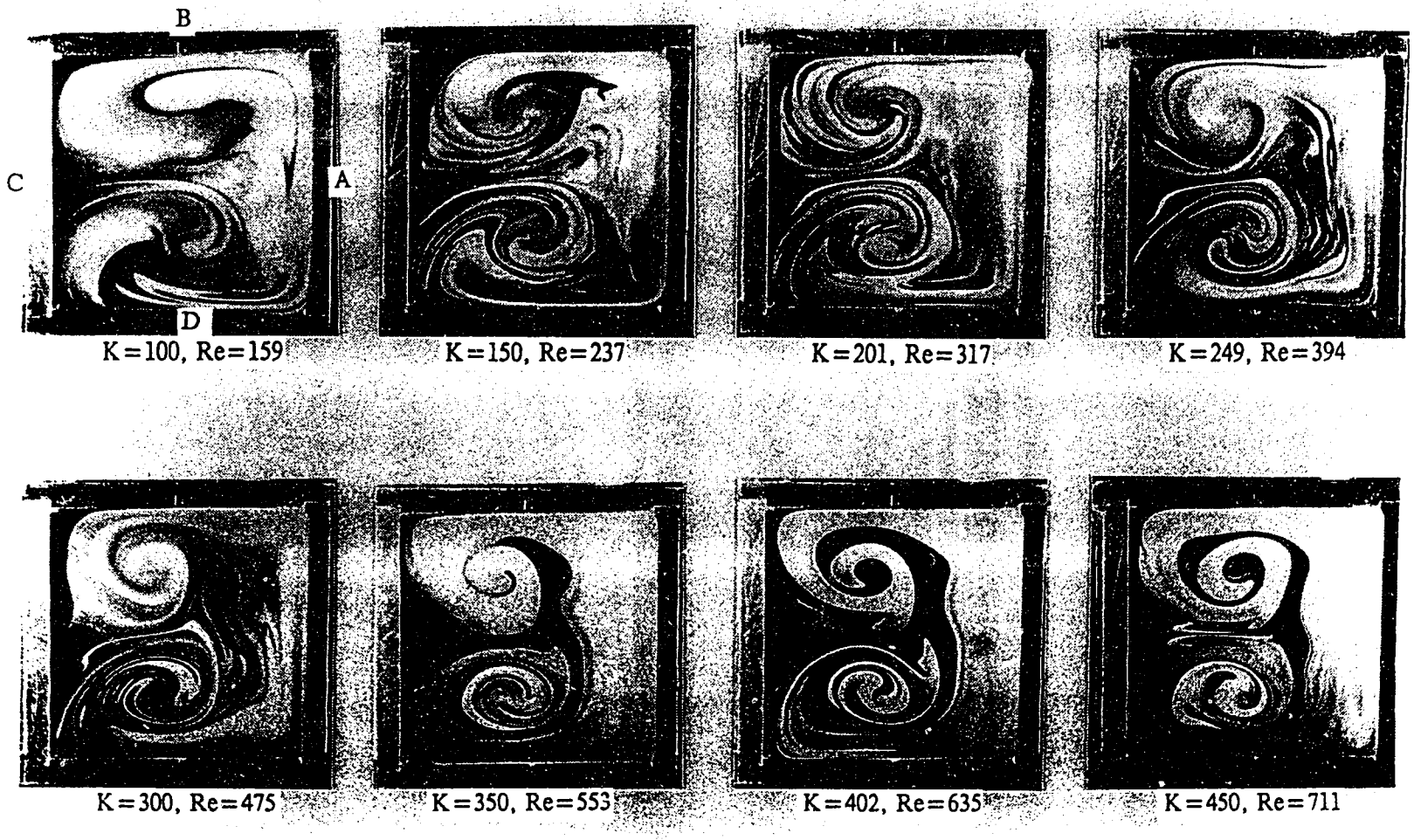

Fig. 2.86 The effect of Dean number on secondary flow patterns at the exit of a 135° square bend with $a/R_c=0.4$

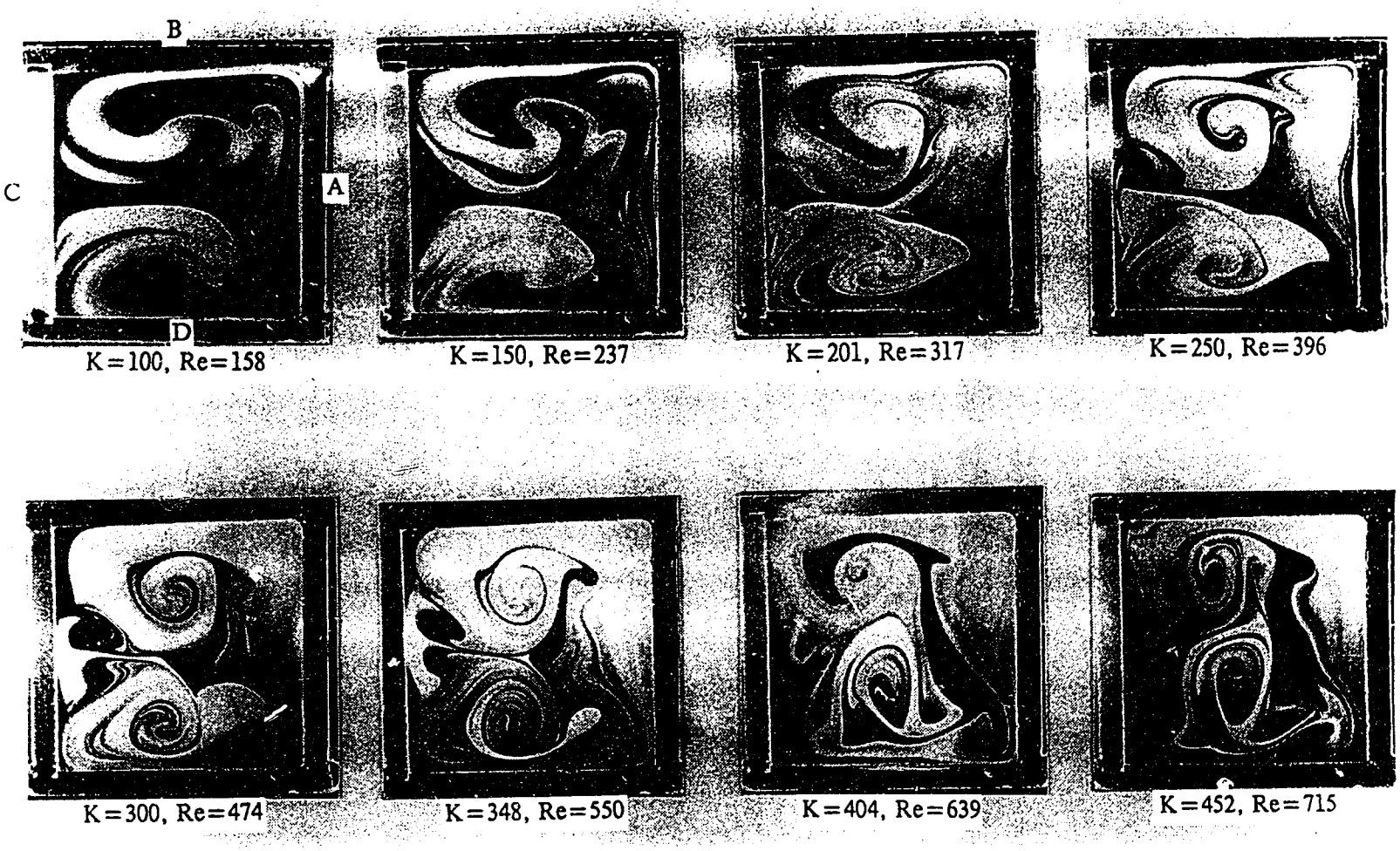

Fig. 2.87 The effect of Dean number on secondary flow patterns at the exit of a 180° square bend with $a/R_c=0.4$

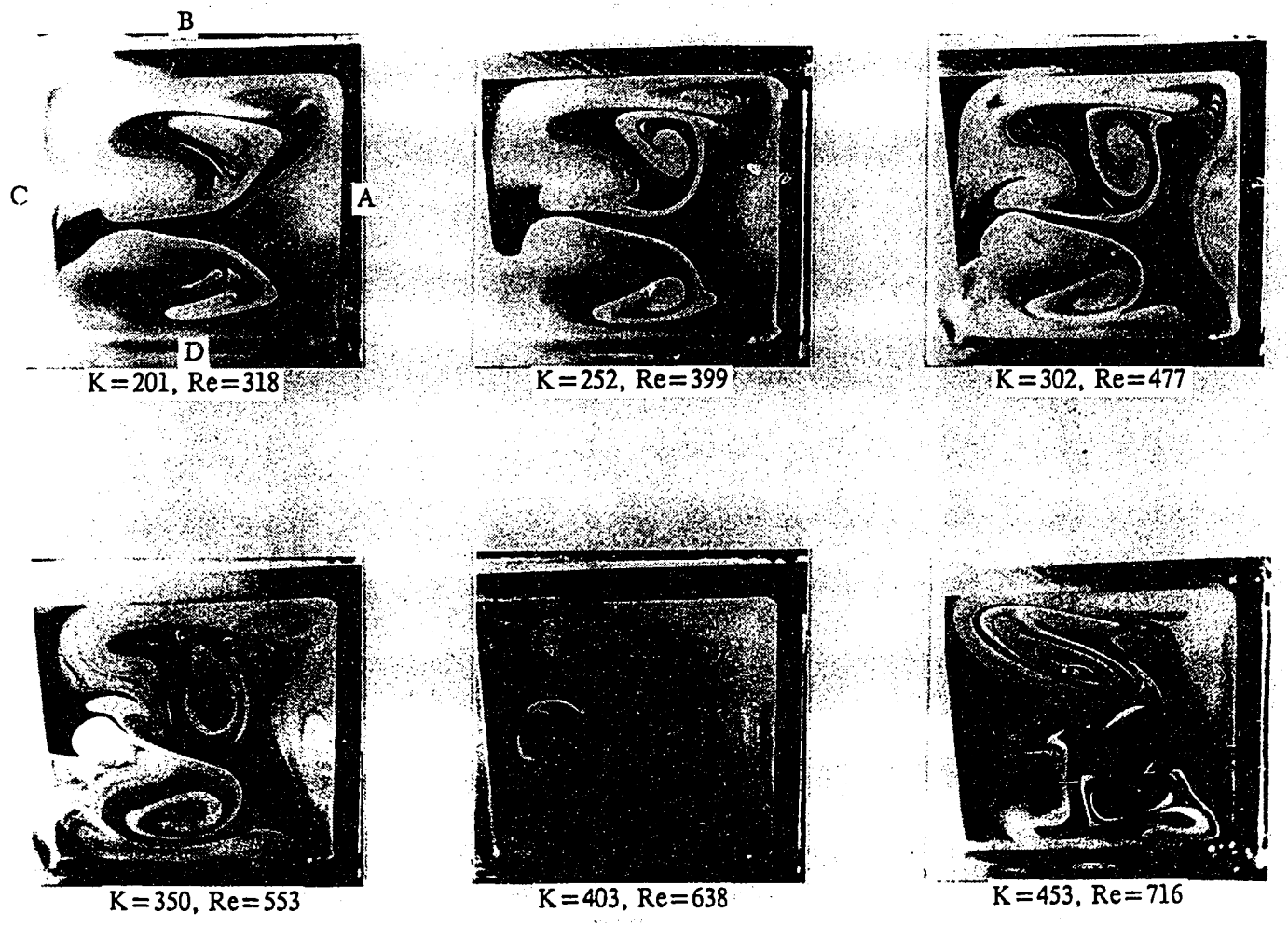

Fig. 2.88 The effect of Dean number on secondary flow patterns at the exit of a 225° square bend with $a/R_c=0.4$

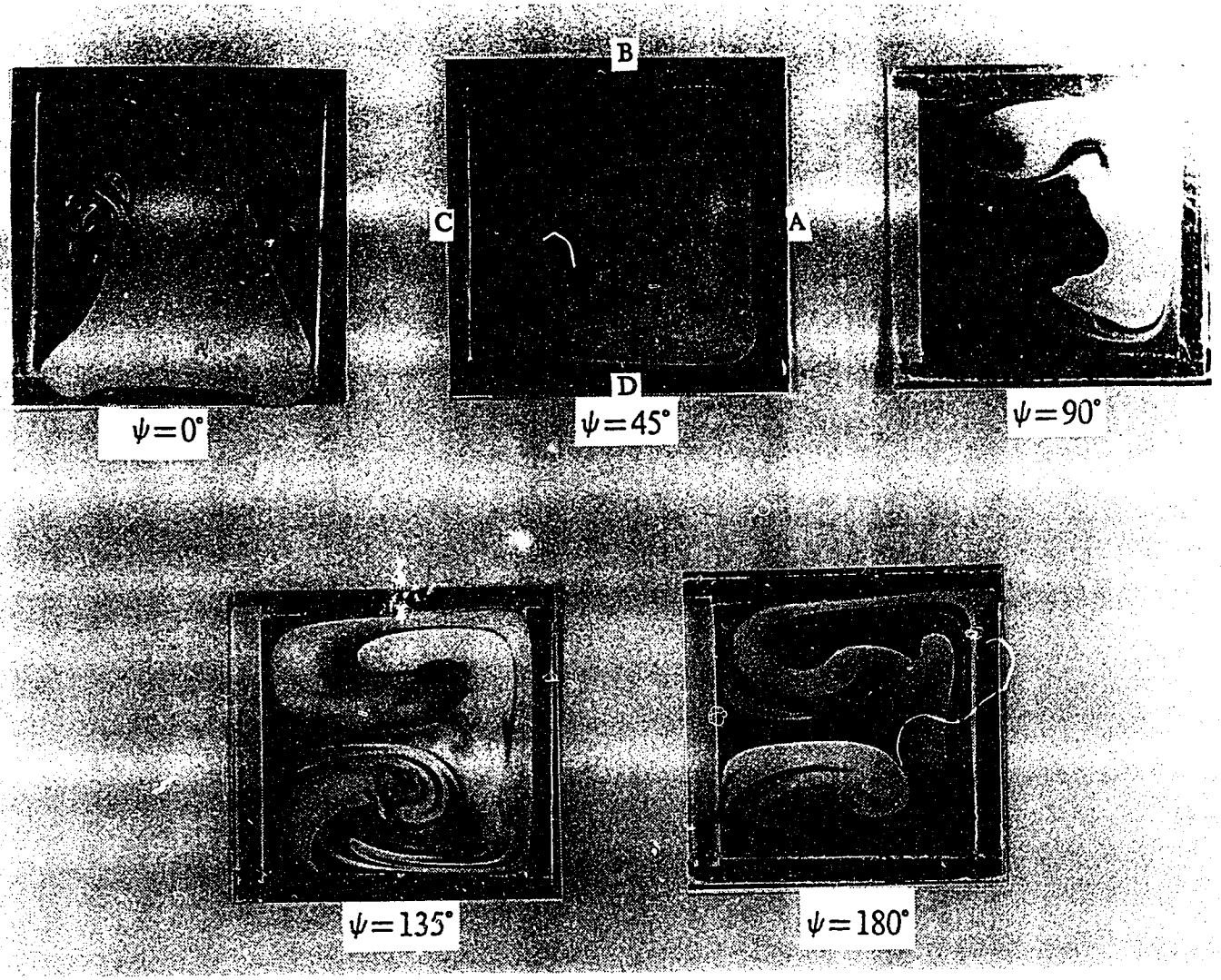

Fig. 2.89 Developing secondary flow patterns in the first square bend with a/R_c=0.4 at K=100

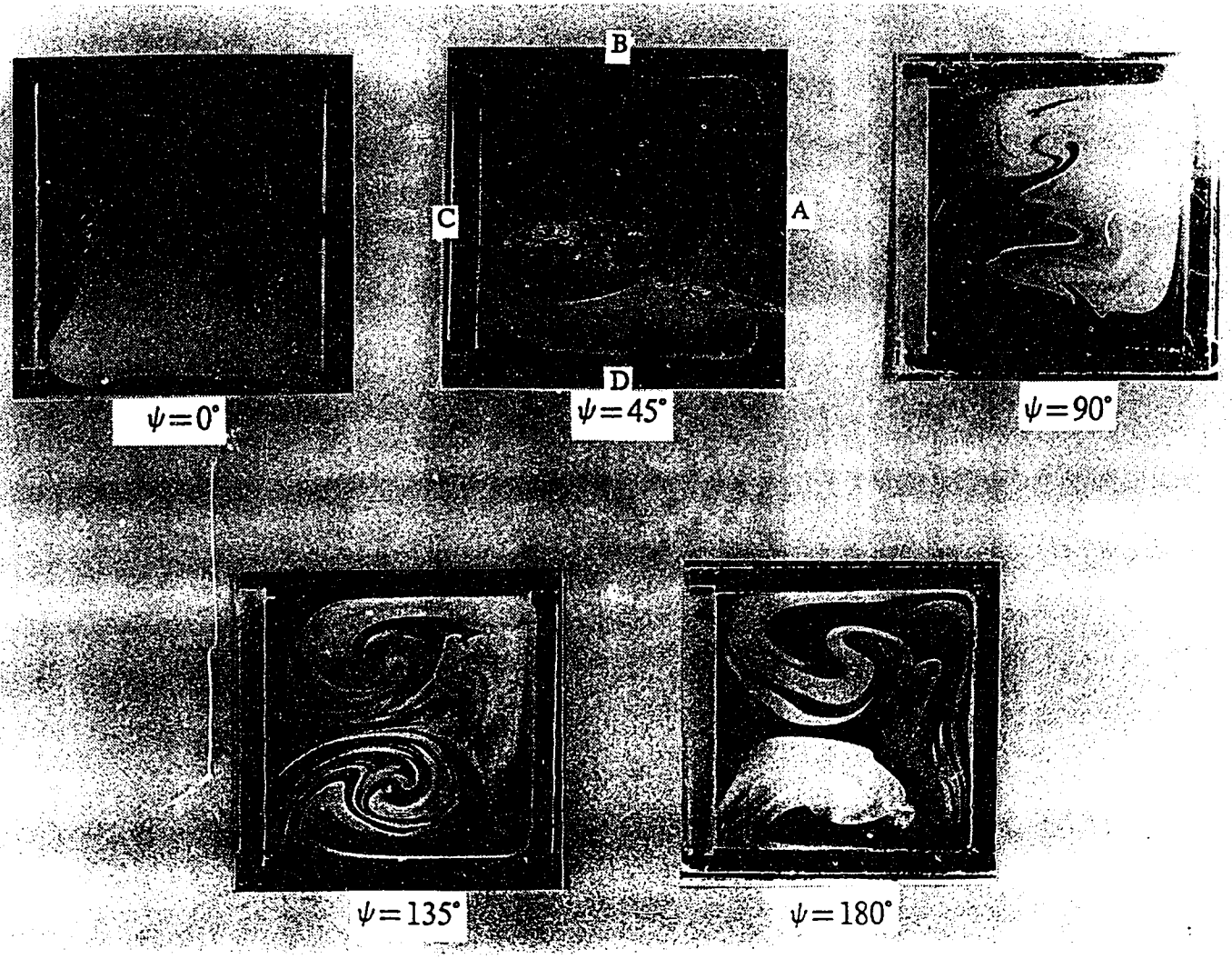

Fig. 2.90 Developing secondary flow patterns in the first square bend with a/R_c=0.4 at K=150

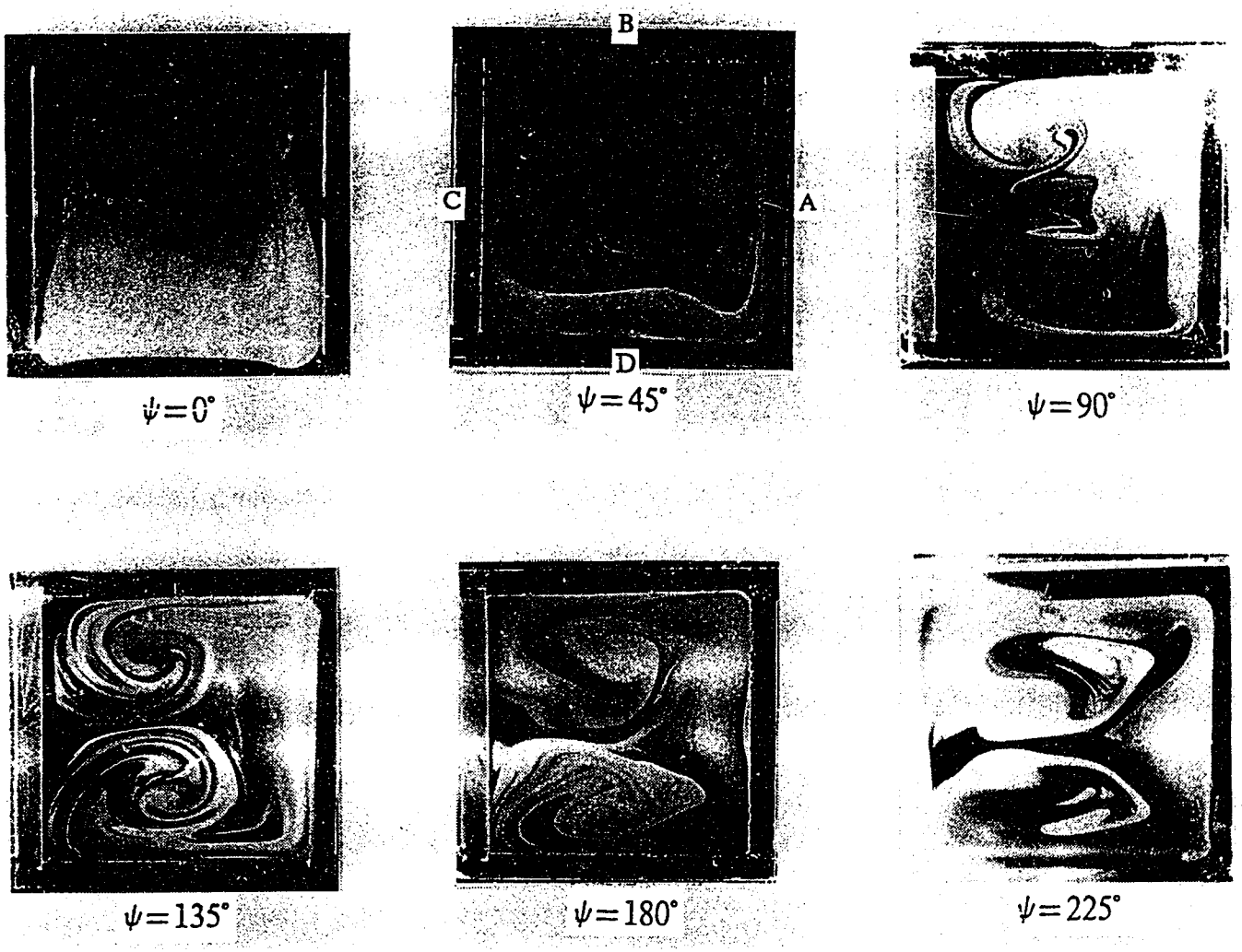

Fig. 2.91 Developing secondary flow patterns in the first square bend with a/R_c=0.4 at K=200

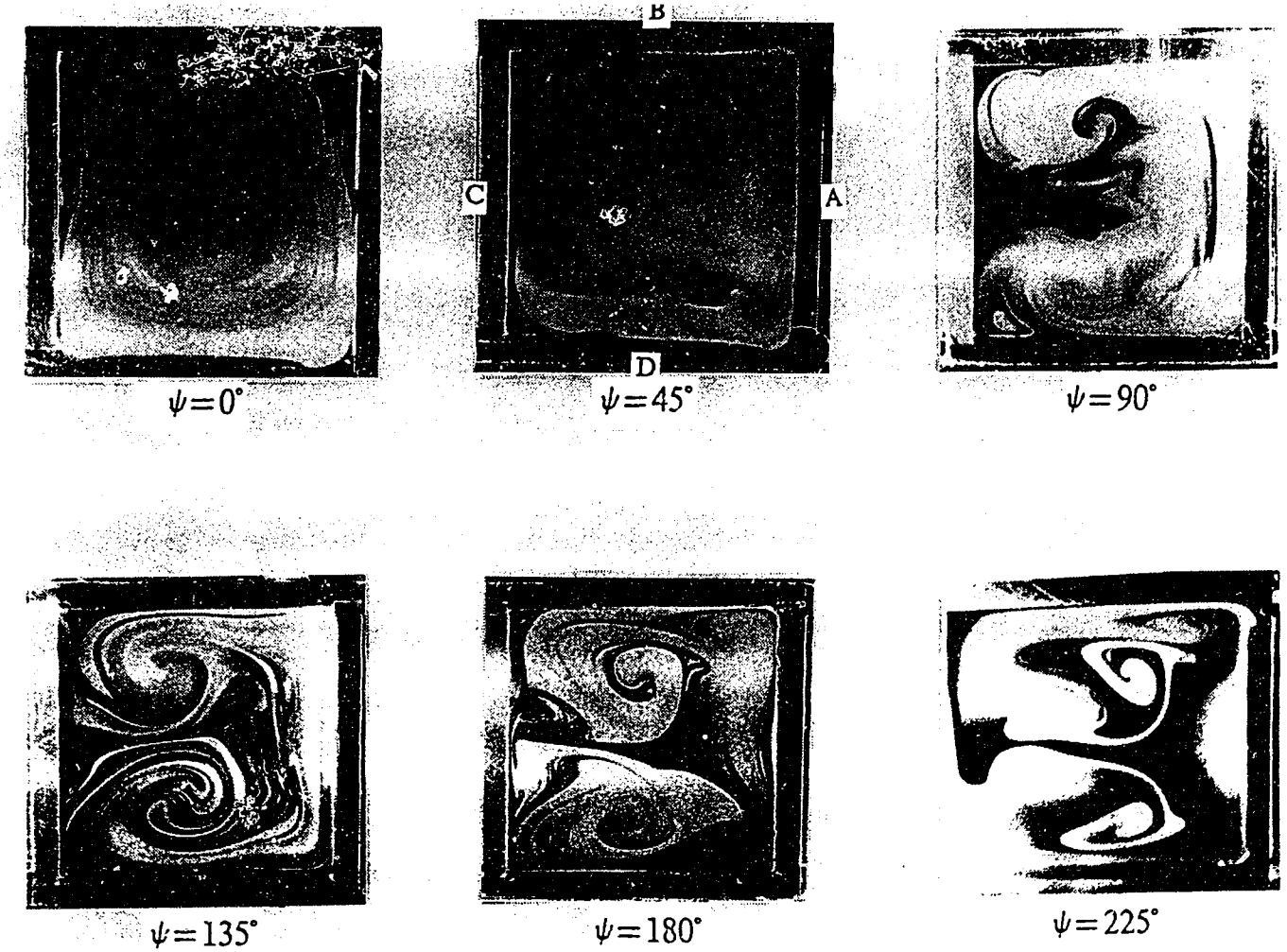

Fig. 2.92 Developing secondary flow patterns in the first square bend with a/R_c=0.4 at K=250

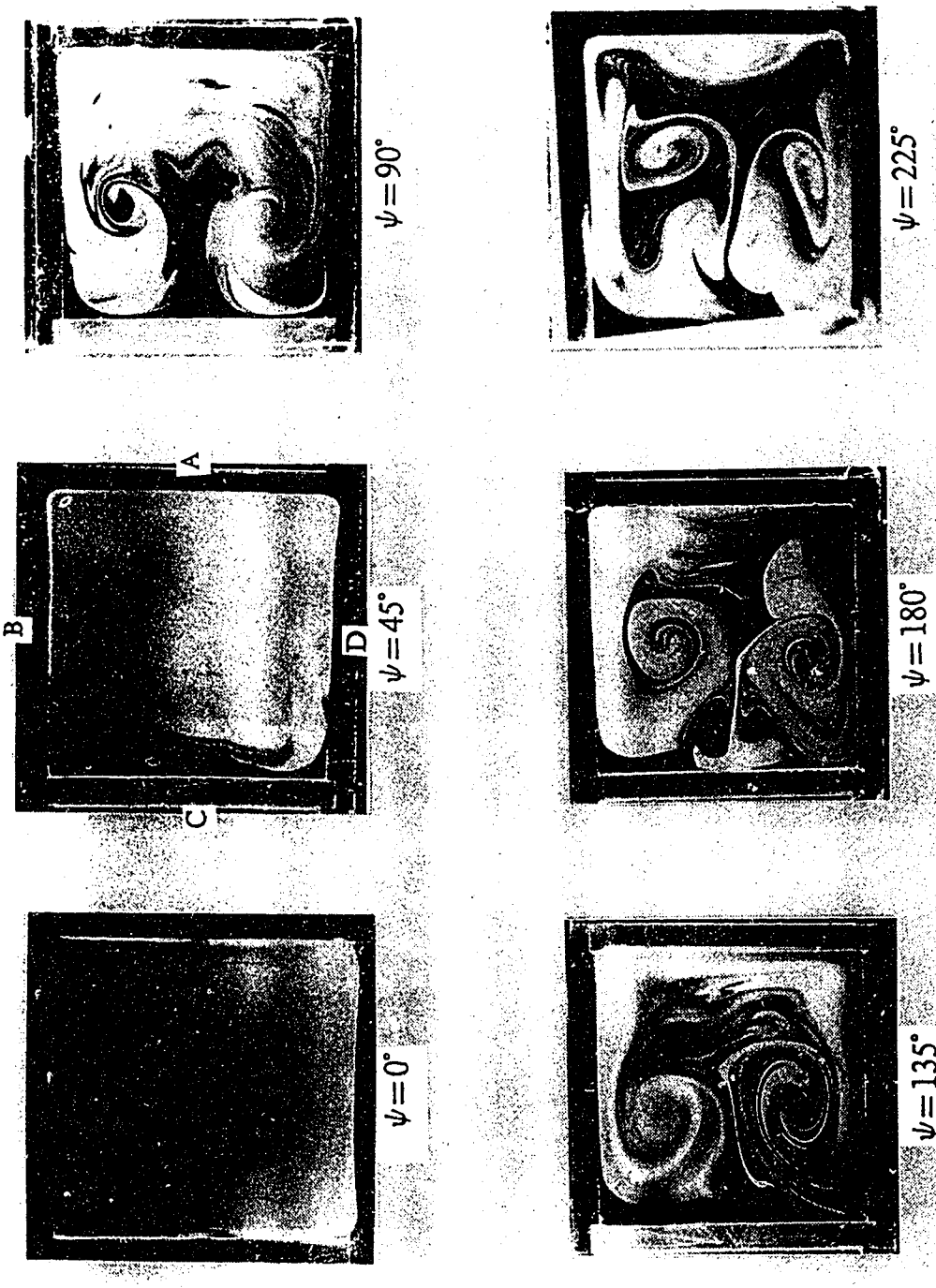

Fig. 2.93 Developing secondary flow patterns in the first square bend with $a/R_c=0.4$ at K=300

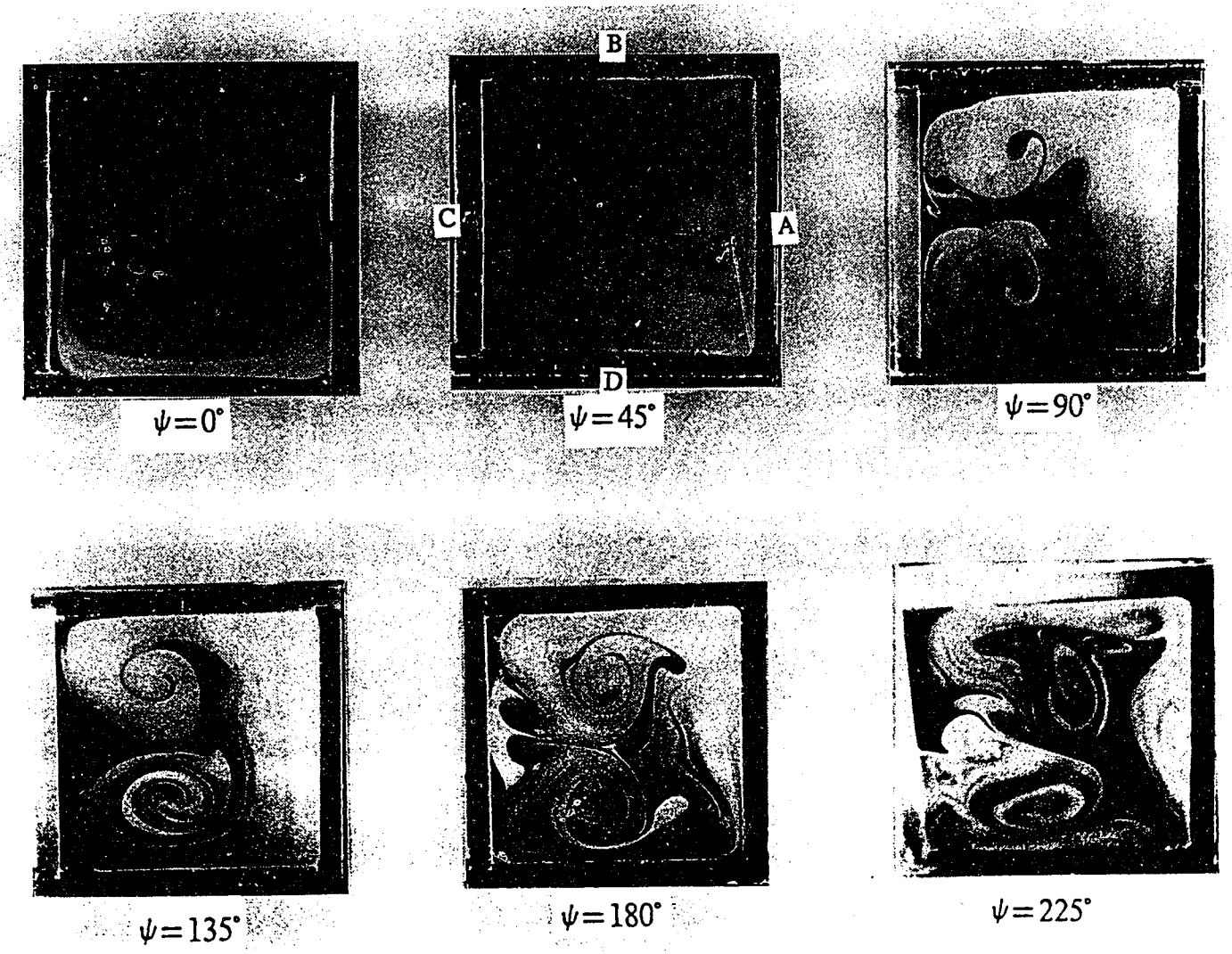

Fig. 2.94 Developing secondary flow patterns in the first square bend with a/R_c=0.4 at K=350

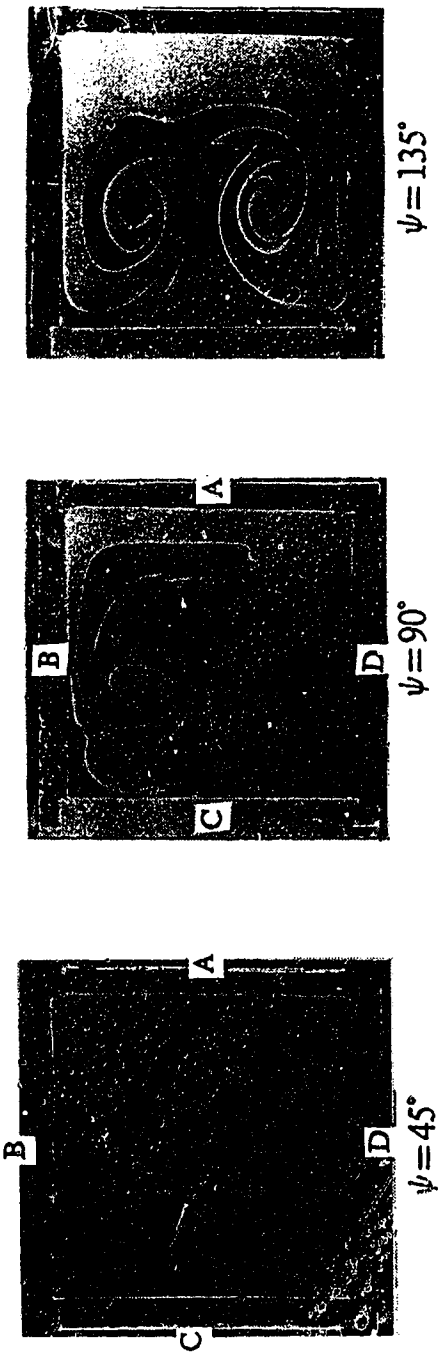

Fig. 2.95 Developing secondary flow patterns in the first square bend with a/R_c=0.4 at K=400

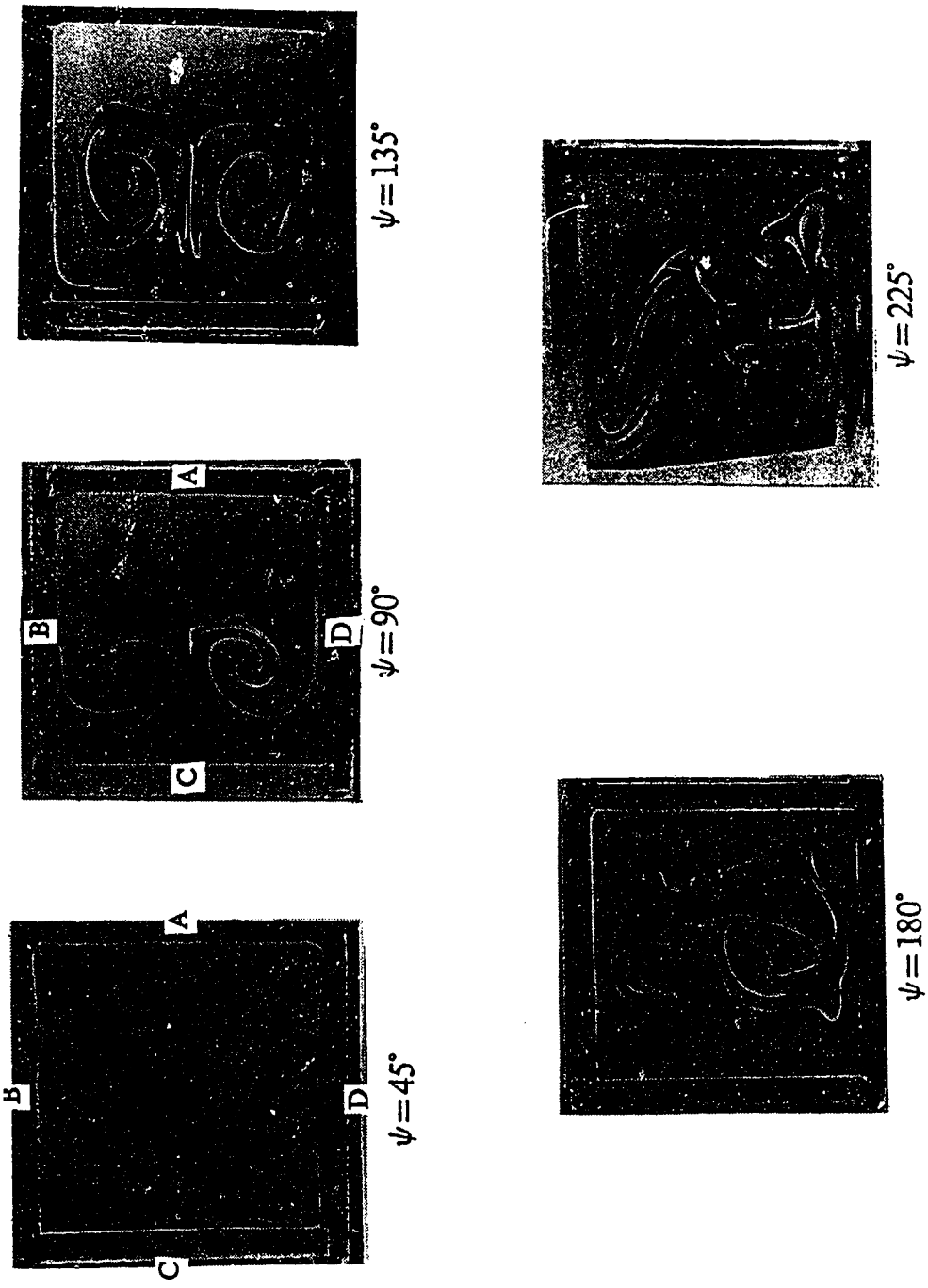

Fig. 2.96 Developing secondary flow patterns in the first square bend with a/R_c=0.4 at K=450

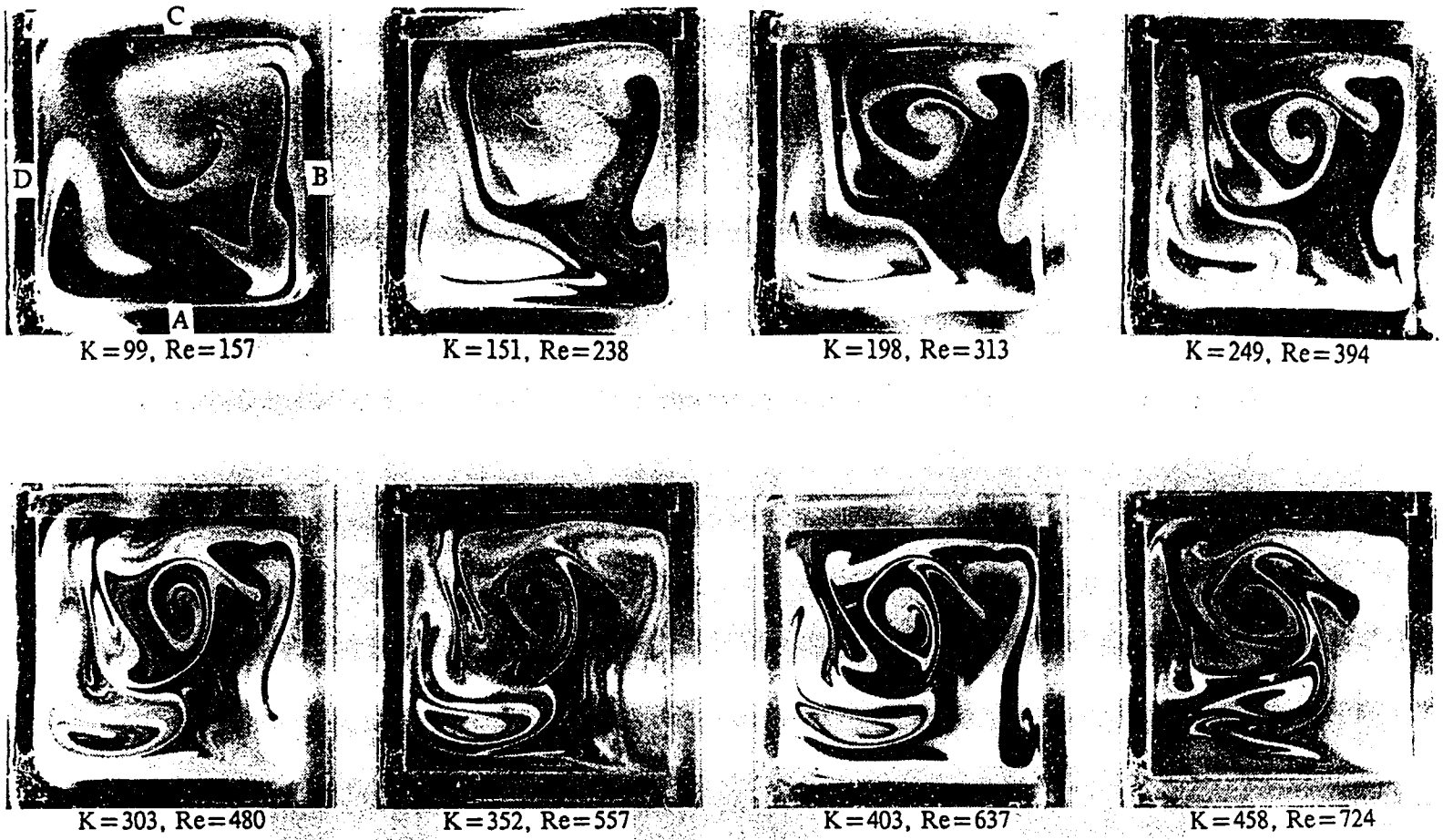

Fig. 2.97 The effect of Dean number on secondary flow patterns at the exit of a 45° second square bend with $a/R_c=0.4$, $\psi=180°$ and $\theta=90°$

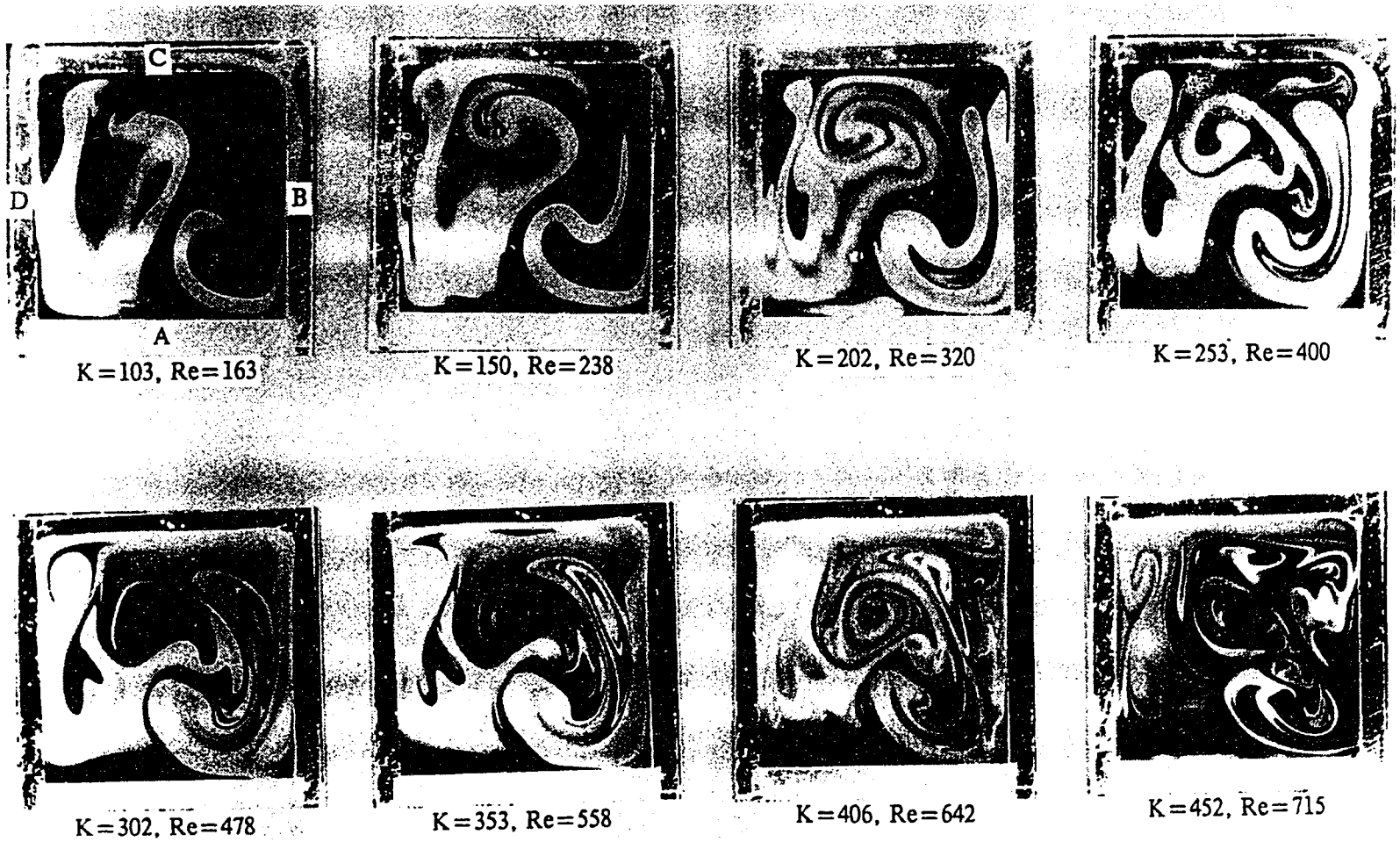

Fig. 2.98 The effect of Dean number on secondary flow patterns at the exit of a 90° second square bend with $a/R_c=0.4$, $\psi=180°$ and $\theta=90°$

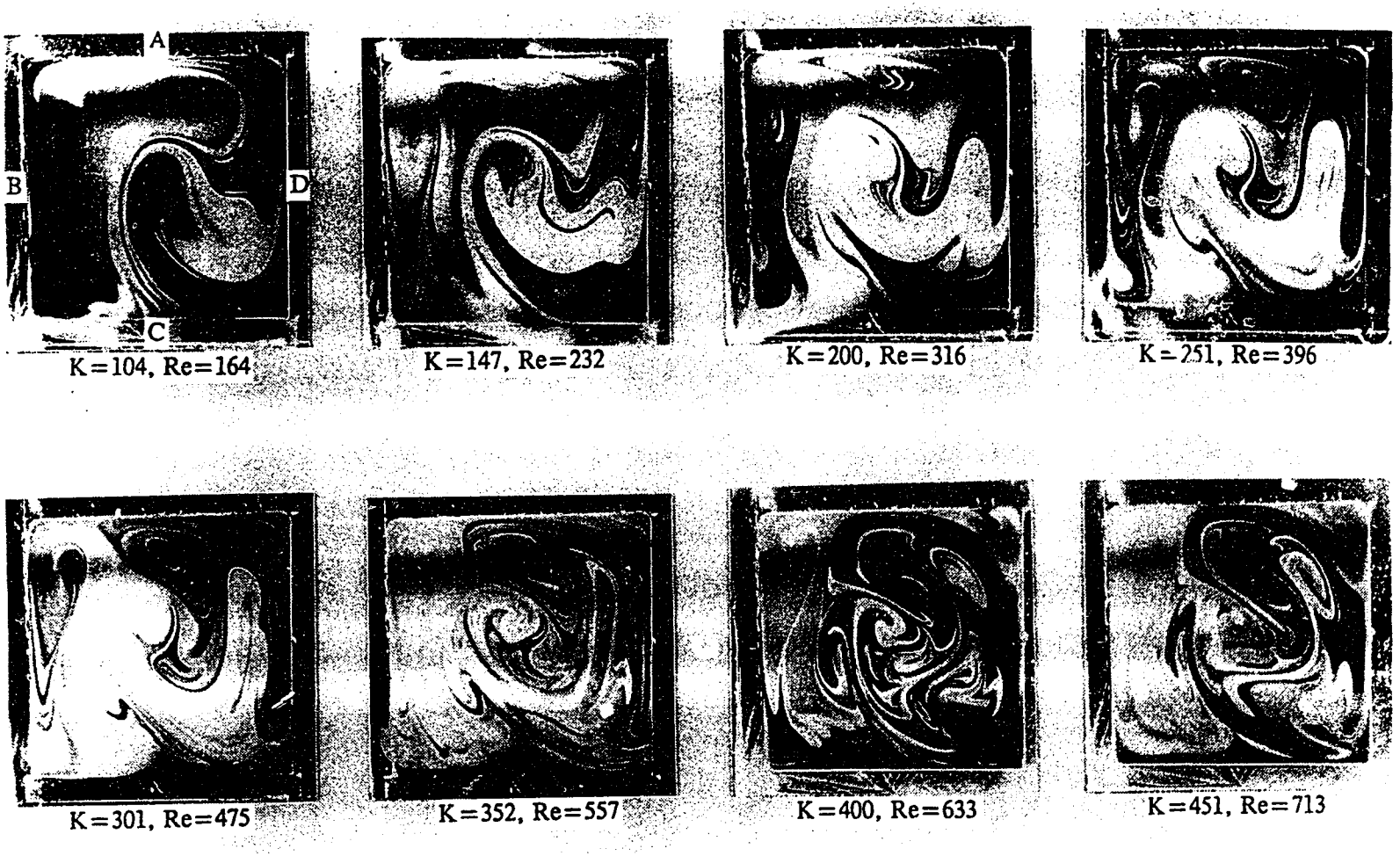

Fig. 2.99 The effect of Dean number on secondary flow patterns at the exit of a 135° second square bend with $a/R_c=0.4$, $\psi=180°$ and $\theta=90°$

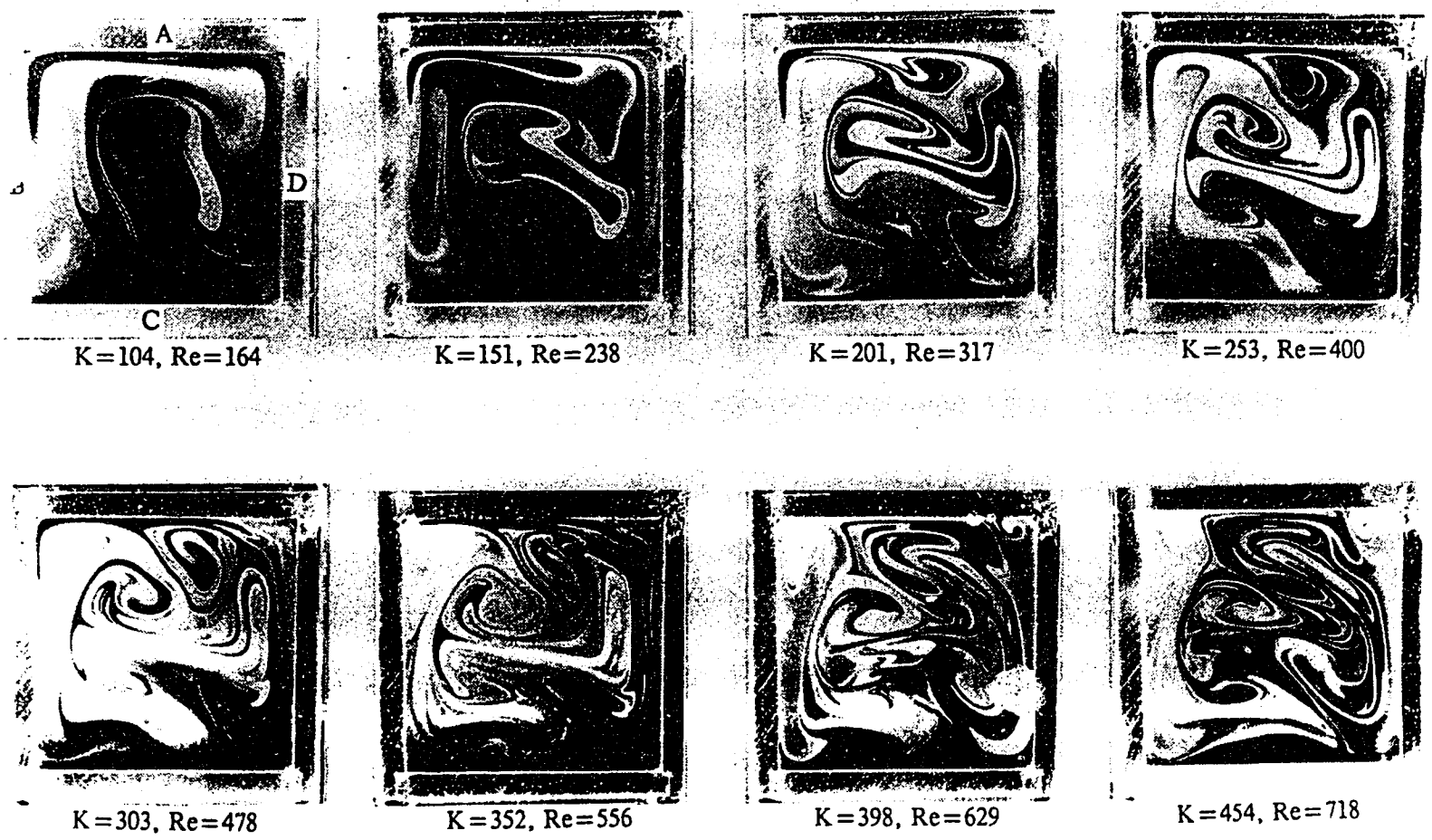

Fig. 2.100 The effect of Dean number on secondary flow patterns at the exit of a 180° second square bend with $a/R_c=0.4$, $\psi=180°$ and $\theta=90°$

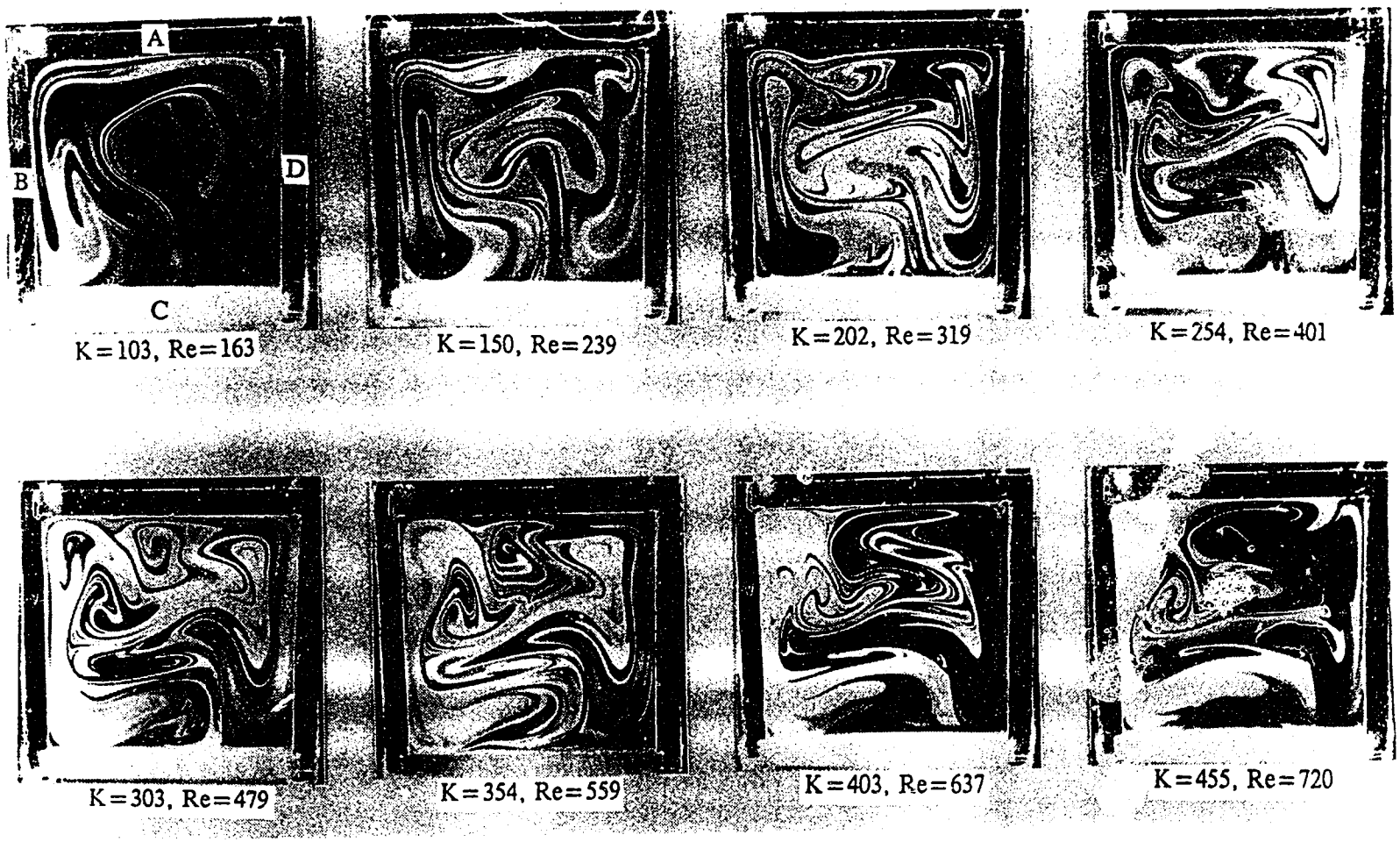

Fig. 2.101 The effect of Dean number on secondary flow patterns at the exit of a 225° second square bend with $a/R_c=0.4$, $\psi=180°$ and $\theta=90°$

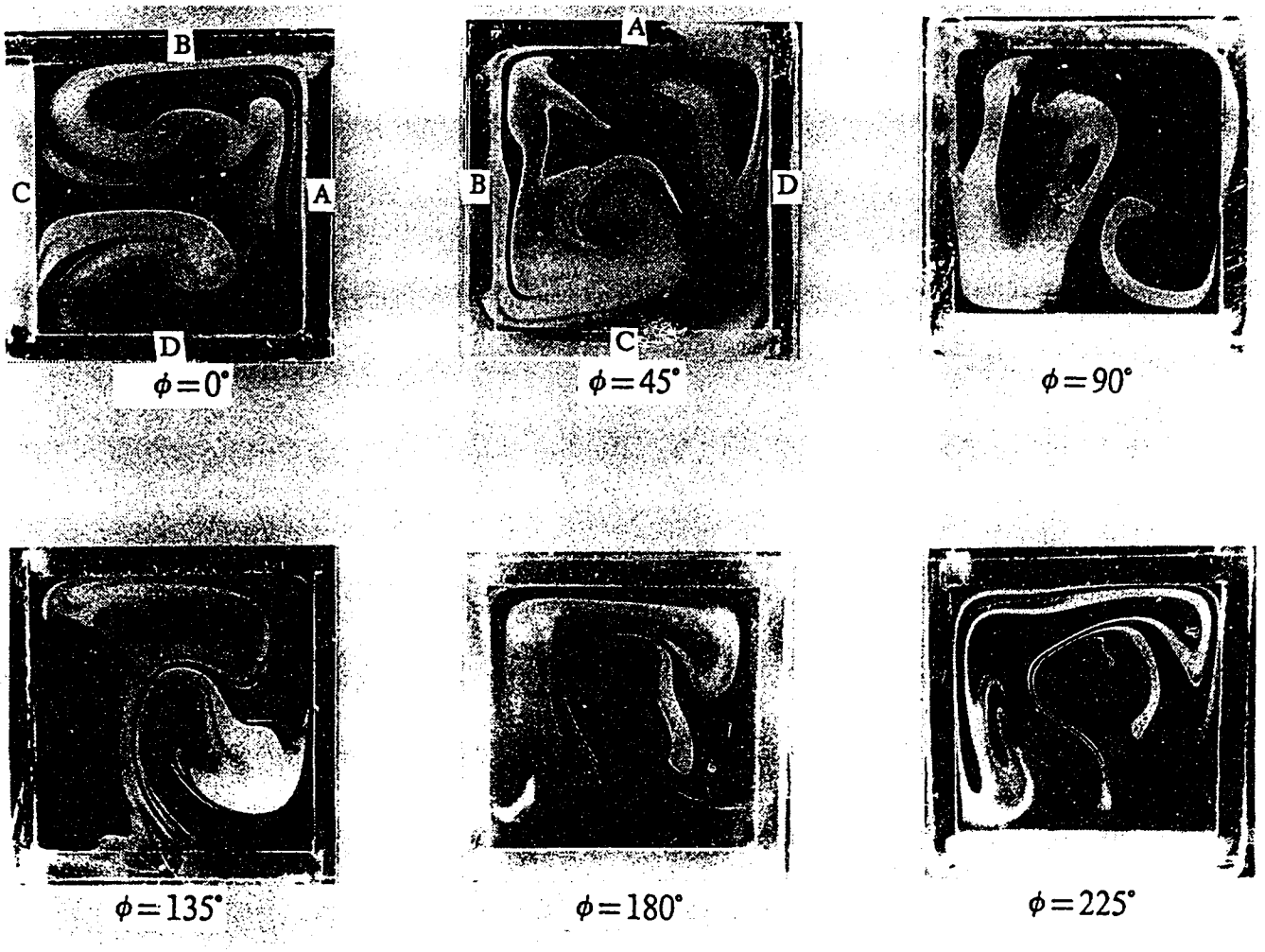

Fig. 2.102 Developing secondary flow patterns in the second square bend with $a/R_c=0.4$, $\psi=180°$ and $\theta=90°$ at K=100

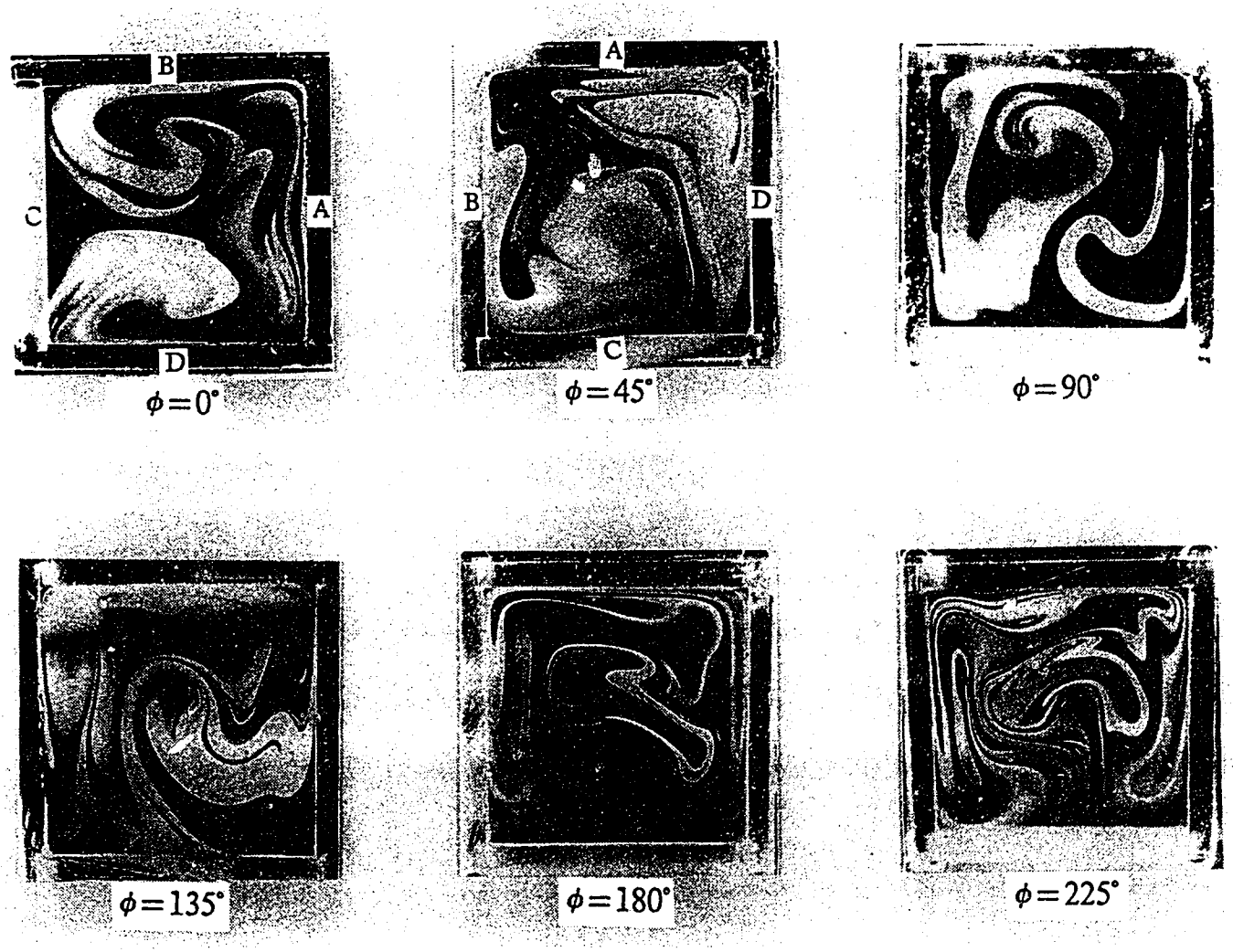

Fig. 2.103 Developing secondary flow patterns in the second square bend with $a/R_c=0.4$, $\psi=180°$ and $\theta=90°$ at K=150

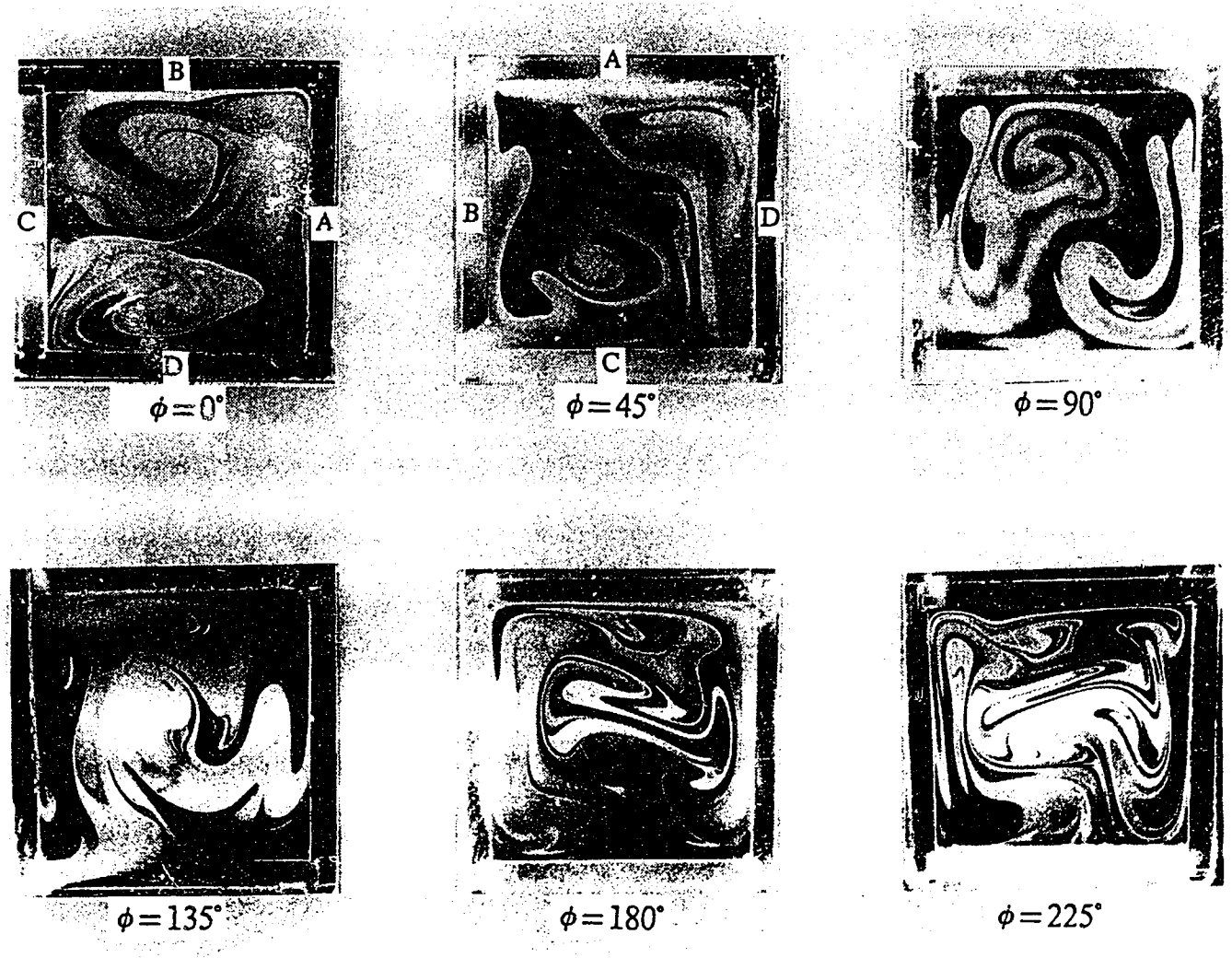

Fig. 2.104 Developing secondary flow patterns in the second square bend with $a/R_c=0.4$, $\psi=180°$ and $\theta=90°$ at K=200

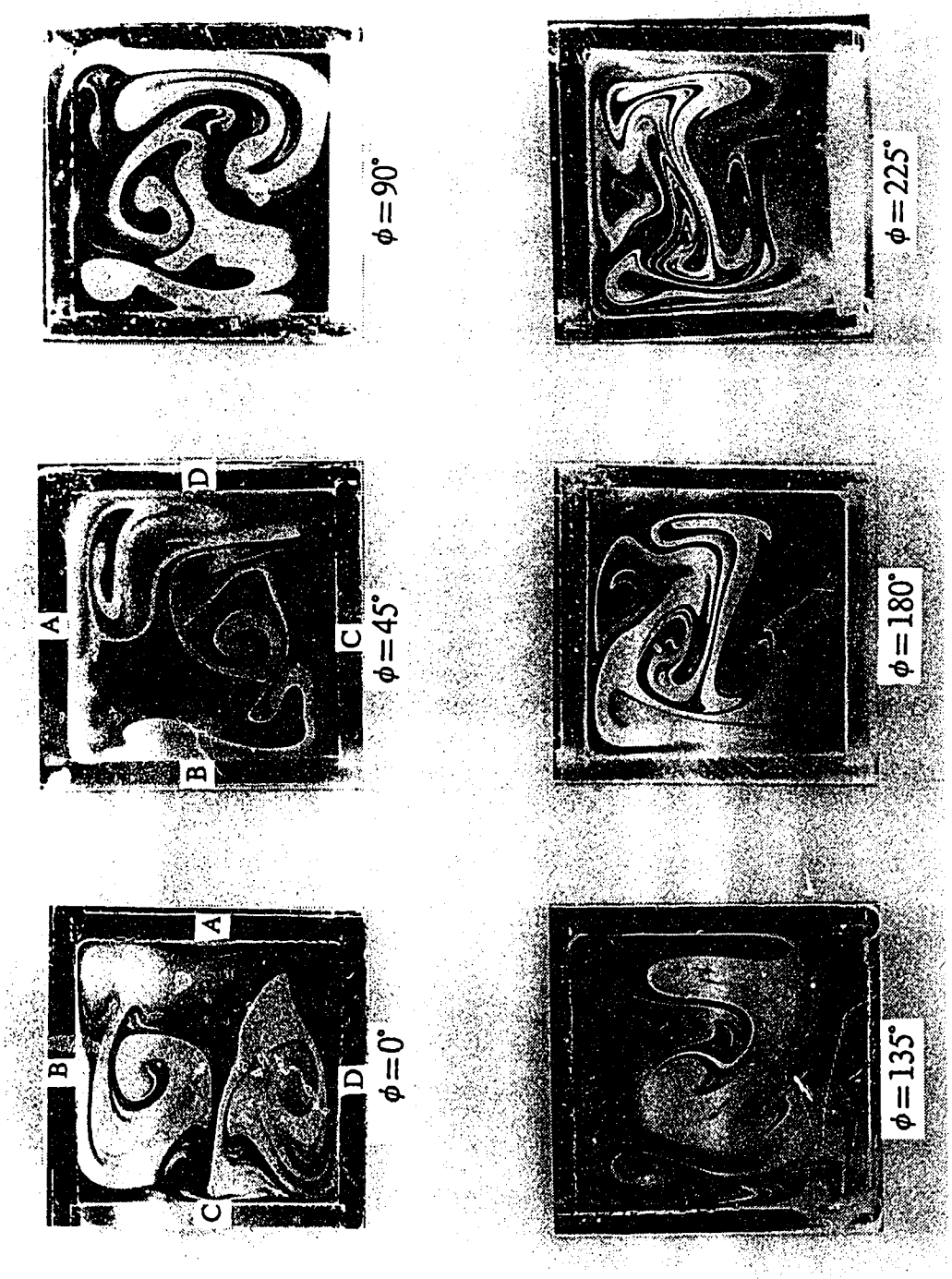

Fig. 2.105 Developing secondary flow patterns in the second square bend with $a/R_c=0.4$, $\psi=180°$ and $\theta=90°$ at K=250

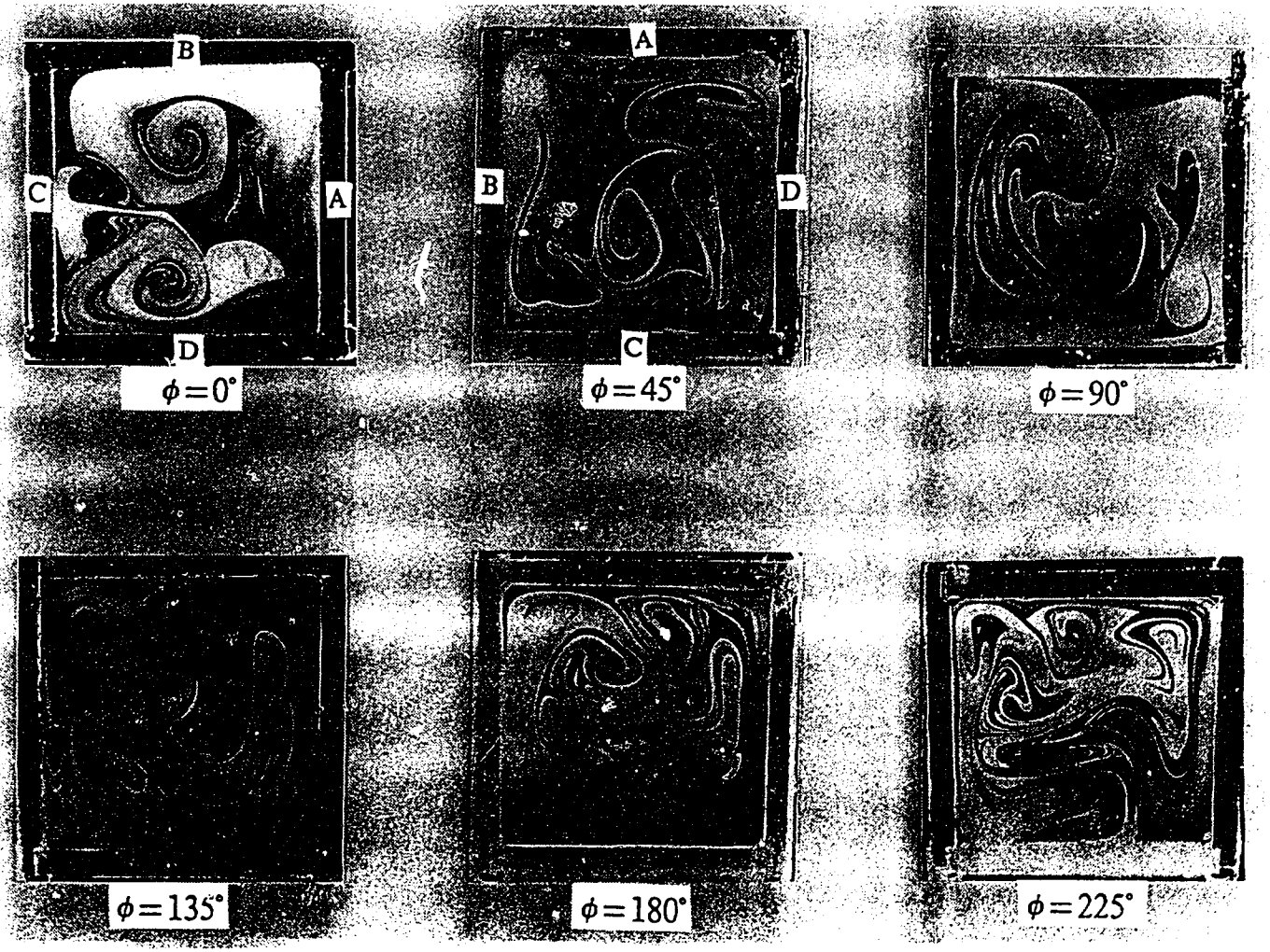

Fig. 2.106 Developing secondary flow patterns in the second square bend with $a/R_c=0.4$, $\psi=180°$ and $\theta=90°$ at K=300

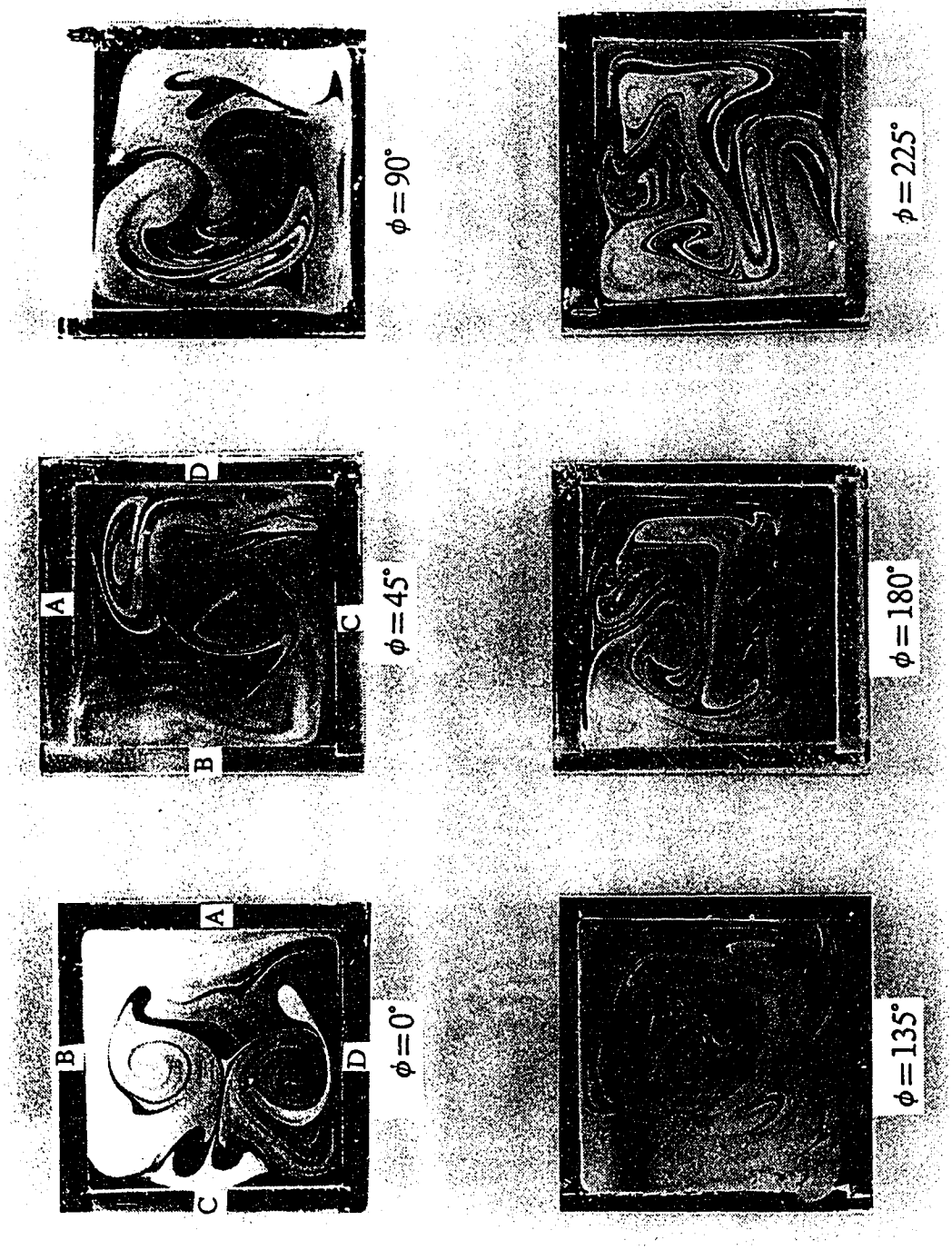

Fig. 2.107 Developing secondary flow patterns in the second square bend with $a/R_c=0.4$, $\psi=180°$ and $\theta=90°$ at K=350

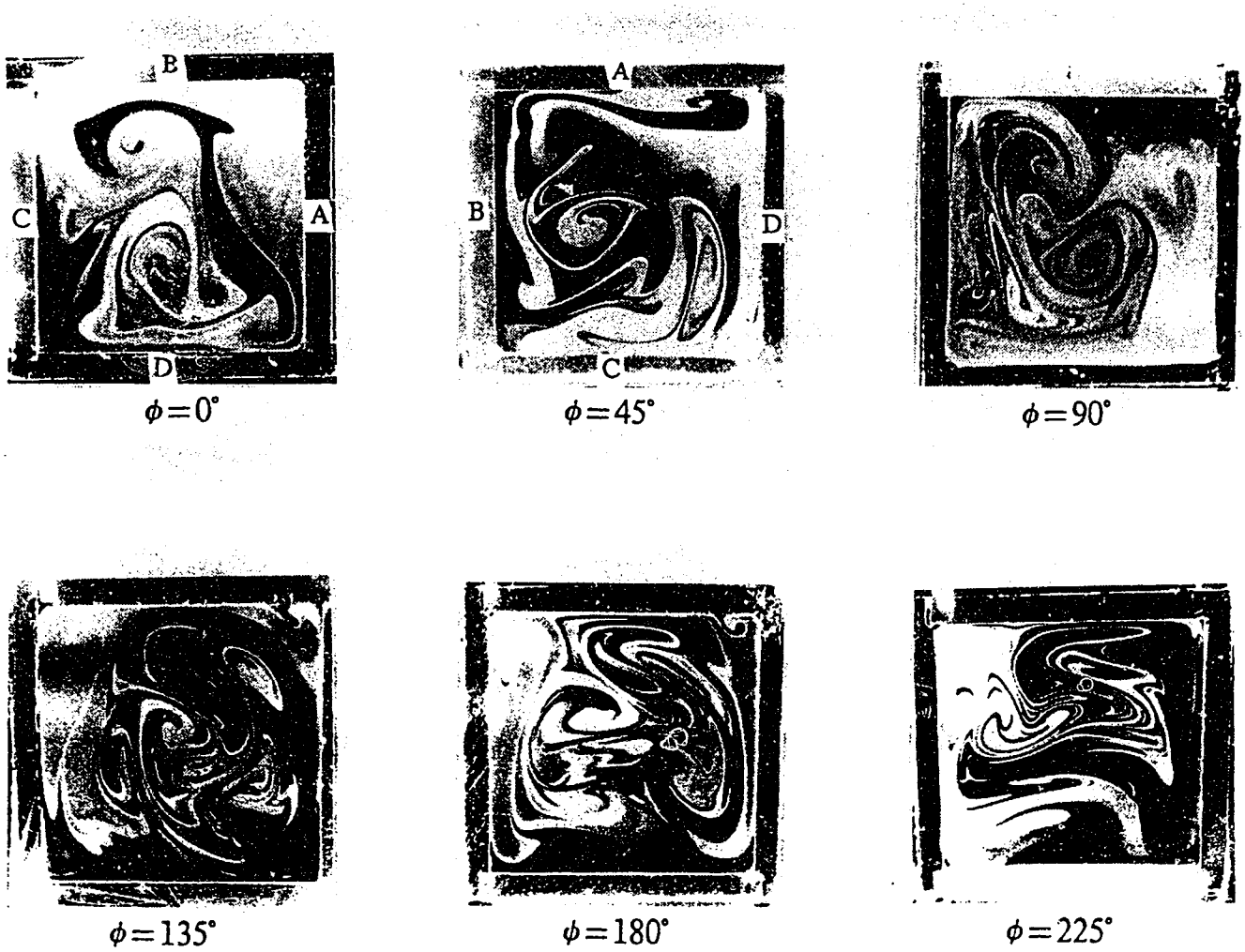

Fig. 2.108 Developing secondary flow patterns in the second square bend with $a/R_c=0.4$, $\psi=180°$ and $\theta=90°$ at K=400

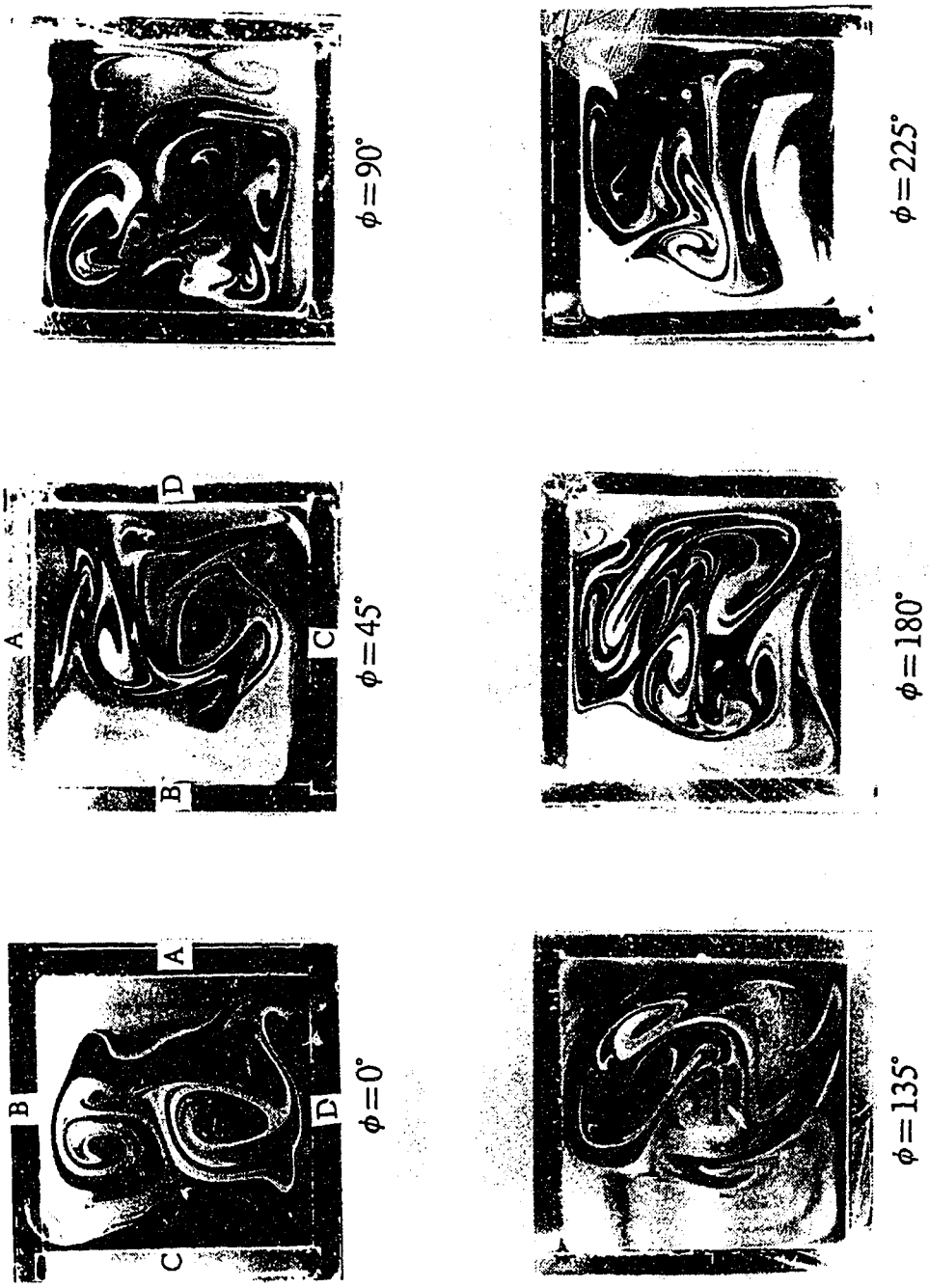

Fig. 2.109 Developing secondary flow patterns in the second square bend with $a/R_c=0.4$,$\psi=180°$ and $\theta=90°$ at K=450

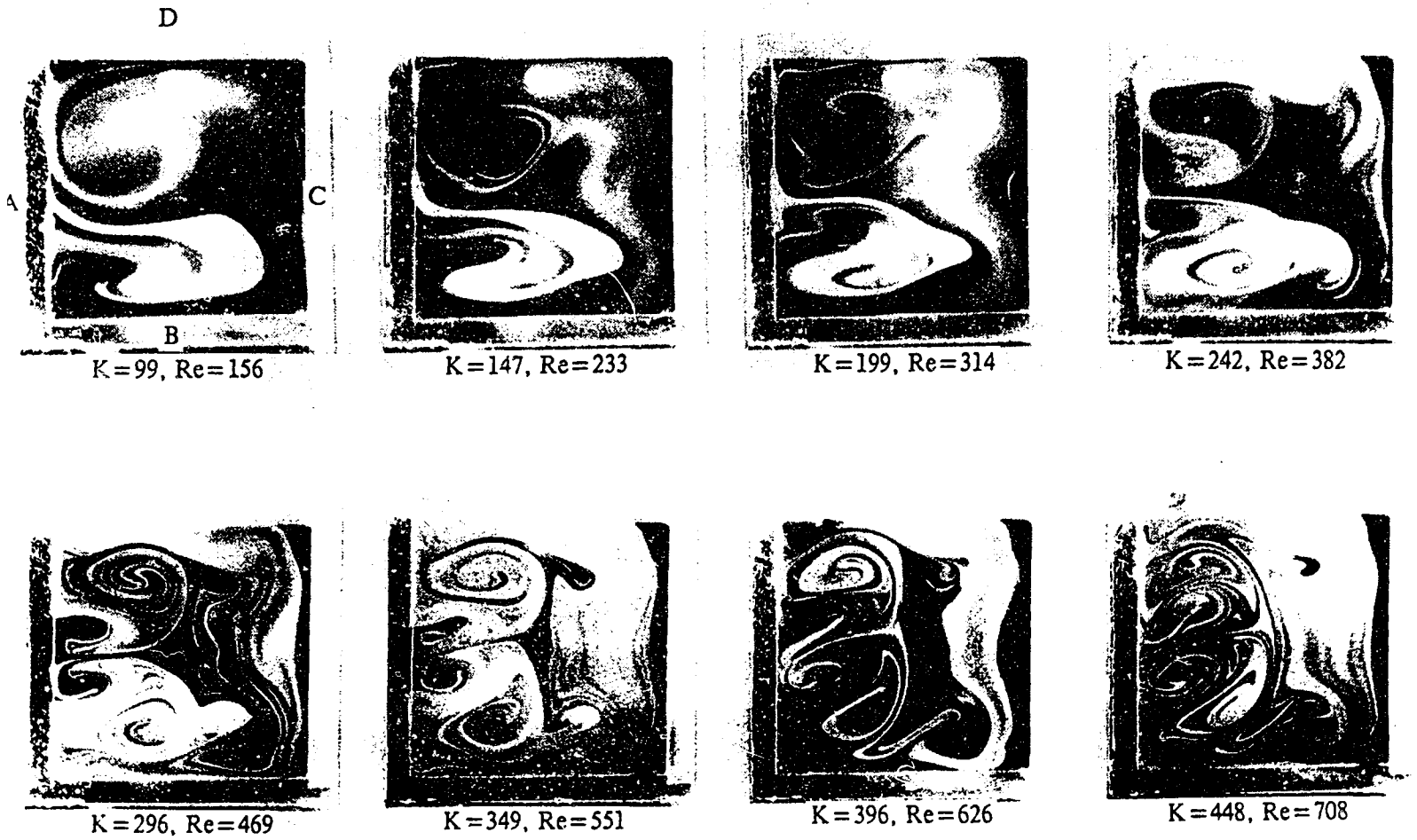

Fig. 2.110 The effect of Dean number on secondary flow patterns at the exit of a 45° second square bend with $a/R_c=0.4$, $\psi=180°$ and $\theta=180°$

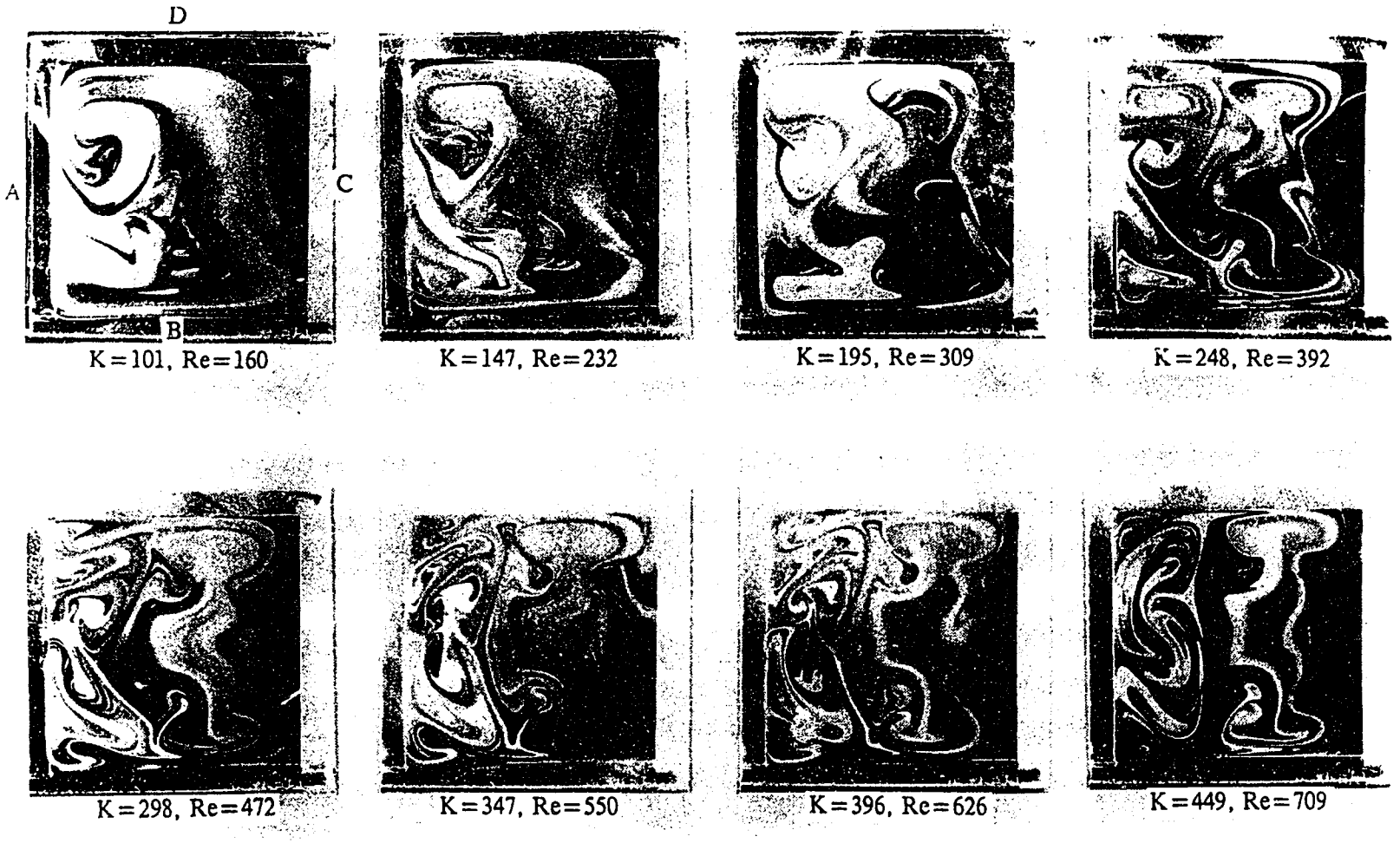

Fig. 2.111 The effect of Dean number on secondary flow patterns at the exit of a 90° second square bend with $a/R_c=0.4$, $\psi=180°$ and $\theta=180°$

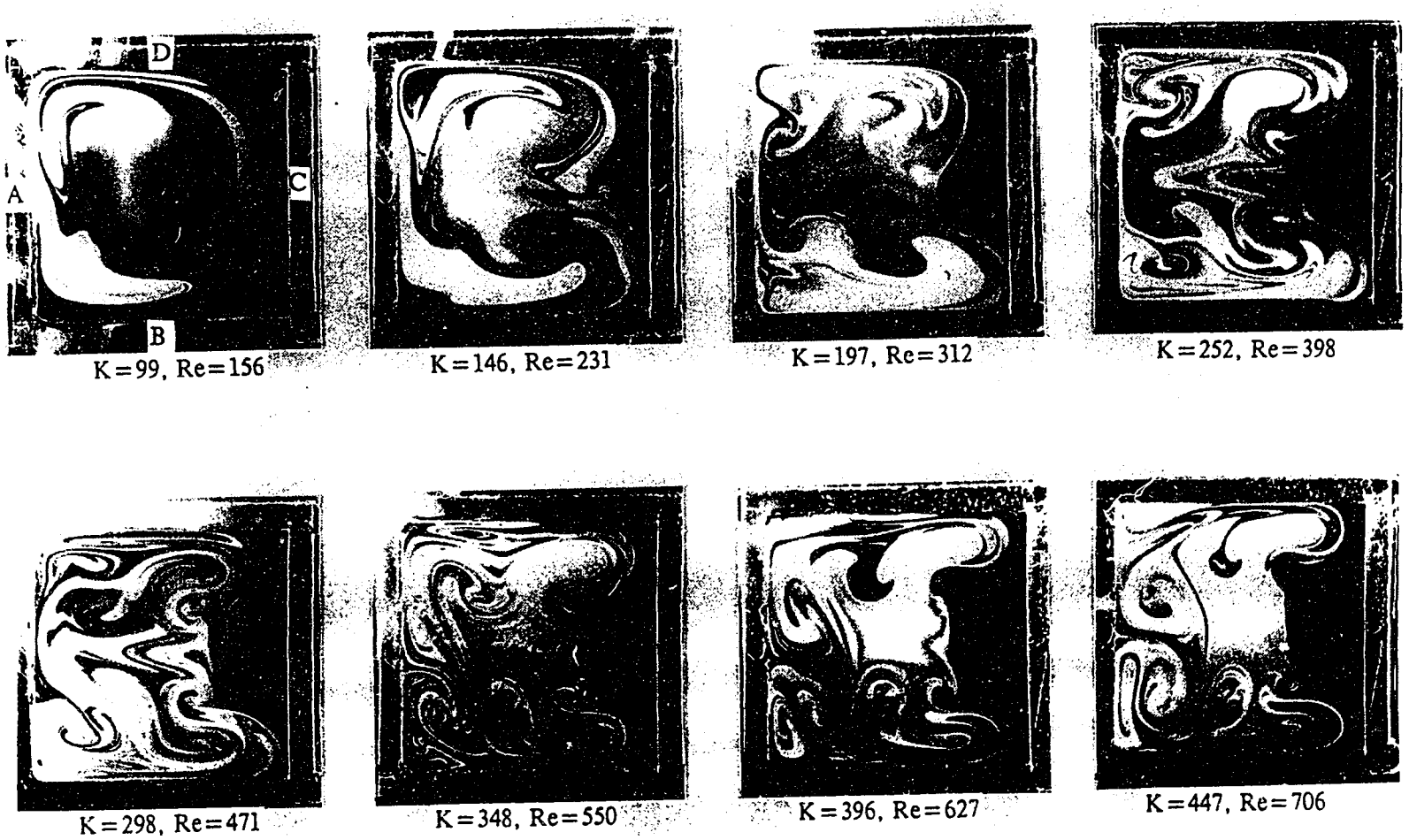

Fig. 2.112 The effect of Dean number on secondary flow patterns at the exit of a 135° second square bend with $a/R_c=0.4$, $\psi=180°$ and $\theta=180°$

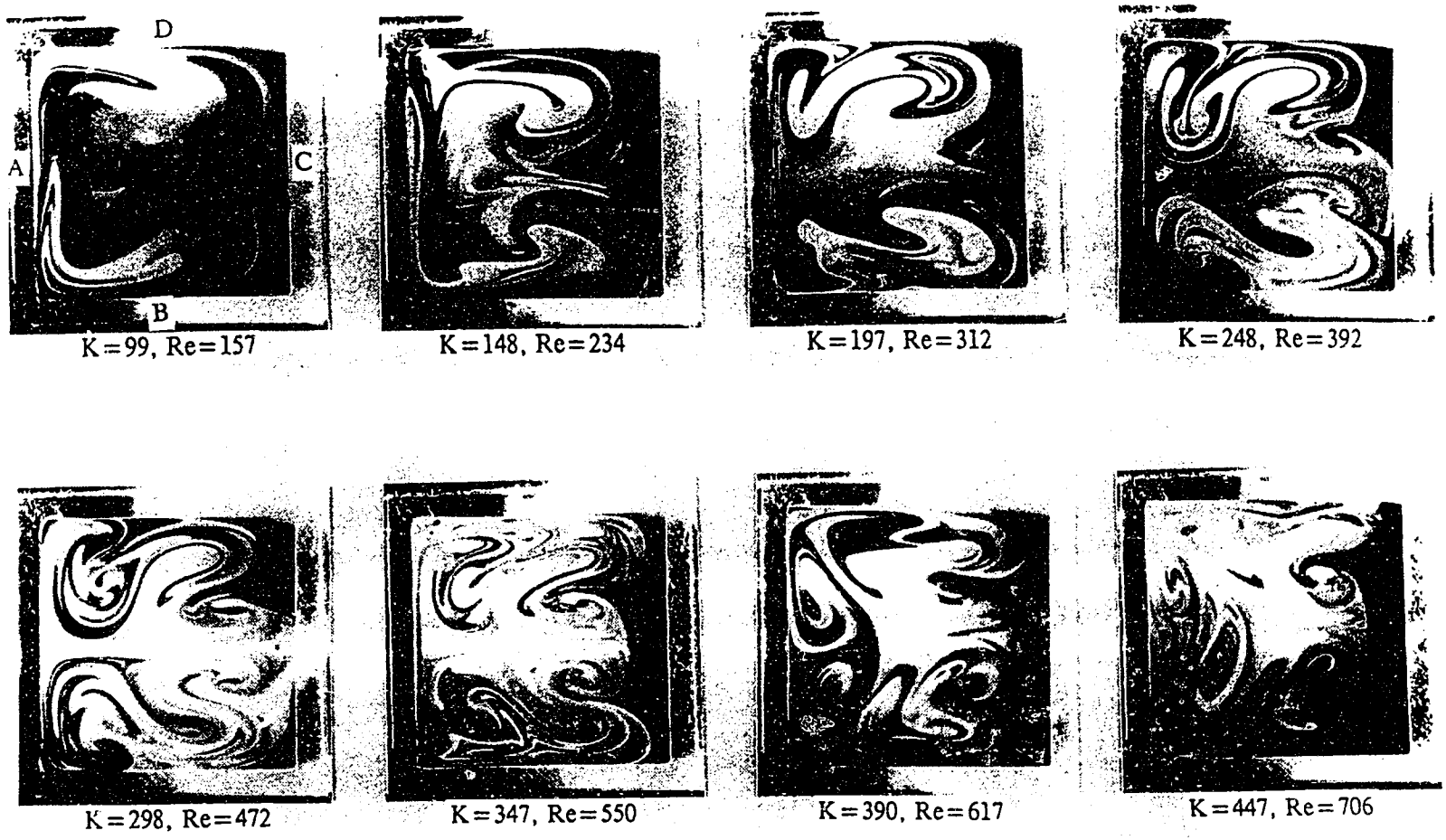

Fig. 2.113 The effect of Dean number on secondary flow patterns at the exit of a 180° second square bend with $a/R_c=0.4$, $\psi=180°$ and $\theta=180°$

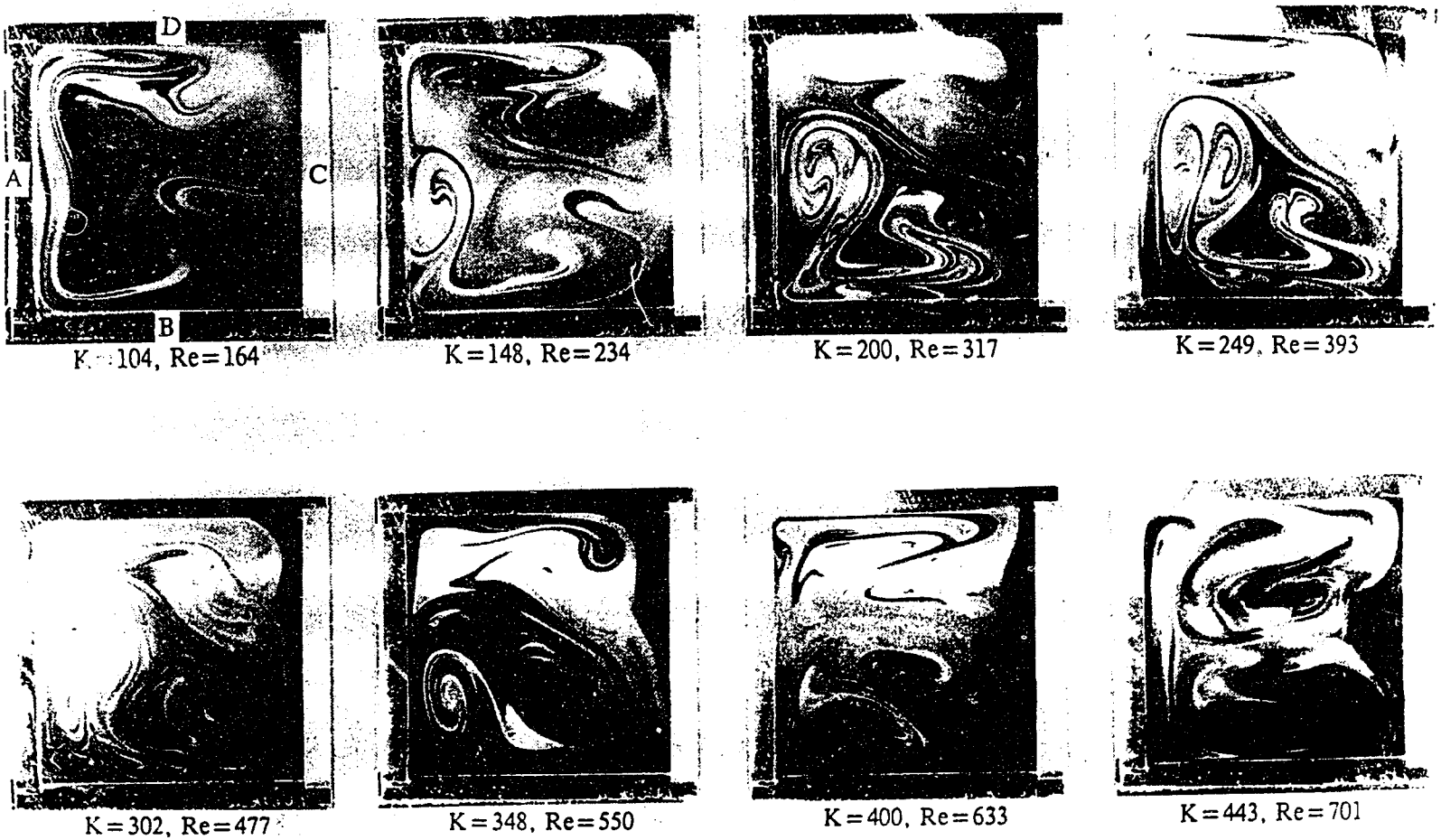

Fig. 2.114 The effect of Dean number on secondary flow patterns at the exit of a 225° second square bend with $a/R_c=0.4$, $\psi=180°$ and $\theta=180°$

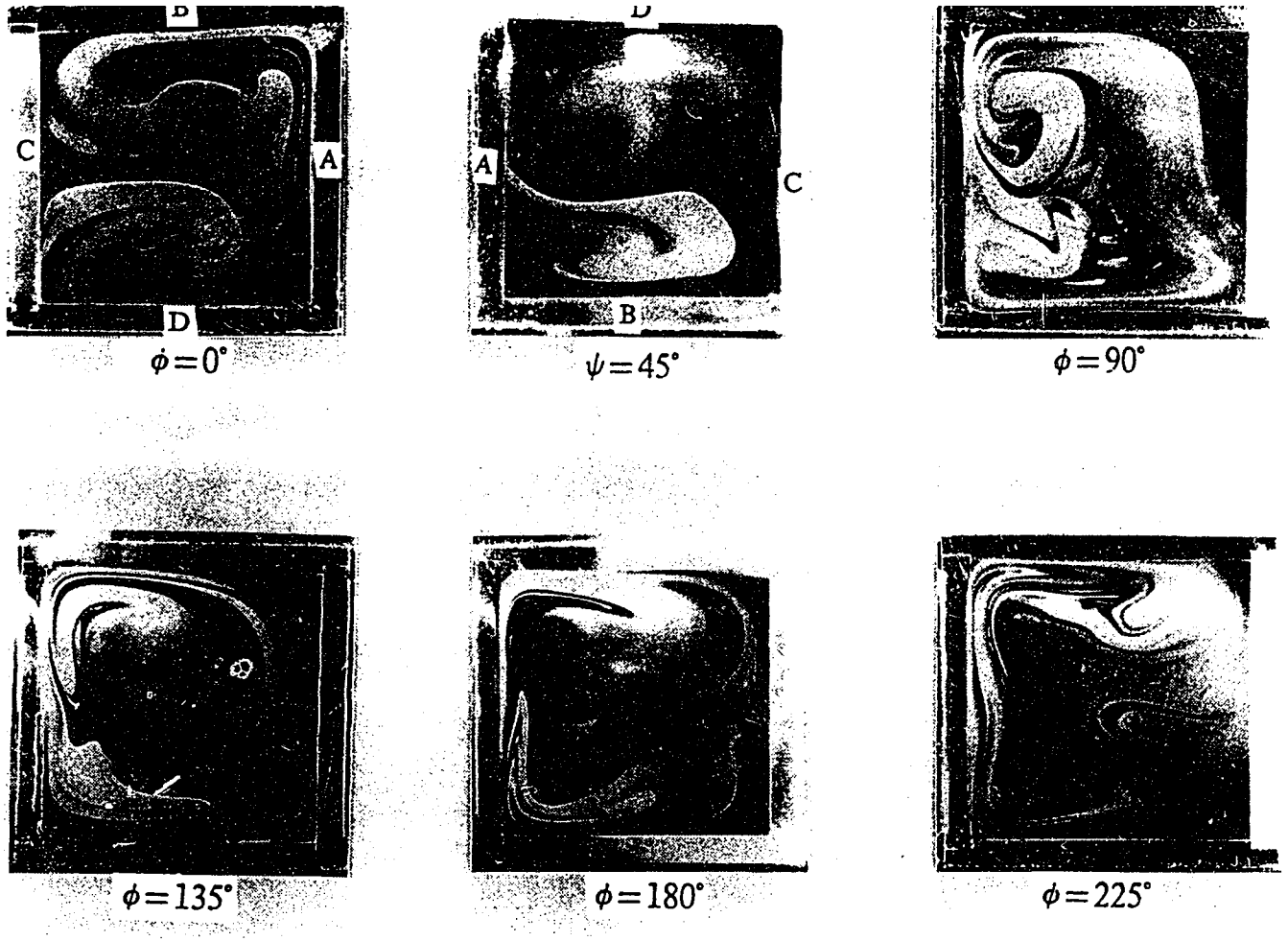

Fig. 2.115 Developing secondary flow patterns in the second square bend with $a/R_c=0.4$, $\psi=180°$ and $\theta=180°$ at $K=100$

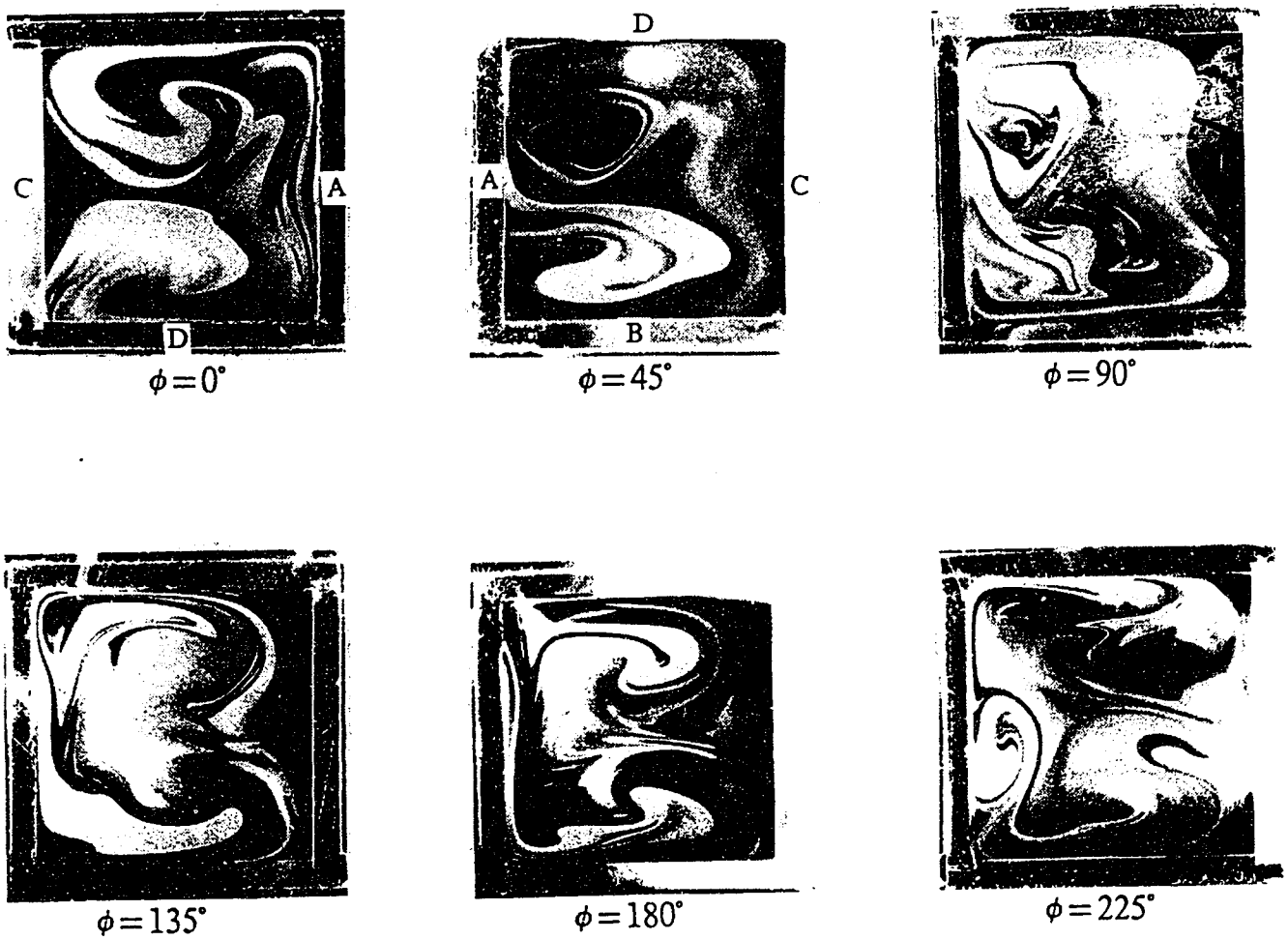

Fig. 2.116 Developing secondary flow patterns in the second square bend with $a/R_c=0.4$, $\psi=180°$ and $\theta=180°$ at K=150

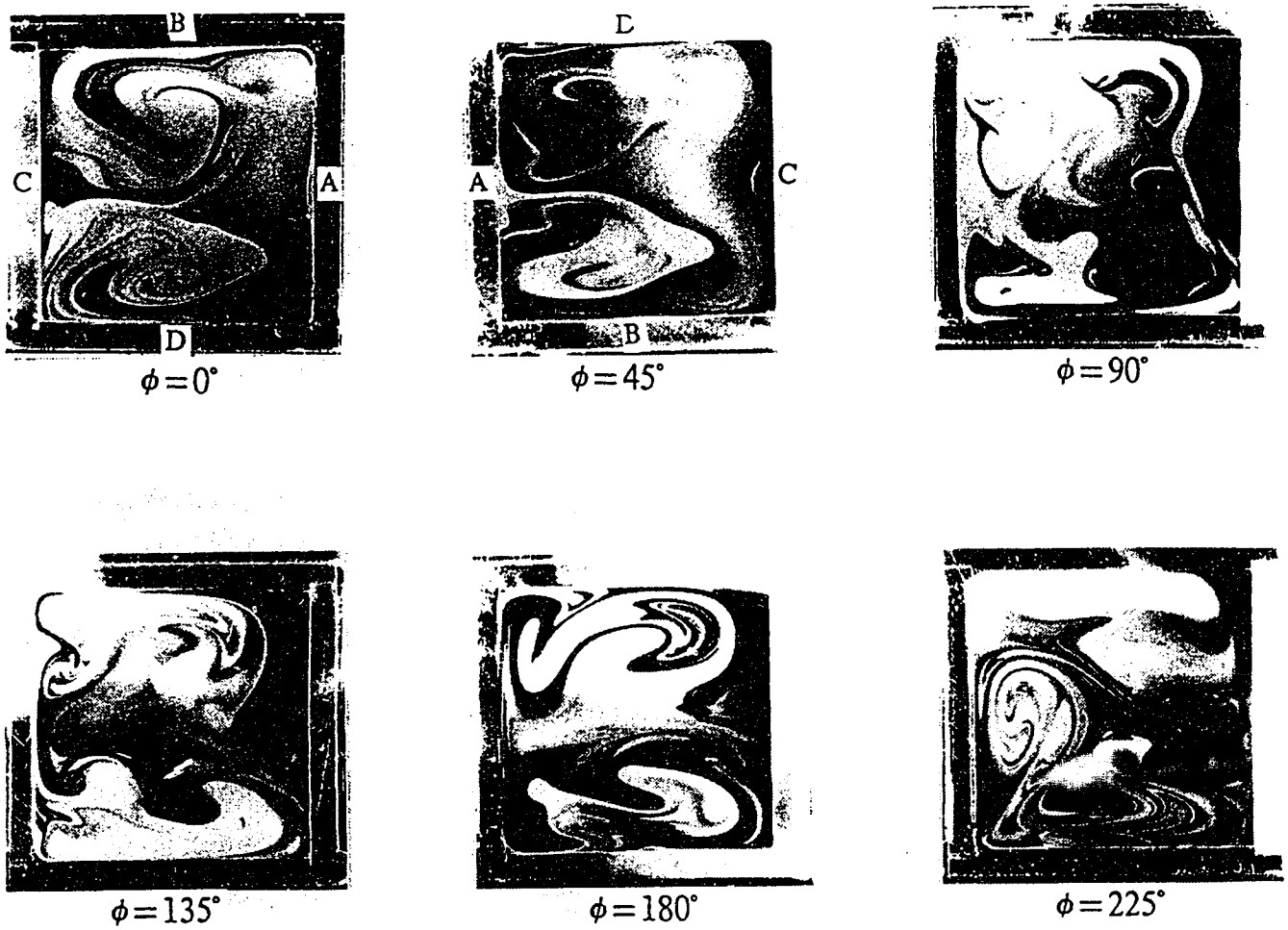

Fig. 2.117 Developing secondary flow patterns in the second square bend with $a/R_c=0.4$, $\psi=180°$ and $\theta=180°$ at K=200

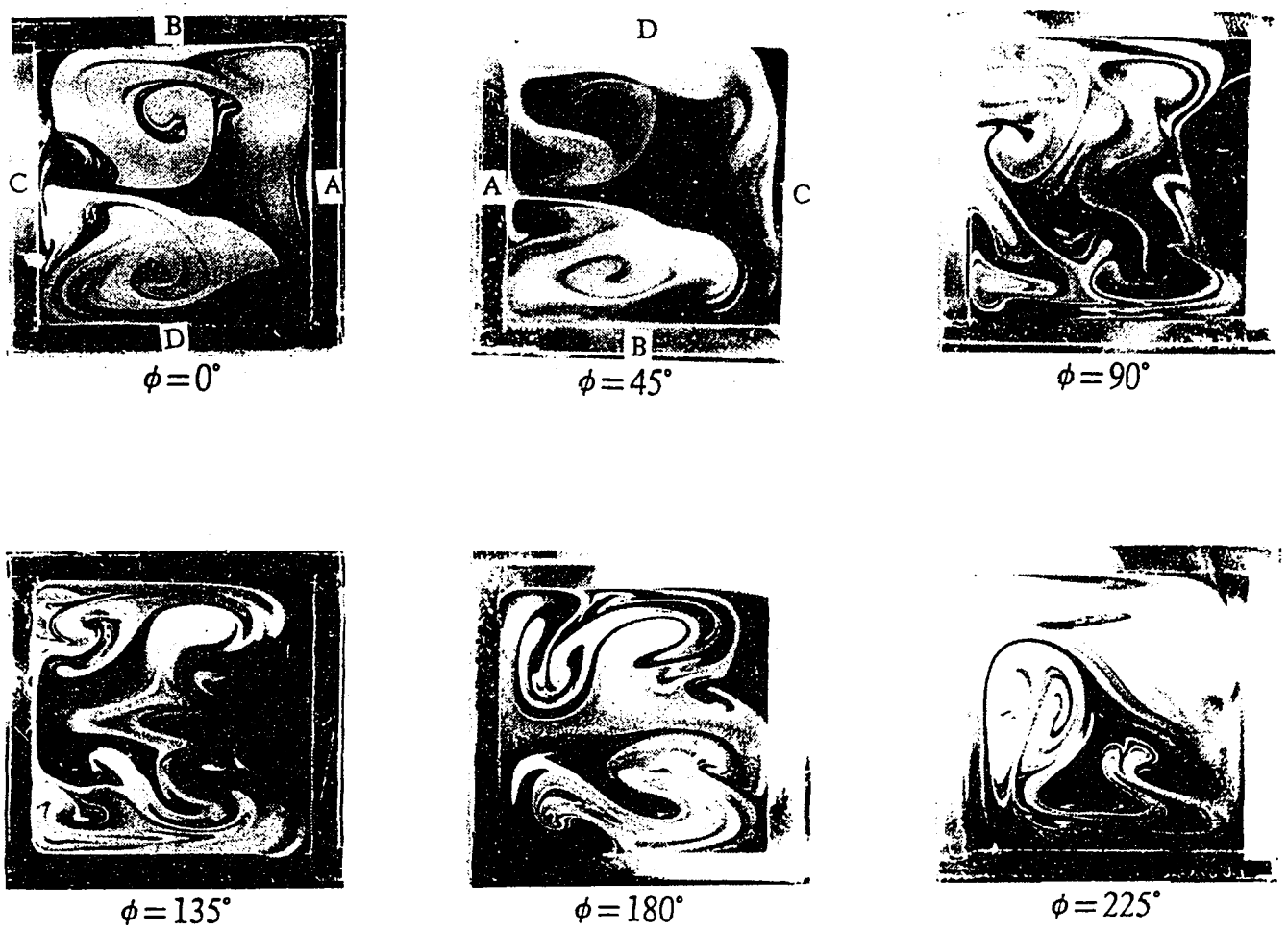

Fig. 2.118 Developing secondary flow patterns in the second square bend with $a/R_c=0.4$, $\psi=180°$ and $\theta=180°$ at $K=250$

Fig. 2.119 Developing secondary flow patterns in the second square bend with $a/R_c=0.4$, $\psi=180°$ and $\theta=180°$ at K=300

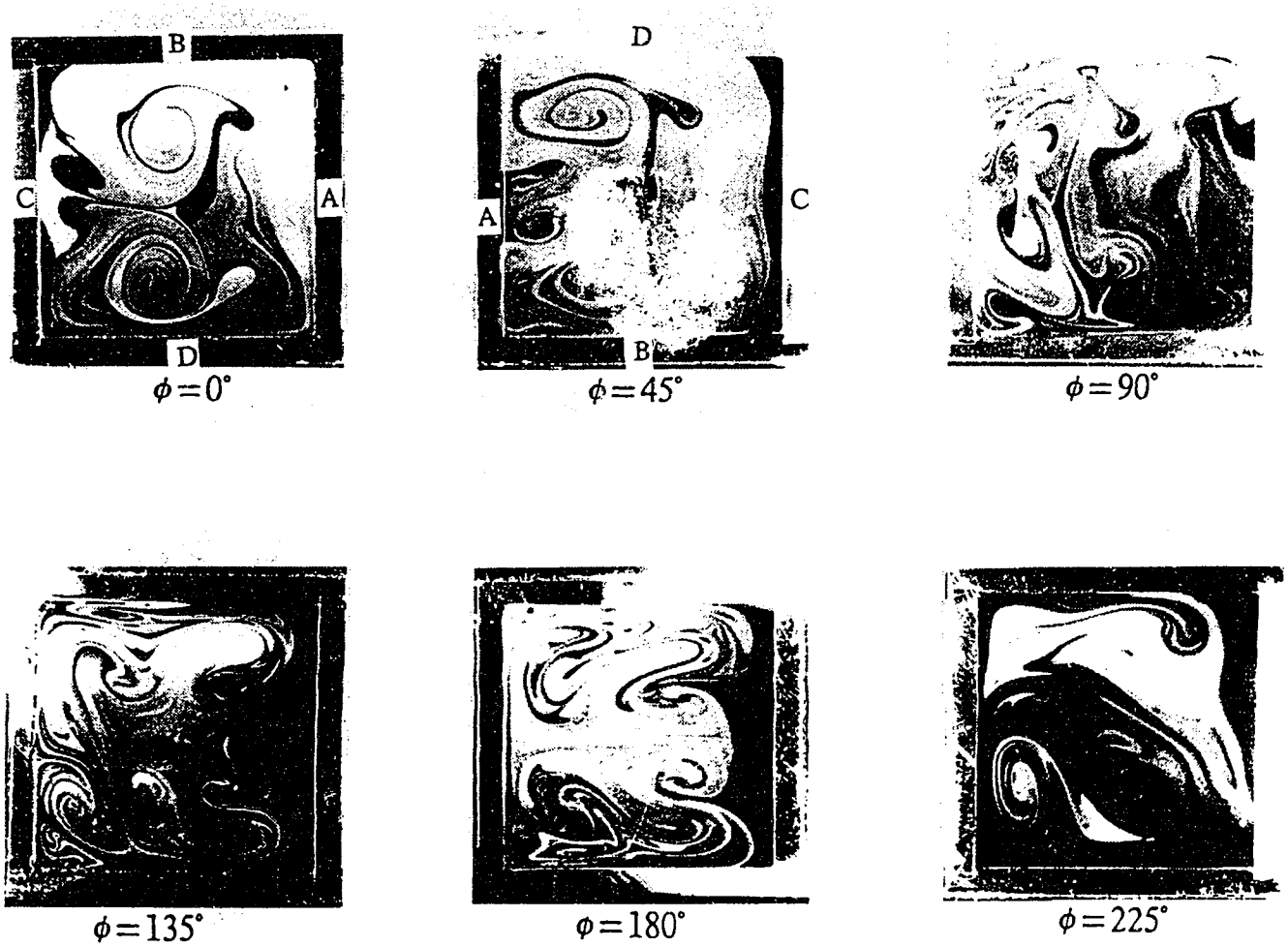

Fig. 2.120 Developing secondary flow patterns in the second square bend with $a/R_c=0.4$, $\psi=180°$ and $\theta=180°$ at K=350

Fig. 2.121 Developing secondary flow patterns in the second square bend with $a/R_c=0.4$, $\psi=180°$ and $\theta=180°$ at $K=400$

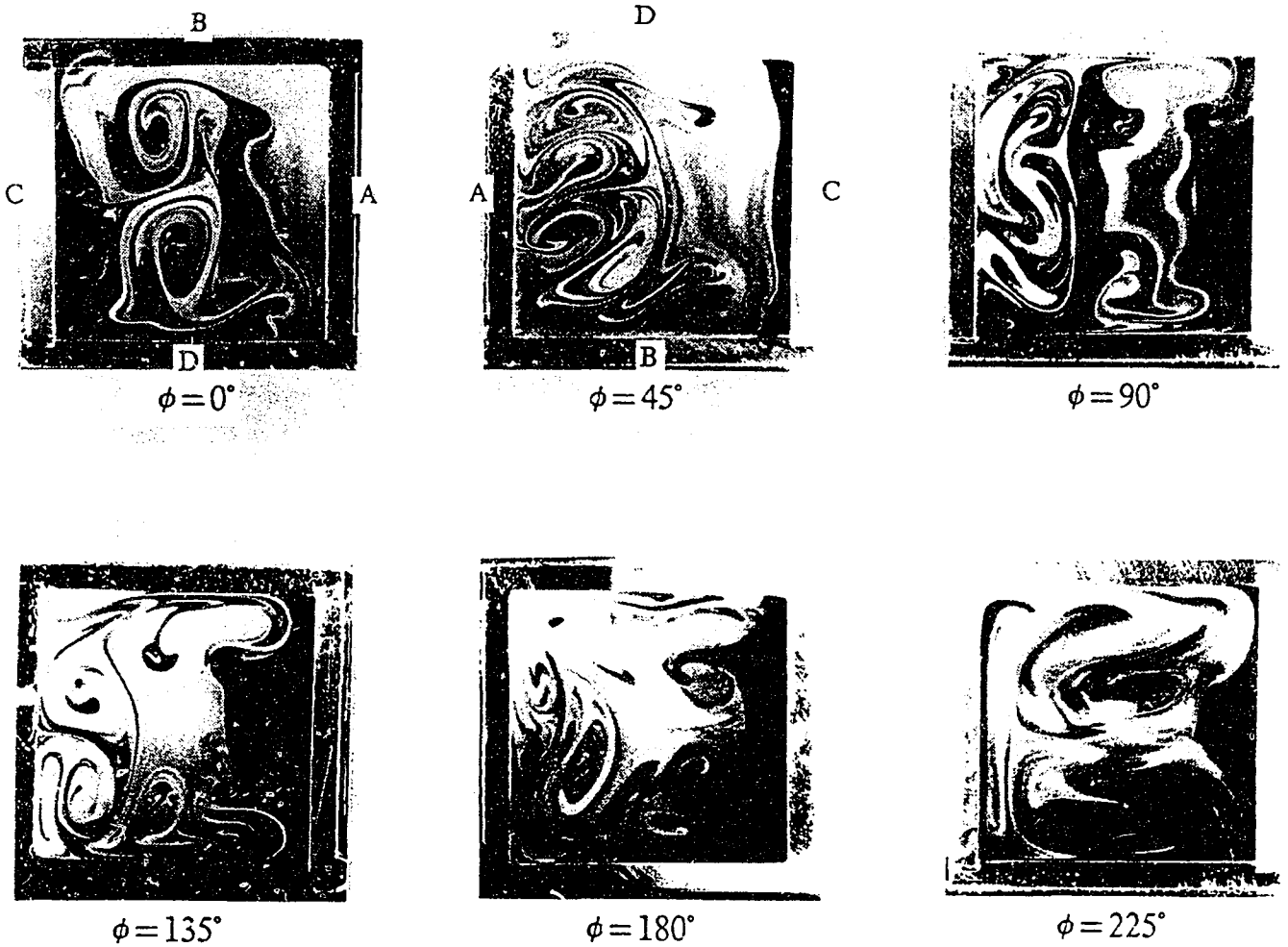

Fig. 2.122 Developing secondary flow patterns in the second square bend with $a/R_c=0.4$, $\psi=180°$ and $\theta=180°$ at K=450

3. Measurements of Developing Axial Velocity Profiles for Laminar Flow in the Entrance Region of S-bends

3.1 Introduction

The secondary flow caused by centrifugal forces in curved channels has been studied by many investigators because of its importance in engineering applications and fluid mechanics. After the publication of Dean's pioneer work in 1927, 1928 [1,2] on fully developed laminar flow in curved pipes, many theoretical and experimental investigations have been carried out in this area.

Dean showed that the flow in curved pipes can be characterized by a simple dimensionless parameter, Dean number, $K=Re(a/R_c)^{1/2}$. It is also known that a secondary flow pattern in the form of a pair of symmetric vortices is the consequence of the centrifugal forces acting on the fluid in the direction of the radius of curvature. Generally speaking, the centrifugal forces induced by the curved flow passage tend to push the fluid in the core region toward the outer wall of the bend. The fluid near the outer wall moves back to the inner wall along the upper and lower wall surface since it is driven by the pressure gradient oriented to the inner wall at the region near the upper and lower walls. Such flow motion superimposed on the main axial flow results in a double helix type secondary flow motion which appears as a pair of symmetric counter-rotating vortices in cross-sectional view.

In consequence, the axial velocity profile will no longer be parabolic. The maximum velocity point moves toward the outer wall. Two local maximum velocity points appear near the upper wall and the lower wall on the vertical plane.

However, the centrifugal force increases and then decreases after reaching a maximum value along the horizontal axis in the direction toward the outer wall. Therefore, the region near the outer wall is potentially unstable and Dean's instability phenomenon [3] may occur. This centrifugal instability phenomenon in the form of an additional pair of vortices appearing near the center of the outer wall has been observed by flow visualization at Dean numbers about K=110 in square curved channels [4]. Similar results are also obtained by numerical calculation [5,6]. Hence, in fact, the secondary flow patterns and the axial velocity profiles are very complex. Further studies are still necessary for a comprehensive understanding of the instability phenomena.

Patankar, Pratap and Spalding [7] obtained the developing axial velocity profiles by solving parabolic Navier-Stokes equations. Humphrey, et al. [8] reported numerical calculation of flow in the entrance region of a square curved duct. Soh and Berger [9] showed the appearance of an additional weak vortex pair near the inner wall of a circular curved pipe in a developing region. Further numerical studies can be found in [10,11,12]. Austin and

Seader [13] published their experimental results for velocity profiles in the entrance region of curved circular pipes. The curved pipes they used were of four different curvature ratios, namely a/R_C=0.034, 0.069, 0.111, 0.144, and the range of Dean number was from 198 to 948. Bovendeerd, et al. [14] reported their experimental results of axial and secondary velocity measurements by Laser-Doppler anemometer for the entry flow in a 90° circular cross-section bend with a curvature ratio a/R_C=1/6. In their study, Dean number was K=286, corresponding to Reynolds number about Re=700. Some other experimental investigations are presented in [15,16,17].

Literature review shows that few studies have been reported on the measurements of developing velocity profiles for curved pipes of curvature ratio larger then a/R_C=0.1, especially for curved ducts with offset bends, which are often used in piping systems.

In order to further understand the phenomena of flow in curved ducts and in s-bends, the purpose of this chapter is to investigate the developing axial velocity profiles on vertical and horizontal planes in the entrance region of curved ducts with curvature ratio a/R_C=0.2 and 0.4. Attention was also given to the effects of curvature ratio and the effects of Dean number K on the velocity profiles. Velocity profiles were measured by a hot-film anemometer at the exit of curved pipes along horizontal axis and vertical axes.

The velocity measurement results and the comparison of these results with the photographs of secondary flow patterns in Chapter 2 are helpful for understanding the flow in curved pipes, especially in s-bends. These results are also believed to be useful for future numerical studies.

3.2 Experimental Apparatus and Procedure

3.2.1 General Description of Test Setup

The schematic diagram of test setup is shown in Fig. 3.1. Some of the experimental apparatuses are identical to what was used in the experiments of Chapter Two, and a detailed description of these apparatuses is given in section 2.2.1 of Chapter Two. For the velocity measurements, smoke is not needed. So air flow was not split into two circuits. A constant temperature hot-film anemometer (Thermo-System Inc., CTA model 1050) with a single hot-film sensor (TSI, model 1210) was used to measure the axial velocity profiles. A traversing mechanism with 0.1 mm resolution was used to position a hot-film support. The possible error of the hot-film sensor's position was less then 0.1 mm.

The schematic diagram of the test section is shown in Fig. 3.2. The secondary bend was connected to a 180° first bend. The offset angle was 180° so the first bend and the secondary bend were on the same horizontal plane.

Fig. 3.3 shows the exit of test section and the coordinate system. The origin is at the center of the pipe. The y-axis is vertical directed toward the upper wall, and the x-axis is horizontal directed toward the outer wall.

The experiments were made for the following four cases:

Case (1) circular bend, $a/R_c=0.2$, K=350

Case (2) circular bend, $a/R_c=0.2$, K=200

Case (3) square bend, $a/R_c=0.2$, K=350

Case (4) square bend, $a/R_c=0.4$. K=350

3.2.2 Calibration of the Hot-film Sensor

The single hot-film sensor (TSI, model 1210) for the constant temperature hot-film anemometer was calibrated against the Merian laminar flow meter. Fig. 3.4 shows the schematic diagram of the hot-film sensor. It is well known that for fully developed laminar flow, the maximum axial velocities for a circular pipe and square duct are $U_o=2U_m$ and $U_o=1.94U_m$, respectively. The value, 1.94, was calculated from the equations (5.110) and (5.111) in [18].

The hot-film sensor was set at the center of the exit of the straight entrance pipe, because the local velocity at the center is also the maximum velocity. The mean velocity in the pipe was changed from 0.05 m/sec. to 0.5 m/sec. and, at the same time, the mean velocities and the output voltages of the anemometer were recorded.

The output voltages of the anemometer depend on the cleanliness of the hot-film surface and the air flow

temperture. But the ratios of the output voltages E to a reference output voltage E_r remain constant. At a proper mean velocity corresponding to K=350, the hot-sensor was located at the center of the straight pipes, the outputs of the anemometer were taken as the E_r for Cases (1), (3), (4), respectively. While for Case (2), E_r was the output at a proper mean velocity corresponding to K=200. In this way, four sets of non-dimensional output voltages E/E_r were obtained. Then, the calibration curve could be obtained with non-dimensional output voltage E/E_r versus local velocity U. The calibration curves are shown in from Figs. 3.5 to 3.8, and the calibration equations are listed in Table 3.1.

Table 3.1 Calibration Results

Case (1):	
$0.012 \le E/E_r < 0.04$	$U=0.375\times(E/E_r)^{0.327}$
$0.04 \le E/E_r < 0.15$	$U=0.445\times(E/E_r)^{0.384}$
$0.15 \le E/E_r < 2.00$	$U=0.524\times(E/E_r)^{0.472}$
Case (2):	
$0.01 \le E/E_r < 0.15$	$U=0.238\times(E/E_r)^{0.315}$
$0.15 \le E/E_r < 0.80$	$U=0.284\times(E/E_r)^{0.407}$
$0.80 \le E/E_r < 4.00$	$U=0.289\times(E/E_r)^{0.477}$

Case (3):

$0.013 \le E/E_r < 0.035$ $\quad U=0.304\times(E/E_r)^{0.296}$

$0.035 \le E/E_r < 0.10$ $\quad U=0.393\times(E/E_r)^{0.374}$

$0.10 \le E/E_r < 0.40$ $\quad U=0.462\times(E/E_r)^{0.445}$

$0.40 \le E/E_r < 1.70$ $\quad U=0.477\times(E/E_r)^{0.479}$

Case (4):

$0.015 \le E/E_r < 0.09$ $\quad U=0.263\times(E/E_r)^{0.320}$

$0.09 \le E/E_r < 0.40$ $\quad U=0.318\times(E/E_r)^{0.399}$

$0.40 \le E/E_r < 3.50$ $\quad U=0.339\times(E/E_r)^{0.471}$

The largest error of these equations is less than 2%.

3.2.3 Velocity Measurement

The hot-film anemometer was given 60 minutes warmup time before measurement started. The flow rate was set at the value corresponding to the desired Dean number. The hot-film sensor was located at the center of the exit of the straight entrance pipe in order to record the anemometer output voltages before and after the measurements for each configuration. The difference between these two voltages obtained before and after experiments for each configuration was less then 1.0%, and the mean value was used as the reference output voltage.

For each test configuration, axial velocity profiles were measured at the exit along the x-axis (horizontal axis) and y-axis (vertical axis), with an interval of 1 mm. The

hot-film sensor was set on the plane of bend exit and perpendicular to the axis long which velocity profiles were measured. In order to reduce the effect of the motion of adjacent room air, a short extension paper cover (about 6 cm long) was attached to the exit of each test section as shown in Fig. 3.9. A schematic diagram of hot-film anemometer measurement system is shown in Fig. 3.10.

3.3 Experimental Parameters

The ranges of the experimental parameters are given in Tables 3.2 and 3.3.

Table 3.2 Ranges of Experimental Parameters for Circular Bends

Curvature ratio, a/R_c	0.2
Reynolds number, Re	447, 783
Dean number, K	200, 350
First bend angle, ψ	45°, 90°, 135°, 180°
Second bend angle, ϕ	45°, 90°, 135°, 180°

Table 3.3 Ranges of Experimental Parameters for Square Bends

Curvature ratio, a/R_c	0.2, 0.4
Reynolds number, Re	783, 553
Dean number, K	350
First bend angle, ψ	45°, 90°, 135°, 180°
Second bend angle, ϕ	90°, 180°

3.4 Results and Discussion

3.4.1 Results for Circular Bends

The experimental results of the axial velocity profiles at the exit of a circular bend with different bend angles are shown in Figs. 3.11 to 3.28. Figs. 3.11 and 3.22 show the velocity profiles at the end of the straight entrance pipe with Re=783 and 447, respectively. As the flow is fully developed laminar flow, typical parabolic velocity profiles are obtained. Figs. 3.12 to 3.19, and Figs. 3.23 to 3.26 are the velocity profiles along vertical and horizontal axes. The velocity profiles along vertical and horizontal axes are plotted in one figure to give a better idea about the shapes of velocity profiles at the exit of each test section.

Figs. 3.20 and 3.21 show the development of axial velocity profiles along the horizontal and vertical axes for

the circular s-bend at K=350. The upper half is the velocity development in the first 180° bend, and the lower half is in the second 180° bend. The profiles at ψ=180° and at ϕ=0° are actually at the same position.

It is seen that, in Fig. 3.20, the initially parabolic profiles are already changed by ψ=45° and the maximum of axial velocity shifts toward the outer wall. But the shape of the curve adjacent to the maximum velocity point is rounder than that of the profiles further downstream and the maximum point is somewhat farther away from the outer wall than that of the downstream profiles. That means the intensity of secondary flow is under development. At ψ=90°, a severely depressed shape is observed in the core region and a second peak occurs. Because the profile is changing gradually, it is believed that a plateau-shaped profile in the core region should exist between ψ=45° and ψ=90°. Further downstream, the depressed shape is decaying, and the plateau-shaped profile is observed at ψ=135°. After these changes, the profile seems to approach the typical skewed profile of fully developed toroidal flow.

After the flow enters the second bend, the outer wall of the first bend becomes the inner wall of the second bend. Therefore, the maximum velocity point near the inner wall of the second bend ϕ=0° will shift toward the outer wall in the second bend. At ϕ=45°, it is seen that the velocity near the outer wall is becoming larger while the maximum velocity is shifting toward the outer wall. Also, a local maximum and a

local minimum are formed. Further downstream, the original maximum becomes smaller, and the maximum peak is decaying. At ϕ=90°, only a small peak is left and this peak disappears by ϕ=135°. In the mean time, the velocities in the outer wall region are becoming larger, but the front portion of the profiles are relatively flat compared with the profiles in the first bend. Also, they remain relatively flat to ϕ=180° and the maximum U/U_o is lower than that in the first bend.

In Fig. 3.21, it is seen that the entrance axial velocity profile along the vertical axis is essentially parabolic. At ψ=45°, because the maximum velocity shifts toward the outer wall, the secondary flow brings the fluid particles with larger axial momentum back to the inner wall along the upper and lower walls. In consequence, two peaks appear near the upper wall and the lower wall, forming an M-shape profile. In the center region of the profile at ψ=90°, another two local maximum points are observed. This kind of profile, called the four-wave shape, has not been reported by investigators in the past. This phenomenon is also due to secondary flow. The secondary flow brings the fluid particles with relatively larger axial momentum back to the inner wall along the upper and lower walls, and then pushes them toward the outer wall again through the center region. At ψ=135°, the profile becomes almost flat, and at ψ=180°, the M-shaped profile is observed again. This will be explained clearly when the secondary flow patterns obtained

by flow visualization are compared in the Section 3.4.3.

In the second bend, the velocity profiles become asymmetric. A distorted M-shape is obtained at φ=45°. At ϕ=90°, a similar four-wave-shape profile is also observed. Further downstream, the velocity profiles become almost flat again.

Fig. 3.27 compares developing axial velocity profiles along the horizontal axis in a circular s-bend for K=200 and K=350. At ψ=90°, for K=350, the profile is still changing while the profile for K=200 is approaching a fully developed one. In addition, the maximum velocity point for K=350 is nearer the outer wall than that for K=200. For larger Dean number flow, the centrifugal force effect is larger. So the centrifugal force can pushes the fluid particles with larger axial momentum to the region closer to the outer wall, and a longer distance is required for the secondary flow to become fully developed. In the second bend, it is noted that the velocity near the outer wall of the second bend becomes larger more rapidly for the case K=350 than the case K=200, because the centrifugal force is larger for the case K=350 than that of the case K=200. Therefor, the fluid particles with large axial momentum shift to the outer wall of the second bend faster for the case K=350 than the case K=200.

A comparison of developing axial velocity profiles along the vertical axis for K=200 and K=350 is shown in Fig. 3.28. The four-wave-shape profile is not observed for the case K=200 at ψ=90° and ϕ=90°. However, the profile is

deeply depressed at ψ=90° for the case K=200 and appear in an M-shape. At ψ=180°, the profile for K=200 is flatter than that for K=350 and the depressed portion appears at r/a≈0.3 instead of the center.

3.4.2 Results for Square Bends

The measurement results of axial velocity profile for square bends are shown in Figs. 3.29 to 3.44. The velocity profiles at the end of the straight entrance pipe are shown in Figs. 3.29 and 3.38 for Re=783 and Re=553. The theoretical profile is calculated according to the equation in [18]. The axial velocity profiles along the vertical axis and the horizontal axis at each angular position for a/R_c=0.2 and a/R_c=0.4 are shown in Figs. 3.30 to 3.35 and in Figs. 3.39 to 3.42, respectively.

Figs. 3.36 and 3.37 show the developing axial velocity profiles along the horizontal and vertical axes in a 180° bend with a/R_c=0.2. The velocity profiles along horizontal axis are similar to the profiles in circular bends. However, the severely depressed shape is not observed at ψ=90°. The profiles along the vertical axis are quite different from the profiles in circular bends. Instead of an M-shape, the profile is almost flat at ψ=45°. A dramatic change is observed at ψ=90°. The center portion of this profile is deeply depressed, and the depressed part is also relatively flat. Then, the velocity profile becomes flat again. Only two small peaks are observed near the upper wall and lower

wall for the profile at ψ=135°, and a weak wave appears in the center region of the profile at ψ=180°.

The effects of curvature ratio on velocity profiles are shown in Figs 3.43 and 3.44. The developing velocity profiles in an s-bend for Case (3) and Case (4) are compared with each other. Fig. 3.43 shows the profiles measured along the horizontal axis, and Fig. 3.44 shows the profiles along the vertical axis. In the first bend, for a/R_c=0.4 at ψ=90°, the velocities in the center region are very low, $U/U_0 \approx 0.25$, and become very high at ϕ=90° in the second bend. At ϕ=180° in the second bend, the velocity in the outer wall region develops faster for the case with larger curvature ratio. In addition, for the case with larger curvature ratio, it is noted that velocity is less stable than that of the case with smaller curvature ratio. This is because the flow separation near the inner wall is more severe for the case with larger curvature ratio.

3.4.3 Effects of the Secondary Flow

The axial velocity profiles of flow in curved pipes are maily affected by the secondary flow. Fig. 3.45 shows some of these effects. In Fig. 3.45, it is seen that, at ψ=45°, the secondary flow is not very strong. It seems that the fluid particles coming from the outer wall are kept moving in the region near the upper wall and the lower wall. Thus, along the vertical axis, the high velocity appears in the upper wall and lower wall regions forming the so-called

M-shape profile.

At ψ=90°, it is seen that the secondary flow vortex carries the fluid particles with high axial momentum forward and backward through the vertical axis, resulting in the four-wave-shape profile. But the vortex does reach the center region. Therefore, the axial velocity at the center is still low, and a profile severely depressed at the center along the vertical axis is observed.

At ψ=135°, the fluid particles with larger axial momentum are circling around in the region near the vertical axis. So the profile along the vertical axis is relatively flat. Further downstream, the secondary flow vortex pair moves toward the upper wall and the lower wall and it seems that the vortices do not reach the center part of the horizontal axis. Thus, the M-shape profile is observed again along the vertical axis. In the second bend, the symmetry of the flow pattern is destroyed so the velocity profiles along vertical axis become asymmetric.

3.5 Concluding Remarks

Developing axial velocity profiles were measured by hot-film anemometer with a single hot-film sensor along vertical and horizontal axes at different bend angles for circular s-bends with a/R_c=0.2, K=200, 350, and for square s-bends with a/R_c=0.2, 0.4, K=350, both at the exit of each bend with different bend angles. Developing velocity profiles are presented for each case. The effects of

secondary flow on the axial velocity profiles are discussed. Attention is also given to the effects of Dean number and the effects of curvature ratio on the axial velocity profiles.

It is noted that there exist some typical shapes for the developing axial velocity profiles of flow in curved pipes. In the present study, for flow in the first bend, there are three kinds of profiles which are measured along the vertical and the horizontal axes. For velocity profiles measured along the vertical axis, an M-shape profile, a flat-front-shape profile and a four-wave shape profile are observed. For velocity profiles measured along the horizontal axis, three typical shapes are also found. The first is the shape where velocity increases gradually from the inner wall to a maximum point near the outer wall. The second is the one depressed in the center region and the third has a flat plateau at the center.

In the second bend, velocity profiles become more complex. Along the vertical axis, three skewed typical shapes of the first bend can be observed. However, the maximum velocity may appear in the center region and profiles are not symmetric.

It seems that effects of Dean number (K=200, 350) and curvature ratio (a/R_c=0.2, 0.4) on the basic developing velocity profiles are small. For larger Dean number flow, the maximum velocity point along the horizontal axis is closer to the outer wall. For the flow in bends with larger

curvature ratio, velocity may become unstable because of the flow separation at the inner wall.

The present study of axial velocity profiles measured by a hot-film anemometer with a single hot-film sensor along vertical and horizontal axes provides physical insights into the flow in s-bends. It is believed that the present velocity profiles will be useful for comparison with those from numerical solutions in the future.

3.6 References

1. Dean, W.R., "Note on the Motion of Fluid in a Curved Pipe", Phil. Mag. 4, 1927, pp. 208-223.

2. Dean, W.R., "The Stream-line Motion of Fluid in a Curved Pipe", Phil. Mag. 5, 1928, pp. 673-695.

3. Dean, W.R., "Fluid Motion in a Curved Channel", Proc. Roy. Soc. London, Vol. 121A, 1928, pp. 402-420.

4. Cheng, K.C., Nakayama, J and Akiyama, M., " Effect of Finite and Infinite Aspect Ratios on Flow Patterns in Curved Rectangular Channels", Flow Visualization(Tokyo, Japan, 1977), Hemisphere Pub. Corp., 1979, pp. 181-186.

5. Masliyah, J.H., "On Laminar Flow in Curved Semi-circular Ducts", J. Fluid Mech., Vol. 99, 1980, pp. 469-479.

6. Nandakumar, K. and Masliyah, J.H., "Bifurcation in Steady Laminar Flow Through Curved Tubes", J. Fluid Mech., Vol. 119, 1982, pp. 475-490.

7. Patankar, S.V., Pratap, V.S. and Spalding, D.B., "Prediction of Laminar Flow and Heat Transfer in Helically Coiled Pipes", J. Fluid Mech., 1974, 62, pp. 539-551.

8. Humphrey, J.A.C., Taylor, A.M.K., Whitelaw, J.H., "Laminar Flow in a Square Duct of Strong Curvature", J. Fluid Mech., 1977, Vol. 103, pp. 50[illegible]-527.

9. Soh, W.Y. and Berger, S.A., "Laminar Entrance Flow in a Curved Pipe", J. Fluid Mech., 1984, Vol. 148, pp. 109-135.

10. Dennis, S.C.R. and Ng, M., "Dual Solution for Steady Laminar Flow Through a Curved Tube", Q. J. Mech. Appl. Maths., 1982, Vol. 35, pp. 305-324.

11. Soh, W.Y. and Berger, S.A., 'Fully Developed Flow in a Curved Pipe of Arbitrary Curvature Ratio", Int. J. Numer. Meth. in Fluids, 1987, Vol. 7, pp. 733-755.

12. Soh, W.Y., "Developing Fluid Flow in a Duct of Square Cross-section and Its Fully Developed Dual Solution", J. Fluid Mech., 1988, Vol. 188, pp. 337-361.

13. Austin, L.R. and Seader, J.D., "Entry Region for Steady Viscous Flow in Coiled Circular Pipes", AICHE J., 1974, Vol. 20, No. 4, pp. 820-822.

14. Bovendeerd, P.H.M., Steenhoven, A.A.Ven, Vosse, F.N.Ven De and Vossers, G., "Steady Entry Flow in a Curved Pipe", J. Fluid Mech., 1987, Vol. 177, pp. 233-246.

15. Agrawal, Y., Talbot, L. and Gong, K.," Laser Anemometer Study of Flow Development in Curved Circular Pipes", J. Fluid Mech., 1978, Vol. 85, pp. 497-518.

16. Choi, U.S., Talbot, L. and Cornet, I., " Experimental Study of Wall Shear Rates in the Entry Region of a Curved Tube", J. Fluid Mech., 1978, Vol. 93, pp. 465-518.

17. Cheng, K.C. and Yuen, F.P., "Flow Visualization Studies on Secondary Flow Patterns in Straight Tubes Downstream of a 180 degree Bend and in Isothermally Heated Horizontal Tubes", ASME J. Heat Transfer, 1987, vol. 109, No. 3, pp. 49-54.

18. Fletcher C.A.J., "Computational Techniques for Fluid Dynamics 1", Springer-Verlag Berlin Heidelberg, 1988.

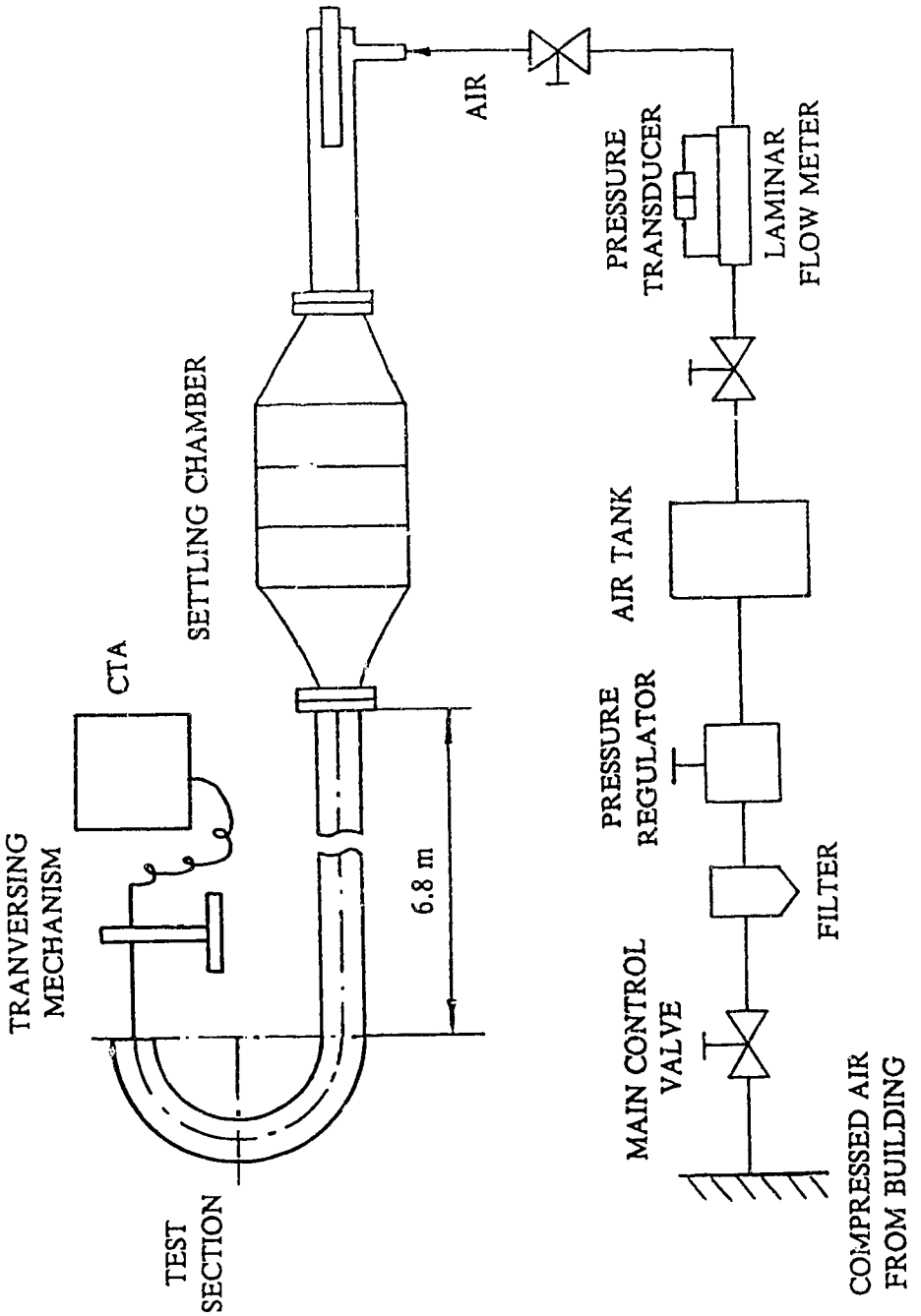

Fig. 3.1 Schematic diagram of test setup

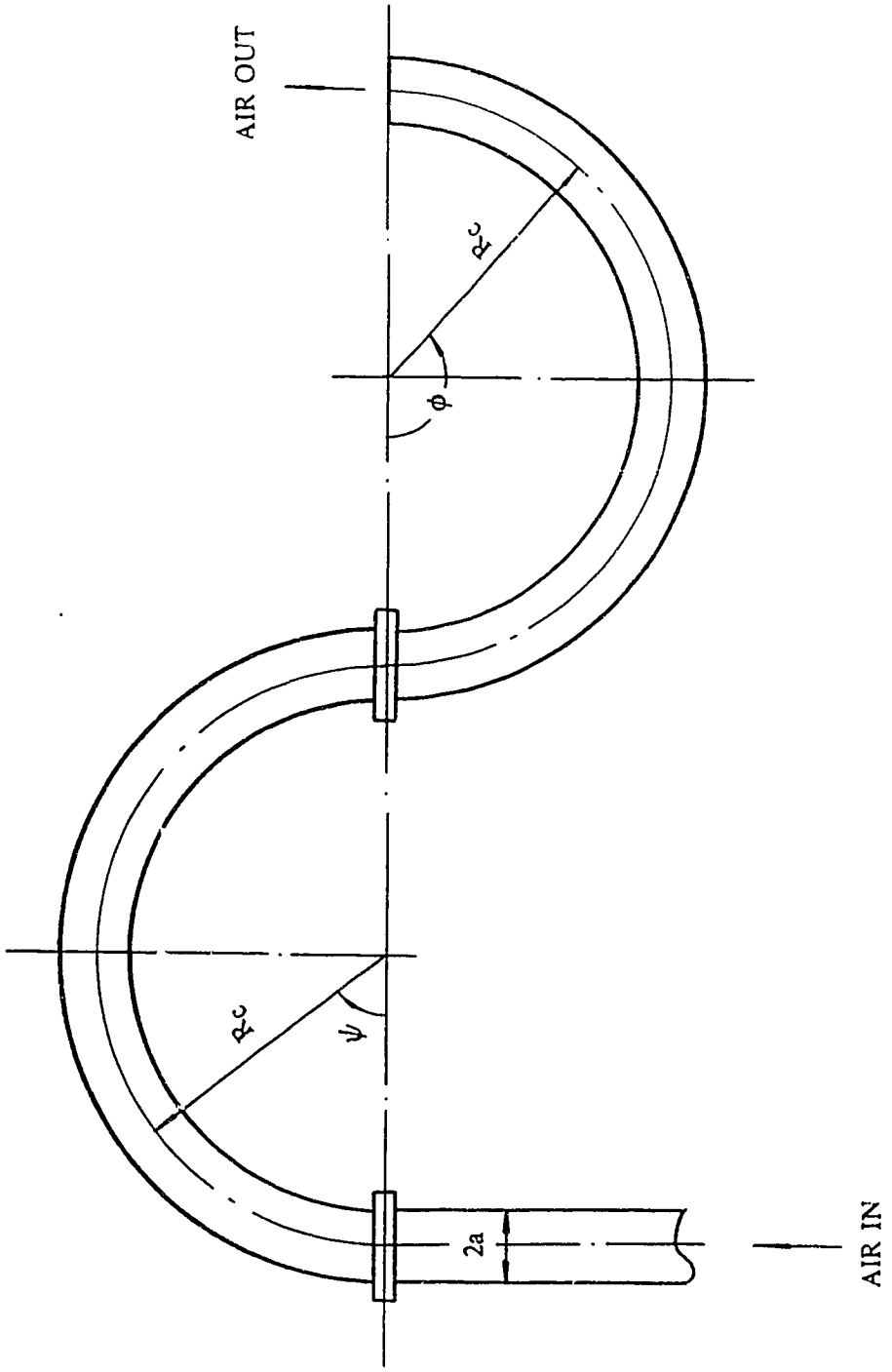

Fig. 3.2 Schematic diagram of the test section

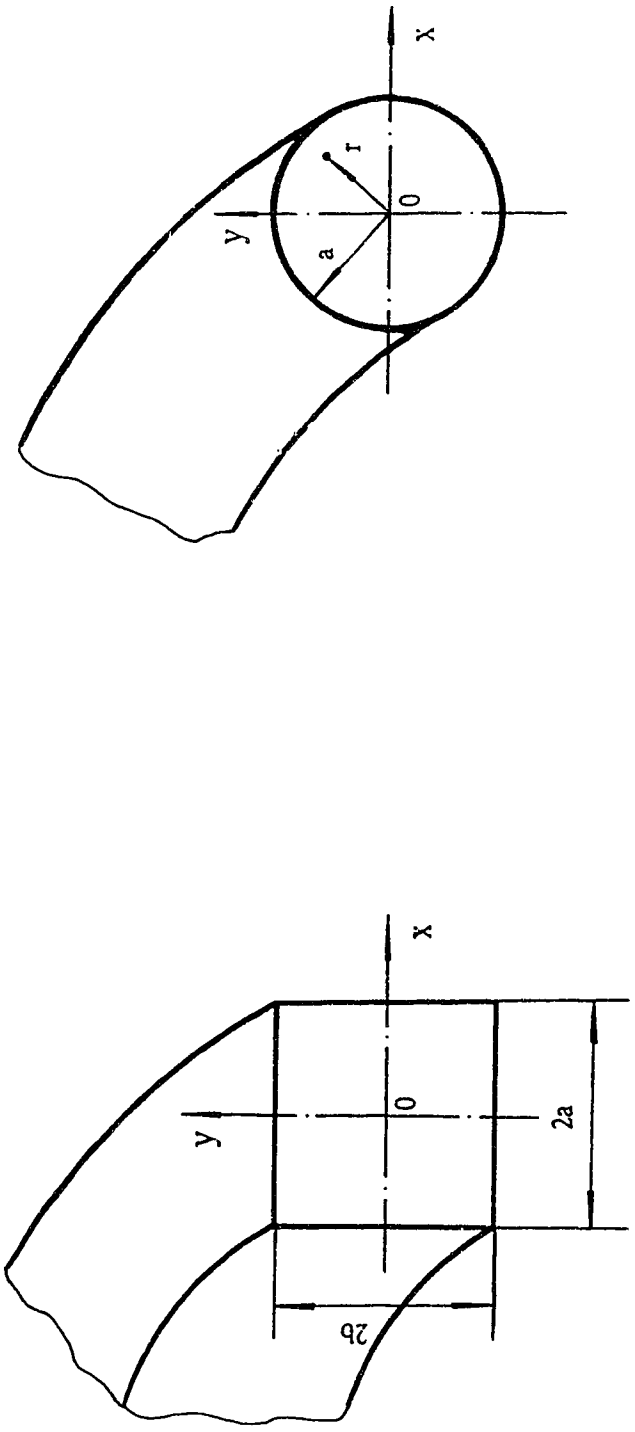

Fig. 3.3 Exit of the test section and coordinate system

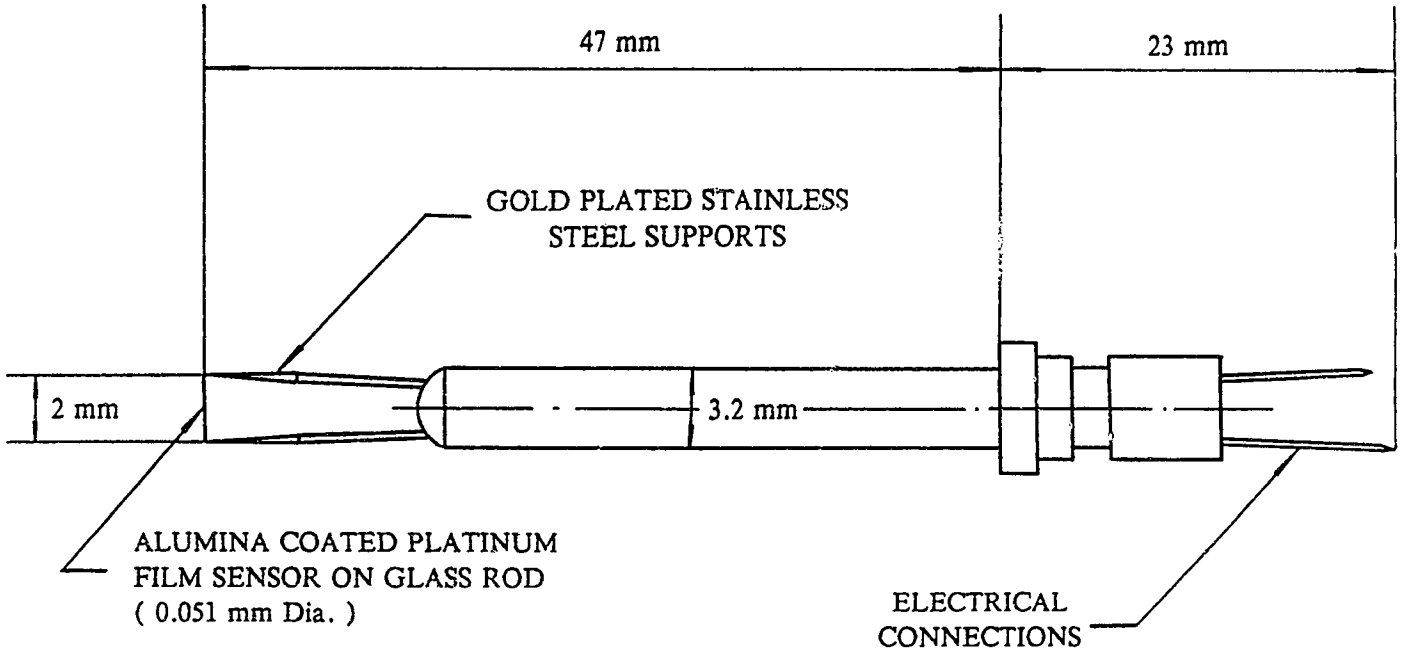

Fig. 3.4 Schematic diagram of the hot-film sensor

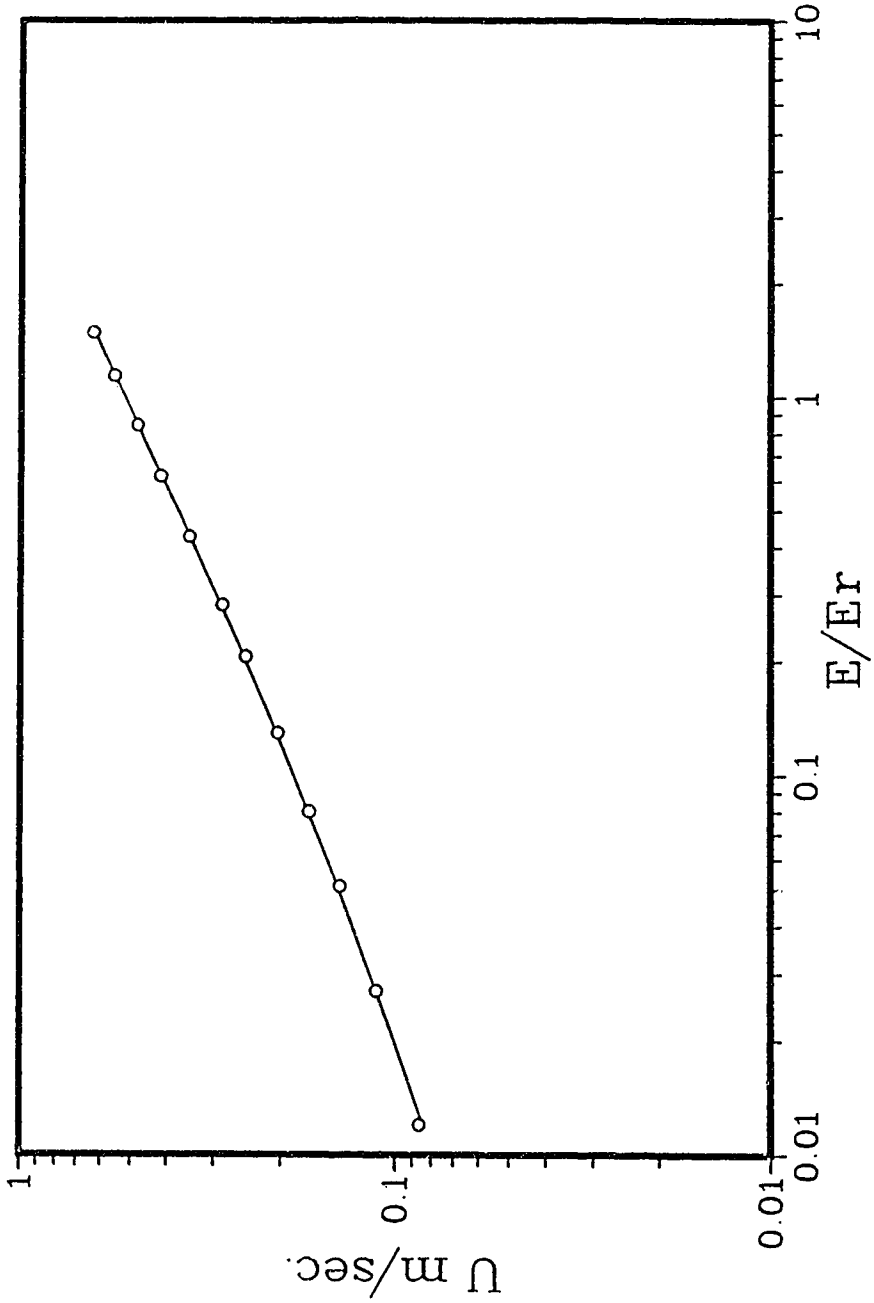

Fig. 3.5 Calibration curve for case (1); K=350, a/R_C=0.2

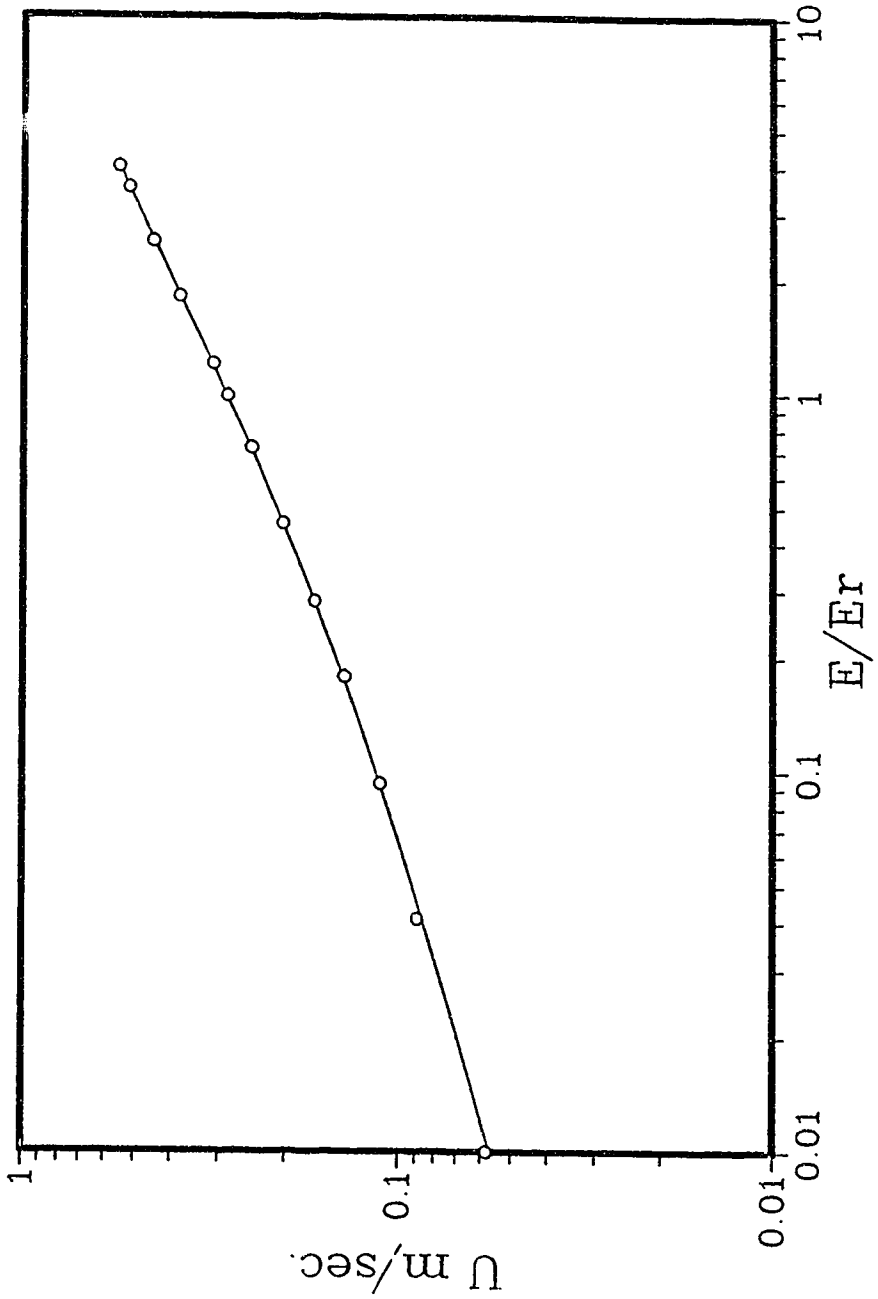

Fig. 3.6 Calibration curve for case (2); K=200, a/R_c=0.2

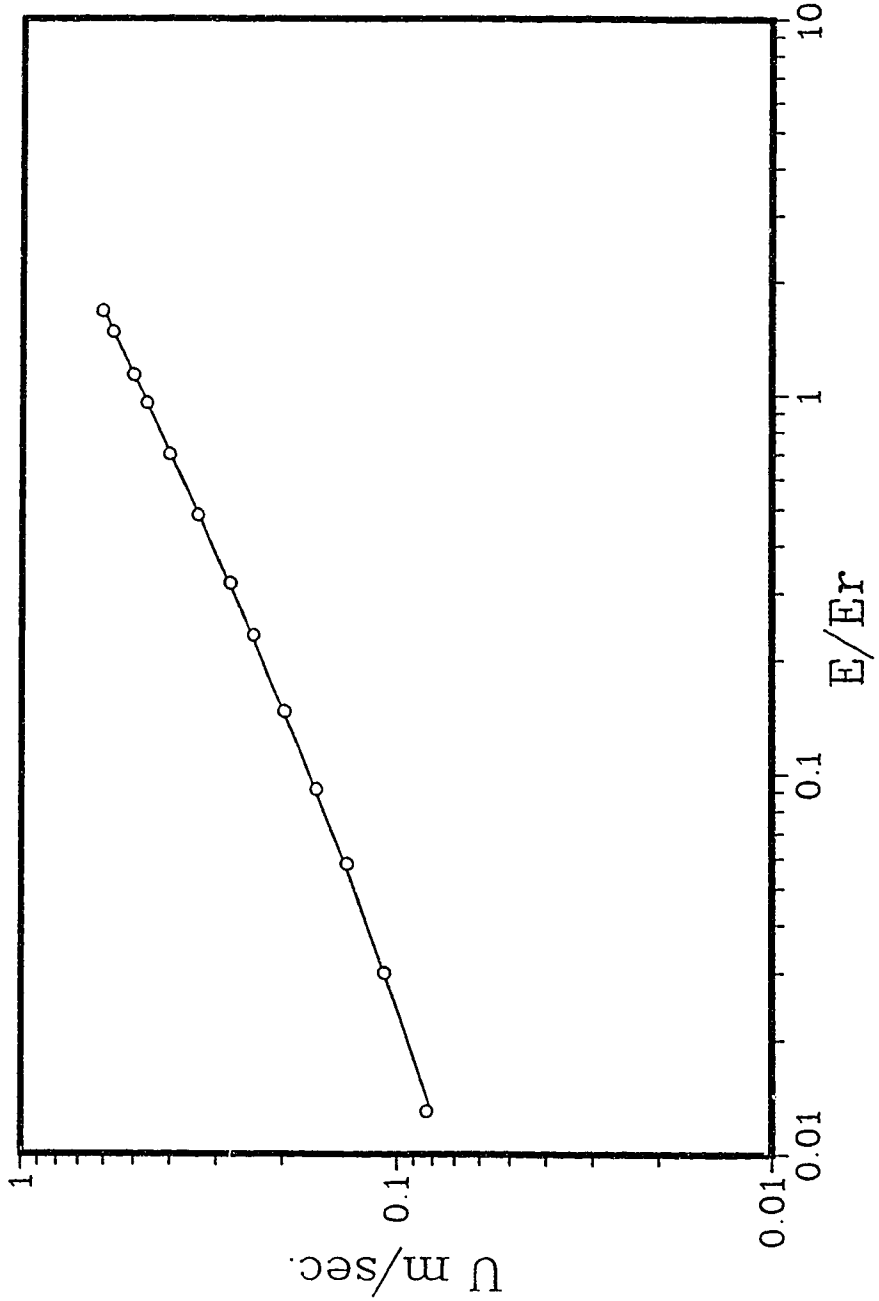

Fig. 3.7 Calibration curve for case (3); κ=350, a/R_C=0.2

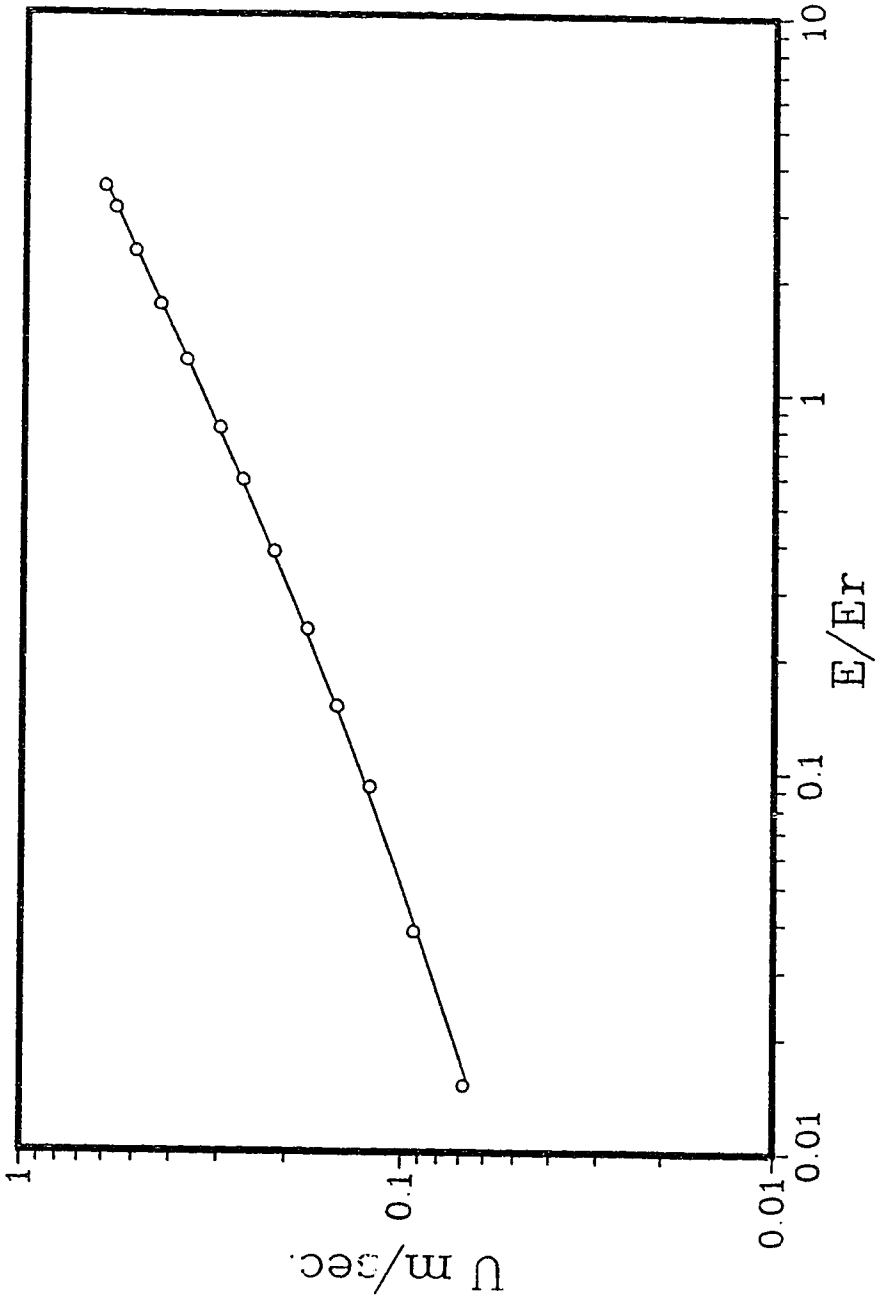

Fig. 3.8 Calibration curve for case (4); K=350, a/R_C=0.4

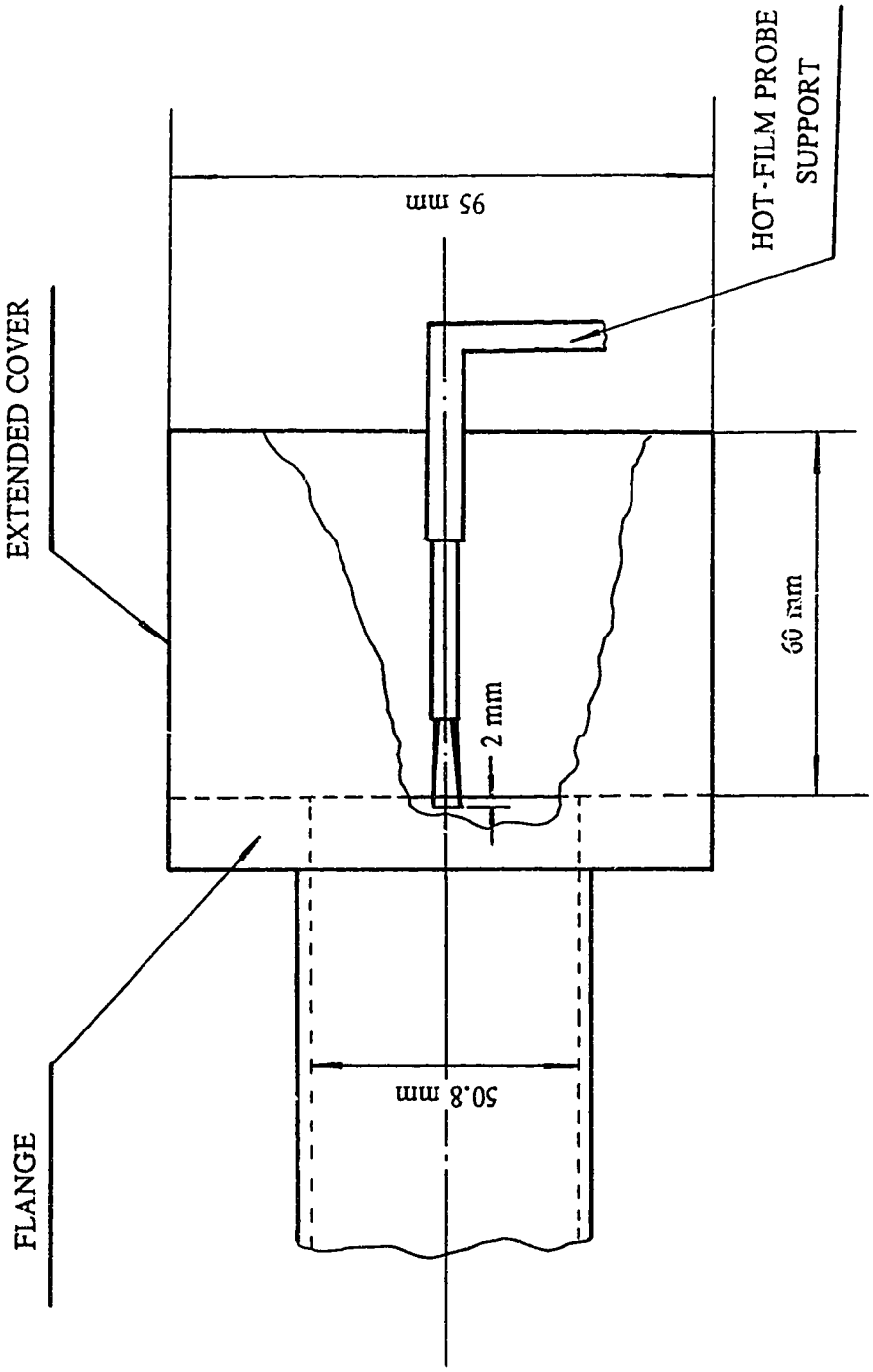

Fig. 3.9 Extended cover for velocity measurement and the location of hot-film probe

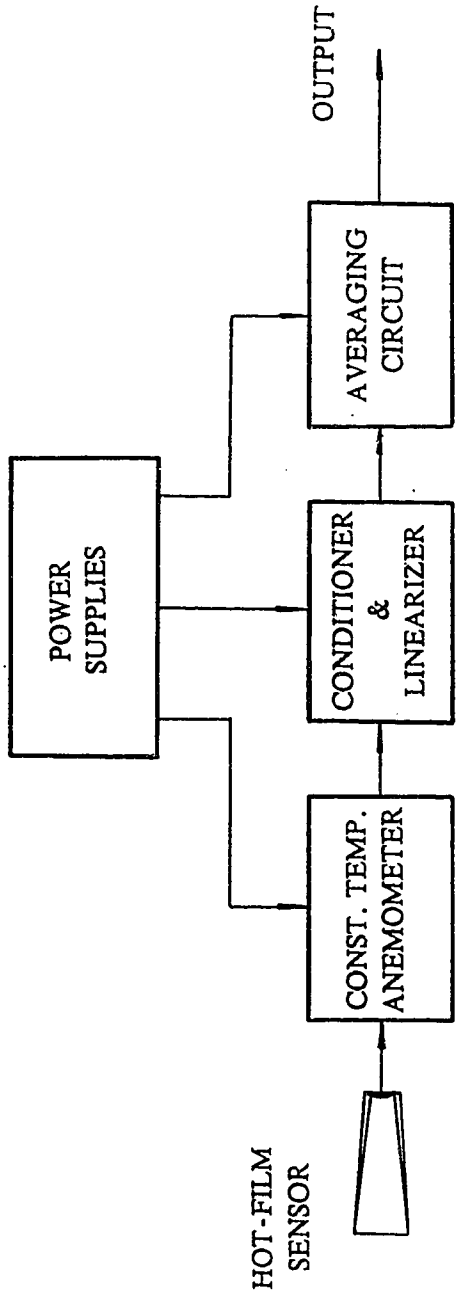

Fig. 3.10 Hot-film anemometer system

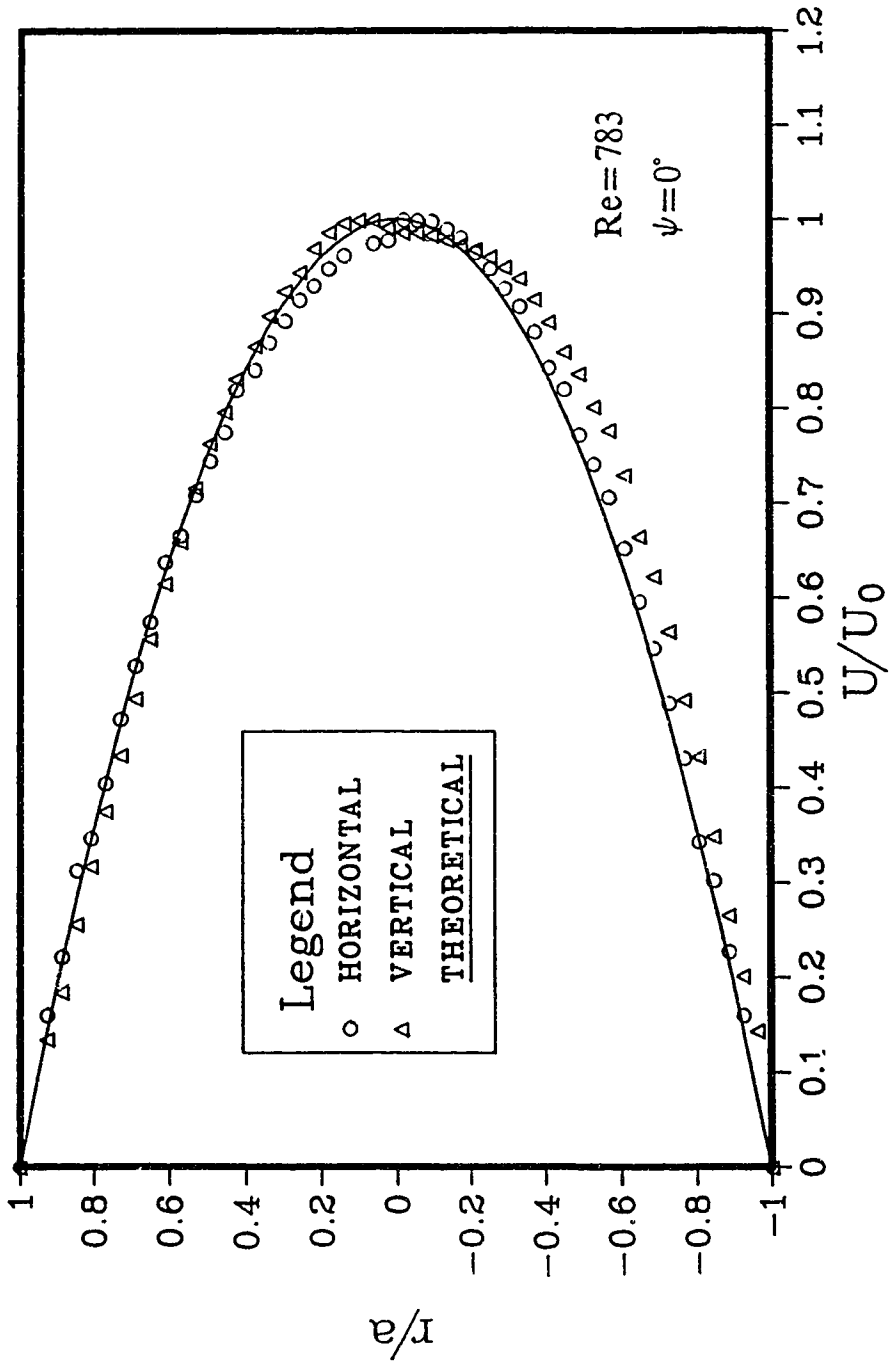

Fig. 3.11 Axial velocity profiles for fully developed laminar flow in a circular pipe at Re=783

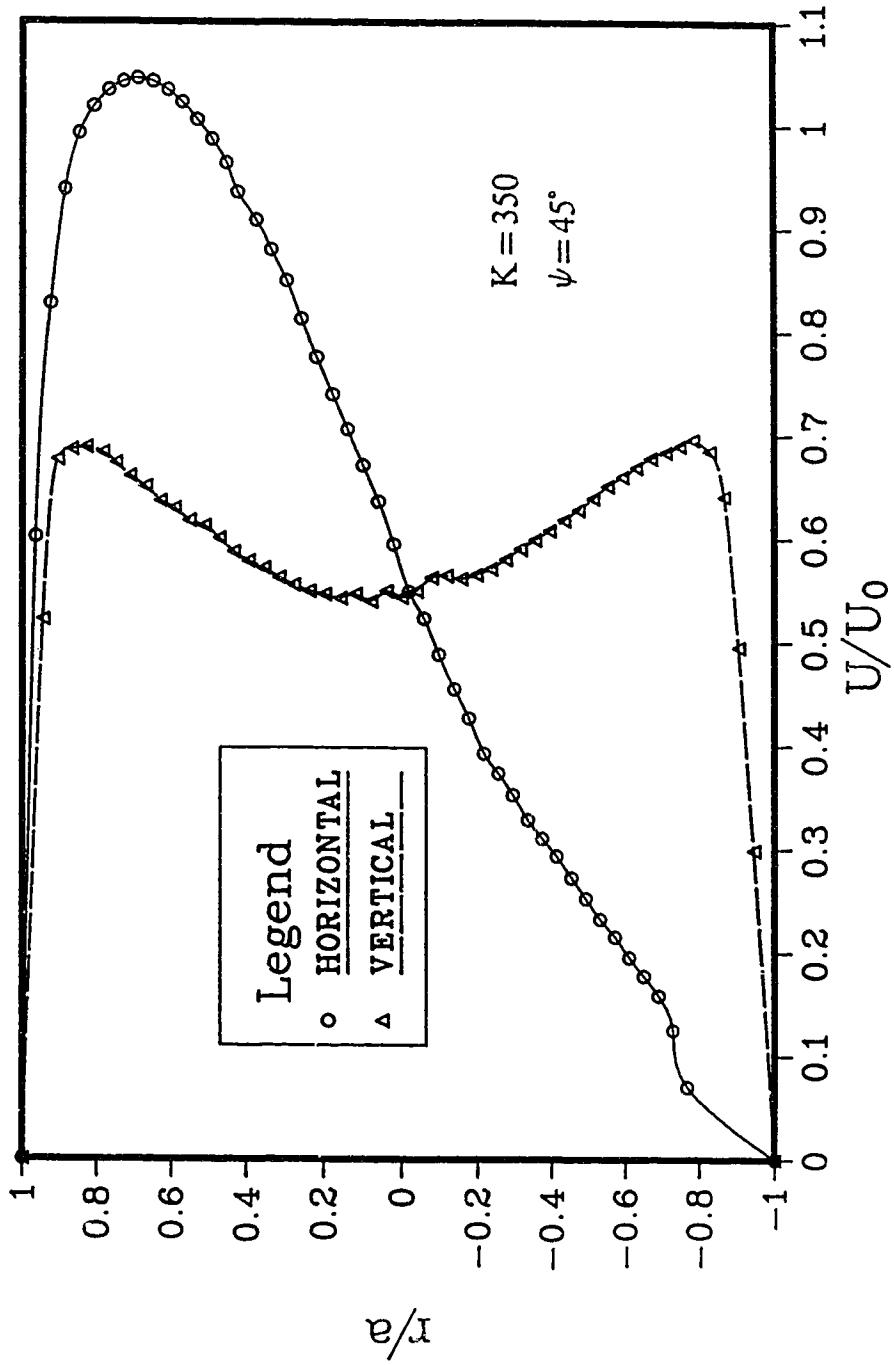

Fig. 3.12 Axial velocity profiles along x and y axes at the exit of a 45° circular bend with $a/R_C=0.2$ and K=350

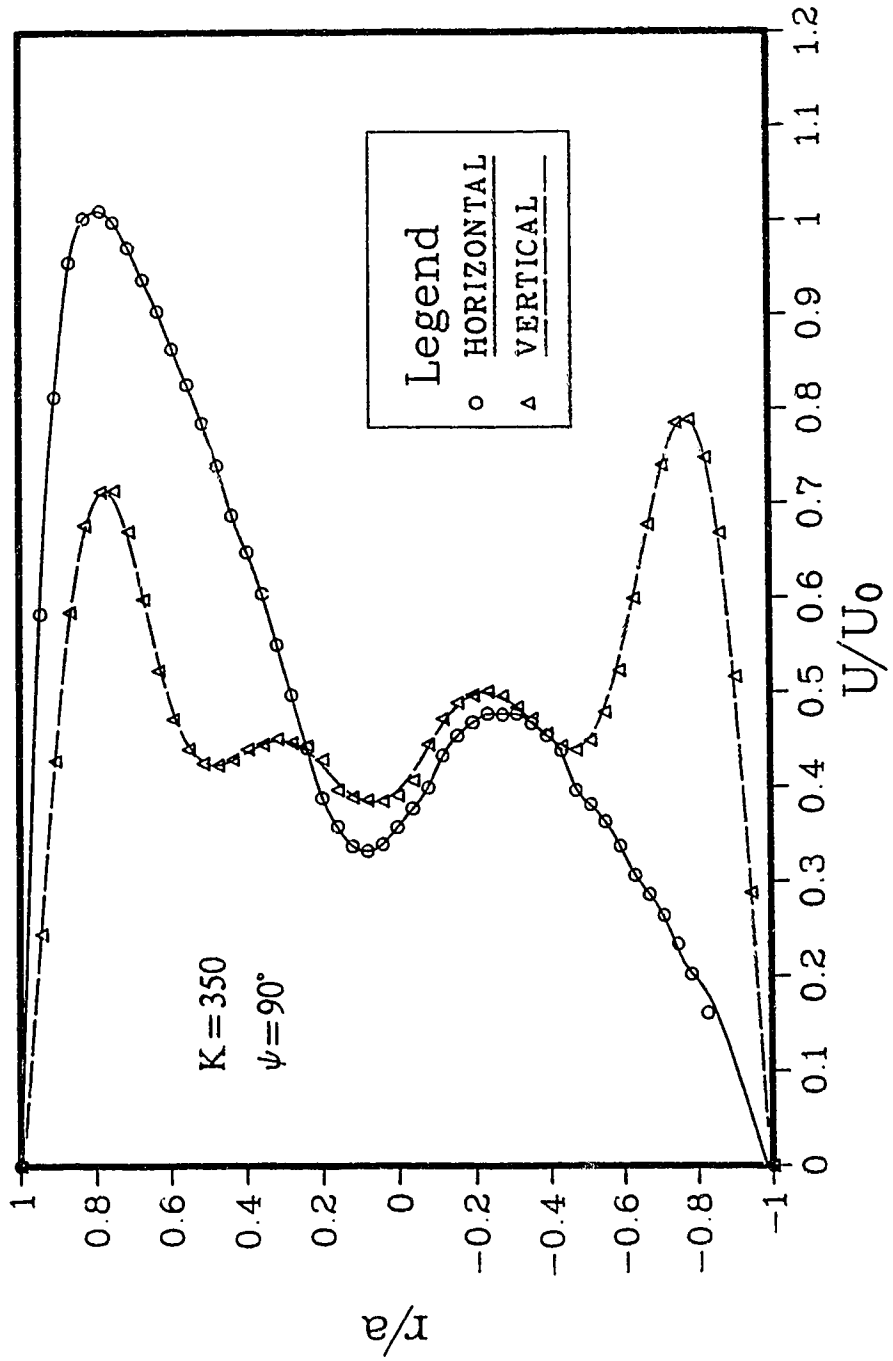

Fig. 3.13 Axial velocity profiles along x and y axes at the exit of a 90° circular bend with $a/R_c=0.2$ and K=350

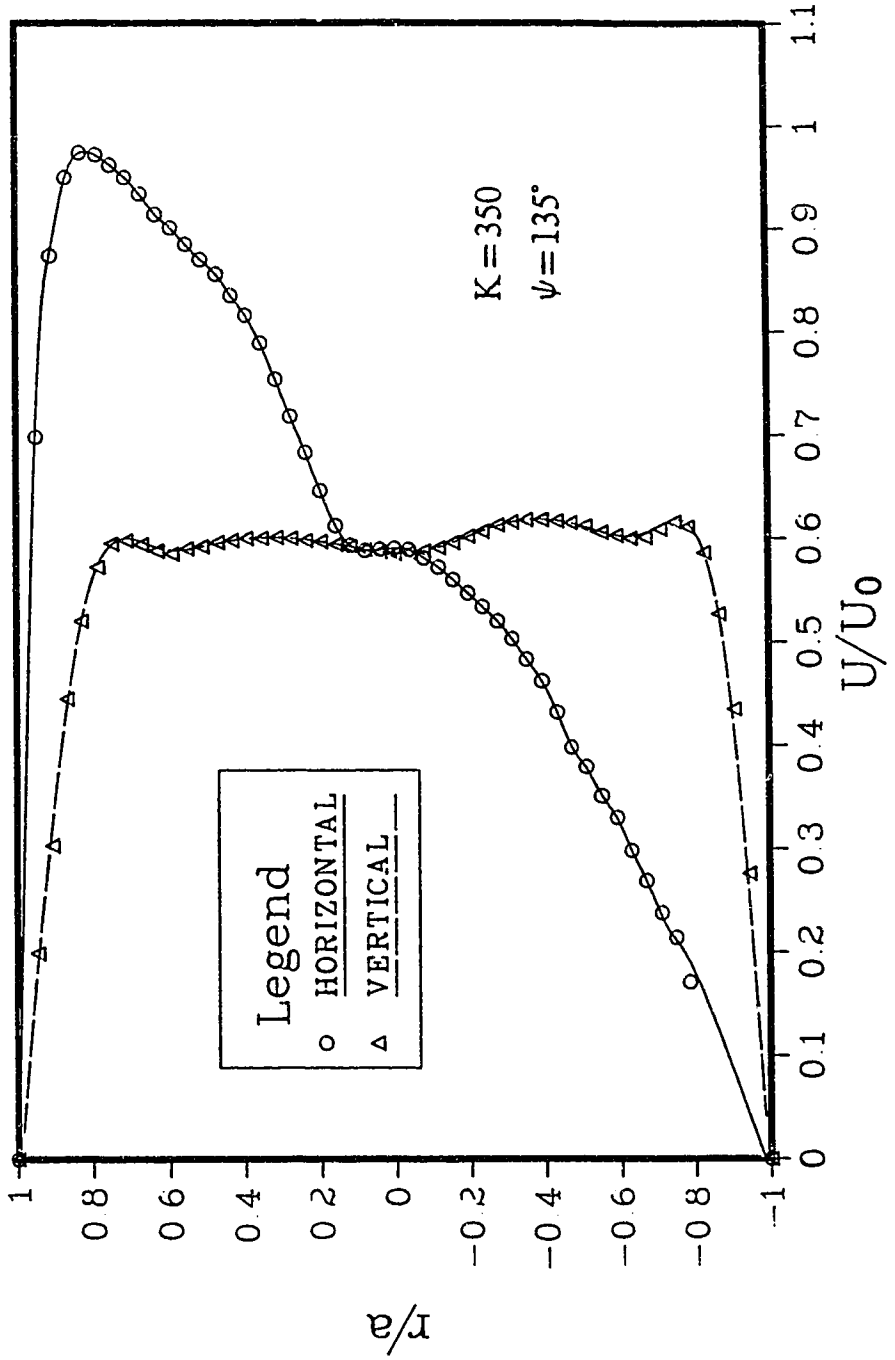

Fig. 3.14 Axial velocity profiles along x and y axes at the exit of a 135° circular bend with $a/R_c=0.2$ and K=350

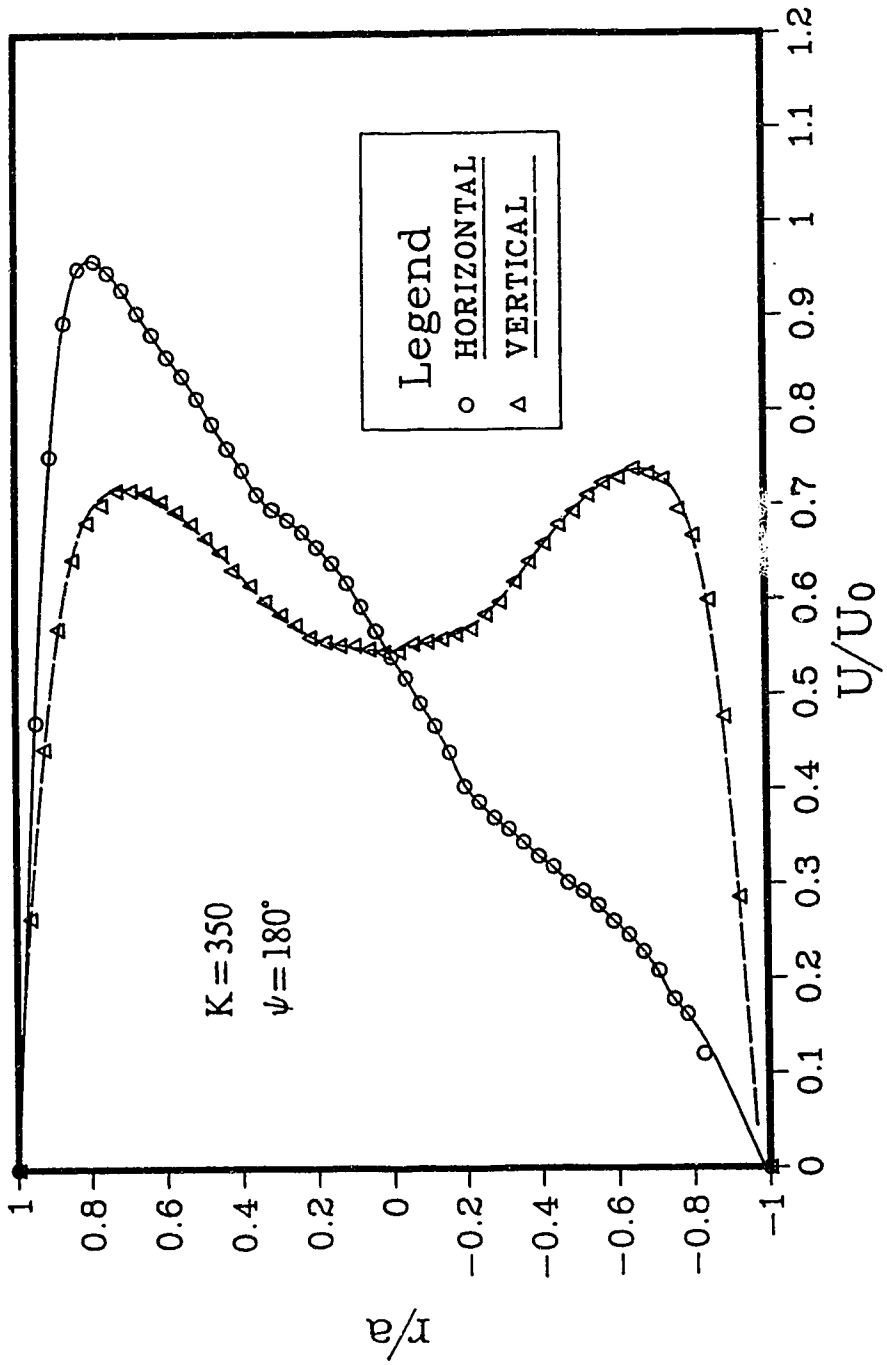

Fig. 3.15 Axial velocity profiles along x and y axes at the exit of a 180° circular bend with $a/R_C=0.2$ and K=350

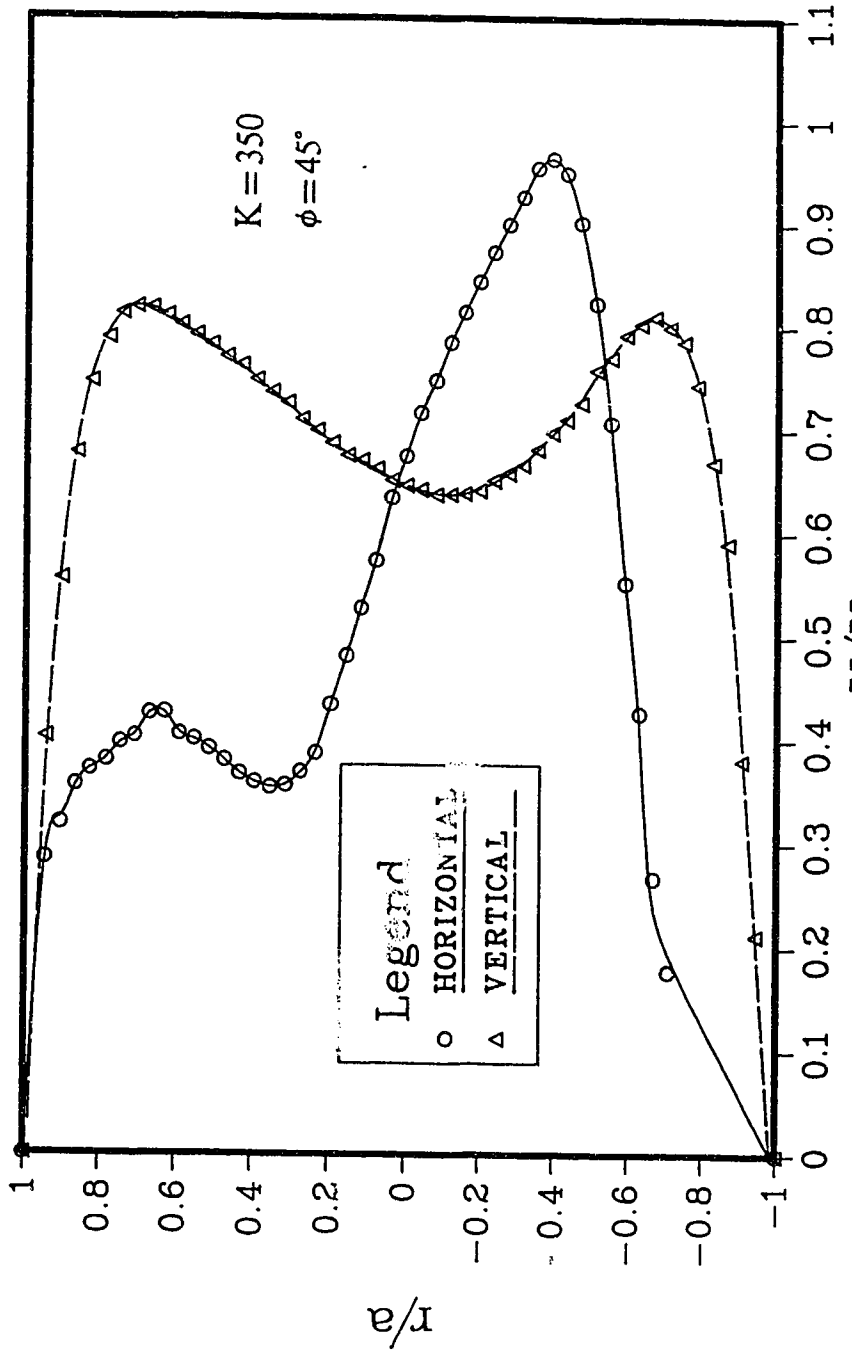

Fig. 3.16 Axial velocity profiles along x and y axes at the exit of a circular s-bend with ϕ=45°, a/R_c=0.2 and K=350

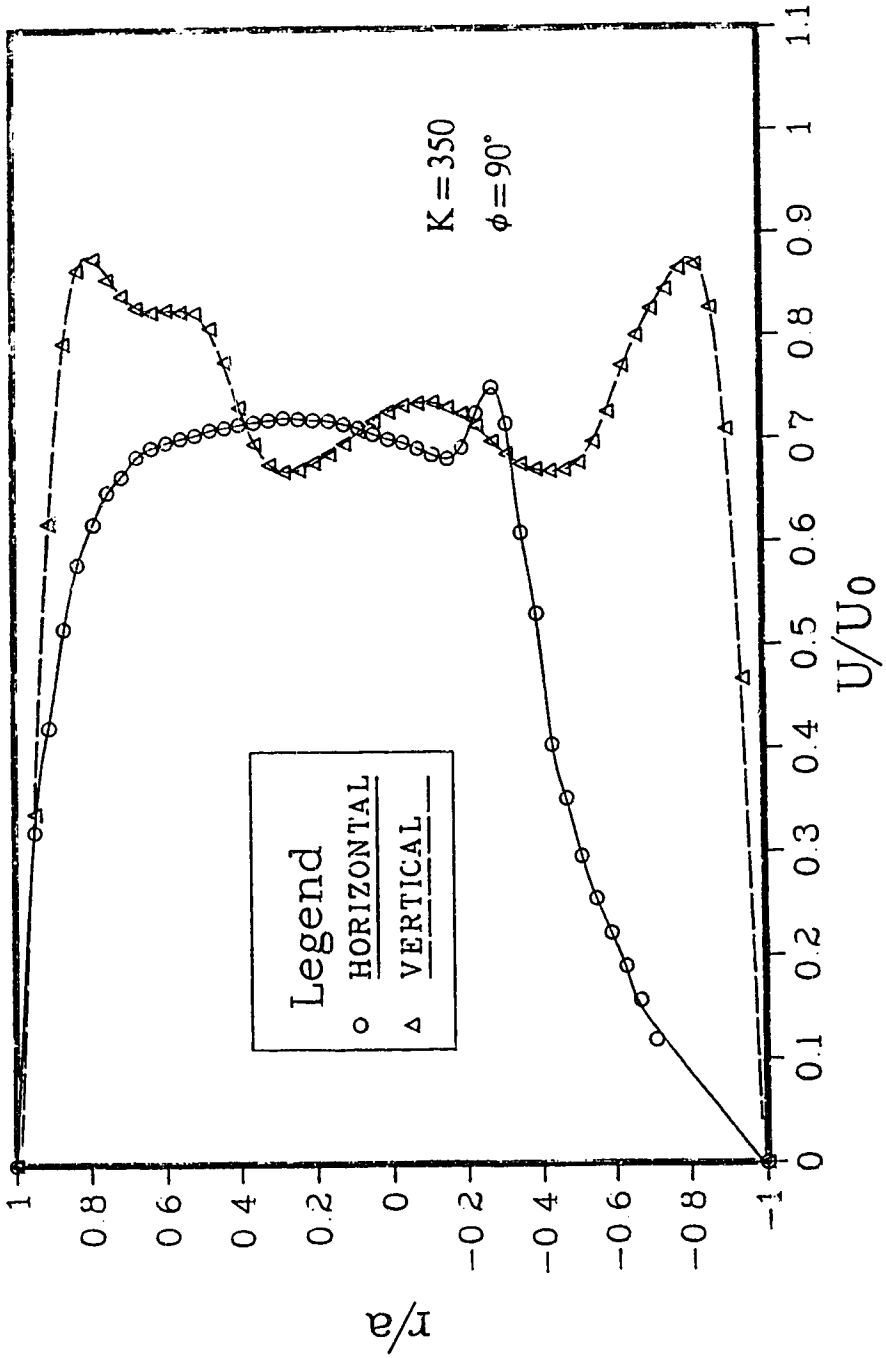

Fig. 3.17 Axial velocity profiles along x and y axes at the exit of a circular s-bend with ϕ=90°, a/R_c=0.2 and K=350

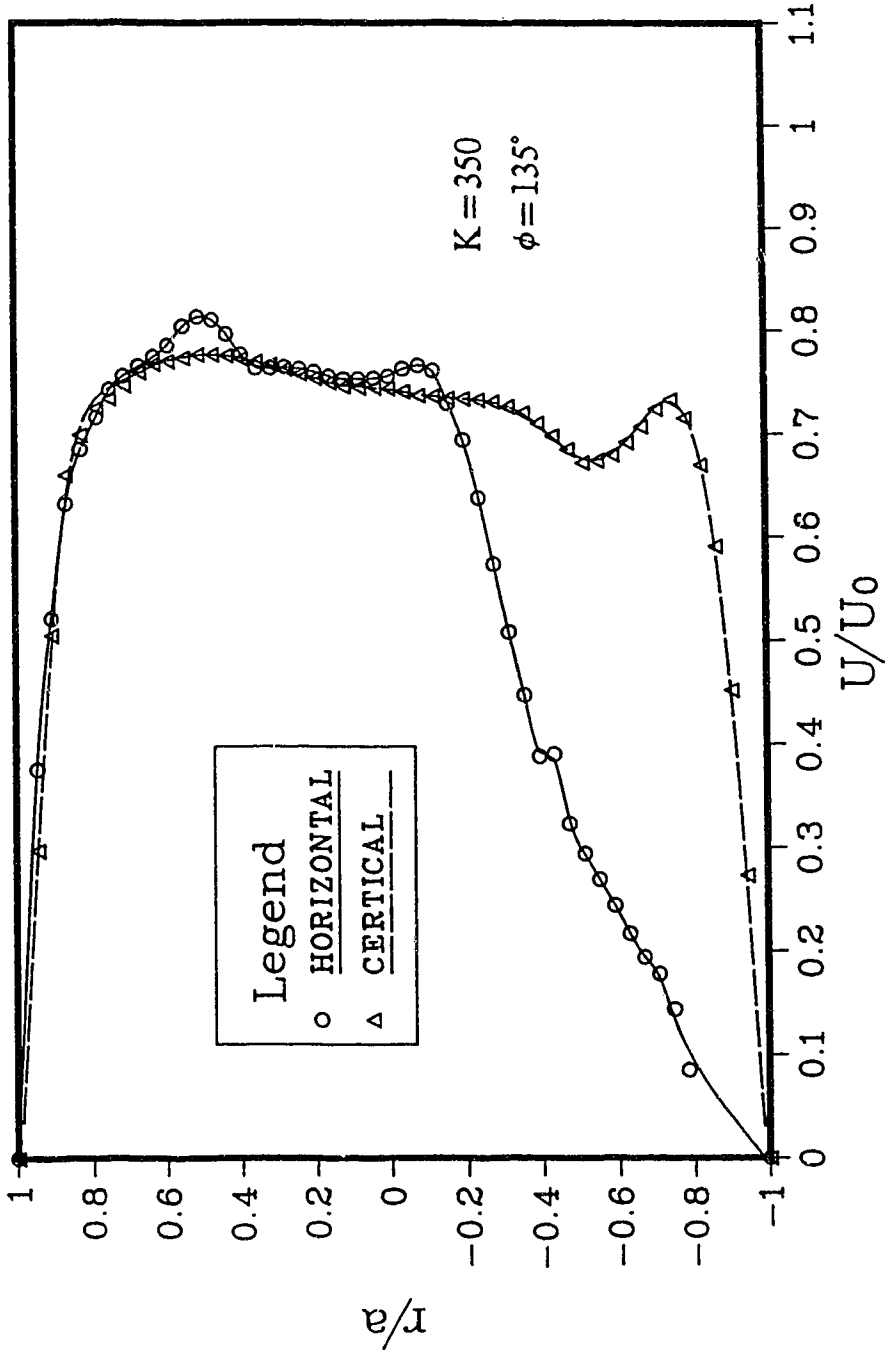

Fig. 3.18 Axial velocity profiles along x and y axes at the exit of a circular s-bend with ϕ=135°, a/R_c=0.2 and K=350

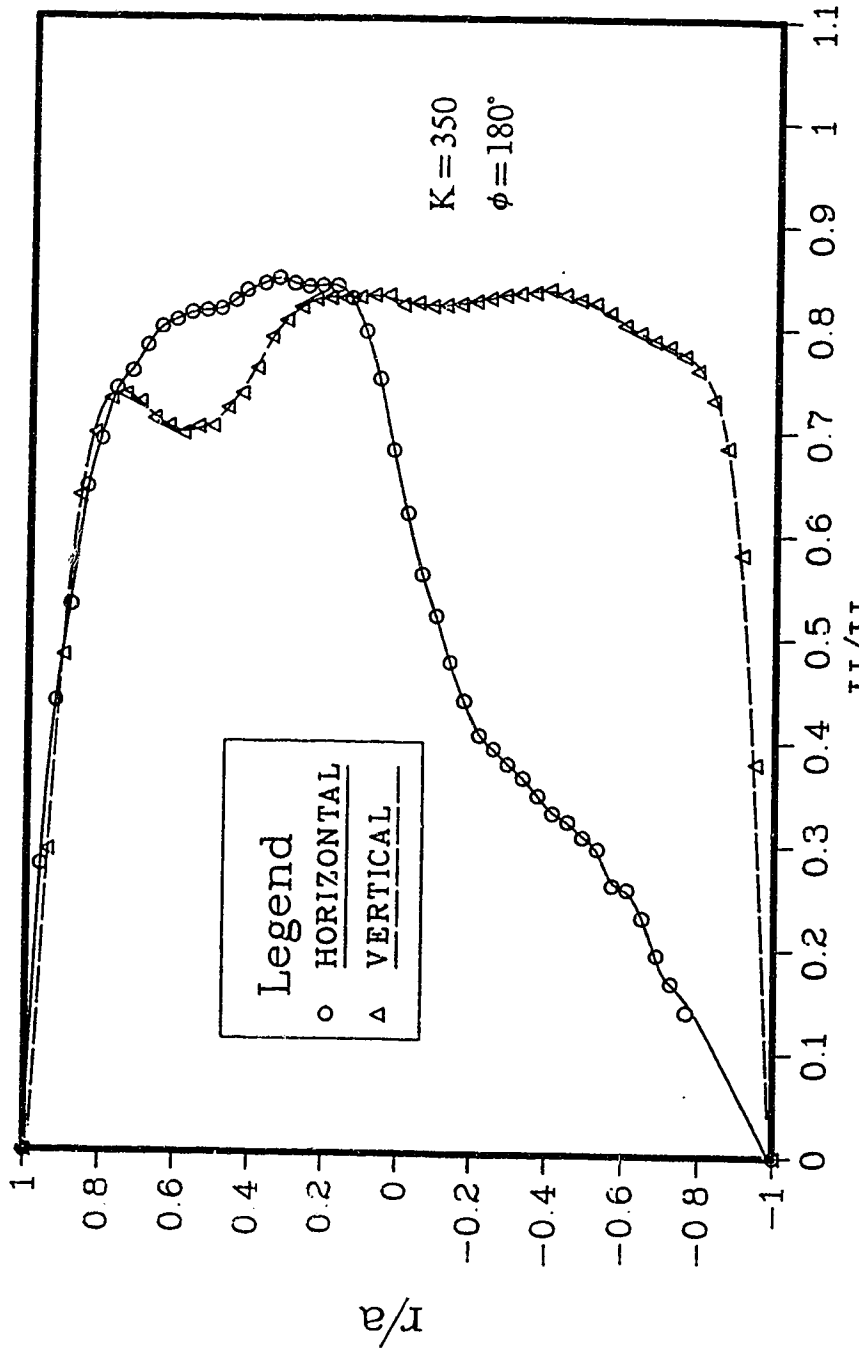

Fig. 3.19 Axial velocity profiles along x and y axes at the exit of a circular s-bend with $\phi=180°$, $a/R_c=0.2$ and K=350

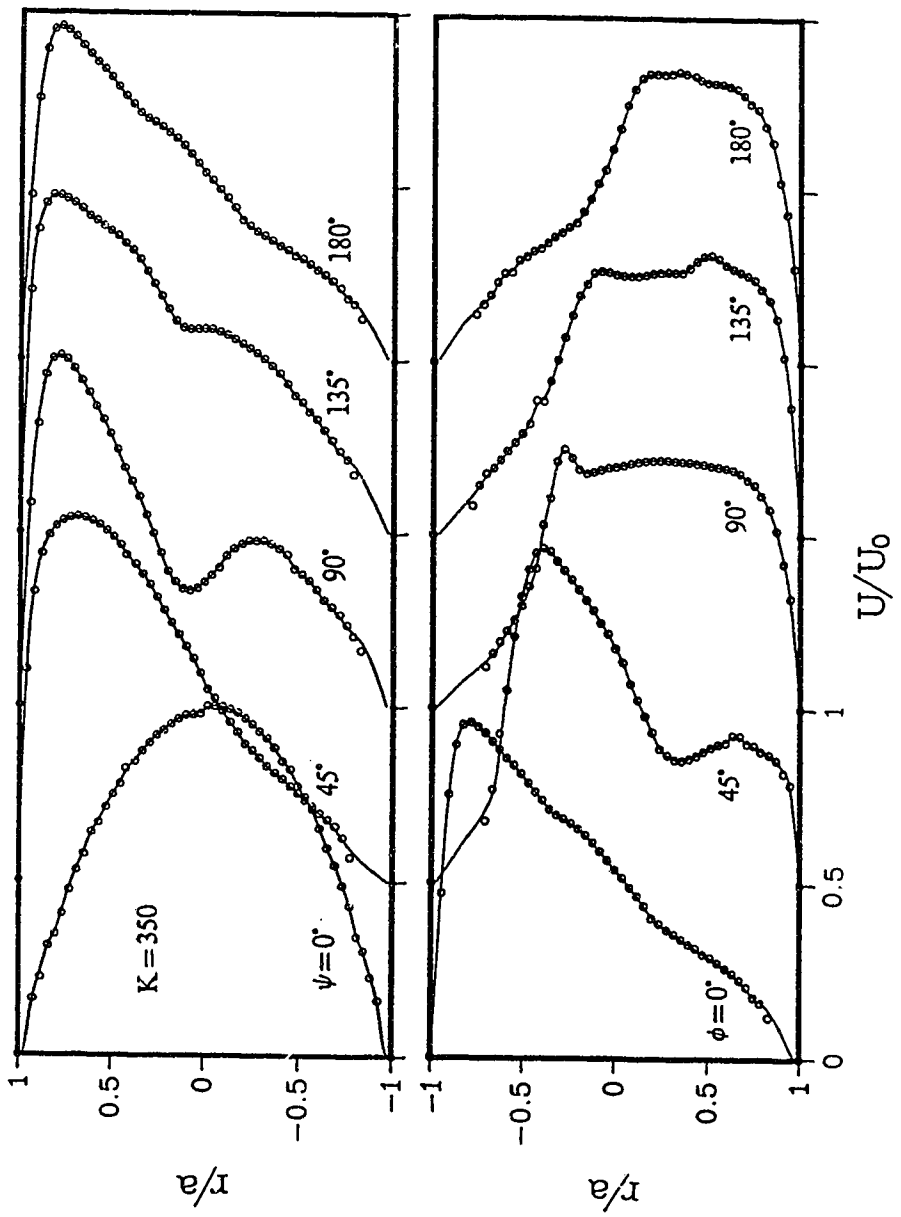

Fig. 3.20 Developing axial velocity profiles along the horizontal axis in a circular s-bend with $a/R_c=0.2$ and K=350

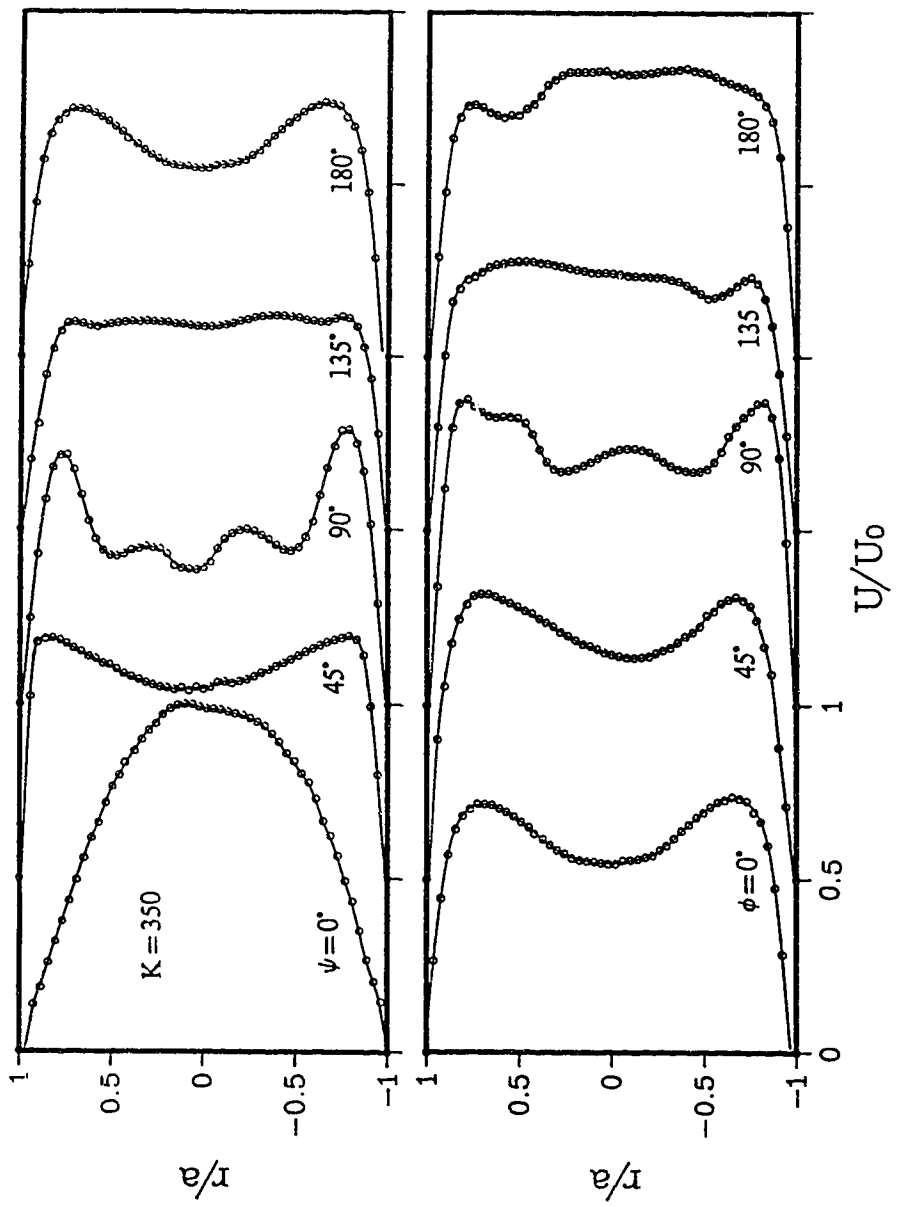

Fig. 3.21 Developing axial velocity profiles along the vertical axis in the circular s-bend with $a/R_c=0.2$ and K=350

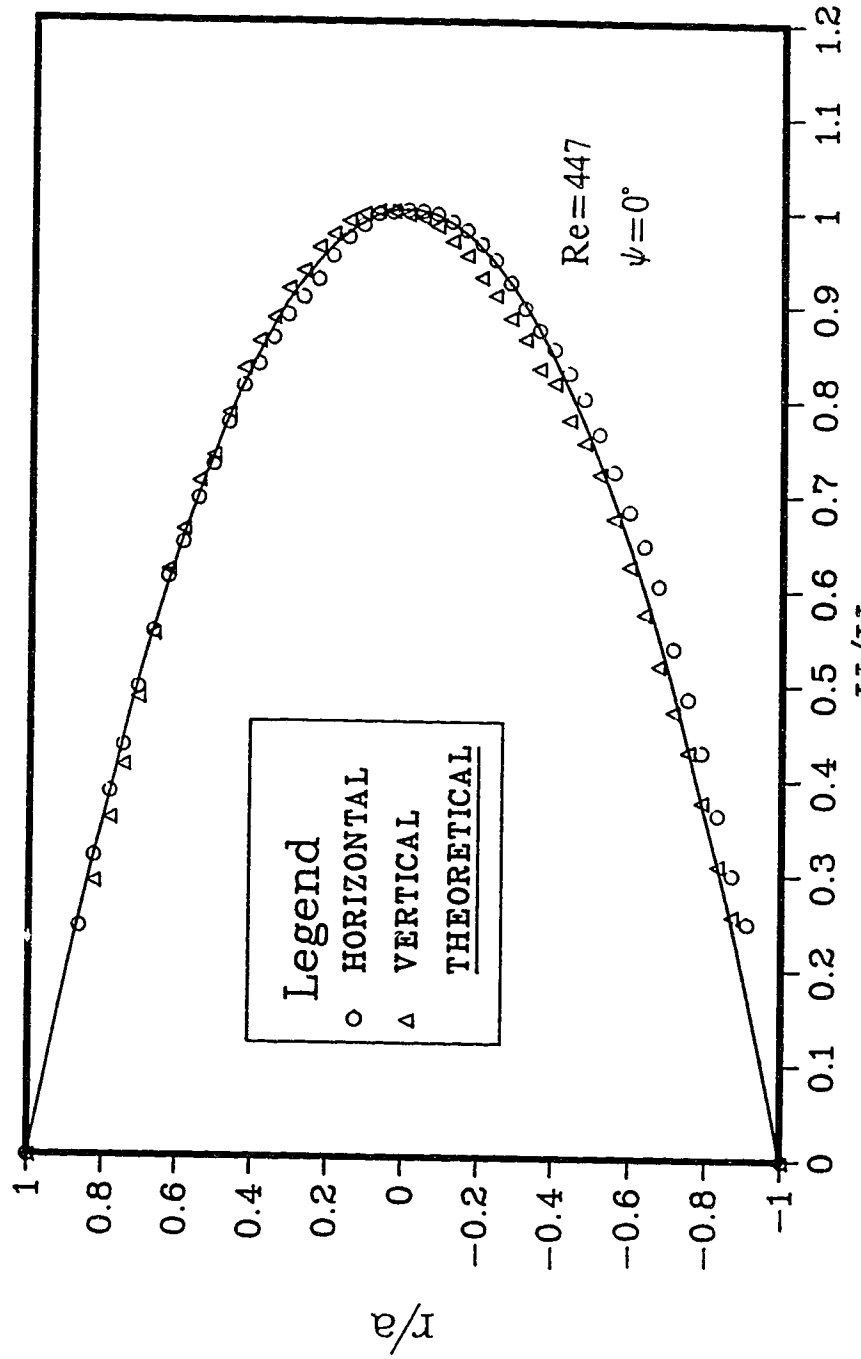

Fig. 3.22 Aixal velocity profiles for fully developed laminar flow in circular pipe at Re=447

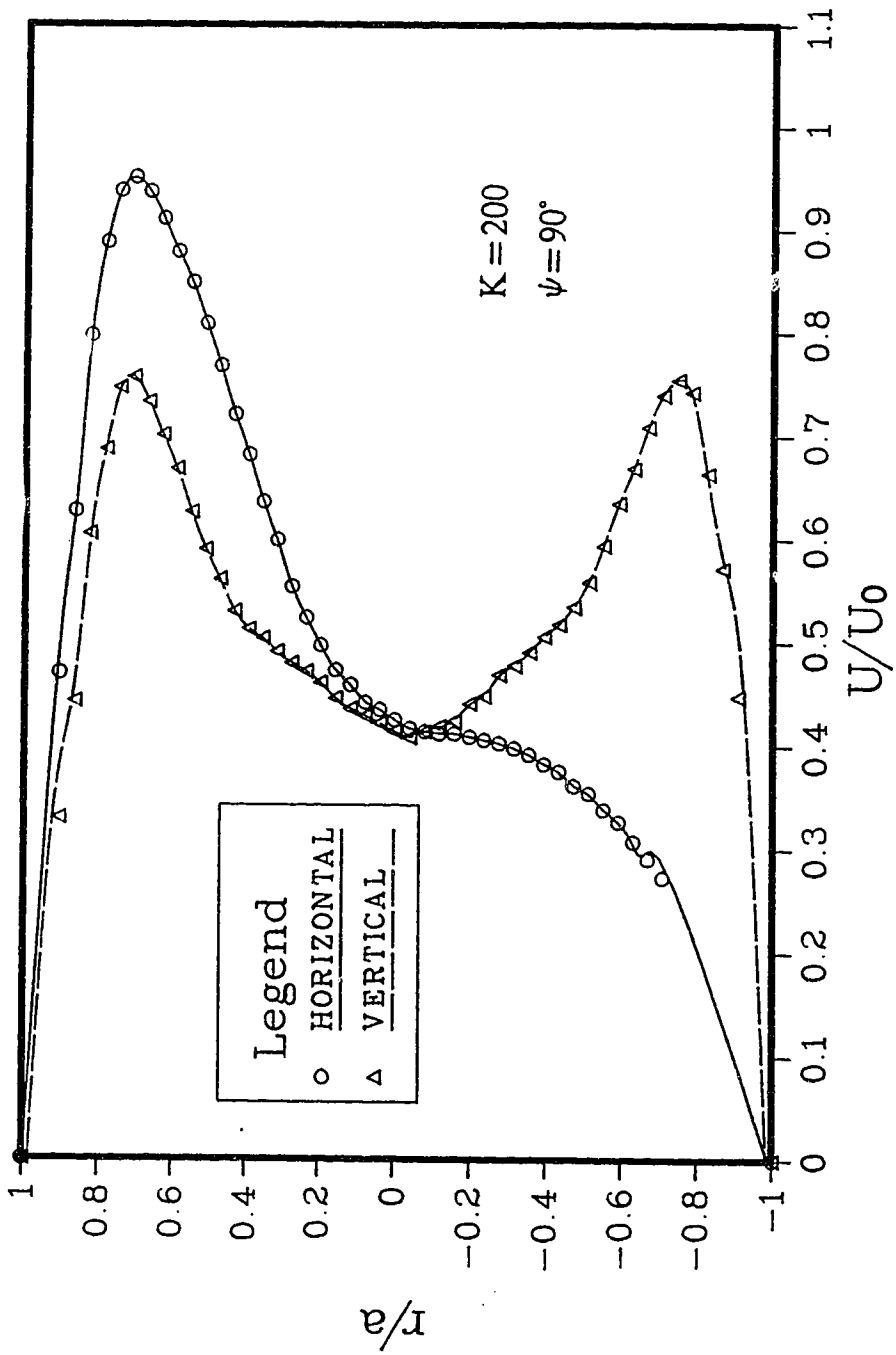

Fig. 3.23 Axial velocity profiles along X and Y axes at the exit of a 90° circular bend with $a/R_C=0.2$ and K=200

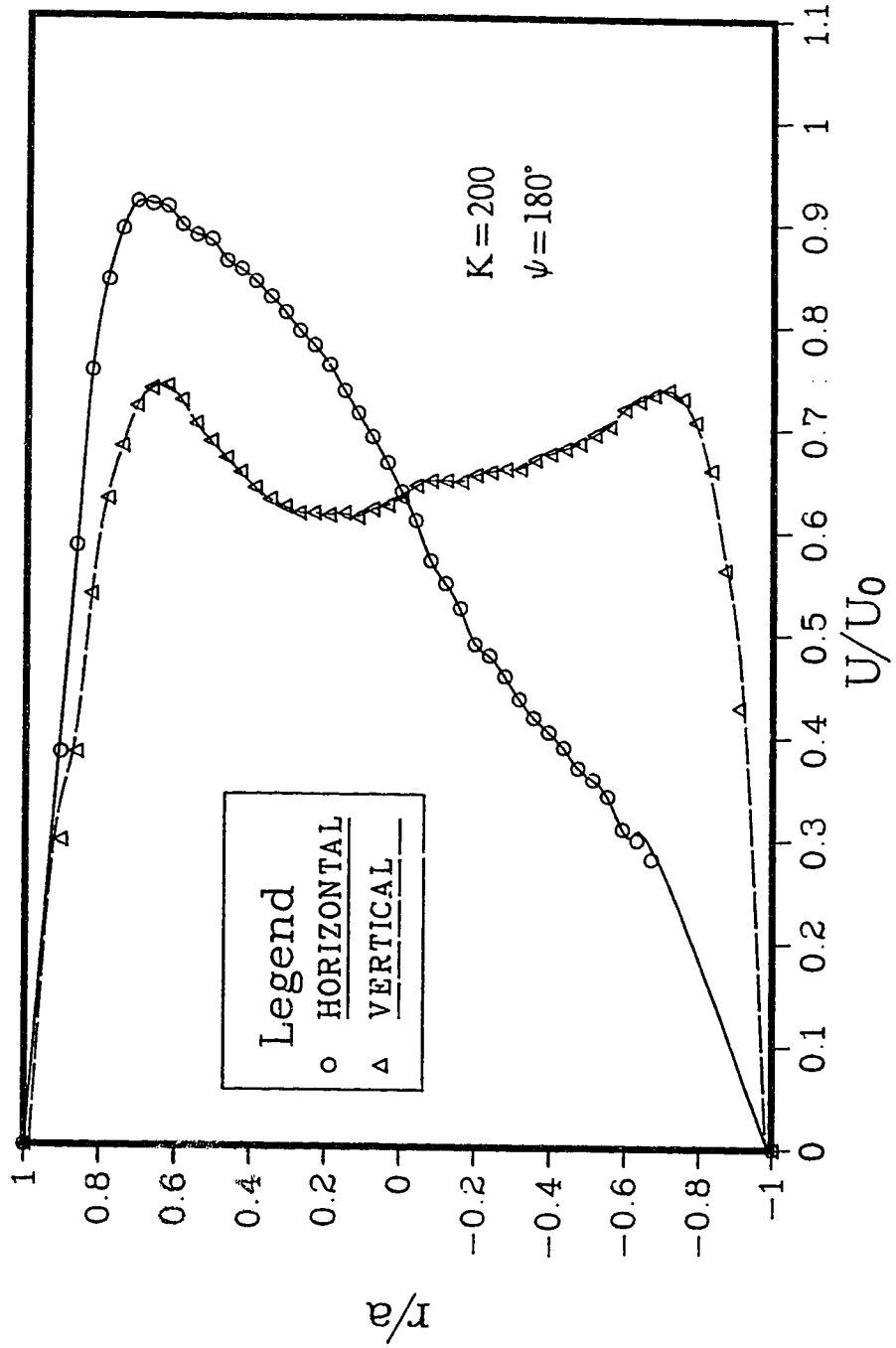

Fig. 3.24 Axial velocity profiles along X and Y axes at the exit of a 180° circular bend with $a/R_c=0.2$ and K=200

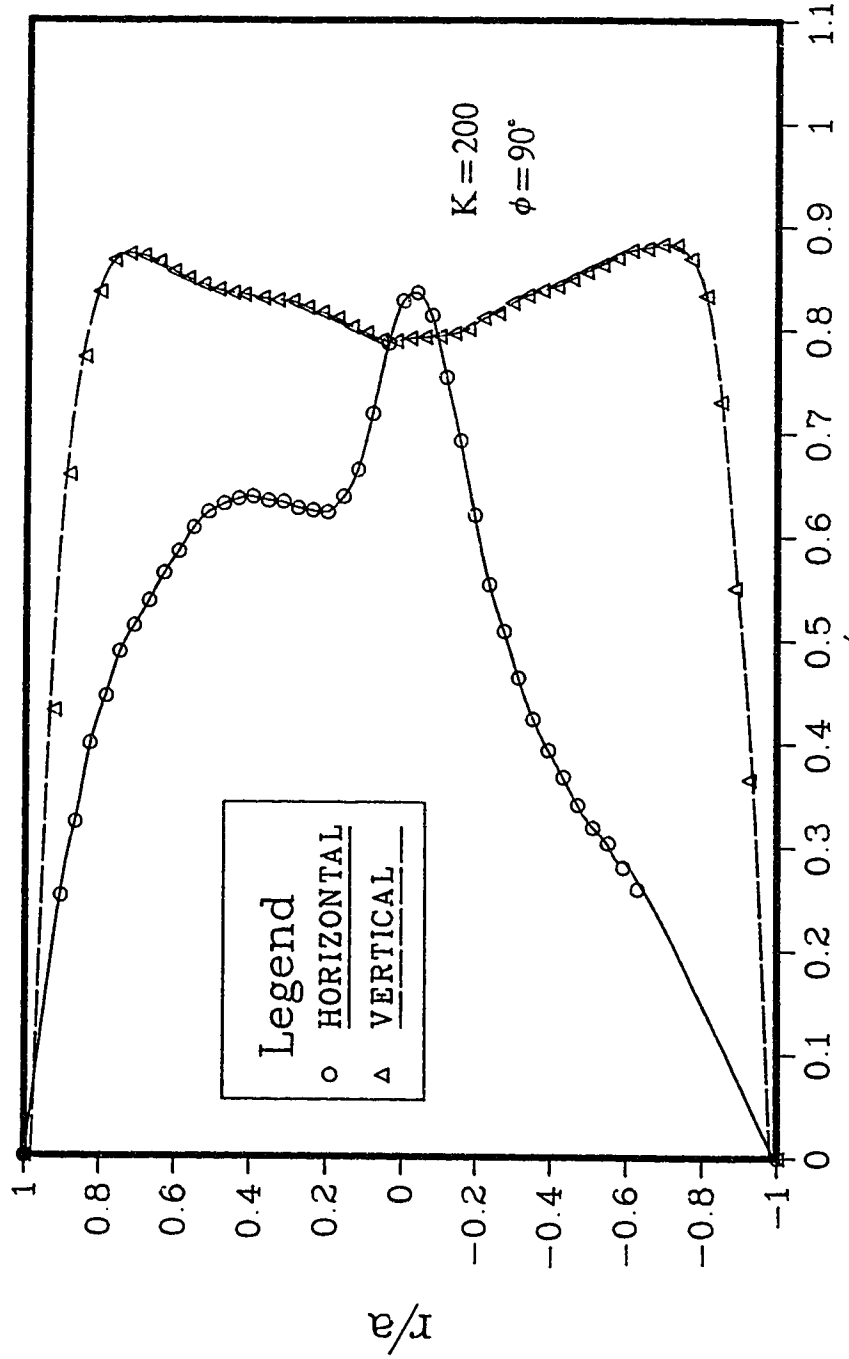

Fig. 3.25 Axial velocity profiles along x and y axes at the exit of a circular s-bend with ϕ=90°, a/R_c=0.2 and K=200

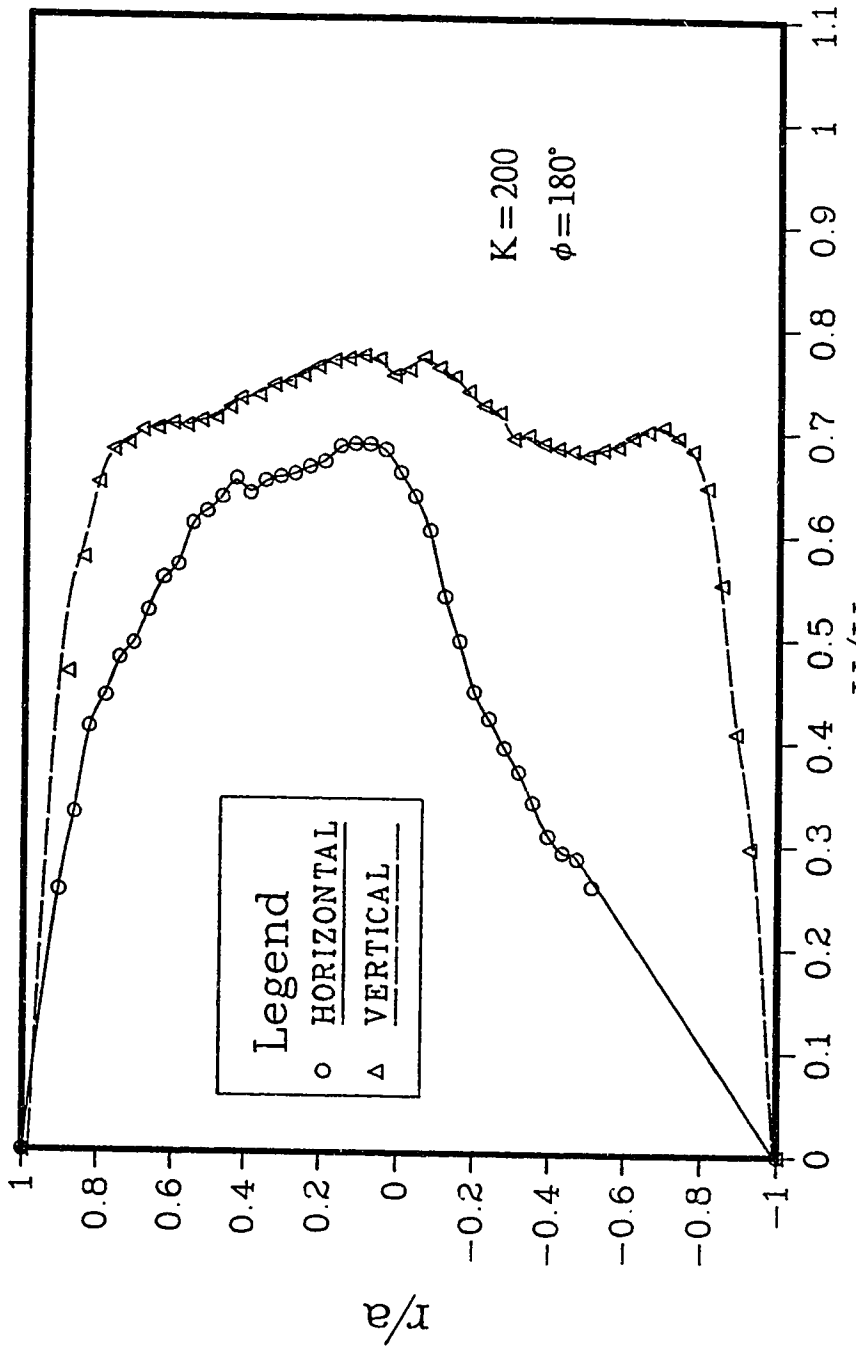

Fig. 3.26 Axial velocity profiles along x and y axes at the exit of a circular s-bend with ϕ=180°, a/R_C=0.2 and K=200

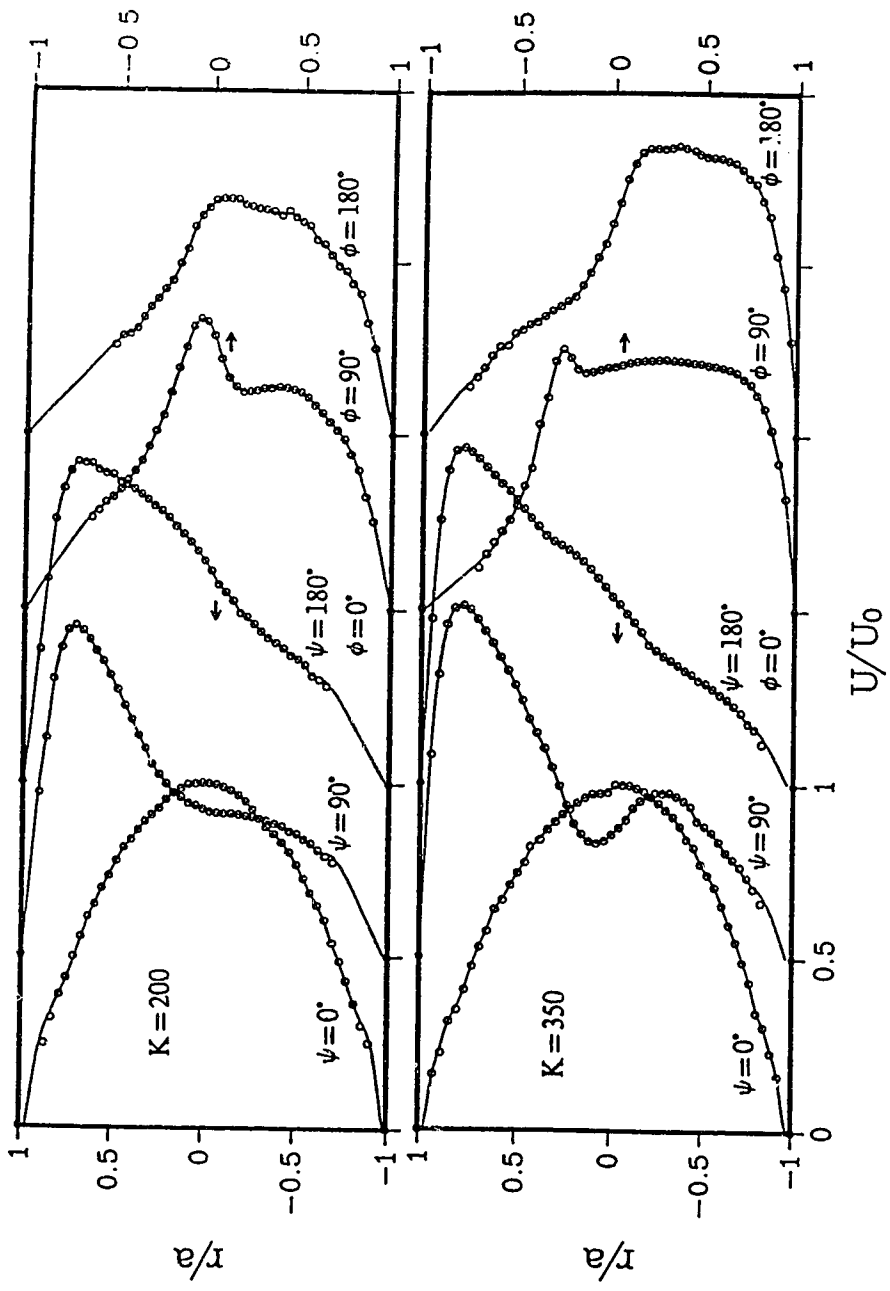

Fig. 3.27 Developing axial velocity profiles along the horizontal axis in a circular s-bend for K=200, 350

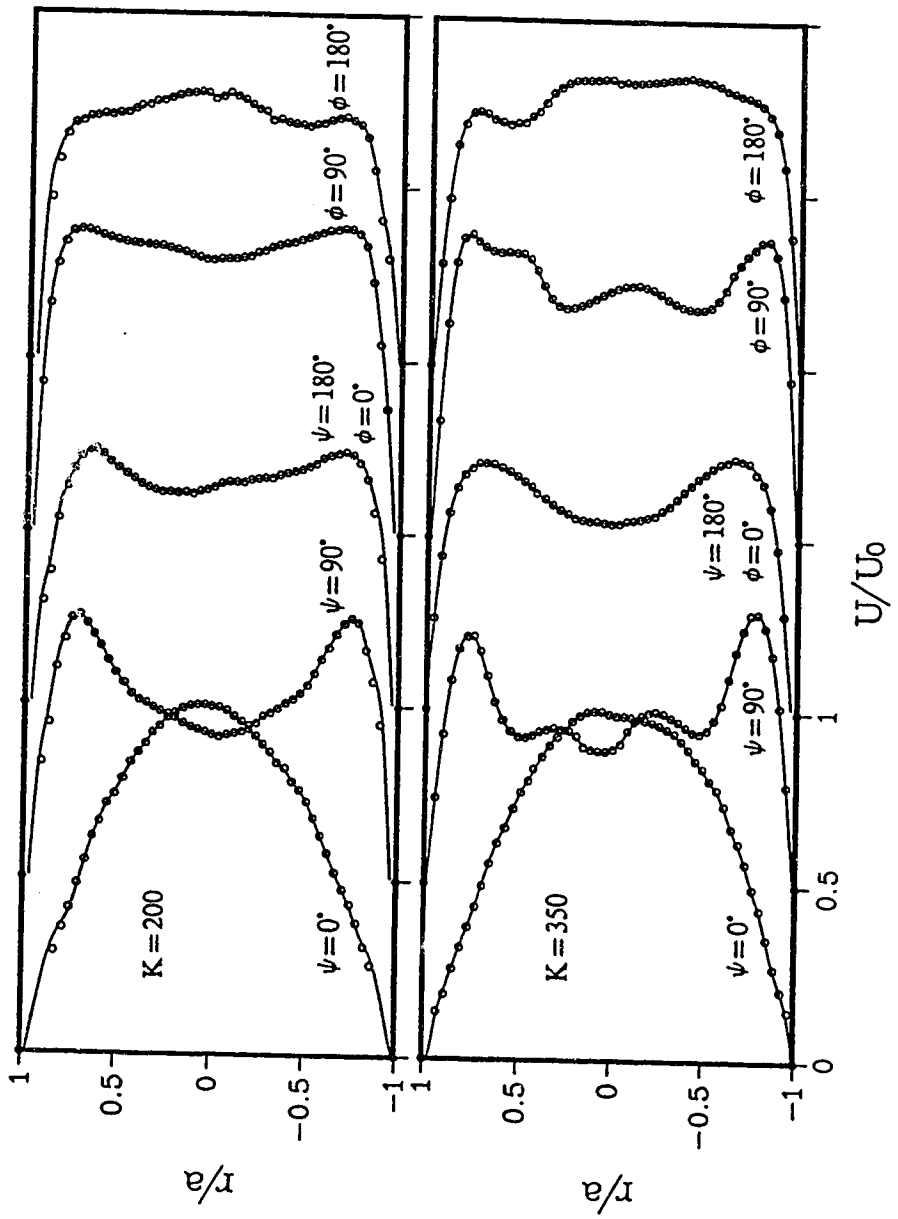

Fig. 3.28 Developing axial velocity profiles along the vertical axis in a circular s-bend for K=200, 350

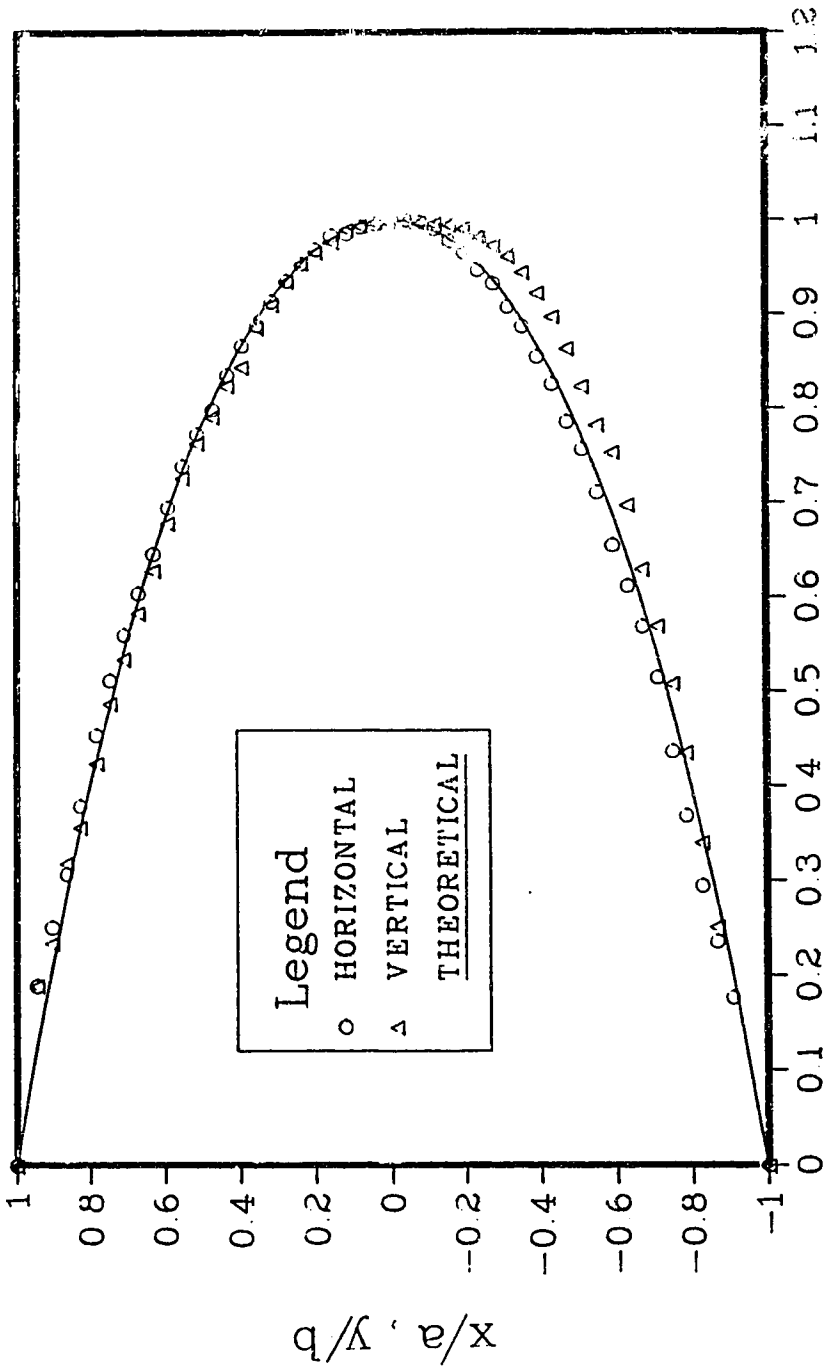

Fig. 3.29 Axial velocity profiles for fully developed laminar flow in a square duct at Re=783

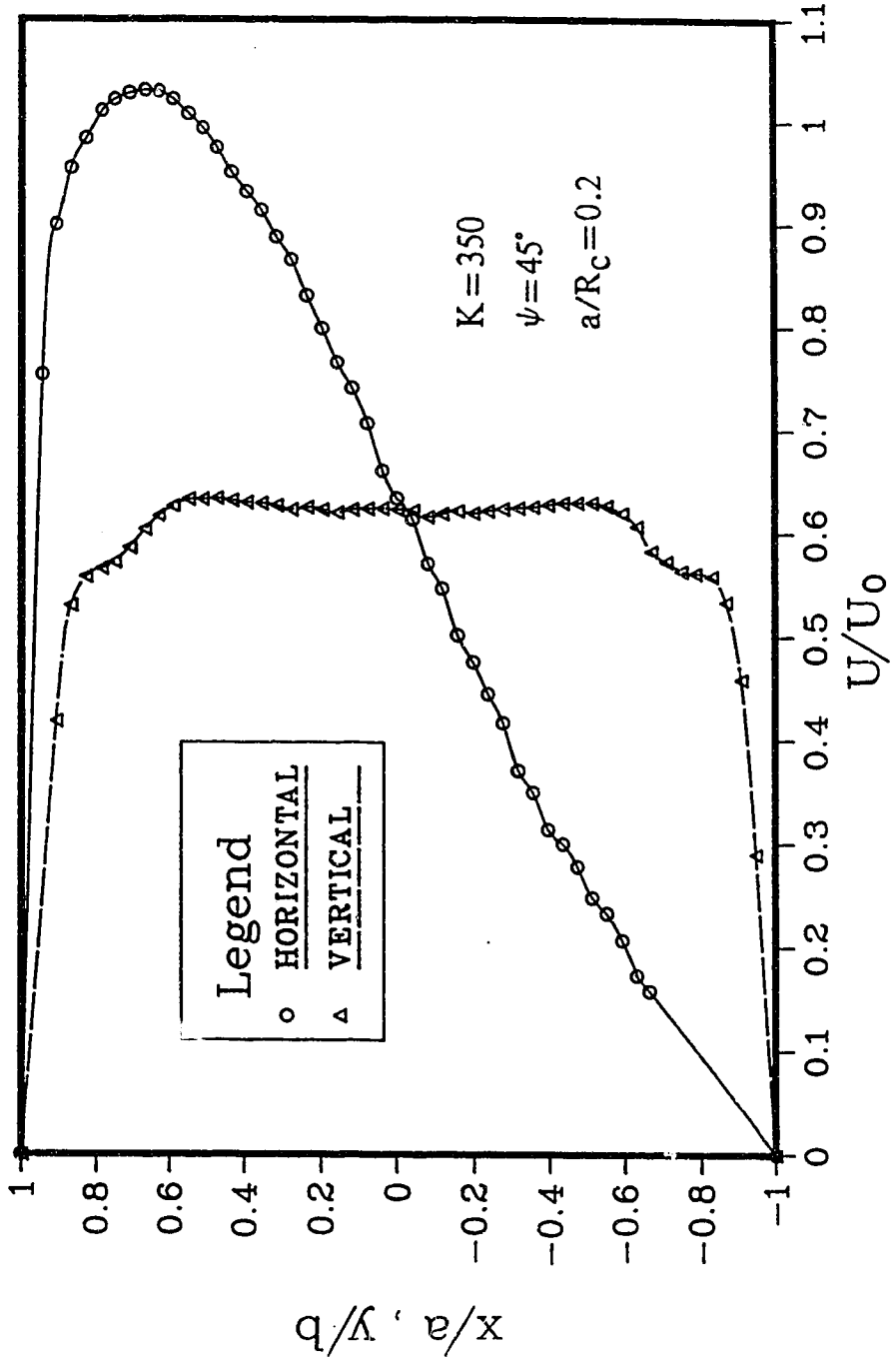

Fig. 3.30 Axial velocity profiles along X and Y axes at the exit of a 45° square bend with $a/R_c=0.2$ and K=350

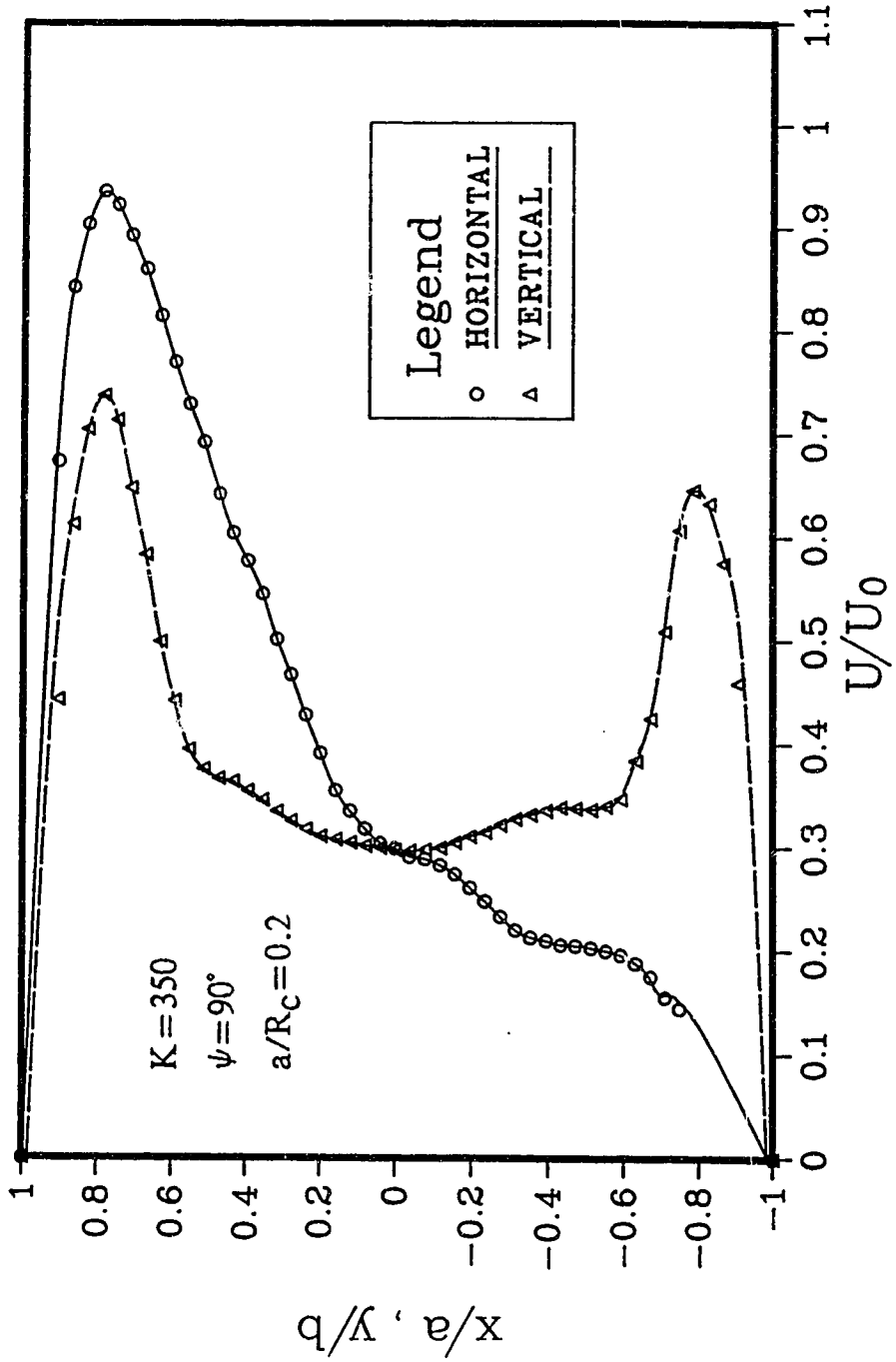

Fig. 3.31 Axial velocity profiles along X and Y axes at the exit of a 90° square bend with a/R_c=0.2 and K=350

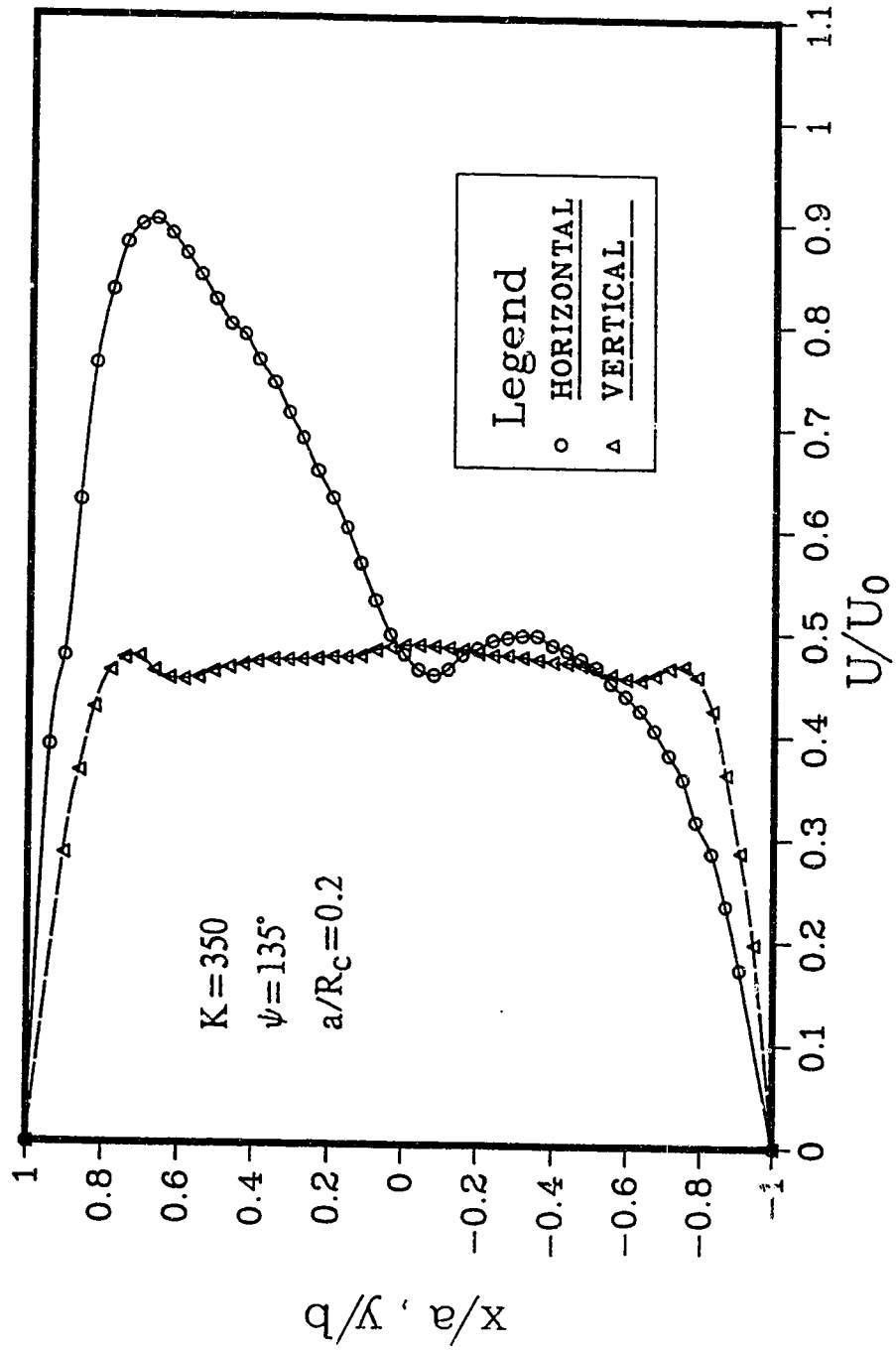

Fig. 3.32 Axial velocity profiles along X and Y axes at the exit of a 135° square bend with a/R_c=0.2 and K=350

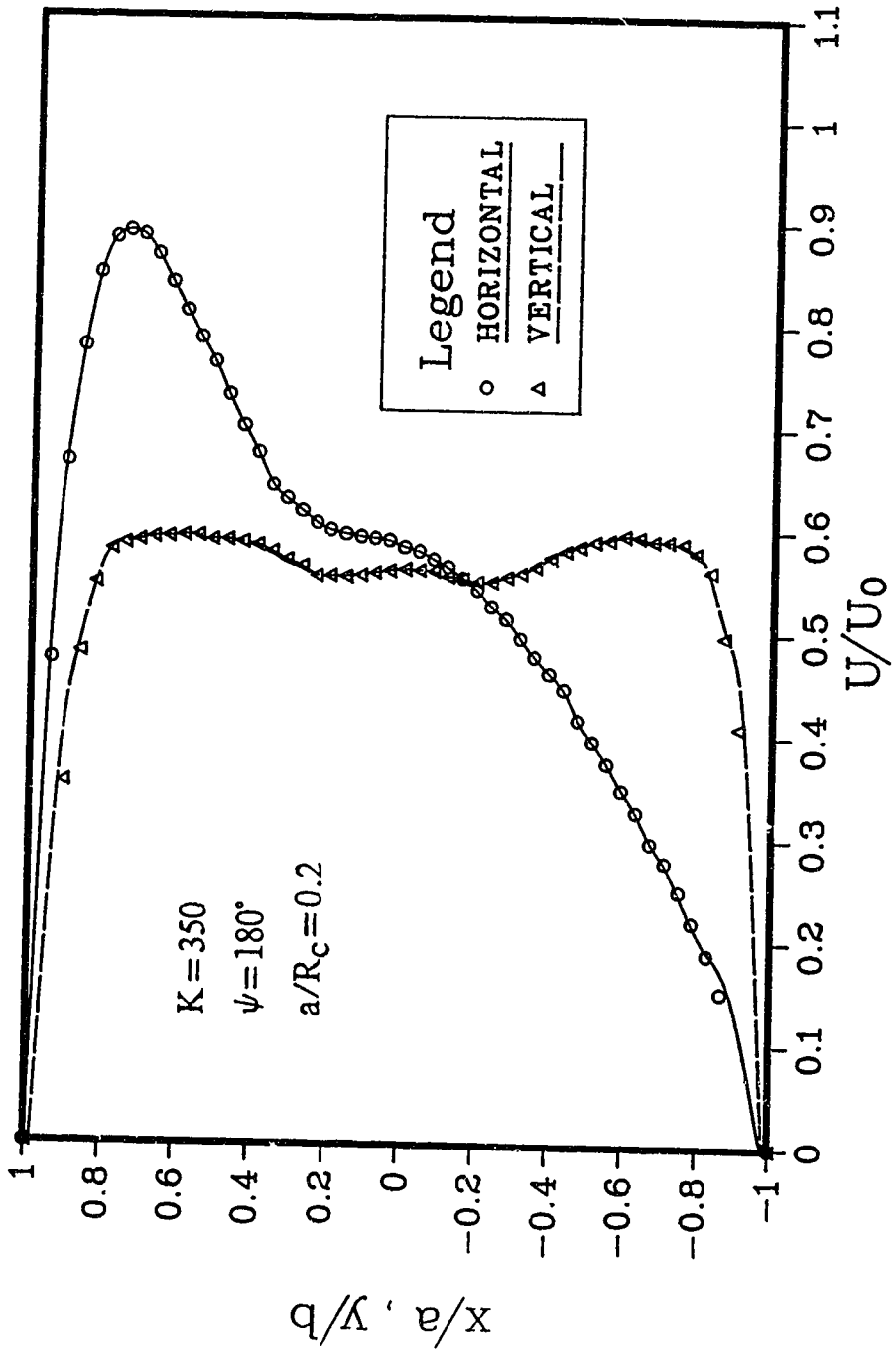

Fig. 3.33 Axial velocity profiles along X and Y axes at the exit of a 180° square bend with a/R_C=0.2 and K=350

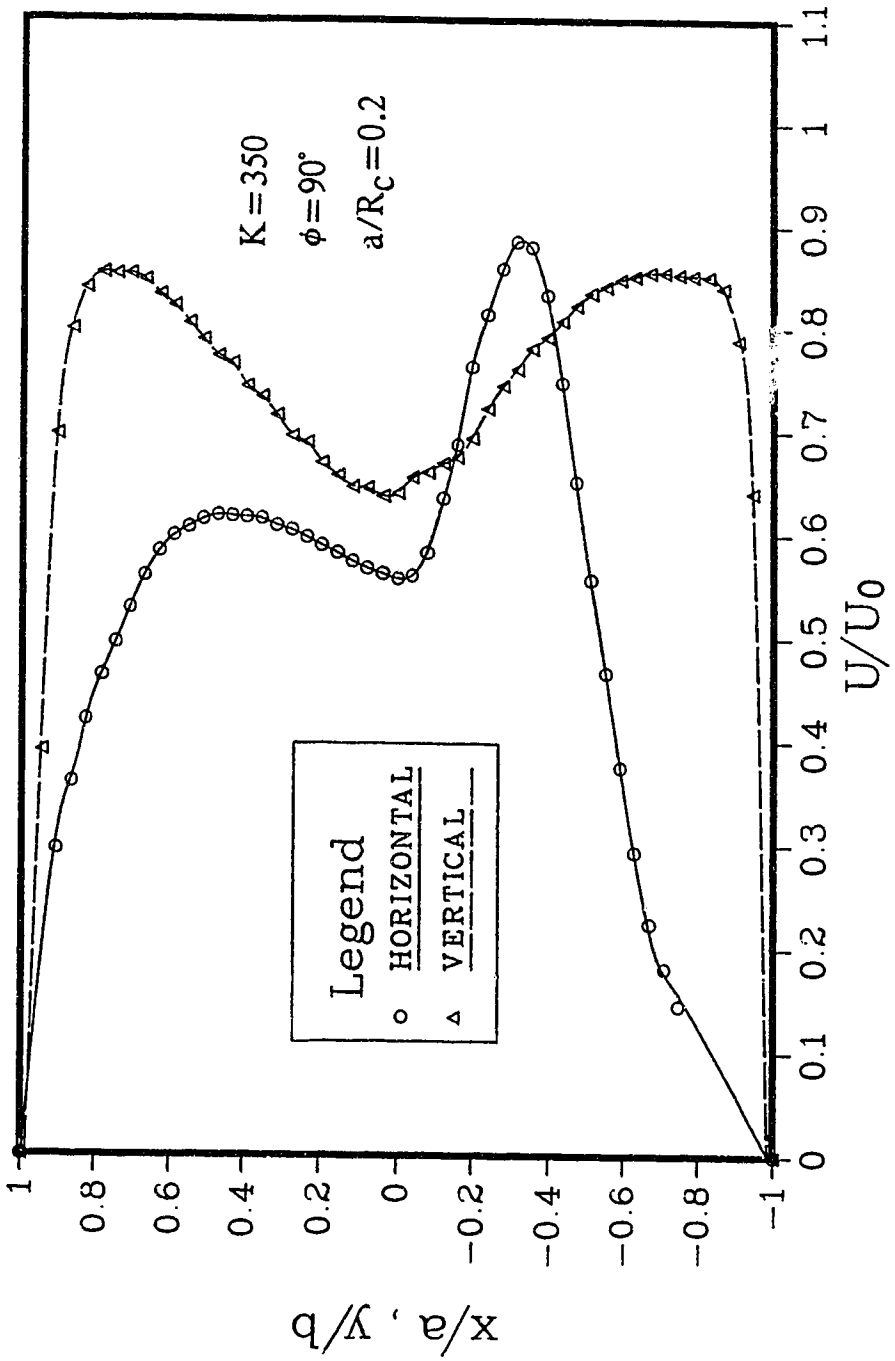

Fig. 3.34 Axial velocity profiles along x and y axes at the exit of a square s-bend with $\phi=90°$, $a/R_c=0.2$ and K=350

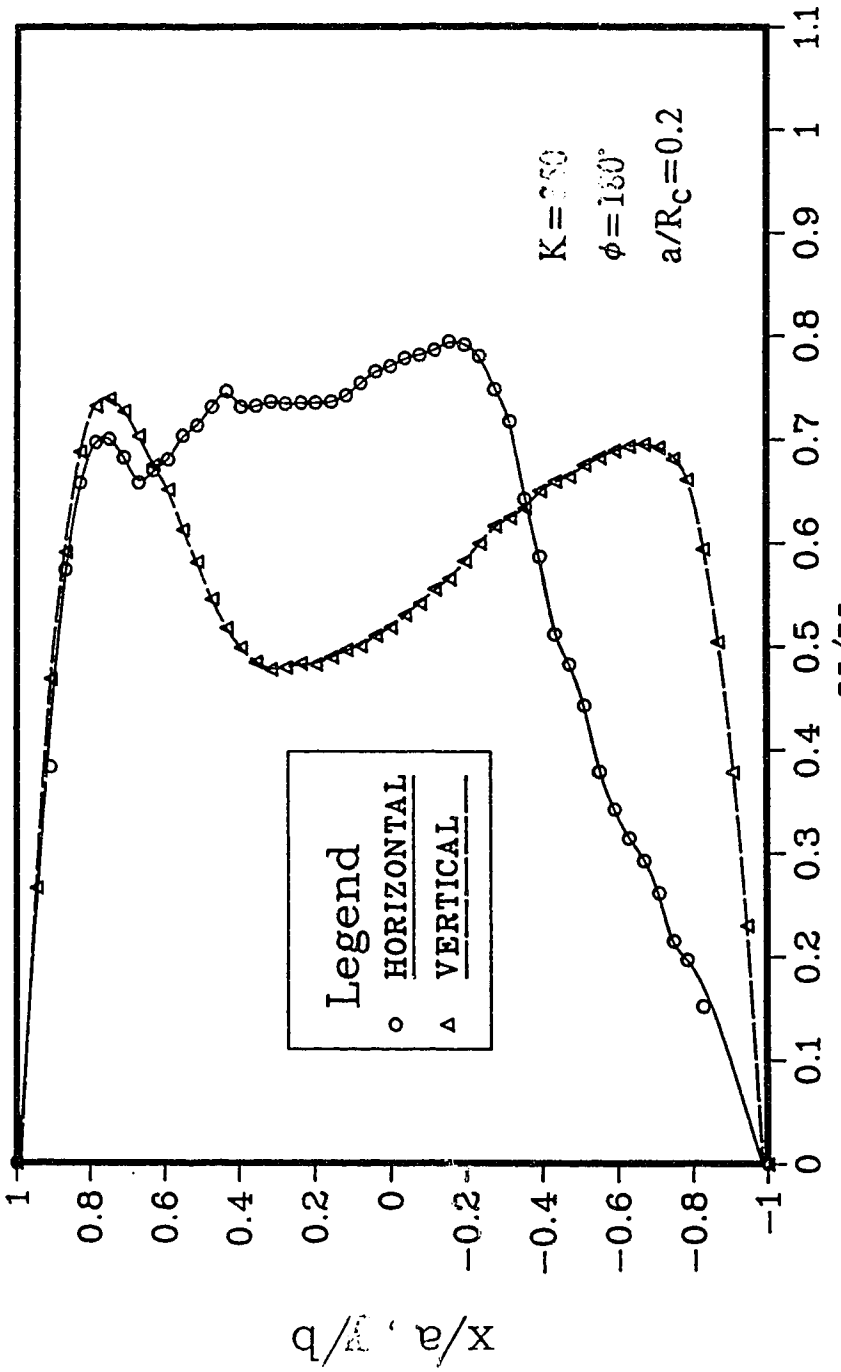

Fig. 3.35 Axial velocity profiles along x and y axes at the exit of a square s-bend with $\phi=180°$, $a/R_c=0.2$ and K=350

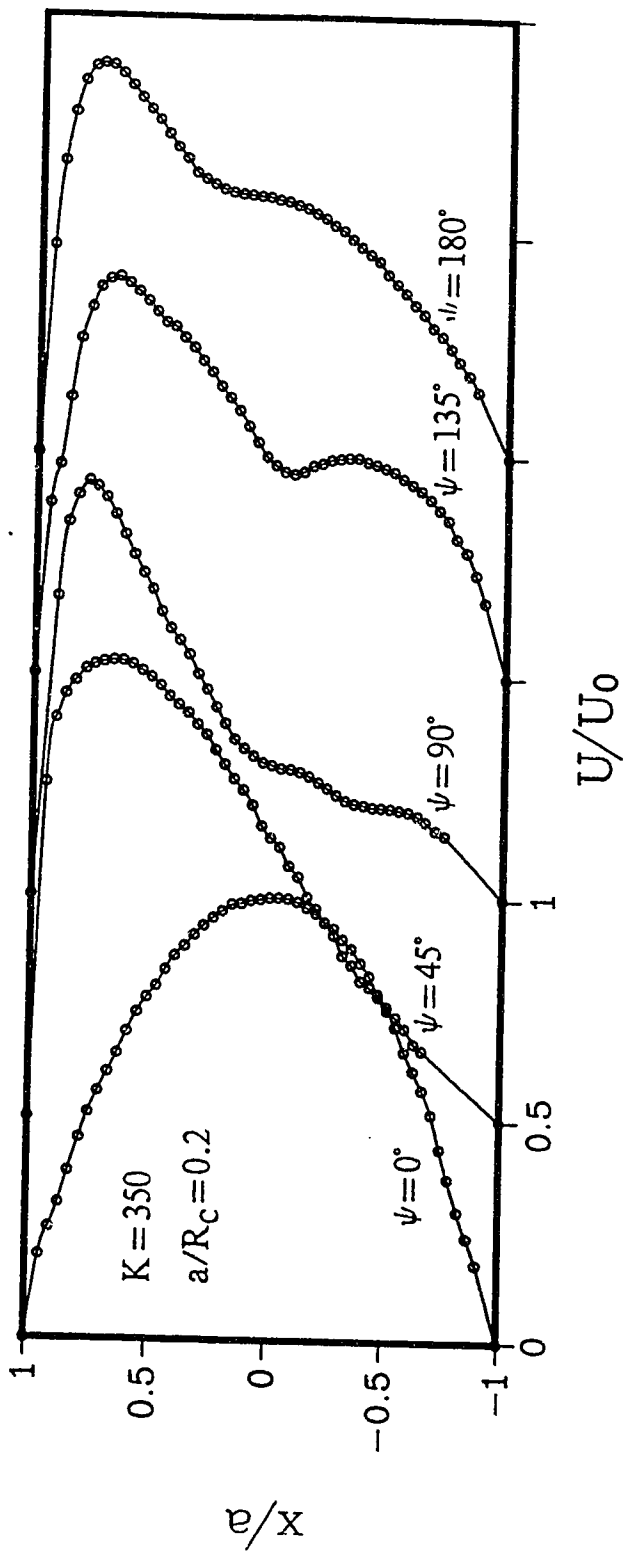

Fig. 3.36 Developing axial velocity profiles along the horizontal axis in a 180° square bend with $a/R_c=0.2$ and K=350

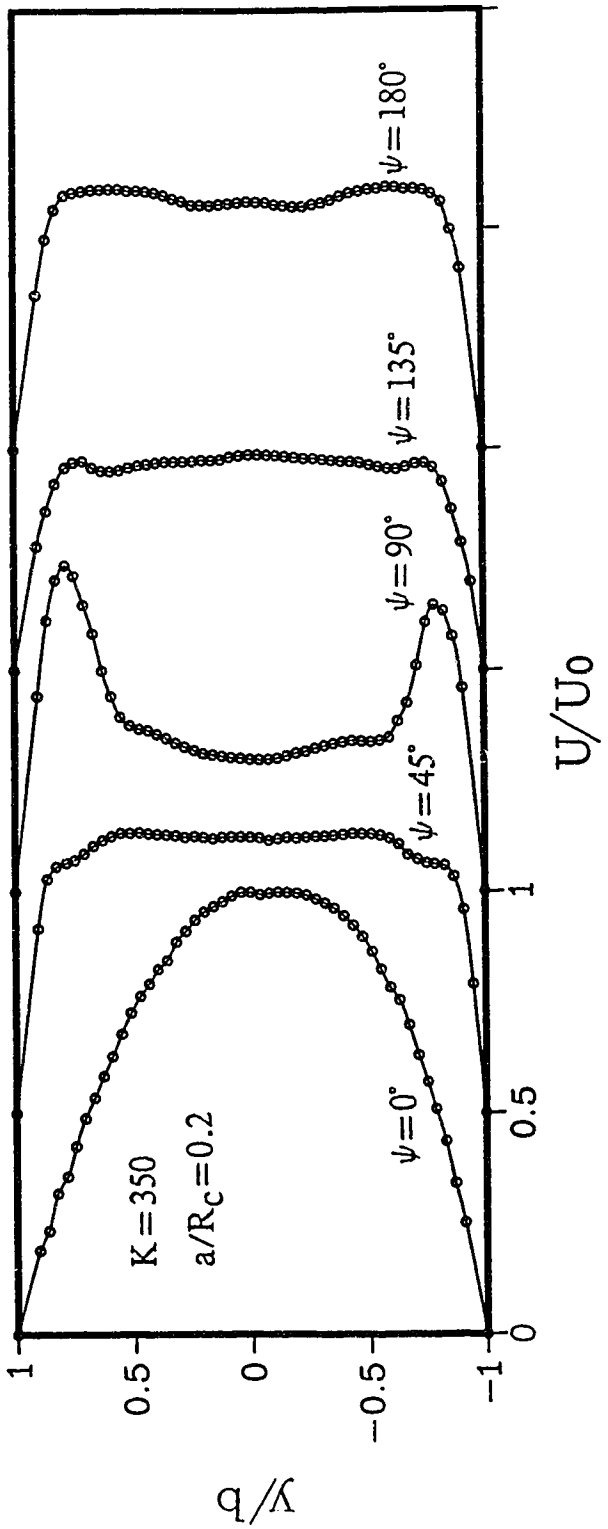

Fig. 3.37 Developing axial velocity profiles along the vertical axis in a 180° square bend with $a/R_c=0.2$ and K=350

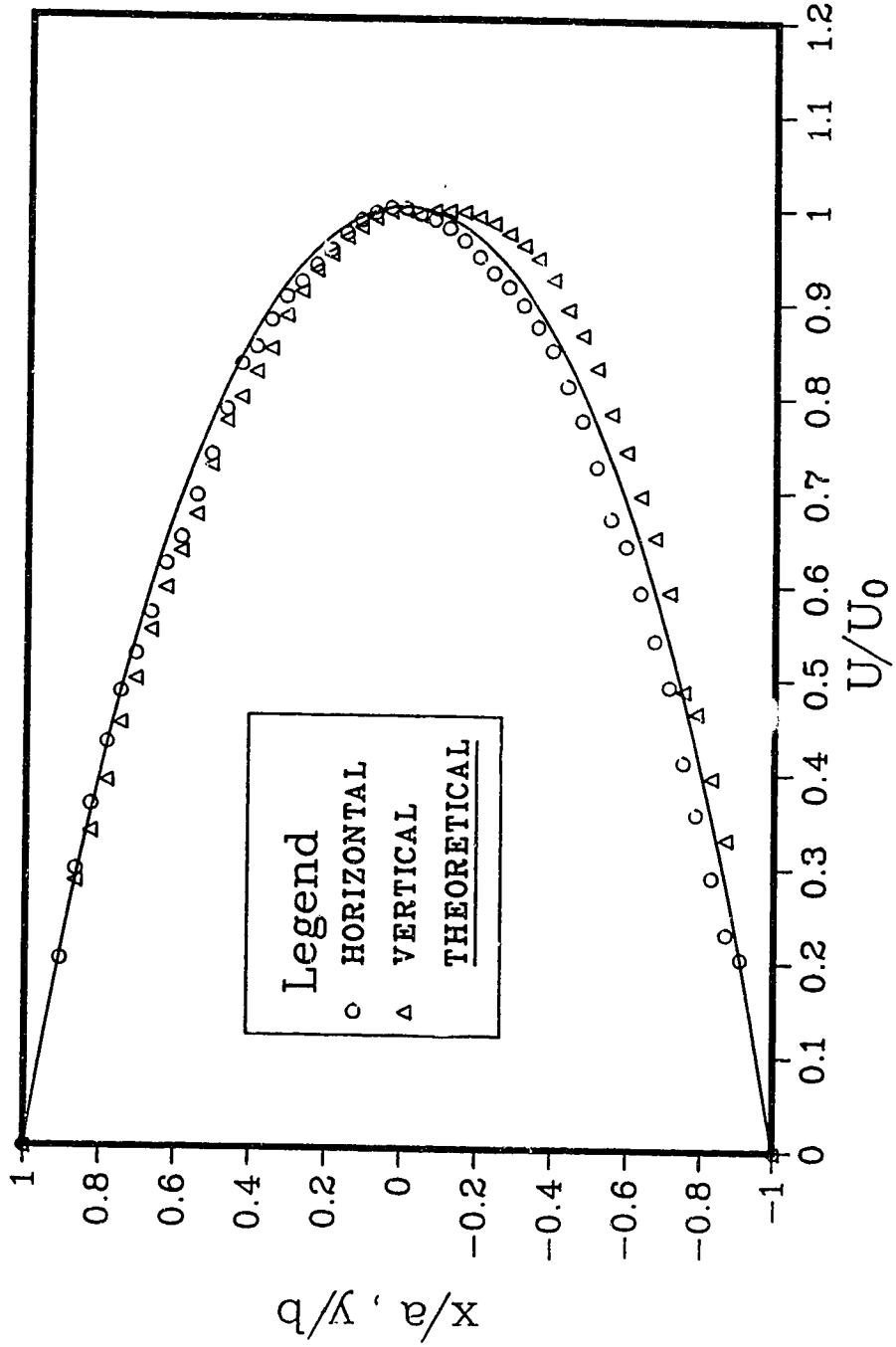

Fig. 3.38 Axial velocity profiles for fully developed laminar flow in a square duct at Re=553

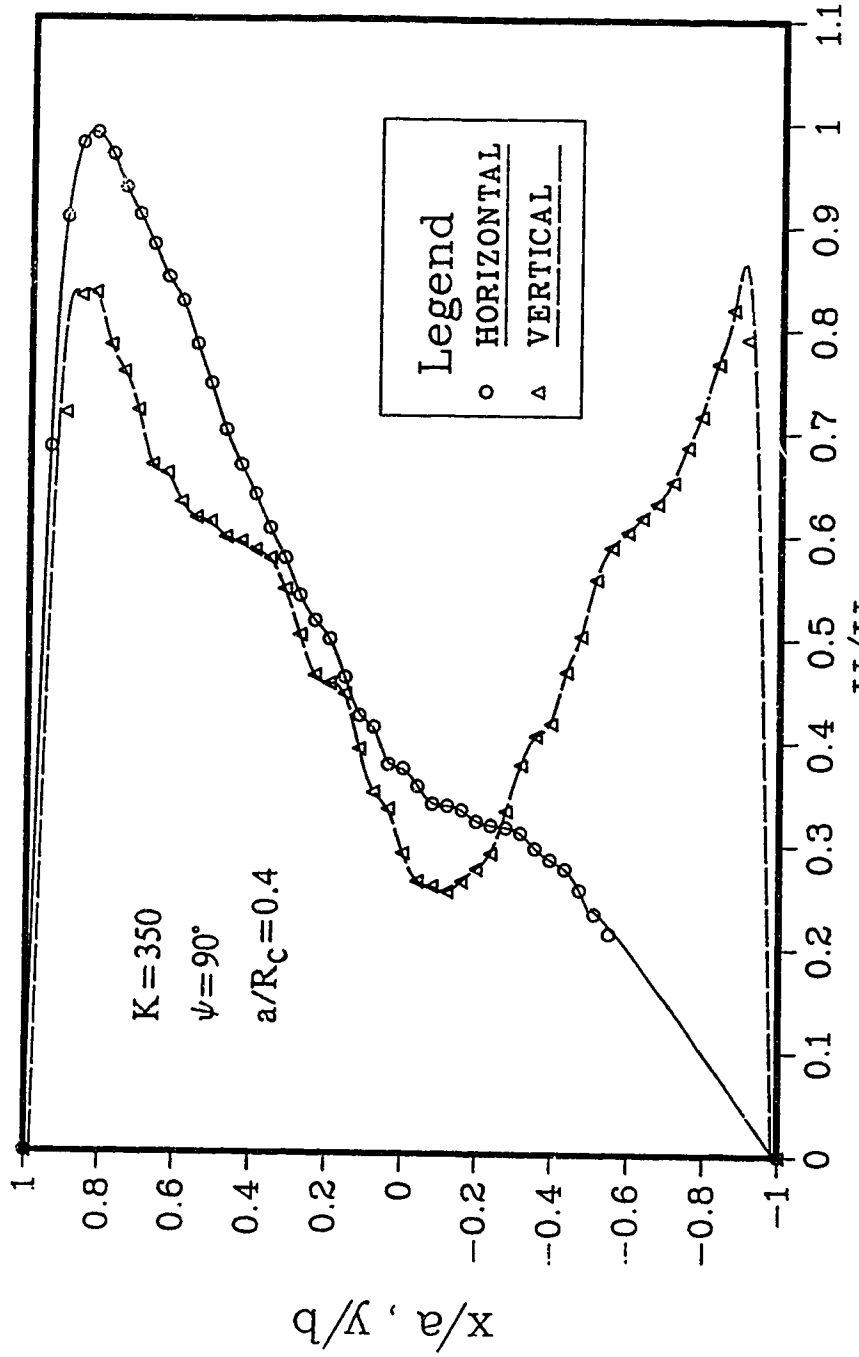

Fig. 3.39 Axial velocity profiles along X and Y axes at the exit of a 90° square bend with a/R_C=0.4 and K=350

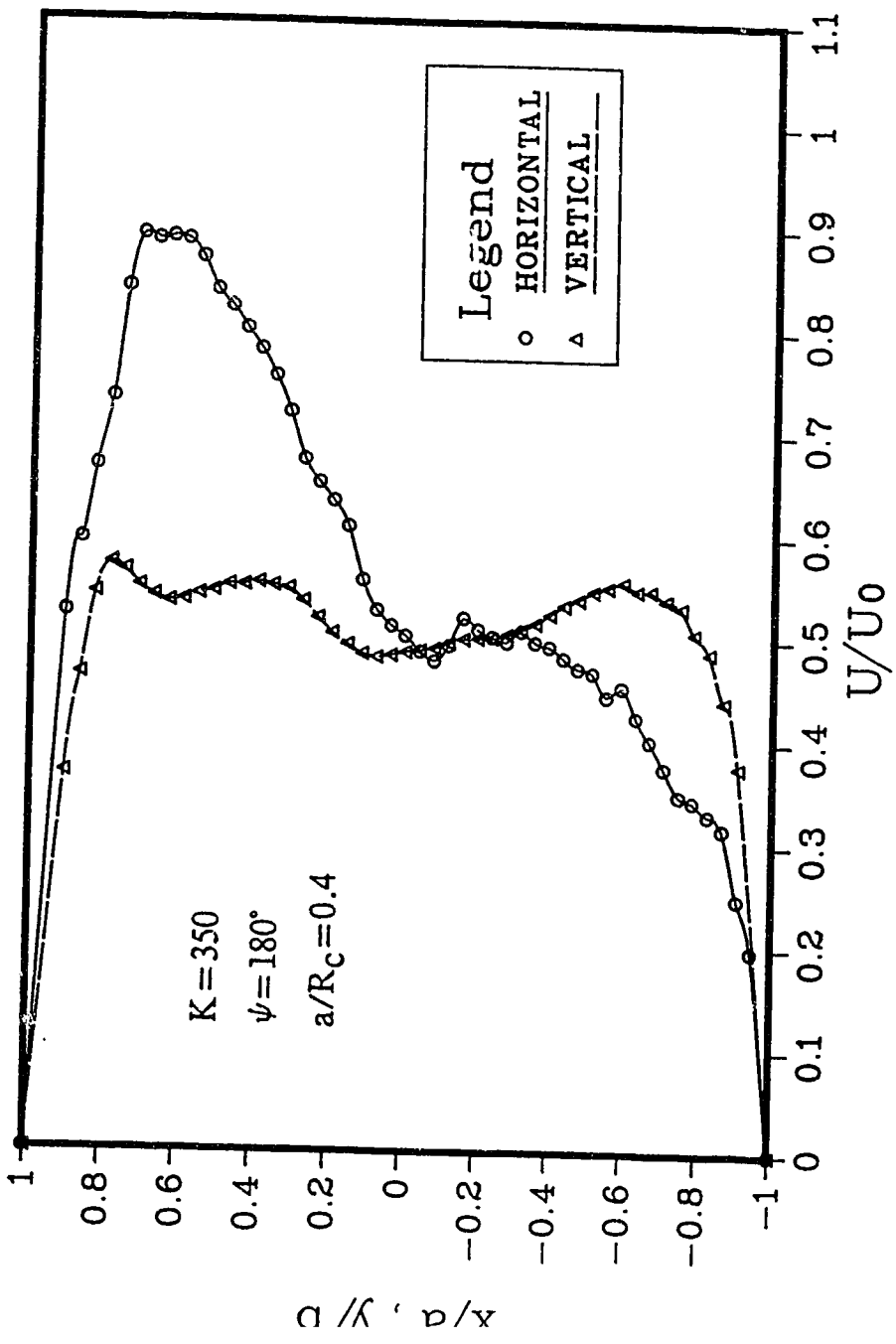

Fig. 3.40 Axial velocity profiles along X and Y axes at the exit of a 180° square bend with a/R_c=0.4 and K=350

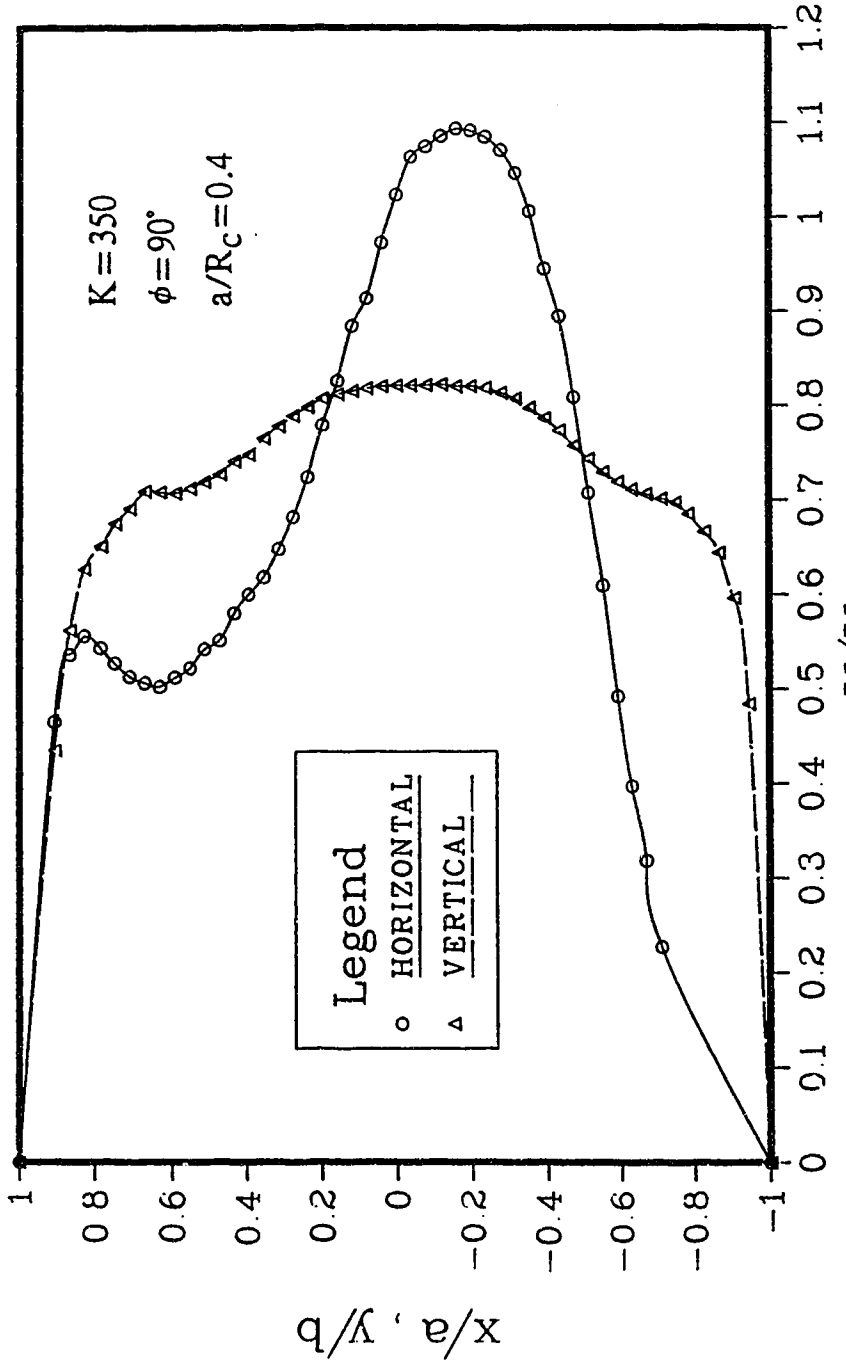

Fig. 3.41 Axial velocity profiles along x and y axes at the exit of a square s-bend with $\phi=90°$, $a/R_c=0.4$ and K=350

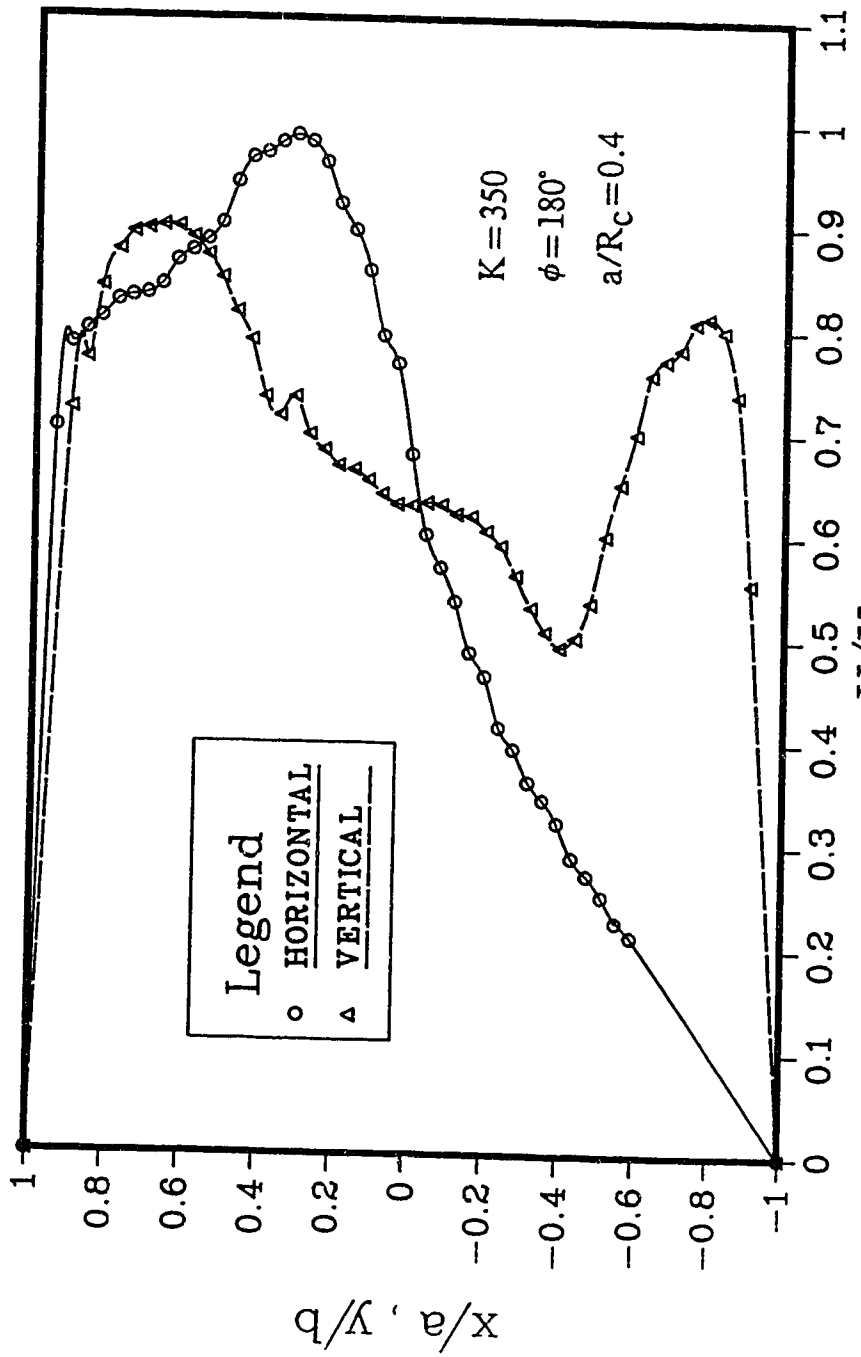

Fig. 3.42 Axial velocity profiles along x and y axes at the exit of a square s-bend with $\phi=180°$, $a/R_c=0.4$ and K=350

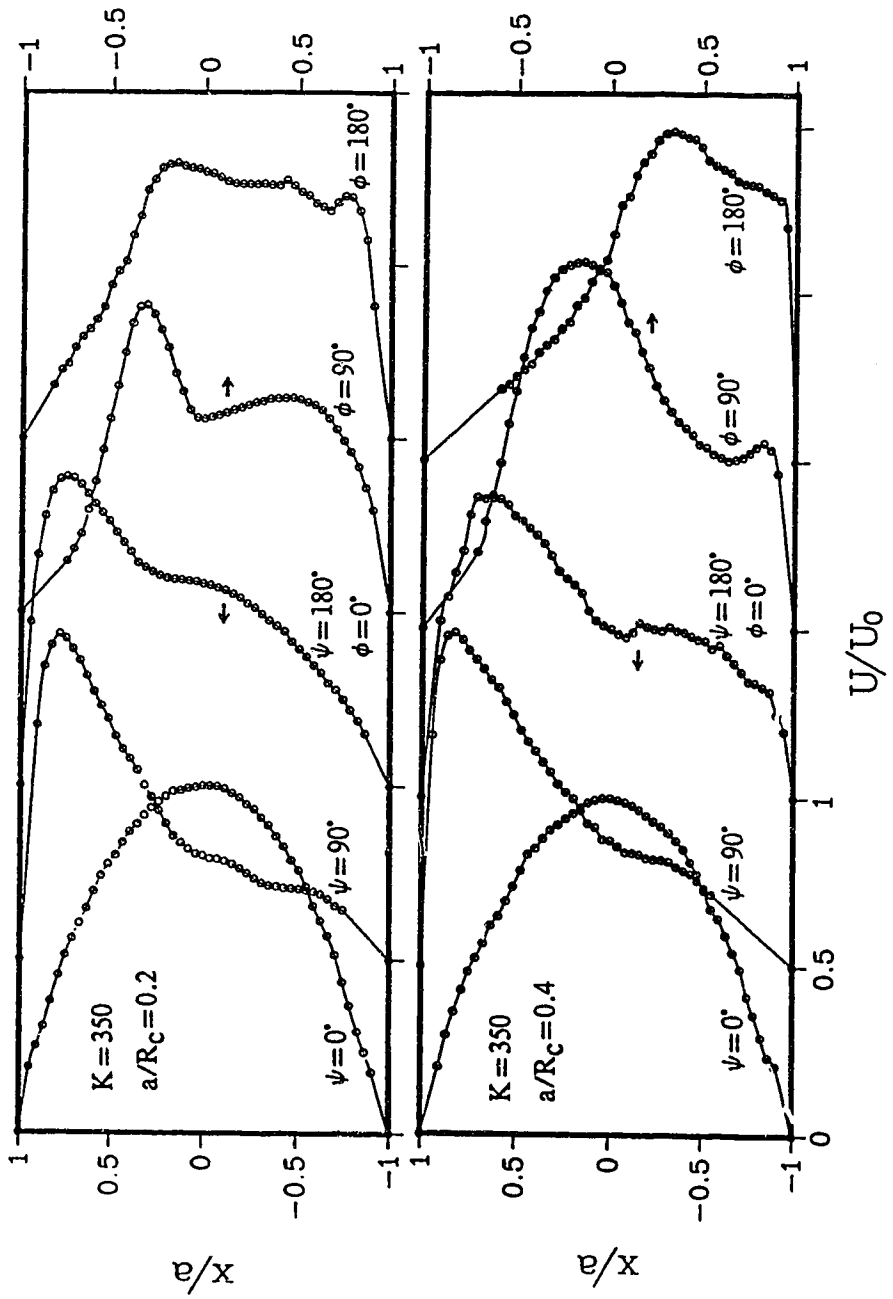

Fig. 3.43 Effects of curvature ratio on developing velocity profiles along the horizontal axis in a square s-bend at a/R_c=0.2, 0.4 and K=350

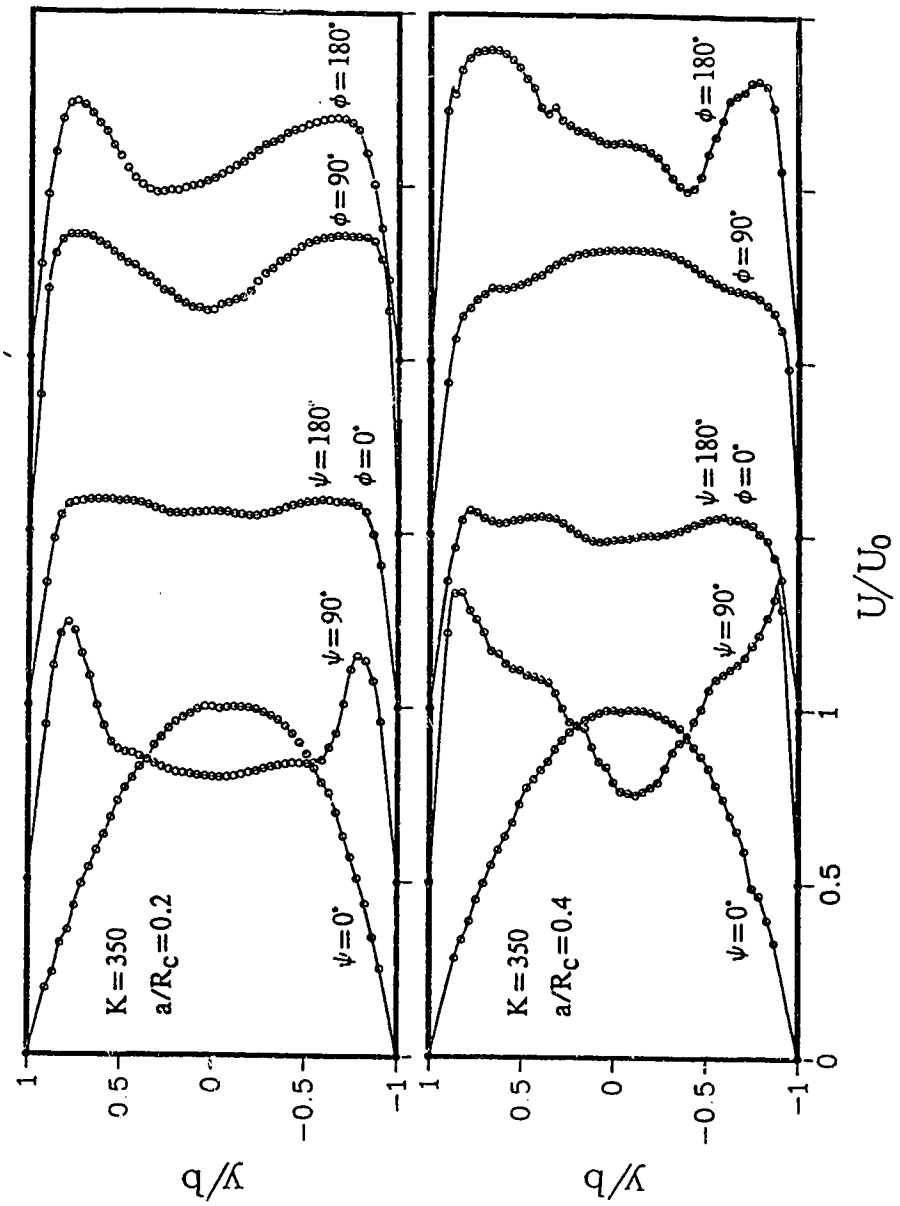

Fig. 3.44 Effects of curvature ratio on developing velocity profiles along the vertical axis in a square s-bend at a/R_c=0.2, 0.4 and K=350

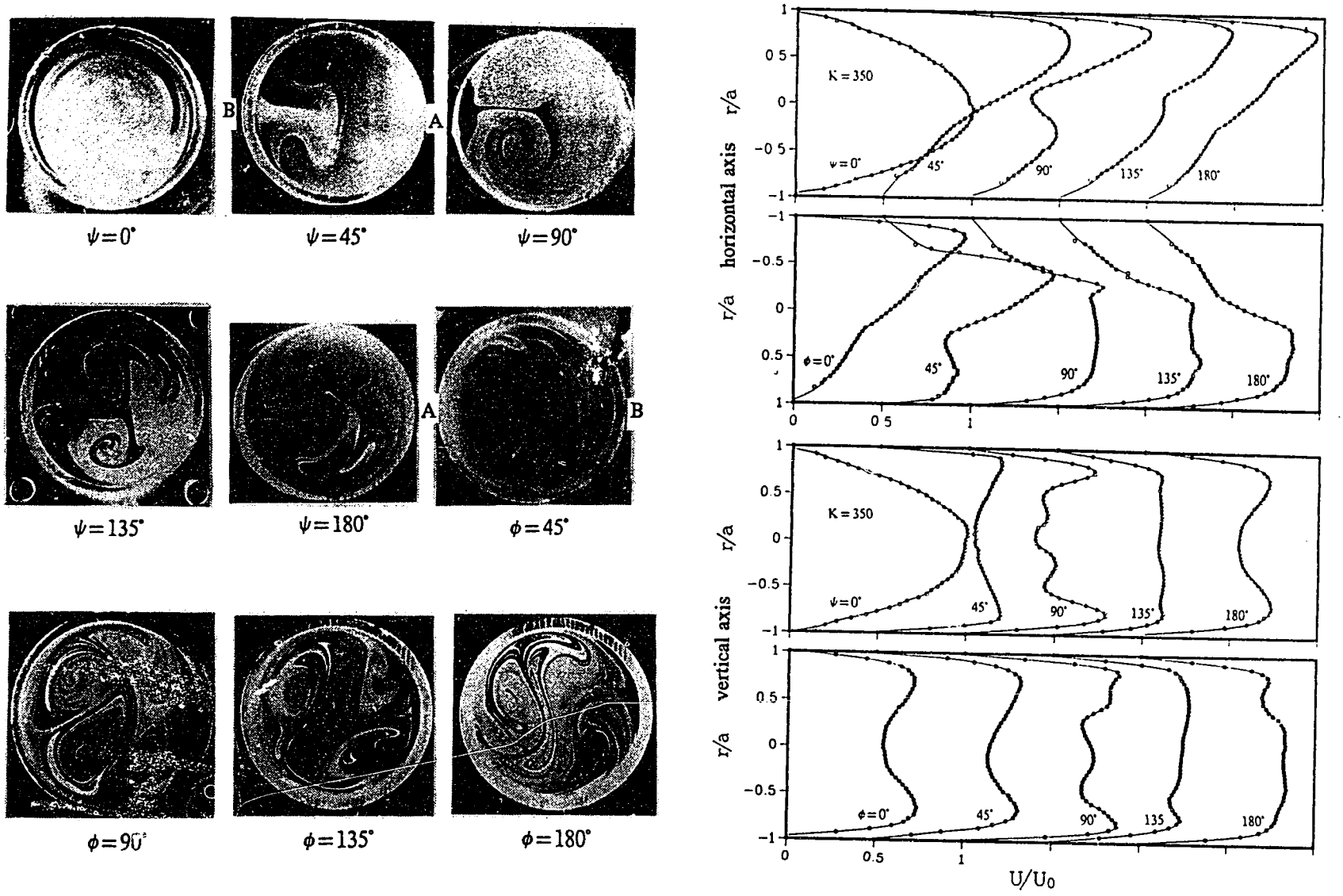

Fig. 3.45 Effects of secondary flow on the axial velocity profiles in a circular s-bend with $a/R_c=0.2$ and K=350

4. Visualization Experiments on Buoyancy Force Induced Secondary Flow in the Entrance Region of Horizontal Rectangular Channels Heated Isothermally from Below and/or Cooled Isothermally from Above

4.1 Introduction

Mixed convective heat transfer in rectangular channels has a variety of engineering applications, such as flat plate solar collectors, compact heat exchangers and electronic component cooling. The characteristics of the mixed convective heat transfer are significantly affected by buoyancy-induced secondary flow.

When fluid passes through a rectangular channel with the bottom plate heated, the fluid near the heated plate becomes less dense, creating a small reduction in pressure which accelerates the flow and enhances heat transfer. However, this effect is usually very small compared with the effect of buoyancy-induced secondary flow caused by convective instability. As the temperature of the bottom plate becomes higher than that of the top plate, a top-heavy situation is formed in the fluid. This situation is not stable and the buoyancy forces can initiate a secondary flow inside the heated boundary layer. The onset of thermal instability arises in the form of longitudinal vortices and a substantial increase in the heat transfer coefficient above the forced convection limit results. Subsequent variation of the heat transfer coefficient with the

longitudinal coordinate may lead to a final value which is typical of turbulent free convection.

As the longitudinal vortex rolls caused by the thermal instability may enhance heat transfer by reducing thermal entrance length and by inducing early transition to turbulence, the effect of buoyancy forces on laminar forced convective flows has been studied by many investigators.

Mori [1] and Sparrow et al. [2] independently studied buoyancy effects in laminar forced convective flow along a heated horizontal semi-infinite flat plate in the early 60's. Sparrow and Husar [3] clearly showed the occurrence of longitudinal vortices in natural convection boundary-layer flows along isothermal surfaces by a flow visualization technique to reveal the flow patterns. Mori and Uchida [4] studied the onset of an infinitesimally small disturbance for fully developed laminar flow between parallel plates by applying linear stability theory. The secondary flow was observed to be in the form of longitudinal vortex rolls, and they also found that, for Rayleigh number less than approximately 18,000, the roll pitch was twice the plate spacing. Nakayama et al. [5] theoretically investigated the convective instability concerning the onset of longitudinal vrotices due to the buoyancy forces for fully developed laminar forced convection between two horizontal plates. This problem was also studied experimentally by Akiyama et al. [6].

Hwang and Cheng [7] theoretically determined the critical Rayleigh number for the onset of convective instability. However, later experimental studies [8, 9, 10] found that the critical Rayleigh number is larger than the theoretical value given by Hwang and Cheng. Recent experiments on mixed convection air flow in horizontal and inclined channels were performed by Maughan and Incropera [11]. They used the departure of spanwise-average longitudinal Nusselt number from the forced convection results to determine the onset and they found that their experimental instability data are in good agreement with the results of previous experiments.

Recent studies include the investigations by Incropera and Schutt [12], Cheng and Kim [13], Incropera, Knox and Maughan [14], Maughan and Incropera [15], Chou and Hwang [16], and by Chou and Lin [17]. Incorpera and Schutt [12] solved a laminar, three-dimensional, steady-state model to study the laminar mixed convection in the entrance region of horizontal rectangular ducts with heated top and bottom surfaces and insulated sidewalls. Cheng and Kim [13] studied the vortex instability of natural convection flow on slightly inclined isothermally heated flat plates by flow visualization using the smoke injection method, and presented the instability data for critical Grashof number and wavelength for the onset of longitudinal vortices. Incropera et al. [14] experimentally studied the mixed-convection flow and heat transfer in the entry region

of a horizontal rectangular duct with uniform bottom heating. Maughan and Incropera [15] performed experiments to investigate onset and development of the buoyancy driven secondary flow in a horizontal parallel plate channel with uniform bottom heating. Chou and Hwang [16] reported their results of numerical solutions by a vorticity-velocity method for combined free and forced laminar convection in the thermal entrance region of a horizontal rectangular channel without assumptions of large Prandtl number and small Grashof number. Chou and Lin [17] reported their systemetic theoretical studies on convective instability in the thermal entrance region of horizontal rectangular channels by means of the vorticity-velocity method. They obtained the variation of the local Nusselt number with dimensionless axial position as a function of Rayleigh number. More literature can be found in [18-21].

Although the problems of the convective instability of forced flow in retangular channels have been studied by many investigators, most studies were concerned about the case of heating from below. The purpose of this chapter is to study the developing secondary flow patterns in the simultaneous hydrodynamic and thermal entrance region of horizontal channels with isothermally heated lower wall and/or isothermally cooled upper wall by the smoke injection method. Photographs for developing secondary flow patterns are presented to study the convective instability and chaotic phenomena due to the buoyancy effects caused by

heating from below and/or cooling from above. The effects of Grashof number and Reynolds number on the instability phenomena are also discussed.

4.2 Experimental Apparatus and Procedure

4.2.1 General Description of Test Setup

Fig. 4.1 shows the schematic diagram of the experiment setup. Except for the settling chamber, the test section and the heating and cooling systems, all other experimental apparatuses are the same as the ones used in the experiments of Chapter Two.

The settling chamber is a steel rectangular box with several screen layers inside, and has a contraction with streamlined outlet portion with large contraction ratio(1:0.13 for a/b=2, 1:0.16 for a/b=7) so that the settling chamber can steady the incoming flow and provide a quite uniform flow at the exit of the chamber.

The bottom plate of the test section was heated by hot water coming from a large hot water tank. The water was heated by an electric heater, and water temperature was kept at a fixed value by a temperature controller. The top plate was cooled by two kryostats (model HAAKE F3-K) using engine antifreeze coolant. A camera was located at the exit of the test section to take photographs.

4.2.2 The Test Section and Temperature Measurement

Fig. 4.2 shows the schematic diagram of the test section which is a rectangular channel with inside height b=28.6 mm. The side walls were made of acrylic resin plates, and the thickness of the side walls was 12 mm. The top plate was an aluminium flat plate with cooling channel. Its temperature was controlled by the circulating antifreeze liquid cooled by the two kryostat units. The top surface was covered by insulation. The bottom was a copper flat plate. Both of the top and bottom plates were 233 mm wide and 1523 mm long. The isothermal condition of the bottom copper plate was maintained by circulating the water at high speed through the water channel attached below the bottom surface of the test plate. The water was heated by an electric heater inside the water tank, and the heater was controlled by a temperature controller. There was a stirrer inside the water tank to mix the heated water evenly.

The temperatures of the bottom and top plates were measured by four 0.3 mm diameter copper-constantan thermocouples attached on each plate. These thermocouples were embedded in a 1 mm deep depression and covered with aluminium epoxy along the plates. The four thermocouple readings for each plate agreed well within the calibration error after the steady-state was reached.

The temperature of the mixed airsmoke flow was also measured by a 0.3 mm diameter copper-constantan thermocouple at the inlet of the settling chamber. The inlet and outlet

temperatures of the circulating water to the test section were monitored by two 0.8 mm iron-constantan sheathed thermocouples. The difference of these two thermocouple readings was less than 0.2°C due to the high speed of the circulating water. All these thermocouple readings were measured by a data acquisition system composed of a Hewlett Packard 85 micro-computer and a Hewlett Packard data acquisition/control unit (model HP 3497A), and converted to temperature by the computer.

4.2.3 Air Flow Rate Measurement, Flow Visualization and Photographic Techniques

The methods of flow rate measurement, flow visualization and photograph were similar to the methods used in the experiments of Chapter Two. Sections 2.2.2 and 2.2.3 give a detailed description of these methods. However, the lens of the camara used here was a 90 mm zoom lens.

4.2.4 Experimental Parameters

The experimental parameters and their ranges for this investigation on thermal instability problems are shown in Table 4.1.

Table 4.1 Ranges of Experimental Parameters

Aspect ratio, a/b	2, 7
Height of the channel, b	28.6 mm
Mean velocity, U_m	0.1, 0.2, 0.3, 0.4 m/sec.
Temp. of top plate, T_c	23°C, -6°C(a/b=2), -17°C
Temp. of bottom plate, T_h	23°C, 51°C
Inlet air temperature, T_{air}	23, 24°C
Reynolds number, Re	2.1×10^2~1.05×10^3(a/b=2), 2.8×10^2~1.32×10^3(a/b=7)
Grashof number, Gr	1.5×10^5~5.0×10^5(a/b=2), 3.6×10^5~1.2×10^6(a/b=7)
Prandtl number, Pr	0.71(air)

The Grashof number is defined based on temperature difference $\Delta T=T_h-T_c$ and hydraulic diameter $De=2ab/(a+b)$. Physical properties of air were determined based on the mean temperature of the top and bottom plates.

The experiments for rectangular channel with a/b=2 were conducted for four cases:

Case (1) $T_h-T_c\approx29°C$ $T_c=T_{air}\approx23°C$

Case (2) $T_h-T_c\approx30°C$ $T_h=T_{air}\approx23°C$

Case (3) $T_h-T_c\approx41°C$ $T_h=T_{air}\approx23°C$

Case (4) $T_h-T_c\approx68°C$ $T_h\approx51°C$, $T_{air}\approx24°C$

The experiments for rectangular channel with a/b=7 were made for three cases:

Case (1) $T_h-T_c\approx30°C$, $T_c=T_{air}\approx23°C$

Case (2) $T_h-T_c\approx30°C$, $T_h=T_{air}\approx24°C$

Case (3) $T_h-T_c\approx69°C$, $T_h\approx52°C$, $T_{air}\approx24°C$

For each case the mean air velocity was set at 0.1, 0.2, 0.3, 0.4 m/sec.. Photographs were taken at positions between l=10 cm to 120 cm measured from the inlet of the channel with a step of 10 cm. On the presented photographs, the position was indicated by the inverse Graetz number z=(l/De)/(RePr).

4.3 Results and Discussion

4.3.1 Results for Aspect Ratio a/b=2

Case (1), $\Delta T=29°C$, $T_c=T_{air}=23°C$

Figs. 4.3 to 4.6 show the cross-sectional views of developing secondary flow patterns for Case (1). In this case, the air flow was heated isothermally from below. It is noted that the air moves up along the side walls and comes down at the center. At small values of inverse Graetz number z, the secondary flow cannot reach the bottom plate when fluid comes down due to the heated layer near the bottom plate. At intermediate values of z, a pair of inverted mushroom-form vortices appears showing the dominating viscous effect. Further downstream, the secondary flow becomes more intense and the flow pattern becomes more complex. It seems that, at locations further downstream, the secondary flow pattern is no longer a single pair of

vortices. The pair of vortices splits into two pairs. This phenomenon can be seen clearly at $z=1.04\times10^{-1}$ in Fig. 4.4, and at $z=5.27\times10^{-2}$ in Fig. 4.5.

It is also noted that, at higher main air flow velocity, the inverted mushroom-shape secondary flow pattern appears later, and the flow pattern is more stable due to the larger effect of Reynolds number relative to that of Grashof number.

Case (2), $\Delta T=30°C$, $T_h=T_{air}=23°C$

Figs. 4.7 to 4.10 show the secondary flow patterns for Case (2). The temperature difference is almost the same as that of Case (1), but the air flow is cooled isothermally from above. It is noted that the secondary flow direction is opposite to that of Case (1), that is, fluid moves up at the center and comes down along the side walls. This difference is caused by the temperature of side walls. When the steady thermal state is reached, the vertical temperature distribution of the side walls is believed to be linear. Thus the sidewall temperature is higher than that of the main stream flow for Case (1), and is lower for Case (2). That means the side walls heat the flow for Case (1), and cool it for Case (2).

It is noted that, at smaller values of z, the secondary flow is quite regular. The two-pair-vortex pattern again appears at $z=5.86\times10^{-2}$ in Fig. 4.8, but the rotation direction is opposite to that of Case (1). For both Cases (1) and (2), a secondary flow pattern with more than two

pairs of vortices seems to be possible at downstream positions (see Figs. 4.5 and 4.8). It is also observed that the flow patterns for Case (2) are less stable than those of Case (1).

Case (3), $\Delta T=41°C$, $T_h=T_{air}=23°C$

Figs. 4.11 to 4.14 show the results of Case (3), which is also a cooling case but the temperature difference is about 10°C larger than that of Case (2). The larger density gradient causes the secondary flow to occur earlier, and the flow patterns are more unstable and more complex at downstream positions as compared with the secondary flow in Case (2). Only six photographs were taken when $U_m=0.1$ m/sec., because the flow became turbulent, and flow patterns were not clear at further downstream positions due to smoke diffusion.

At $z=3.5\times10^{-3}$ and 1.05×10^{-2} in Fig. 4.14, a pair of vortices is formed at the center of the top plate in the form of an inverted mushroom-shape. It seems that the fluid cooled by the top plate comes down, but then is pushed back by the fluid which is moving up.

Case (4), $\Delta T=68°C$, $T_h=51°C$, $T_{air}=24°C$

The results of Case (4) are shown in Figs. 4.15 to 4.19. In this case, the fluid is heated from below and cooled from above simultaneously with large temperature difference $\Delta T=68°C$. Hence the buoyancy force effect is significant. The secondary flow patterns are very unstable, especially for the case with smaller main flow velocity. It

is more difficult to obtain a clear secondary flow pattern due to smoke diffusion. At position $z=2.07\times10^{-2}$ in Fig. 4.17 the flow pattern with two pairs of vortices is also observed. At position $z=2.32\times10^{-2}$ in Fig. 4.18, a large inverted mushroom-shape vortex appears, but the flow pattern is not symmetric. In fact, most of these buoyancy force induced secondary flow patterns are not symmetric and become chaotic to some degree for the case with large temperature difference.

4.3.2 Results for Rectangular Channel with a/b=7

Case (1), $\Delta T=30°C$, $T_c=T_{air}=23°C$

Figs. 4.19 to 4.22 show the results of Case (1). Fluid is heated from below, and the effect of side walls is heating. Before the formation of the secondary flow, most of the smoke appears near the bottom plate due to its larger density. The vortices appearing earlier near the side walls are caused by the effect of side walls. It is noted that the vortex rolls appear later for the channel with a/b=7, because the side walls are farther away from the center region, and the side walls have little effect on the flow at the center.

It is noted from Fig. 4.19 that, after the onset of thermal instability, some small mushroom-shape vortices appear. At position $z=5.14\times10^{-2}$, three pairs of vortices are formed in addition to the vortices at the side walls. Further downstream at $z=8.22\times10^{-2}$, the number of vortex pair

is reduced to two. After that the flow patterns become very unstable and unclear. At larger main flow velocity, the onset of thermal instability appears later, and the secondary flow becomes less unstable and develops more slowly.

Case (2), $\Delta T=30°C$, $T_h=T_{air}=24°C$

Figs. 4.23 to 4.26 show the Case (2), in which the fluid is cooled at the top plate, and the effect of side walls is cooling. The temperature difference is almost the same as that of Case (1), but it is noted that the buoyancy force induced secondary flow is more unstable, and the onset of thermal instability appears earlier for the cooling case. At position $z=3.42\times10^{-2}$ in Fig. 4.23, three pairs of vortices are observed. However, most of the flow patterns are complex and the number of vortex pair is not clear.

Case (3), $\Delta T=69°C$, $T_h=52°C$, $T_{air}=24°C$

The results of Case (3) are shown in Figs. 4.27 to 4.30. In this case, the fluid is heated from below and cooled from above. The temperature difference between the top and the bottom plates is about 70°C. It is found that the onset point of thermal instability does not change much as compared with that of Case (2), but the secondary flow develops faster after the onset point, and becomes turbulent more quickly especially for the flow with small main flow velocity.

4.3.3 Concluding Remarks

The buoyancy force induced secondary flow patterns of flow in rectangular channels with aspect ratio a/b=2 and 7 were studied by a flow visualization technique of smoke injection. The fluid in the channels was heated isothermally from below and/or cooled isothermally from above with mean velocity of the main flow varied from 0.1 to 0.4 m/sec..

It was found that, at the same temperature difference, the cooling case flow is more unstable. For the case of aspect ratio a/b=2, the direction of secondary flow for the heating case is opposite to that for cooling because the side wall effect is different. For channels with small aspect ratio, the effect of side walls is very significant, and the secondary flow appears earlier. So that heat transfer in channels with smaller aspect ratio should be more efficient.

In the case of aspect ratio a/b=7 with simultaneous heating and cooling, the onset position of thermal instability is not much different from that for the case of cooling. However, the secondary flow develops much faster after the onset point than the heating and cooling cases. For larger mean velocity flow, the onset of thermal instability appears later, and longitudinal vortex rolls become stable. In other words, the main flow has a stabilizing effect.

The present visualization study clearly reveals the buoyancy force induced complex secondary flows in heated

and/or cooled rectangular channels with different aspect ratios. It is also believed that the present photographs of the longitudinal vortex rolls provide considerable physical insight into mixed convection flow in rectangular channels. Many new secondary flow patterns were revealed in this study and the results should be useful for future investigations.

4.4 References

1. Mori, Y., "Buoyancy Effects in Forced Laminar Convection Flow Over a Horizontal Flat Plate", ASME J. Heat Transfer, 1961, Vol. 83, pp. 479-482.

2. Sparrow, E.M., and Minkowycz, W.J., "Buoyancy Effects on Horizontal Boundary Layer Flow and Heat Transfer", Int. J. Heat Transfer, 1962, Vol. 5, pp. 501-511.

3. Sparrow, E.W., and Husar, R.B., "Longitudinal Vortices in Natural Convection Flow on Inclined Plates", J. Fluid Mech., 1969, Vol. 37, pp. 251-225.

4. Mori, Y., and Uchida, Y., "Forced Convective Heat Transfer Between Horizontal Flat Plates", Int. J. Heat Mass Transfer, 1966, Vol. 9, pp. 803-817.

5. Nakayama, W., Hwang, G.J., and Cheng, K.C., "Thermal Instability in Plane Poiseuille Flow", ASME J. Heat Transfer, 1970, Vol. 92, pp. 61-68.

6. Akiyama, M., Hwang, G.J., and Cheng, K.C., "Experiments on the Onset of Longitudinal Vortices in Laminar Forced Convection Between Horizontal Plates", ASME J. Heat Transfer, 1971, Vol. 93, pp. 335-341.

7. Hwang, G.J., and Cheng, K.C., " Convective Instability in the Thermal Entrance Region of a Horizontal Parallel Plate Channel Heated From Below", ASME J. Heat Transfer, 1973, Vol. 95, pp. 72-77..

8. Hwang, G.J., and Liu, C.L., "An Experiment Study of Convective Instability in the Thermal Entrance Region of a Horizontal Parallel-Plate Channel Heated From Below", Candian J. Chem. Eng., 1976, Vol. 54, pp. 521-525.

9. Kamotani, Y., and Ostroch, S., "Effect of Thermal Instability on Thermally Developing Laminar Channel Flow", ASME J. Heat Transfer, 1976, Vol. 98, pp. 62-66.

10. Kamotani, Y., Ostrach, S., and Miao, H., "Convective Heat Transfer Augmentation By Means of Thermal Instability", ASME J. Heat Transfer, 1979, Vol. 101, pp. 222-226.

11. Maughan, J.R., and Incropera, F.P., "Experiments on Mixed Convection Heat Transfer for Airflow in a Horizontal and Inclined Channel", Int. J. Heat Mass Transfer, 1987, Vol. 30, pp. 1307-1318.

12. Incropero, F.P and Schuut, J.A., "Numerical Simulation of Laminar Mixed Convection in the Entrance Region of Horizontal Rectangular Ducts", Numerical Heat Transfer, 1985, Vol. 8, pp. 707-729.

13. Cheng, K.C., and Kim, W., "Flow Visualization Studies on Vortex Instability of Natural Convection Flow Over Horizontal and Slightly Inclined Contant Temperature Plates", ASME Winter Annual Meeting, Dec. 1986, 86-WA/HT-85.

14. Incropera, F.P., Knox, A.L., and Maughan, J.R., "Mixed-Convection Flow and Heat Transfer in the Entry Region of a Horizontal Rectangular Duct", ASME J. Heat Transfer, 1987, Vol. 109, pp. 434-439.

15. Maughan, J.R., and Incropero, F.P., "Secondary Flow in Horizontal Channels Heated from Below", Experiments in Fluid, 1987, Vol. 5, pp. 334-343.

16. Chou, F.C., and Hwang, G.J., "Vorticity-Velocity Method for Graetz Problem and the Effect of Natural Convection in a Horizontal Rectangular Channel with Uniform Wall Heat Flux", ASME J. Heat Transfer, 1987, Vol. 109, pp. 704-710.

17. Chou, F.C., and Lin, J.N., "Convective Instability in the Thermal Entrance Region of Horizontal Rectangular Channels", National Heat Transfer Conference, 1989, HTD-Vol. 107.

18. Cheng, K.C., Hong, S.W., and Hwang, G.J., "Buoyancy Effects on Laminar Heat Transfer in the Thermal Entrance Region of Horizontal Rectangular Channels with Uniform Wall Heat Flux for Larger Prandtl Number Fluid", Int. J. Heat Mass Transfer, 1972, Vol. 15, pp. 1819-1836.

19. Mahaney, H.V., Incropera, F.P., and Ramadhyani, S., "Development of Laminar Mixed Convection Flow in a Horizontal Rectangular Duct with Uniform Bottom

Heating", Numerical Heat Transfer, 1987, Vol. 12, pp. 137-155.

20. Chou, F.C., and Hwang, G.J., "Combined Free and Forced Laminar Convection in Horizontal Rectangular Channels for High ReRa", Canadian J. Chemical Engineering, 1984, Vol. 62, pp. 830-836.

21. Cheng, K.C., and Ou, J.W., "Mixed Laminar Convection in the Thermal Entrance Region of Horizontal Rectangular Channels Heated from Below", Procs. 2nd ASME-JSME Thermal Engineering Joint Conference, 1987, Vol. 4, pp. 159-164.

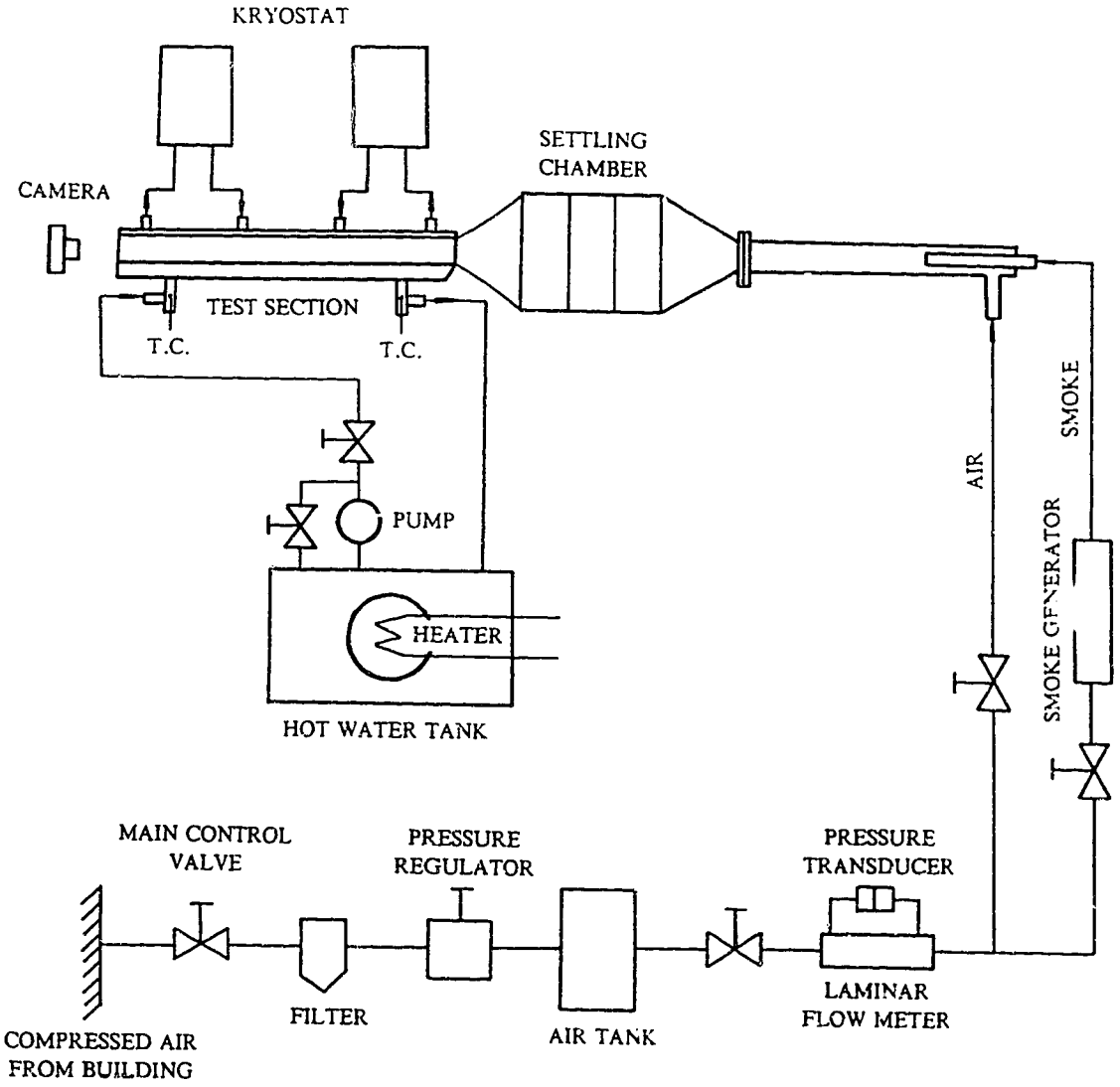

Fig. 4.1 Schematic diagram of test setup

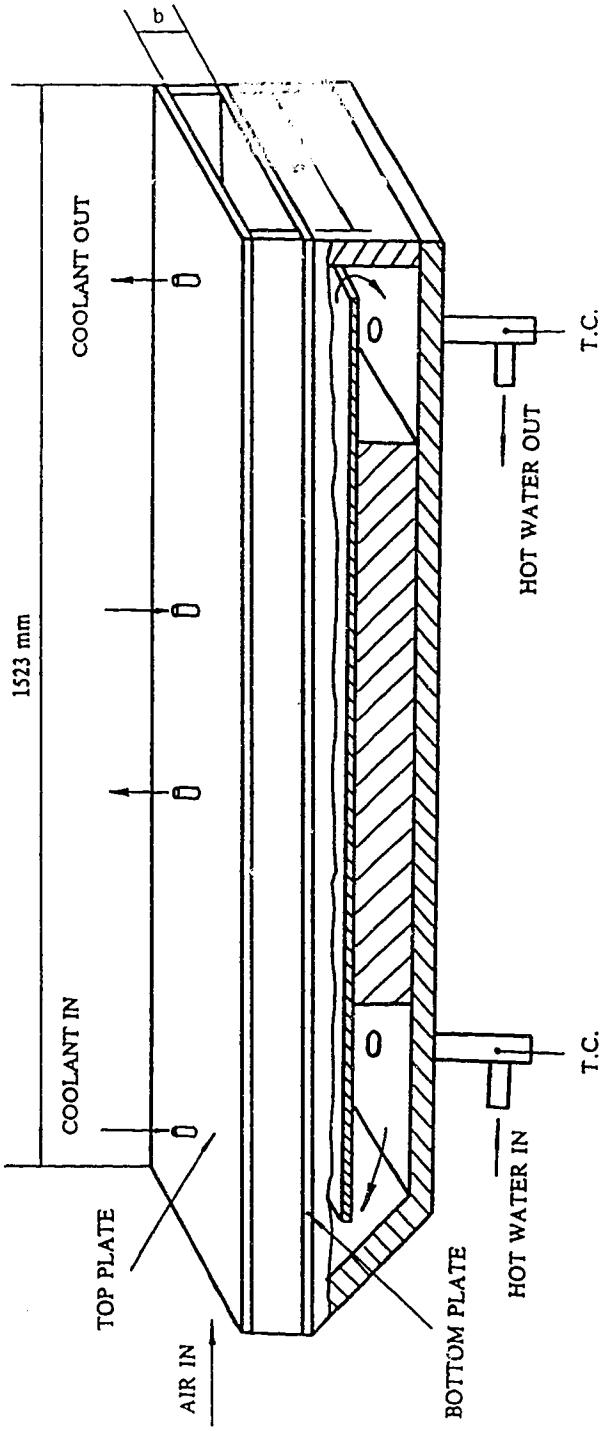

Fig. 4.2 Schematic diagram of the test section

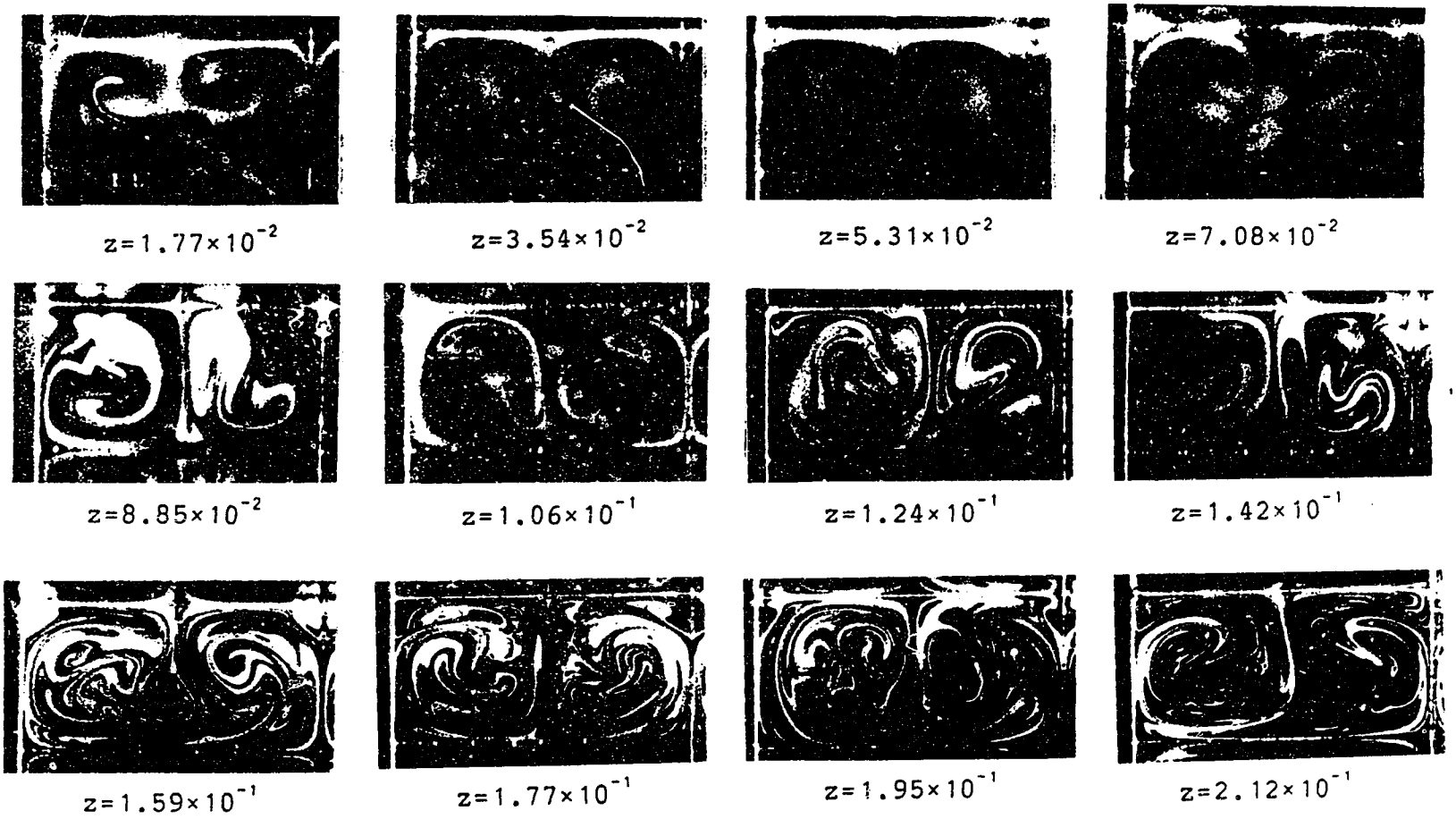

Fig. 4.3 Cross-sectional views of developing secondary flow patterns for the case U_m=0.1 m/sec., T_h-T_c=28.8°C, $T_c=T_{air}$=23.4°C, Re=2.10×10^2, Gr=1.56×10^5, Pr=0.71 and a/b=2

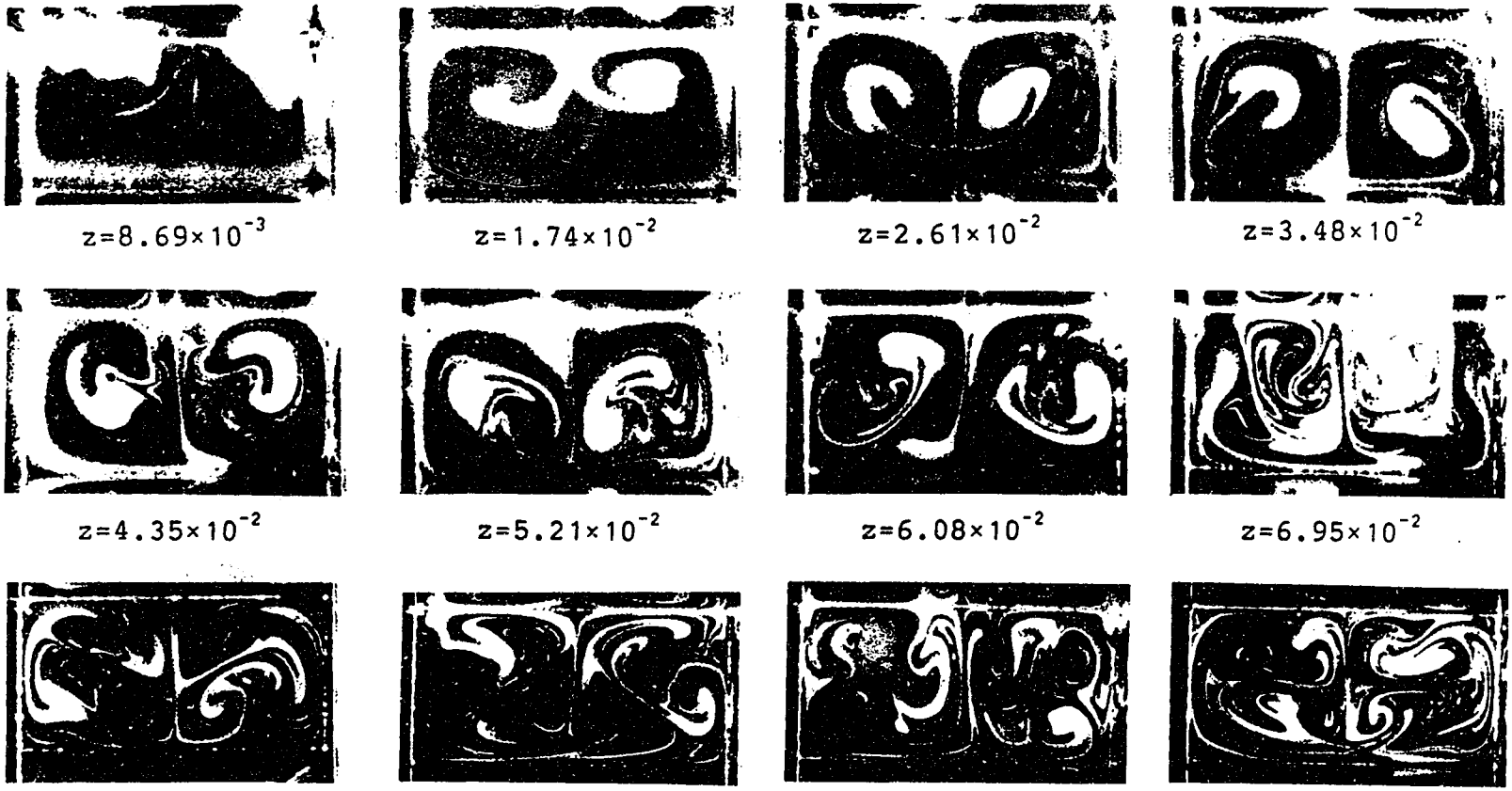

Fig. 4.4 Cross-sectional views of developing secondary flow patterns for the case U_m=0.2 m/sec., T_h-T_c=28.8°C, $T_c=T_{air}$=23.2°C, Re=4.27×10^2, Gr=1.56×10^5, Pr=0.71 and a/b=2

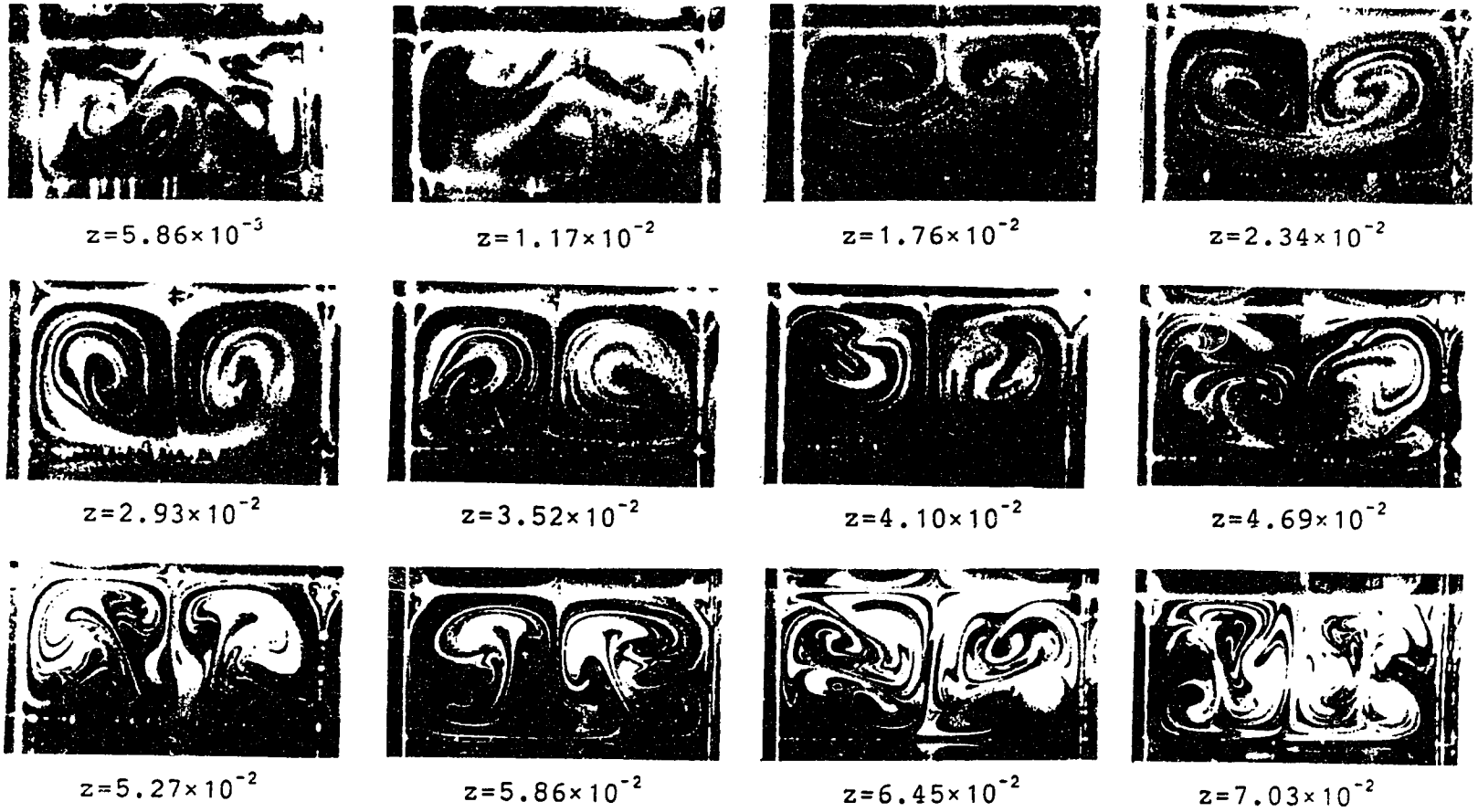

Fig. 4.5 Cross-sectional views of developing secondary flow patterns for the case U_m=0.3 m/sec., T_h-T_c=29.2°C, $T_c=T_{air}$=23.5°C, Re=6.34×10^2, Gr=1.57×10^5, Pr=0.71 and a/b=2

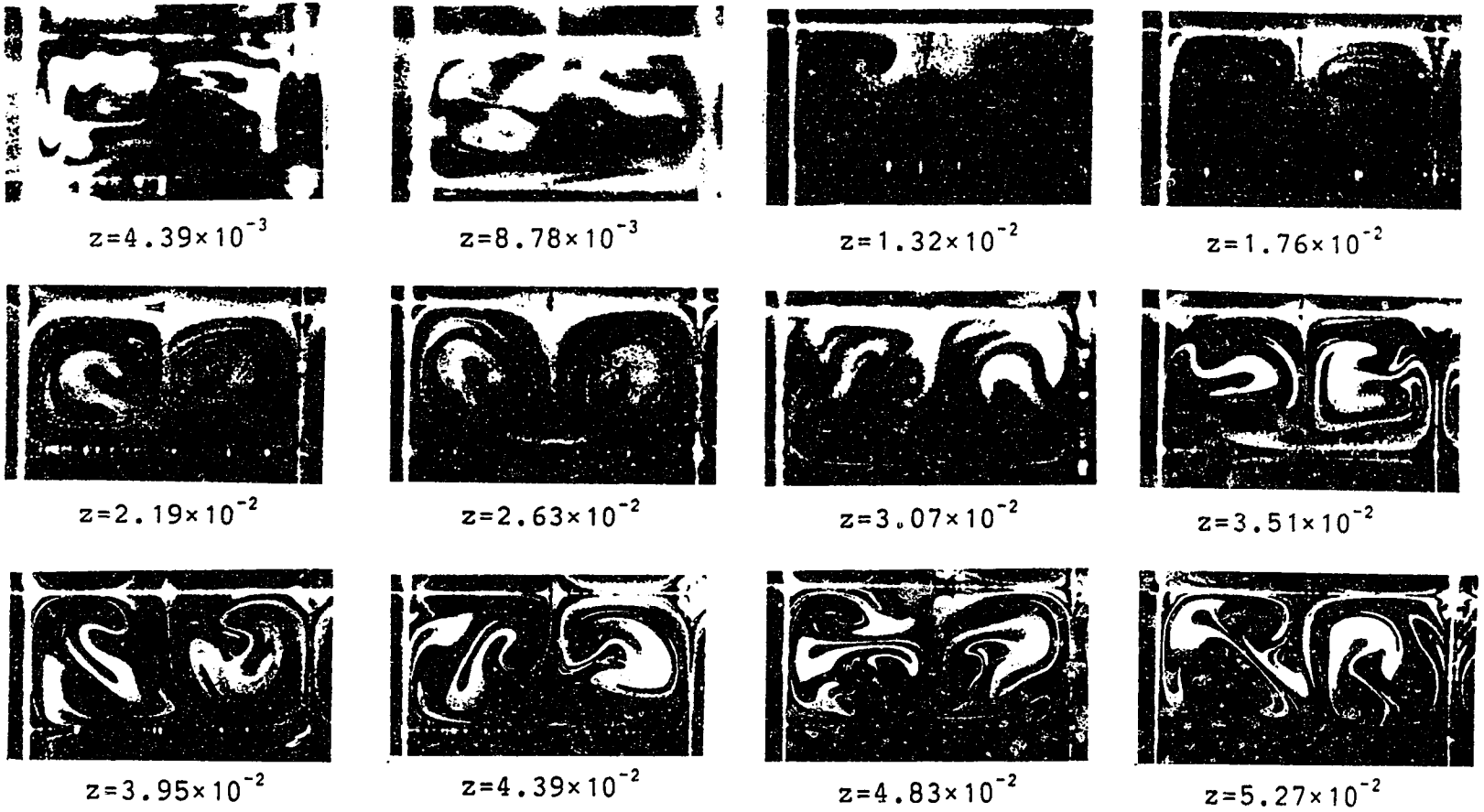

Fig. 4.6 Cross-sectional views of developing secondary flow patterns for the case U_m=0.4 m/sec., T_h-T_c=29.2°C, $T_c=T_{air}$=23.4°C, Re=8.46×10^2, Gr=1.57×10^5, Pr=0.71 and a/b=2

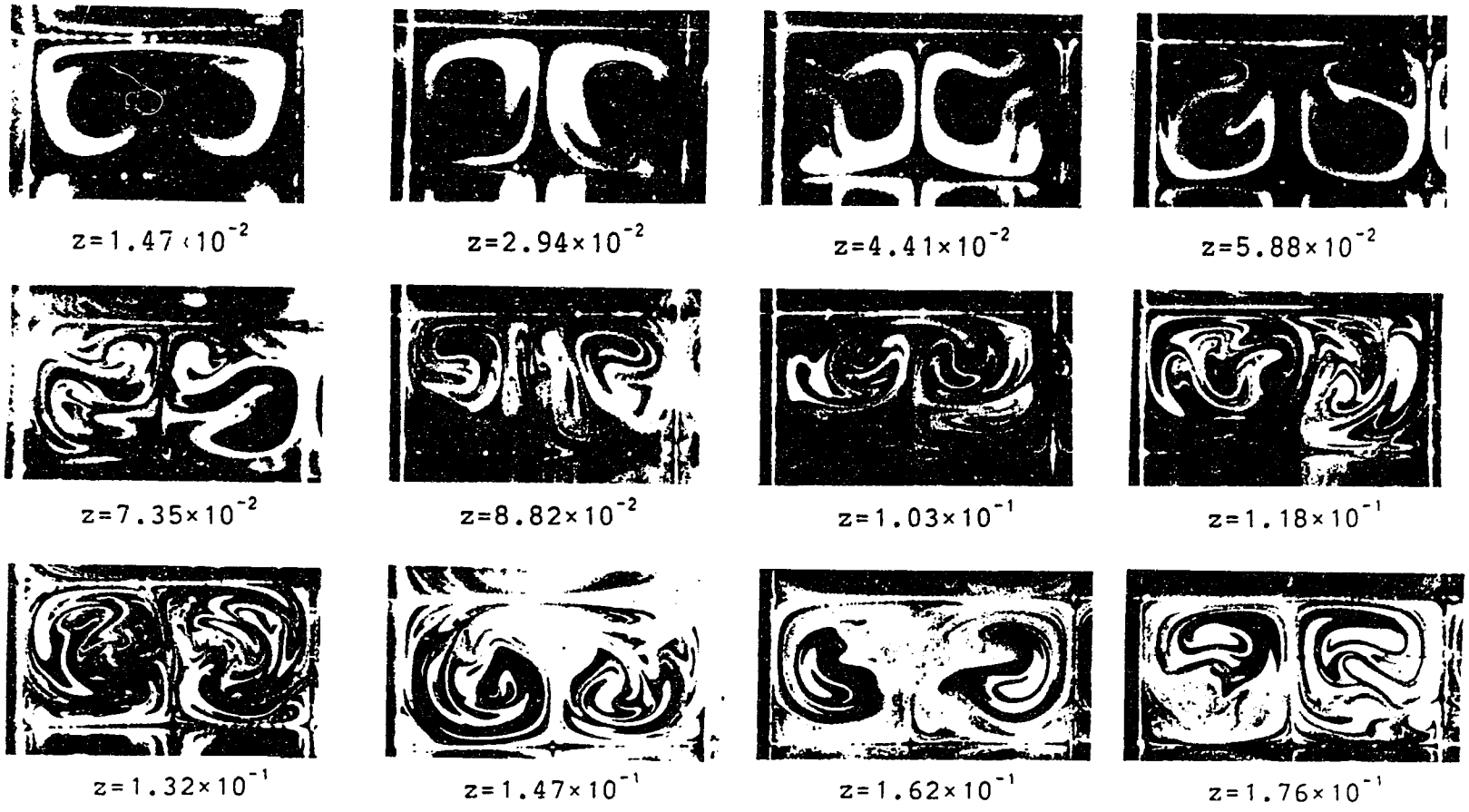

Fig. 4.7 Cross-sectional views of developing secondary flow patterns for the case U_m=0.1 m/sec., T_h-T_c=30.1°C, $T_h=T_{air}$=23.9°C, Re=2.50×10^2, Gr=2.53×10^5, Pr=0.71 and a/b=2

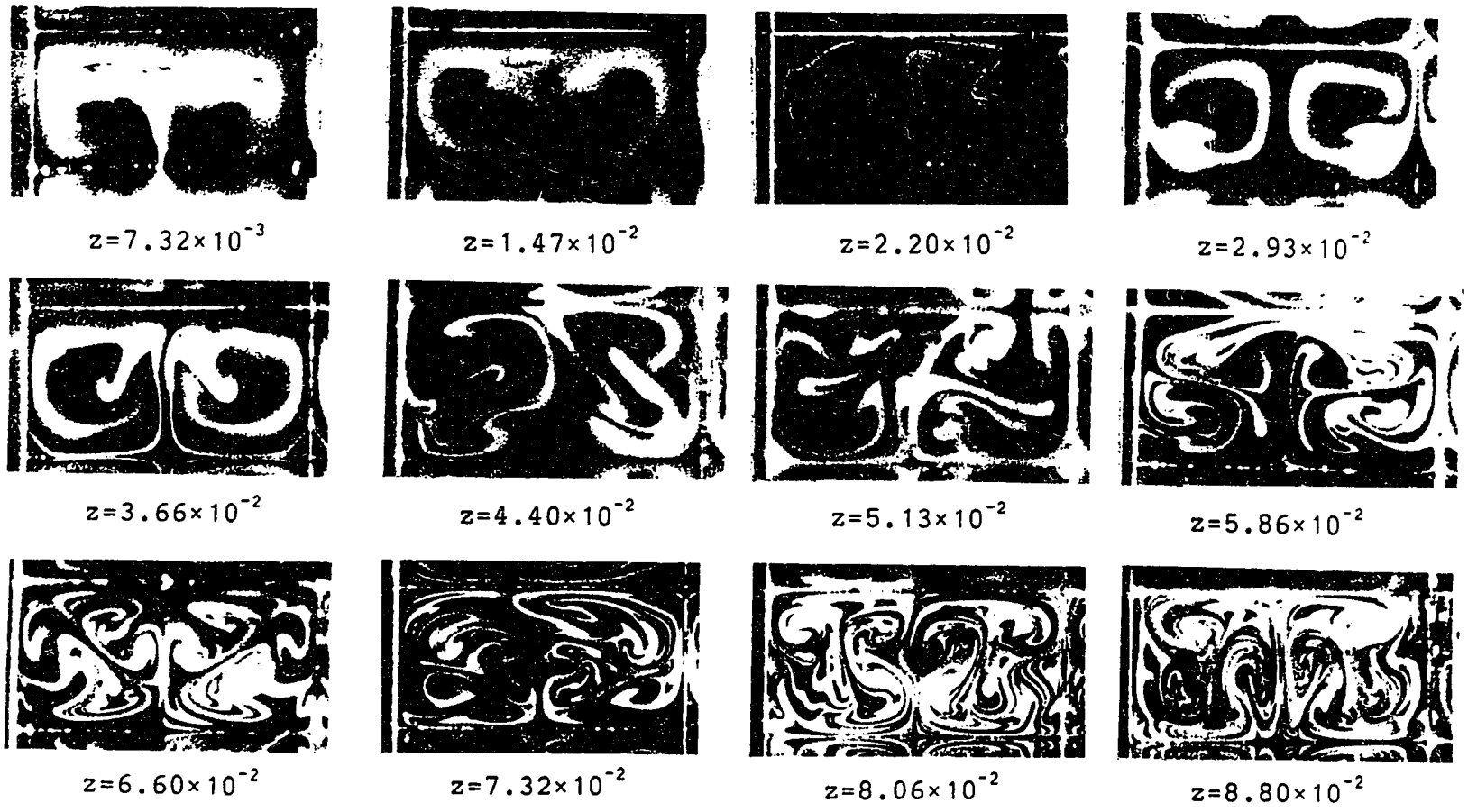

Fig. 4.8 Cross-sectional views of developing secondary flow patterns for the case U_m=0.2 m/sec., T_h-T_c=29.7°C, $T_h=T_{air}$=23.4°C, Re=5.04×10^2, Gr=2.50×10^5, Pr=0.71 and a/b=2

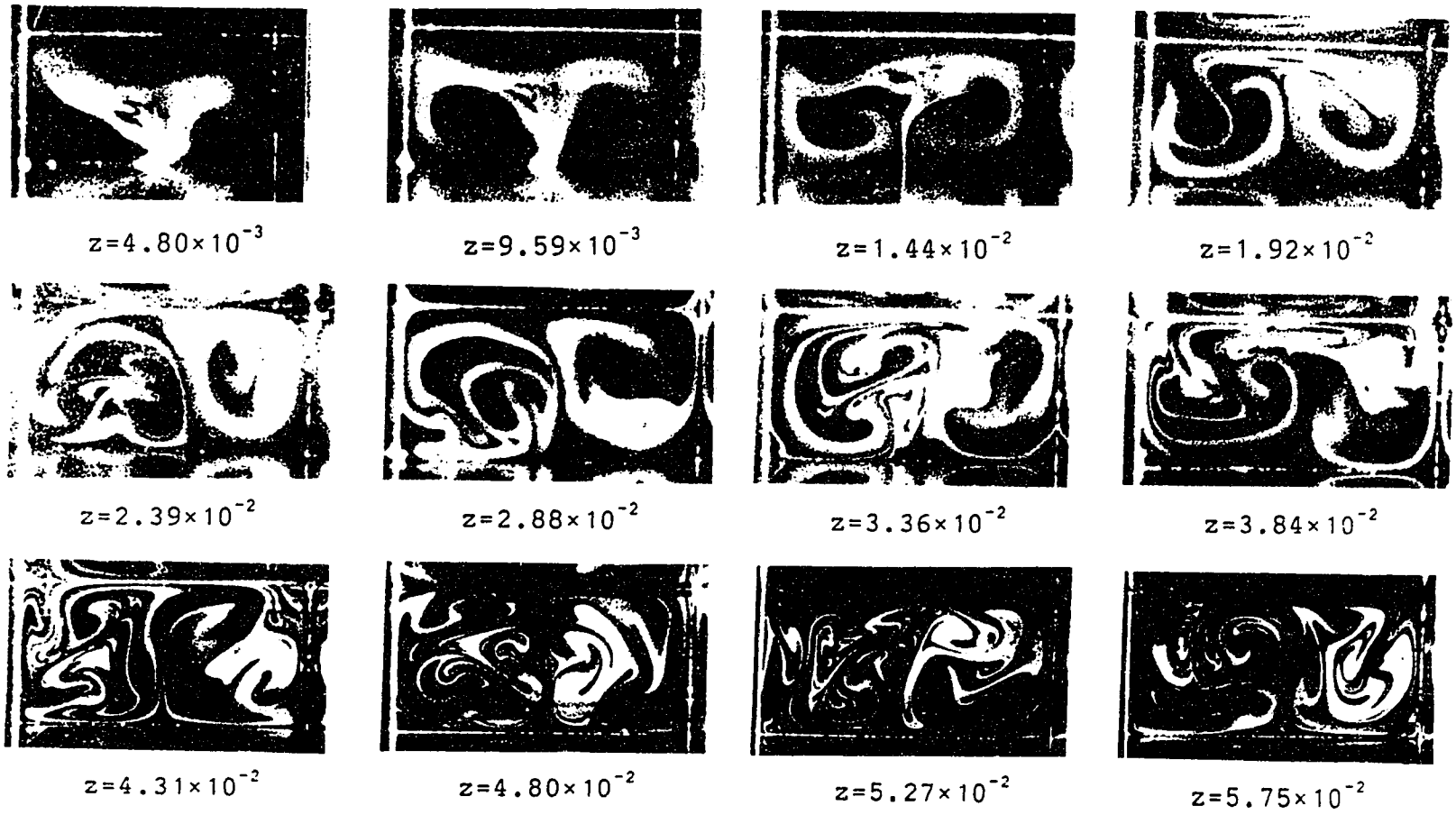

Fig. 4.9 Cross-sectional views of developing secondary flow patterns for the case U_m=0.3 m/sec., T_h-T_c=30.6°C, T_h=T_{air}=24.2°C, Re=7.70×10^2, Gr=2.57×10^5, Pr=0.71 and a/b=2

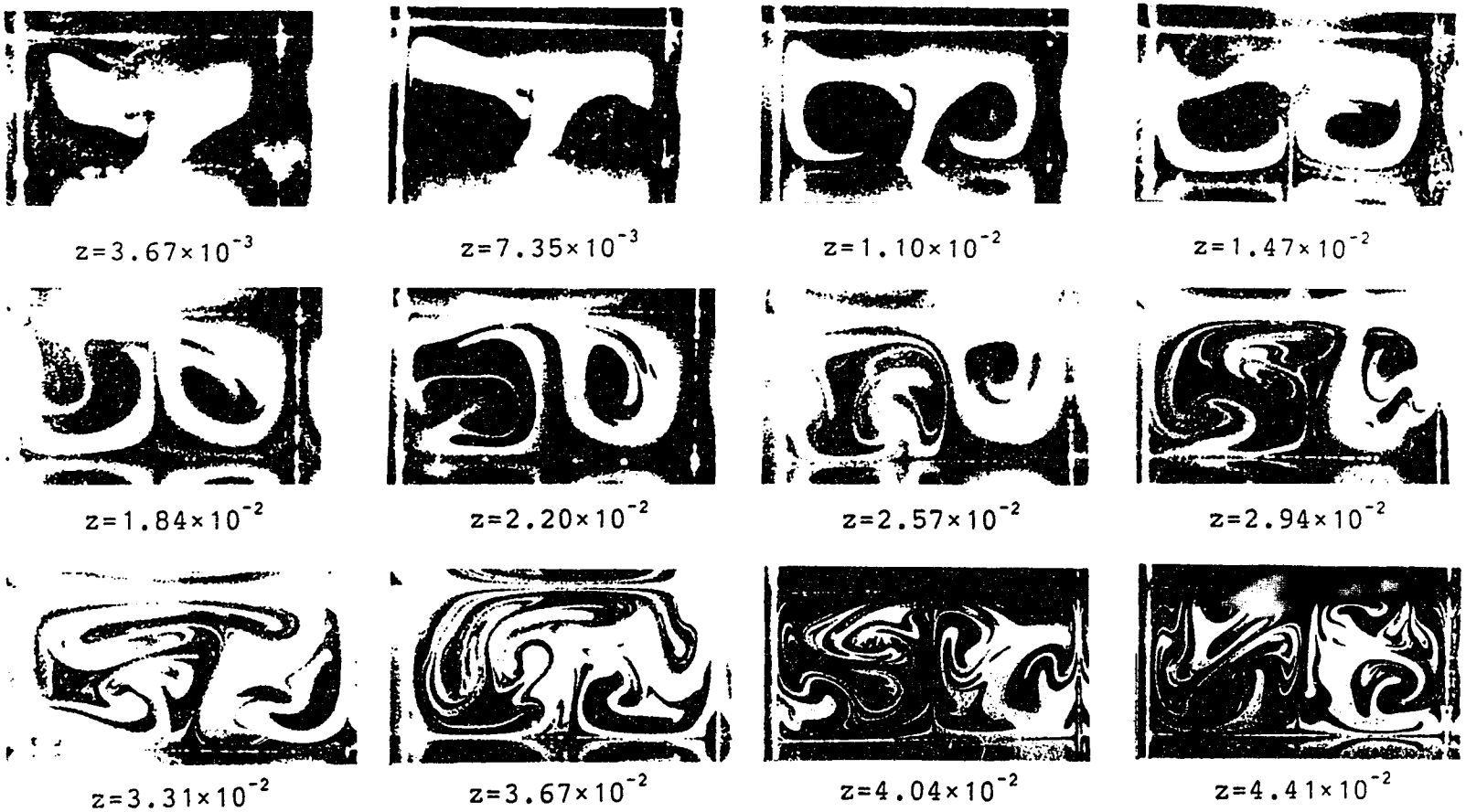

Fig. 4.10 Cross-sectional views of developing secondary flow patterns for the case U_m=0.4 m/sec., T_h-T_c=30.9°C, $T_h=T_{air}$=24.1°C, Re=1.00×10^3, Gr=2.58×10^5, Pr=0.71 and a/b=2

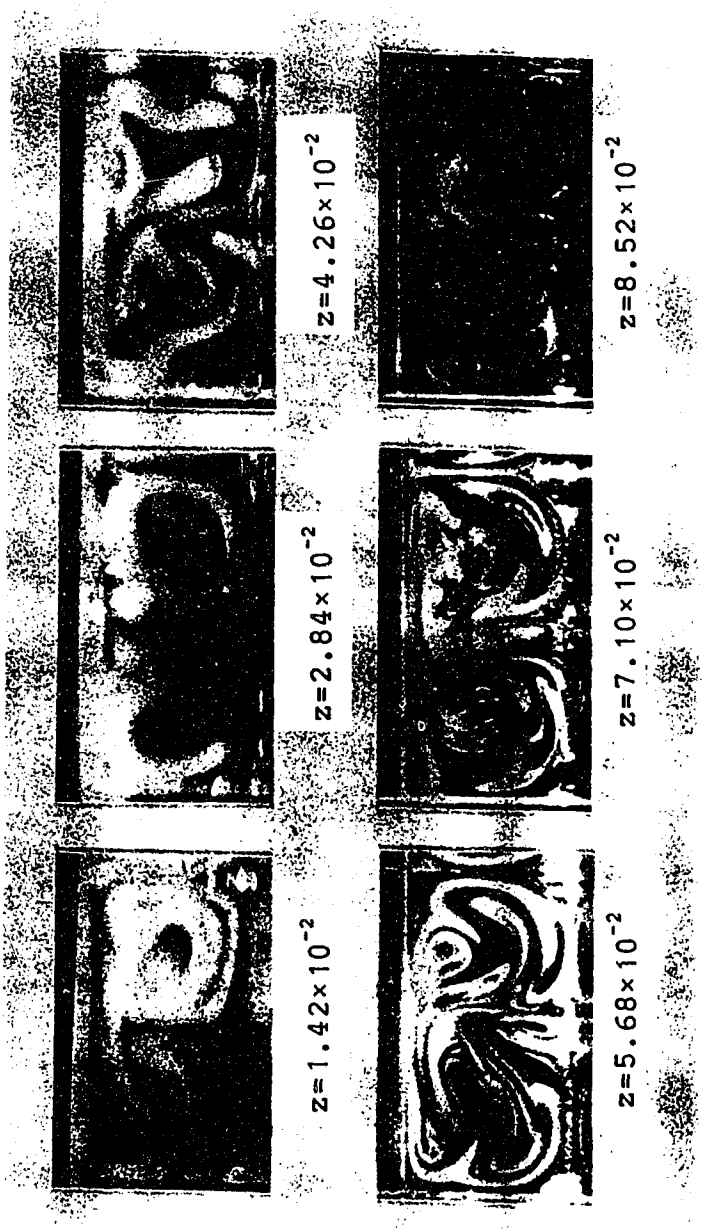

Fig. 4.11 Cross-sectional views of developing secondary flow patterns for the case U_m=0.1 m/sec, T_h-T_c=40.8°C, $T_h=T_{air}$=22.9°C, Re=2.59×10², Gr=3.83×10⁵, Pr=0.71 and a/b=2

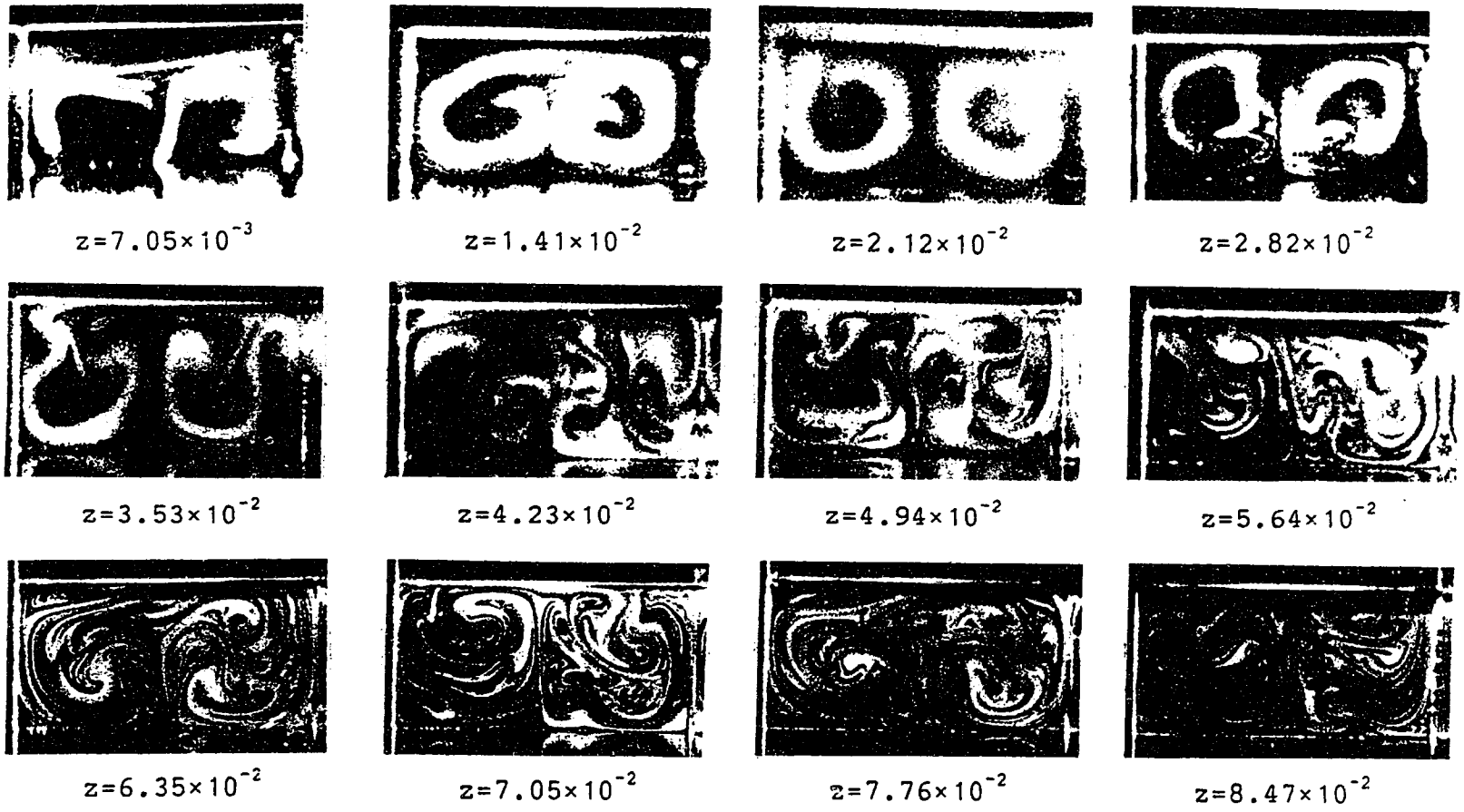

Fig. 4.12 Cross-sectional views of developing secondary flow patterns for the case U_m=0.2 m/sec., T_h-T_c=41.0°C, $T_h=T_{air}$=23.7°C, Re=5.21×10^2, Gr=3.83×10^5, Pr=0.71 and a/b=2

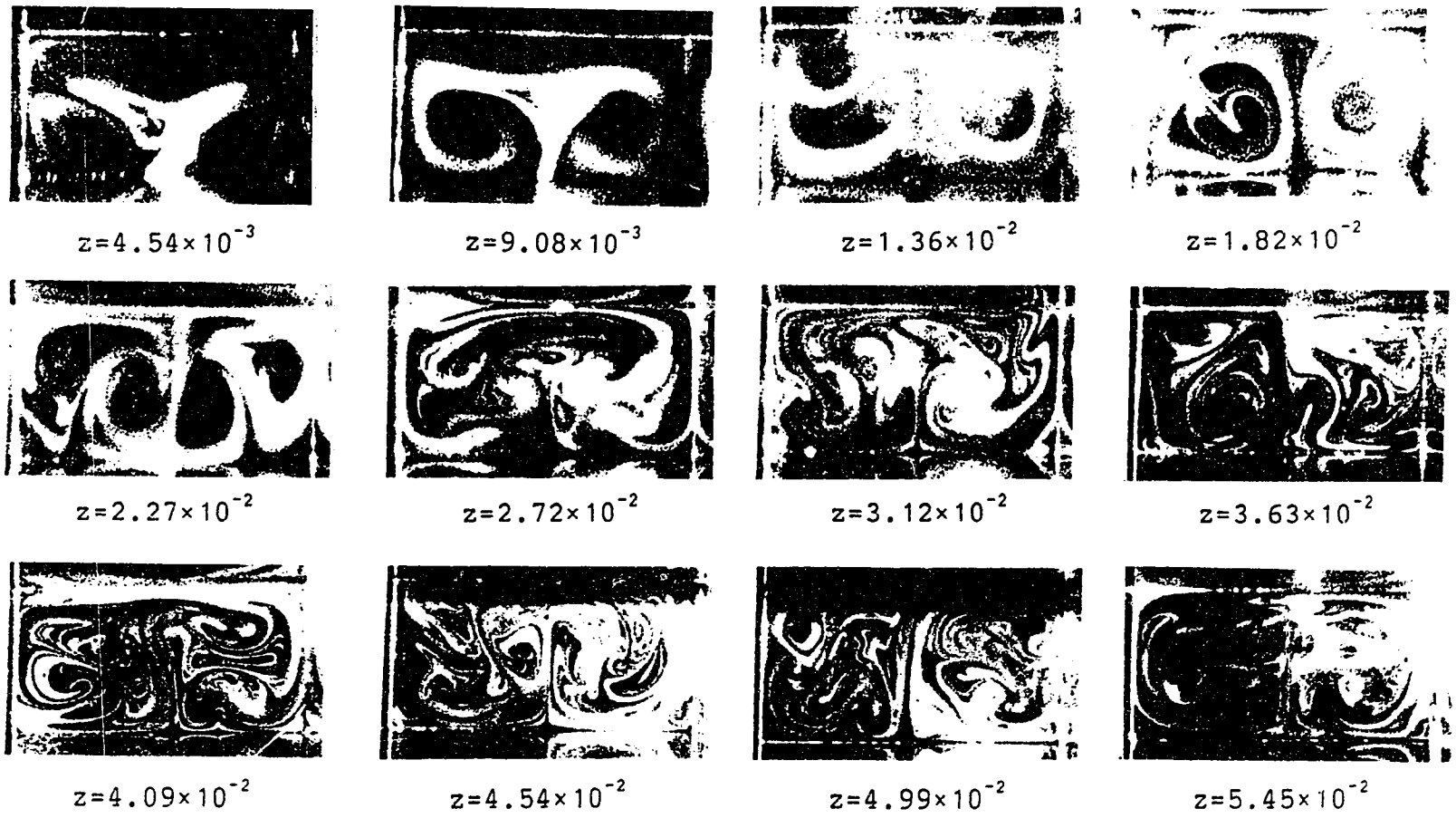

Fig. 4.13 Cross-sectional views of developing secondary flow patterns for the case U_m=0.3 m/sec., T_h-T_c=41.1°C, $T_h=T_{air}$=23.1°C, Re=8.11×10^2, Gr=3.86×10^5, Pr=0.71 and a/b=2

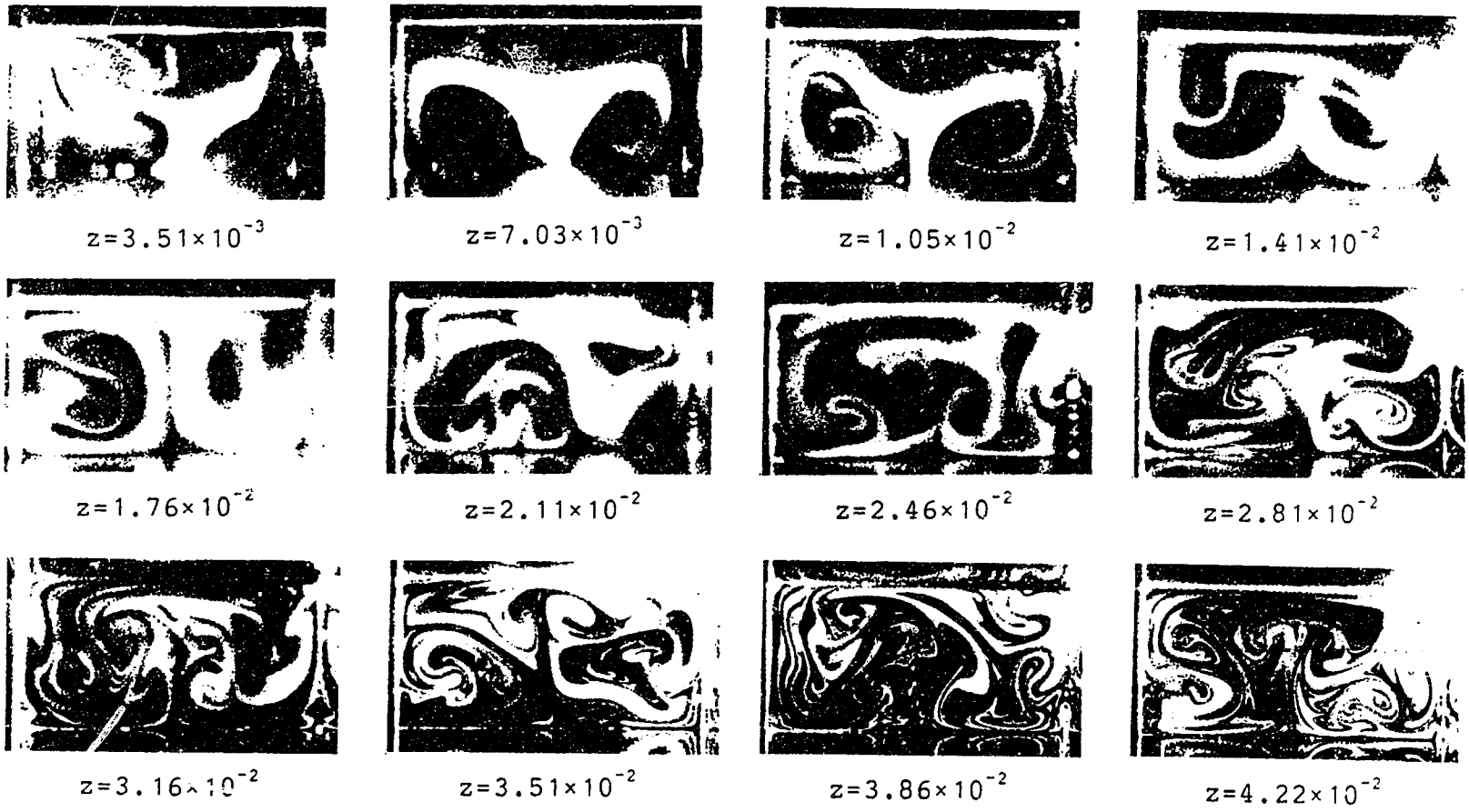

Fig. 4.14 Cross-sectional views of developing secondary flow patterns for the case U_m=0.4 m/sec., T_h-T_c=41.3°C, $T_h=T_{air}$=24.3°C, Re=1.05×10^3, Gr=3.87×10^5, Pr=0.71 and a/b=2

$z=1.55\times10^{-2}$

$z=3.10\times10^{-2}$

$z=4.65\times10^{-2}$

Fig. 4.15 Cross-sectional views of developing secondary flow patterns for the case U_m=0.1 m/sec., T_h-T_c=68.6°C, T_H=51.4°C, T_{air}=24.2°C, Re=2.38×10^2, Gr=5.08×10^5, Pr=0.71 and a/b=2

Fig. 4.16 Cross-sectional views of developing secondary flow patterns for the case U_m=0.2 m/sec., T_h-T_c=68.4°C, T_h=51.6°C, T_{air}=24.0°C, Re=4.76×10^2, Gr=5.04×10^5, Pr=0.71 and a/b=2

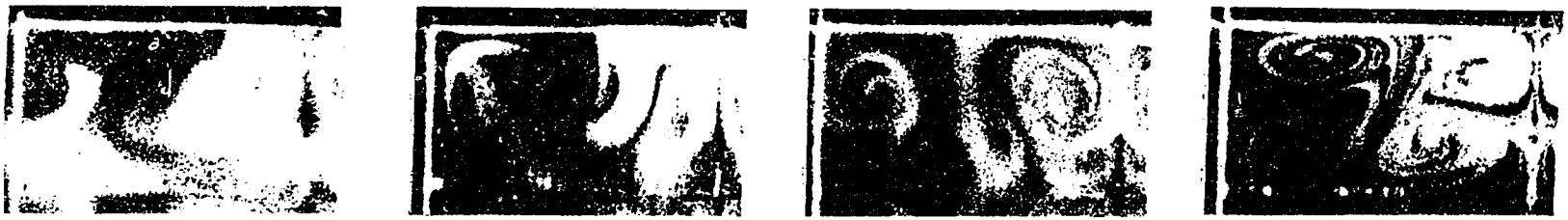

Fig. 4.17 Cross-sectional views of developing secondary flow patterns for the case U_m=0.3 m/sec., T_h-T_c=68.1°C, T_h=51.6°C, T_{air}=23.8°C, Re=7.14×10^2, Gr=5.02×10^5, Pr=0.71 and a/b=2

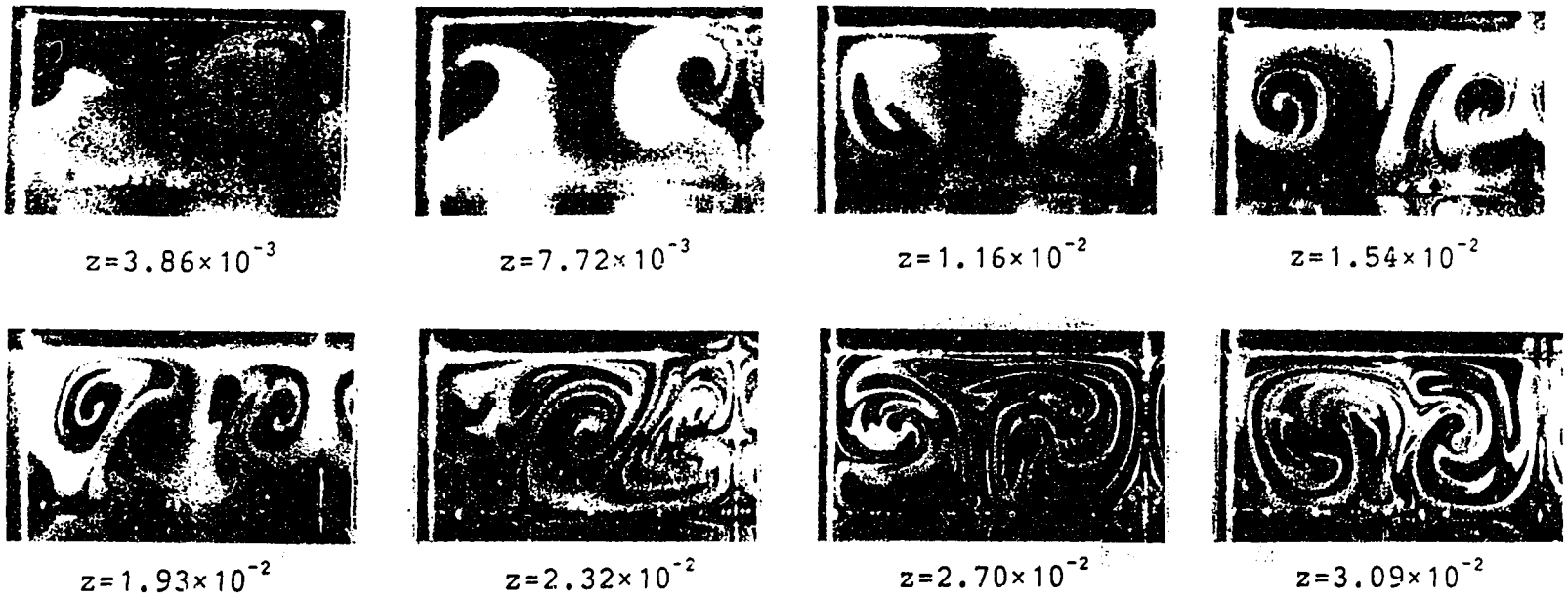

Fig. 4.18 Cross-sectional views of developing secondary flow patterns for the case U_m=0.4 m/sec., T_h-T_c=68.0°C, T_h=51.6°C, T_{air}=23.5°C, Re=9.56×10^2, Gr=5.00×10^5, Pr=0.71 and a/b=2

$z=1.03\times10^{-2}$

$z=5.14\times10^{-2}$

$z=2.06\times10^{-2}$

$z=6.18\times10^{-2}$

$z=3.08\times10^{-2}$

$z=7.20\times10^{-2}$

$z=4.11\times10^{-2}$

$z=8.22\times10^{-2}$

Fig. 4.19 Cross-sectional views of developing secondary flow patterns for the case $U_m=0.1$ m/sec., $T_h-T_c=29.7°C$, $T_c=T_{air}=23.5°C$, $Re=2.75\times10^2$, $Gr=3.61\times10^5$, $Pr=0.71$ and $a/b=7$

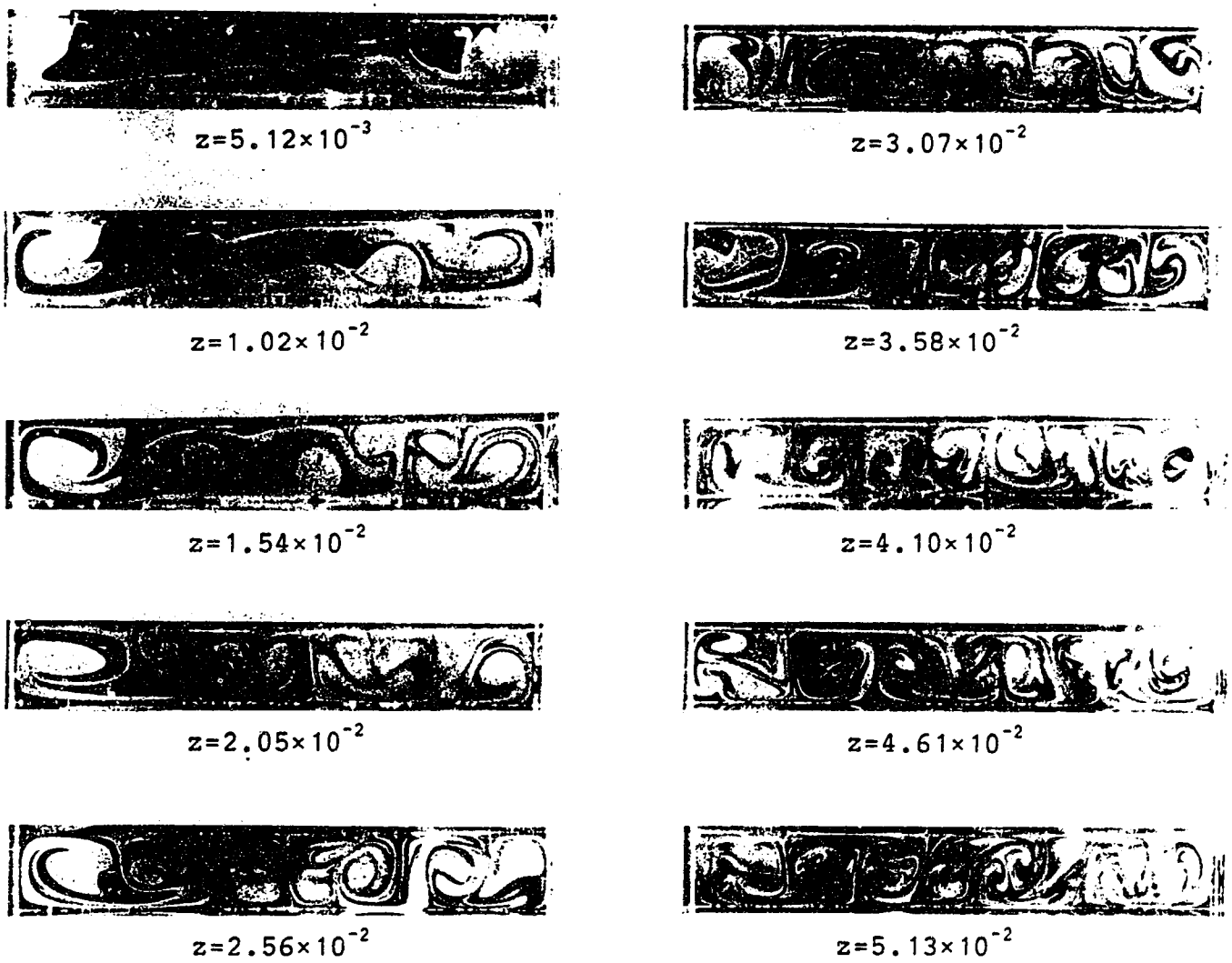

Fig. 4.20 Cross-sectional views of developing secondary flow patterns for the case U_m=0.2 m/sec., T_h-T_c=29.9°C, $T_c=T_{air}$=23.4°C, Re=5.52×10^2, Gr=3.63×10^5, Pr=0.71 and a/b=7

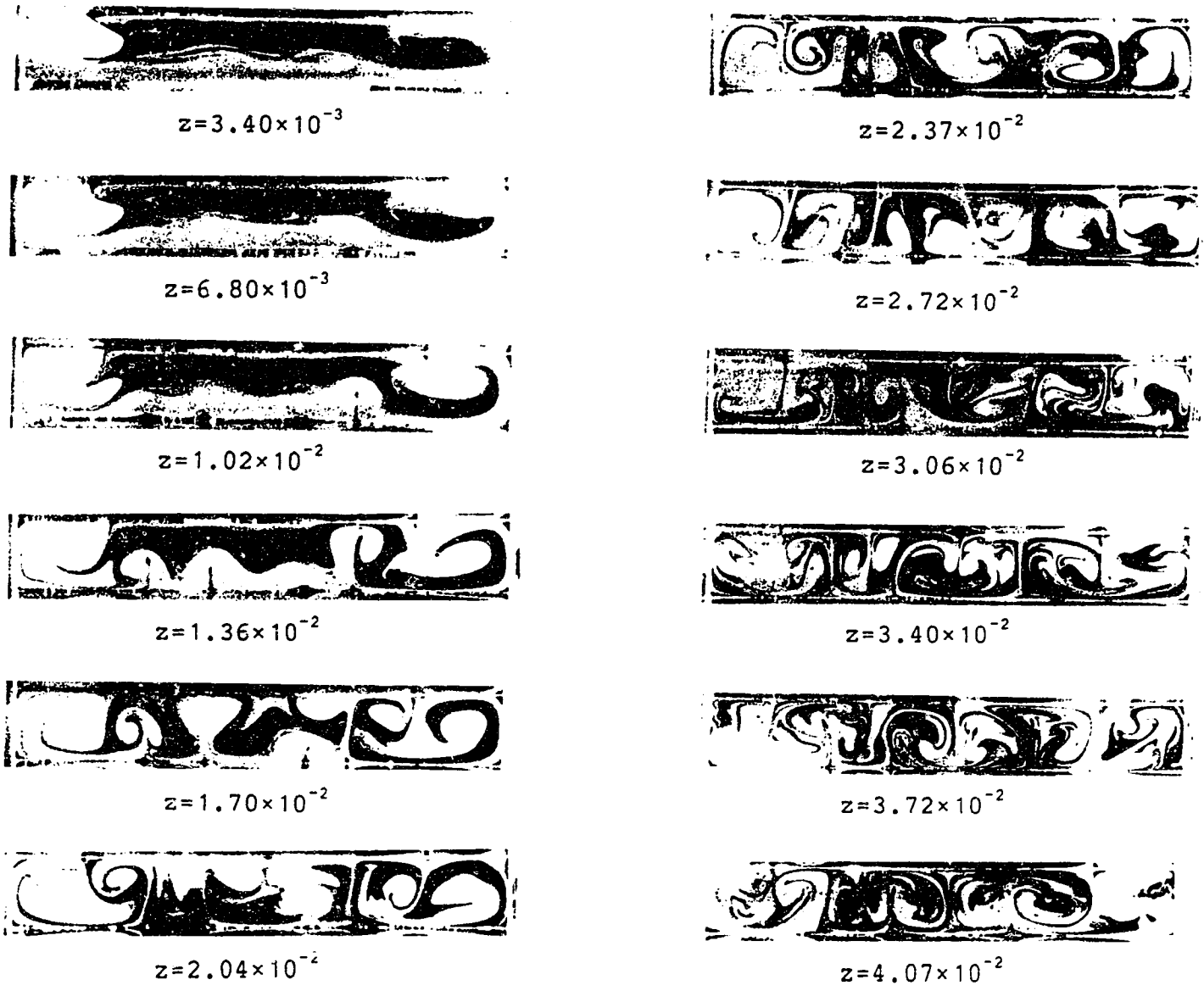

Fig. 4.21 Cross-sectional views of developing secondary flow patterns for the case U_m=0.3 m/sec., T_h-T_c=30.0°C, $T_c=T_{air}$=23.4°C, Re=8.33×10^2, Gr=3.65×10^5, Pr=0.71 and a/b=7

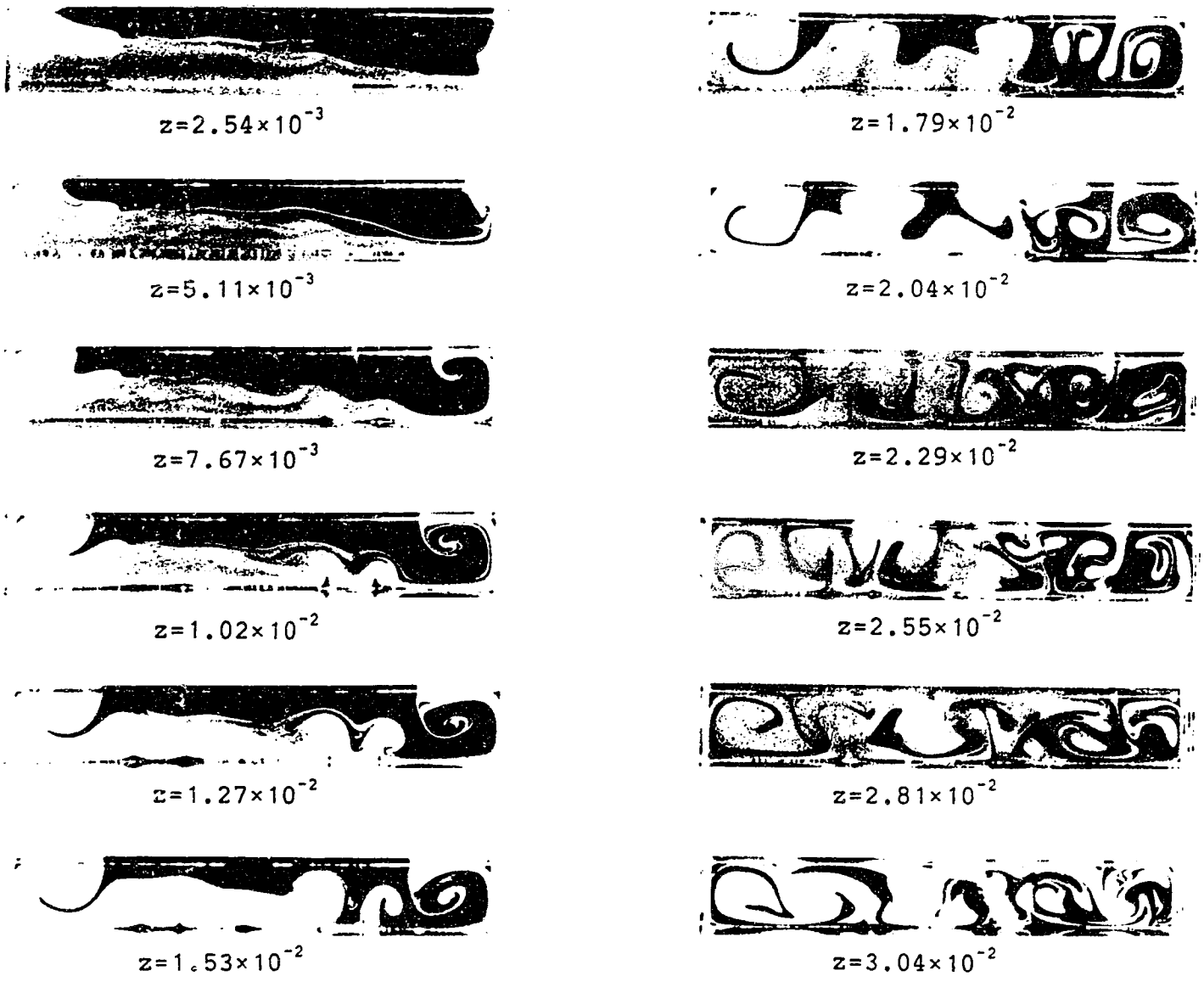

Fig. 4.22 Cross-sectional views of developing secondary flow patterns for the case U_m=0.4 m/sec., T_h-T_c=29.8°C, $T_c=T_{air}$=23.0°C, Re=1.11×10^3, Gr=3.66×10^5, Pr=0.71 and a/b=7

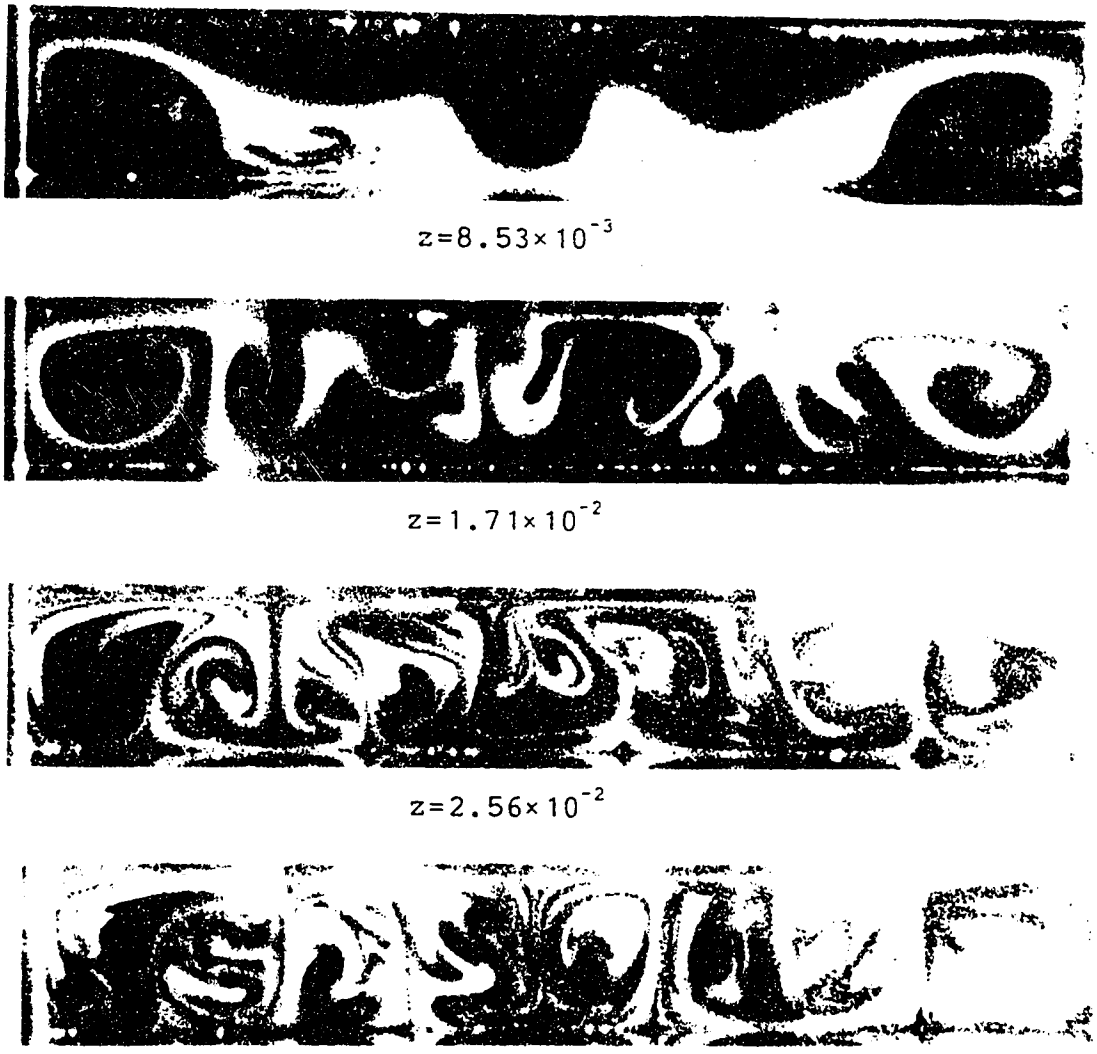

Fig. 4.23 Cross-sectional views of developing secondary flow patterns for the case U_m=0.1 m/sec., T_h-T_c=30.2°C, $T_h=T_{air}$=24.0°C, Re=3.29×10^2, Gr=5.81×10^5, Pr=0.71 and a/b=7

Fig. 4.24 Cross-sectional views of developing secondary flow patterns for the case U_m=0.2 m/sec., T_h-T_c=30.5°C, $T_h=T_{air}$=23.8°C, Re=6.61×10^2, Gr=5.58×10^5, Pr=0.71 and a/b=7

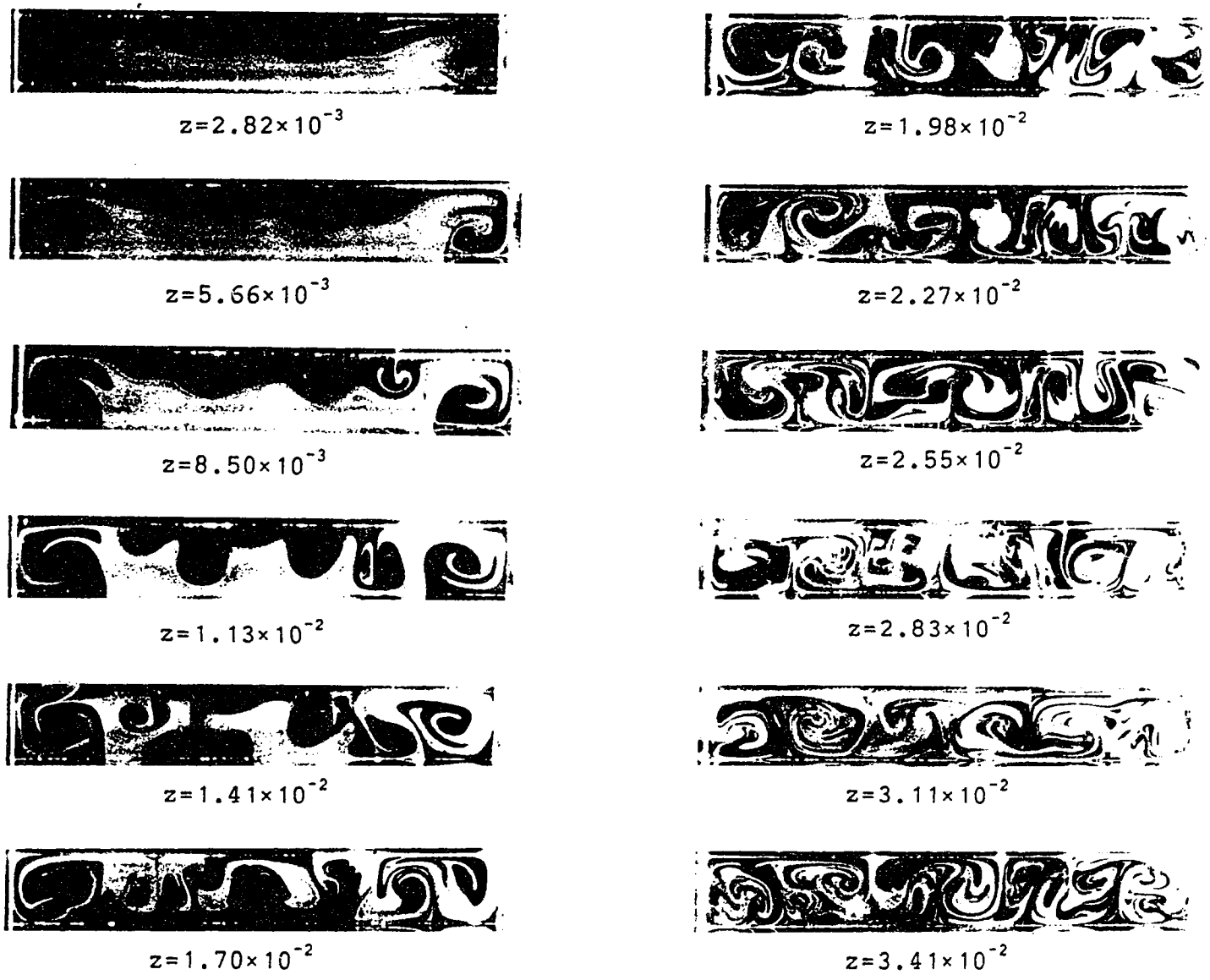

Fig. 4.25 Cross-sectional views of developing secondary flow patterns for the case U_m=0.3 m/sec., T_h-T_c=30.6°C, $T_h=T_{air}$=23.8°C, Re=9.91×10², Gr=5.86×10⁵, Pr=0.71 and a/b=7

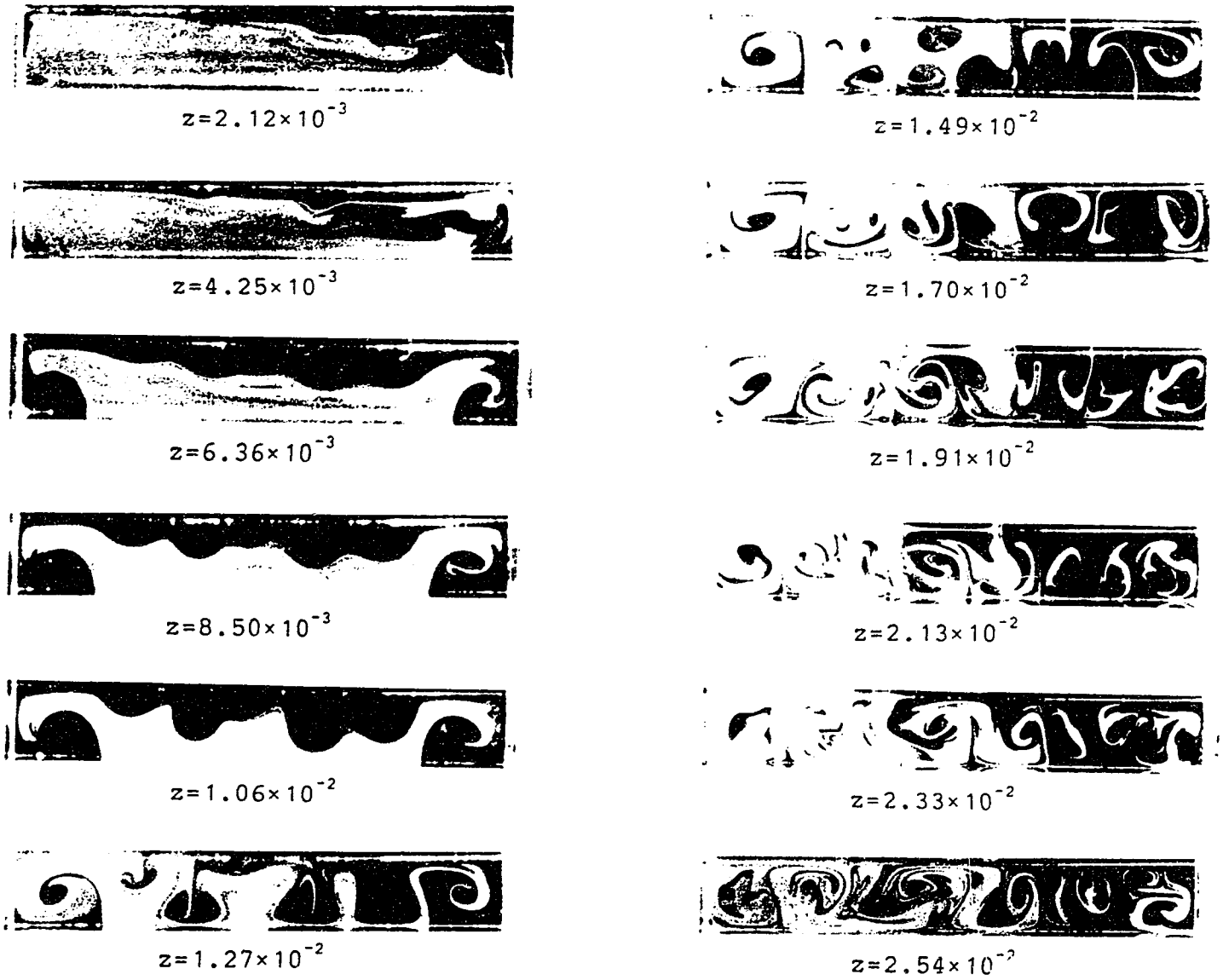

Fig. 4.26 Cross-sectional views of developing secondary flow patterns for the case U_m=0.4 m/sec., T_h-T_c=30.8°C, $T_h=T_{air}$=23.9°C, Re=1.32×10^3, Gr=5.88×10^5, Pr=0.71 and a/b=7

$z=8.98\times10^{-3}$

$z=1.80\times10^{-2}$

Fig. 4.27 Cross-sectional views of developing secondary flow patterns for the case U_m=0.1 m/sec., T_h-T_c=69.0°C, T_h=51.9°C, T_{air}=24.1°C, Re=3.14×10^2, Gr=1.16×10^6, Pr=0.71 and a/b=7

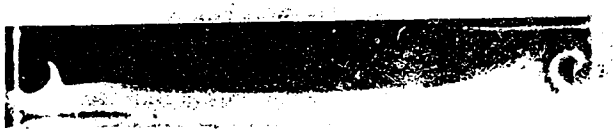

$z=4.48\times10^{-3}$

$z=1.35\times10^{-2}$

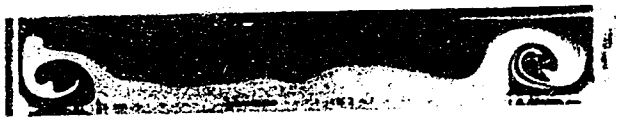

$z=8.98\times10^{-3}$

$z=1.79\times10^{-2}$

Fig. 4.28 Cross-sectional views of developing secondary flow patterns for the case $U_m=0.2$ m/sec., $T_h-T_c=69.1°C$, $T_h=51.9°C$, $T_{air}=24.1°C$, $Re=6.27\times10^2$, $Gr=1.16\times10^6$, $Pr=0.71$ and $a/b=7$

Fig. 4.29 Cross-sectional views of developing secondary flow patterns for the case U_m=0.3 m/sec., T_h-T_c=69.2°C, T_h=51.9°C, T_{air}=23.8°C, $Re=9.41\times10^2$, $Gr=1.16\times10^6$, Pr=0.71 and a/b=7

Fig. 4.30 Cross-sectional views of developing secondary flow patterns for the case U_m=0.4 m/sec., T_h-T_c=69.2°C, T_h=51.9°C, T_{air}=23.8°C, Re=1.26×10^3, Gr=1.16×10^6, Pr=0.71 and a/b=7

5. Conclusions

5.1 Secondary Flow in Curved Ducts with and without Offset Bends

In order to obtain some further physical understanding of flow in larger curvature ratio ducts with and without offset bends, visualization experiments were conducted for circular bends with curvature ratio $a/R_C=0.2$ and for square bends with $a/R_C=0.2$ and 0.4. The Dean number varied from K=25 to 350 for both the circular bends and the square bends with $a/R_C=0.2$, and from K=100 to 450 for the square bends with $a/R_C=0.4$. The offset bends had two offset positions, offset angle $\theta=90°$ and 180°. The flow at the inlet of the test section was fully developed laminar flow. Photographs of the secondary flow patterns at the exit of each bend were presented.

When Dean number $K\leq100$, the effect of the second bend dominates the flow patterns. However, at high Dean number, the flow from the first bend has a strong effect on the flow patterns. Also, if the second bend angle is less than 45°, the flow patterns are mainly controlled by the first bend.

Dean's instability phenomena were observed in the s-bends. It was also found that Dean's instability phenomena occur more easily in the square cross-sectional bends. It was also found that another two vortices appear in the inner top and bottom corners in addition to the Dean's instability vortices.

It seems that the effects of Dean number K on secondary flow patterns and the development tendency of the secondary flow in square bends with $a/R_c=0.4$ are not much different from those for square bends with $a/R_c=0.2$. However, compared with the square bends with $a/R_c=0.2$, it was found that the Dean's instability vortices appear in the at higher Dean number for the square s-bends with $a/R_c=0.4$. It was also noted that a pair of small vortices appeared near the center of the inner wall for the case of $a/R_c=0.4$.

5.2 Developing Axial Velocity Profiles for Laminar Flow in the Entrance Region of S-bend

Axial velocity was measured by means of a hot-film anemometer with a single hot-film sensor for circular s-bends with $a/R_c=0.2$ and for square s-bends with $a/R_c=0.2$ and 0.4 to further understand the phenomena of flow in large curvature ratio ducts, especially in s-bends. The Dean numbers were K=200 and 350 for the circular s-bends, and K=350 for the square s-bends. Axial velocity profiles along vertical and horizontal axes, and the development of axial velocity in the s-bends were presented.

Present studies revealed three kinds of velocity profiles in the first bends. If the velocity was measured along the vertical axis, the M-shape profile, flat-front-shape profile and four-wave-shape profile were observed. If the velocity was measured along the horizontal axis, three typical profile shapes were produced: the shape

with the maximum velocity point located close to the outer wall, the shape with a depressed center region, and the shape with a flat plateau at the center.

It was noted that the velocity profiles become more complex in the second bend. Along the vertical axis, three skewed typical shapes of the first bends were observed, but the maximum velocity could appear in the center region and the profiles were not symmetric.

It was found that the Dean number K with the range K=25 to 350 and the curvature ratio, a/R_C=0.2 and 0.4, have little effect on the basic developing velocity profiles. However, for larger Dean number flow, the maximum velocity point along the horizontal axis is closer to the outer wall. For the flow in larger curvature ratio bends, the velocity may become unstable because of the flow separation at the inner wall.

5.3 Buoyancy Force Induced Secondary Flow in the Entrance Region of Horizontal Rectangular Channels Heated Isothermally from Below and/or Cooled Isothermally from Above

The developing buoyancy force induced secondary flow patterns in the simultaneous hydrodynamic and thermal entrance region of horizontal rectangular channels with an isothermally heated lower wall and/or an isothermally cooled upper wall were studied by flow visualization methods. The mean velocities of main air flow were U_m=0.1, 0.2, 0.3, 0.4

m/sec..

It was noted that the flow for the cooled case was more unstable than that for the heating case at the same Grashof number. The direction of secondary flows for the cooled case was generally opposite to that for the heating case due to the different wall effects. The wall effect was very considerable, and the longitudinal vortex rolls appeared earlier for channels with small aspect ratio. Thus, the entrance length for small aspect ratio channels is shorter, and the heat transfer coefficient is consequently to be higher.

It was noted that, for the case of heating and cooling simultaneously , the onset position of thermal instability is not much different from that of the cooling case. However, the secondary flow develops much faster after the thermal instability onset point. For larger main flow velocity, the onset of thermal instability appears later, and the longitudinal vortex rolls become less unstable.